Three Dimensional Dynamics of Micro Tools and Miniature Ultra-High-Speed Spindles

Submitted in partial fulfillment of the requirements for

the degree of

Doctor of Philosophy

in

Mechanical Engineering

Bekir Bediz

B.S., Mechanical Engineering, Middle East Technical University Ankara, Turkey
M.S., Mechanical Engineering, Middle East Technical University Ankara, Turkey

Carnegie Mellon University
Pittsburgh, PA

December, 2014

To

the memory of

my grandfather Bekir Bediz

Acknowledgements

I came to the end of a long journey; a journey that started in August, 2009. It was not an easy one, I encountered lots of difficulties; but I always felt lucky to be surrounded by dear friends. It is a great feeling to know that somebody cares about you and will be by your side in every situation. And it is a great pleasure to express my gratitude and sincere appreciation to all of them.

First of all, I would like to express my deepest gratitude to my family for their understanding, support, and patience. And I want to thank Tuğçe Yüksel for her support and advice throughout my academic life and especially during my doctoral studies. She has always been the one who helped me to stay sane and motivated throughout my Ph.D. studies.

I wish to thank my advisor, Prof. O. Burak Ozdoganlar for his invaluable guidance, advice, and criticism that made this study possible. He has always been passionate on the topics he is working on, which brings a constant source of energy and motivation to his students. I also wish to thank my committee members, Prof. Jacobo Bielak and Prof. Kenji Shimada and Prof. Tony L. Schmitz for serving on my committee, providing helpful suggestions regarding my research and presentation, and helping me obtain an important perspective on the applicability of my research.

I want to thank John Fulmer and Ed Wojciechowski of the Mechanical Engineering machine shop and Larry Hayhurst of the Chemical Engineering machine shop for their practical guidance and help in fabrication of various components and fixtures. I want to thank Bobbi Kostyak and Chris Hertz for their assistance in administrative issues.

During my time in Carnegie Mellon University, I had the privilege of knowing and working with many great people. I would like to express my thanks to all (past and present) members of the MMDL that I had the pleasure of working with, and special thanks to my colleagues Arda Gozen and Emrullah Korkmaz for their friendship and technical support throughout my Ph.D. period.

Lastly, I would like to acknowledge the financial support of the National Science Foundation, and John and Claire Bertucci Fellowship.

Abstract

Application of mechanical micromachining for fabricating complex three-dimensional (3D) micro-scale features and small parts on a broad range of materials has increased significantly in the recent years. In particular, mechanical micromachining finds applications in manufacturing of biomedical devices, tribological surfaces, energy storage/conversion systems, and aerospace components. Effectively addressing the dual requirements for high accuracy and high throughput for micromachining applications necessitates understanding and controlling of dynamic behavior of micromachining system, including positioning stage, spindle, and the (micro-) tool, as well as their coupling with the mechanics of the material removal process. The dynamic behavior of the tool-collet-spindle-machine assembly, as reflected at the cutting edges of a micro-tool, often determines the achievable process productivity and quality. However, the common modeling techniques (such as beam based approaches) used in macro-scale to model the dynamics of cutting tools, cannot be used to accurately and efficiently in micro-scale case. Furthermore, classical modal testing techniques poses significant challenges in terms of excitation and measurement requirements, and thus, new experimental techniques are needed to determine the speed-dependent modal characteristics of miniature ultra-high-speed (UHS) spindles that are used during micromachining.

The overarching objective of this thesis is to address the aforementioned issues by developing new modeling and experimental techniques to accurately predict and analyze the dynamics of micro-scale cutting tools and miniature ultra-high-speed spindles, including rotational effects arising from the ultra high rotational speeds utilized during micromachining, which are central to understanding the process stability. Accurate prediction of the dynamics of micromachining requires **(1)** accurate and numerically-efficient analytical approach to model the rotational dynamics of realistic micro-tool geometries that will capture non-symmetric bending and coupled torsional/axial dynamics including the rotational/gyroscopic effects; and **(2)** new experimental approaches to accurately determine the speed-dependent dynamics of ultra-high-speed spindles. The dynamic models of cutting tools and ultra-high-speed spindles developed in this work can be coupled together with a mechanistic micromachining model to investigate the process stability of mechanical micromachining.

To achieve the overarching research objective, first, a new three-dimensional spectral-Tchebychev approach is developed to accurately and efficiently predict the dynamics of (micro) cutting tools. In modeling the cutting tools, considering the efficiency and accuracy of

the solution, a unified modeling approach is used. In this approach, the shank/taper/extension sections, vibrational behavior of which exhibit no coupling between different flexural motion, of the cutting tools are modeled using one-dimensional (1D) spectral-Tchebychev (ST) approach; whereas the fluted section (that exhibits coupled vibrational behavior) is modeled using the developed 3D-ST approach. To obtain the dynamic model for the entire cutting tool, a component mode synthesis approach is used to '*assemble*' the dynamic models.

Due to the high rotational speeds needed to attain high material removal rate while using micro tools, the gyroscopic/rotational effects should be included in predicting the dynamic response at any position along the cutting edges of a micro-tool during its operation. Thus, as a second step, the developed solution approach is improved to include the effects arising from the high rotational speeds. The convergence, accuracy, and efficiency of the presented solution technique is investigated through several case studies. It is shown that the presented modeling approach enables high-fidelity dynamic models for (micro-scale) cutting-tools.

Third, to accurately model the dynamics of miniature UHS spindles, that critically affect the tool-tip motions, a new experimental (modal testing) methodology is developed. To address the deficiency of traditional dynamic excitation techniques in providing the required bandwidth, repeatability, and impact force magnitudes for accurately capturing the dynamics of rotating UHS spindles, a new impact excitation system (IES) is designed and constructed. The developed system enables repeatable and high-bandwidth modal testing of (miniature and compliant) structures, while controlling the applied impact forces on the structure. Having developed the IES, and established the experimental methodology, the speed-dependent dynamics of an air bearing miniature spindle is characterized.

Finally, to show the broad impact of the develop modeling approach, a macro-scale endmill is modeled using the presented modeling technique and coupled to the dynamics of a (macro-scale) spindle, that is obtained experimentally, to predict the tool-point dynamics.

Specific contributions of this thesis research include: **(1)** a new 3D modeling approach that can accurately and efficiently capture the dynamics of pretwisted structures including gyroscopic effects, **(2)** a novel IES for repeatable, high-bandwidth modal testing of miniature and compliant structures, **(3)** an experimental methodology to characterize and understand the (speed-dependent) dynamics of miniature UHS spindles.

Contents

Acknowledgements **ii**

Abstract **iii**

List of Figures **x**

List of Tables **xv**

1 Introduction **1**

1.1 Motivation 1

1.2 Literature Review 4

1.2.1 Dynamics of mechanical micromachining processes 5

1.2.2 Modeling three-dimensional dynamics of cutting tools 6

1.2.2.1 Modeling three-dimensional dynamics of pretwisted beams 7

1.2.2.2 Modeling three-dimensional dynamics of rotating structures 10

1.2.3 Identification and modeling of miniature UHS spindles 11

1.3 Research Objectives 13

1.4 Research Contributions 15

1.5 Thesis Organization 16

2 One-Dimensional Spectral-Tchebychev Technique **18**

2.1 Timoshenko Beam Model 18

2.2 Spectral-Tchebychev Technique 19

2.2.1 Tchebychev polynomials and expansion 19

2.2.2 Gauss-Lobatto sampling 20
2.2.3 Differentiation and integration in Tchebychev domain 21
2.3 Obtaining the Discretized Equations of Motion 22

3 Modeling the Three-Dimensional Dynamics of Pretwisted Beams 24
3.1 Boundary-Value Problem for Three-Dimensional Beams 24
3.2 Formulation of the Boundary-Value Problem for Pretwisted Beams 26
3.3 Three-Dimensional Spectral-Tchebychev Technique 29
3.4 Obtaining the Discretized Equations of Motion 32
3.5 Model Application 33
3.5.1 Convergence study 33
3.5.1.1 Convergence of spectral Tchebychev approach 33
3.5.1.2 Convergence of finite element simulations 35
3.5.2 Dynamics of a pretwisted rectangular beam 36
3.5.2.1 Comparison to 1D/2D solution 41
3.5.3 Dynamics of a pretwisted beam with curved cross-section 43
3.5.4 Dynamics of a pretwisted airfoil 47
3.6 Summary and Conclusions 50

4 Modeling Three-Dimensional Dynamics of Rotating Structures under Mixed Boundary Bonditions 52
4.1 Model Development 52
4.1.1 Formulation of the boundary value problem 54
4.1.2 Solution of the boundary value problem 57
4.2 Model Application 61
4.2.1 Dynamics of rotating/spinning parallelepipeds 61
4.2.1.1 Rotating thin plates 62
4.2.1.2 Rotating/spinning beams 66
4.2.2 Dynamics of a rotating pretwisted blade with airfoil cross-section . . 71

4.3 Summary and Conclusions 74

5 Modeling Three-Dimensional Rotational Dynamics of Endmills 76

5.1 Model Development 76

5.1.1 Geometry of micro-endmill including setup errors 77

5.1.2 Formulation of the boundary value problem 78

5.1.2.1 Derivation of the one-dimensional model 79

5.1.2.2 Derivation of the three-dimensional model 83

5.1.3 Solution of the integral boundary value problem 83

5.1.4 System matrices for the entire micro-endmill 83

5.2 Model Application 85

5.2.1 Comparison with finite element method 86

5.2.2 Effect of rotational speed 87

5.2.3 Effect of attachment(setup) errors and response of micro-endmills . 89

5.3 Summary and Conclusions 92

6 An Impact Excitation System for Repeatable, High Bandwidth Modal Testing of Miniature Structures 93

6.1 Introduction 93

6.2 Impact Excitation System 96

6.3 Model Development 98

6.3.1 Analytical model of the flexure and the impact load cell system . . . 100

6.3.2 An empirical model for electromagnetic pull force and damping . . . 102

6.3.3 Impact dynamics model 105

6.3.4 Selection of control parameters 106

6.4 Modal Validation 107

6.4.1 Experimental validation of the structural dynamics model for the IES body 108

6.4.2 Validation of the electromagnetic damping model 110

6.4.3 Validation of overall model of impact excitation system 110

6.5 The Effect of Control Parameters on the IES Performance 112
6.5.1 The effect of flexure geometry 113
6.5.2 The effect of impact mass 113
6.5.3 The effect of impact-tip radius 114
6.6 System Evaluation and Comparisons with a Miniature Impact Hammer . . 114
6.7 Application of the IES: Modal Testing of a Miniature Contact Probe 118
6.8 Summary and Conclusions 120

7 Dynamics of Ultra-High-Speed (UHS) Spindles used for Micromachining 123
7.1 Experimental Setup 123
7.1.1 Dynamic excitations 124
7.1.2 Measurement of dynamic response 125
7.1.3 Data acquisition 126
7.1.4 Laser beam alignment 126
7.1.5 Test procedure 128
7.1.6 Removal of unwanted spindle error motions 130
7.1.7 Processing of measurement data to obtain FRFs 132
7.2 Results and Discussion 133
7.2.1 Obtaining spindle dynamics 133
7.2.2 Effect of spindle speed 138
7.2.3 Effect of collet pressure 141
7.3 Summary and Conclusions 142

8 Modeling and Experimentation for Three-Dimensional Dynamics of Macro-scale Endmills 144
8.1 Modeling and Spectral-Tchebychev Solution of Macro-scale Endmill Dynamics 144
8.2 Receptance Coupling Substructure Analysis 145
8.3 Experimental Methods 147
8.3.1 Description of endmill geometries 148

8.3.2 Experimental setups and conditions 149
8.4 Alternative Modeling Techniques for Comperative Analysis 151
8.4.1 Finite element modeling (FEM) of macro-endmills 151
8.4.2 Equivalent diameter approach 152
8.5 Modal Assessment 153
8.5.1 Comparison of tool modeling techniques 153
8.6 Tool Point Measurements and Predictions 156
8.7 Summary and Conclusion 160

9 Summary and Conclusions **164**

10 Future Work **168**
10.1 Future Work Regarding the Micromachining Dynamics 168
10.1.1 Creating and evaluating a 3D dynamic characterization approach for UHS spindles 168
10.1.2 Characterizing and modeling dynamics of different miniature UHS spindles at varying spindle speeds 169
10.1.3 Combining the dynamics of the micro-scale cutting tools and miniature UHS spindles 169
10.1.4 Constructing a simulation framework incorporating spindle error motions and machining dynamics 169
10.1.5 Investigating the stability of the micromachining processes 170
10.2 Future Work Regarding the Developed ST Technique 170

List of Figures

1.1 Examples of micro-scale complex features: **(a)** Poly-methyl methacrylate (PMMA) bevel shape microneedle [1], **(b)** polylactide (PLA) microbarbs [2], **(c)** carboxymethyl cellulose (CMC) brain probe [3], and **(d)** Green state ceramic wall. 2

1.2 Three-axis micro-machine-tool (μMT) designed and constructed in Multi-scale Manufacturing and Dynamics Laboratory (MMDL) at Carnegie Mellon University (CMU). 3

1.3 Micromachining of a channel with two different cutting conditions [4]. . . . 4

1.4 Schematic views of **(a)** shearing and **(b)** plowing mechanisms. 5

1.5 Schematic showing the unified modeling approach for a micro endmill. . . . 7

1.6 Overall theme describing the research objectives. 14

3.1 Description of a pretwisted beam having a general cross-section. 25

3.2 **(a)** The pretwisted beam in the physical domain, **(b)** the straight beam with curved cross-section obtained after the first transformation, **(c)** the straight beam with rectangular cross-section obtained after the cross-sectional mapping. 27

3.3 A fourth-order polynomial mapping of the curved cross-section to a rectangular domain. The cross-section in **(a)** the physical domain and **(b)** the mapped rectangular domain. 28

3.4 Convergence study for pretwisted beam with rectangular cross-section for a twist rate of 2. First row is for $N_z = 11, 12, 13$ (from left to right), middle row is for $N_z = 14, 15, 16$ (from left to right), last row is for $N_z = 17, 18, 19$ (from left to right). 35

3.5 The mode shapes of an unconstrained pretwisted beam. The undeflected geometries of the beams are provided on the left column. The first nine mode shapes are given on the right column where the red lines indicate the undeflected geometries. 38

3.6 Modal Assurance Criteria (MAC) analysis of the pretwisted beam with rectangular cross-section for the twist rates of **(a)** 0, **(b)** 0.25, **(c)** 0.5, **(d)** 1, and **(e)** 2. 39

3.7 **(a)-(c)** Normal stresses due to bending (σ_z) for the first bending mode computed on the cross-section (z=2.5). **(d)-(f)** Axial displacement (w) for the first torsional-axial mode on the bottom cross-section (z=0). The left column is for no twist, the middle column is for a twist rate of 0.5, and the right column is for a twist rate of 1. 40

3.8 Natural frequencies from the 3D linear elasticity based solutions (on the left) and beam (1D/2D) solutions (on the right). Solid lines - bending modes, dashed lines - torsion dominated torsional-axial modes, dashed dotted lines - axial dominated torsional-axial mode. 42

3.9 The cross-sectional mapping for the two fluted cutting tool geometry. 43

3.10 The mode shapes of an unconstrained pretwisted beam with cutting tool geometry. The undeflected geometries of the beams are provided on the left column. The first nine mode shapes are given on the right column where the red lines indicate the undeflected geometries. 45

3.11 Change in the natural frequencies of an unconstrained pretwisted beam with two fluted cutting tool geometry. Solid lines - bending modes, dashed lines - torsion dominated torsional-axial modes, dashed dotted lines - axial dominated torsional-axial mode. 46

3.12 **(a)-(c)** Normal stresses due to bending (σ_z) for the first bending mode computed on the cross-section (z=2). **(d)-(f)** Axial displacement (w) for the first torsional-axial mode on the bottom cross-section (z=0). Left column is for no twist, middle column is for half twist, and right column is for full twist. 46

3.13 Mapping procedure for airfoil geometry cross-section. 47

3.14 The mode shapes of an unconstrained pretwisted beam with airfoil geometry. The undeflected geometries of the beams are provided on the left column. The first nine mode shapes are given on the right column where the red lines indicate the undeflected geometries. 49

3.15 Change in the natural frequencies of an unconstrained pretwisted beam with airfoil geometry. 49

3.16 **(a)-(b)** Normal stresses due to bending (σ_z) for the first bending mode computed on the cross-section (z=1.5). **(c)-(d)** Axial displacement (w) for the first torsional-axial mode on the bottom cross-section (z=0). Left column is for no twist, and right column is for the 0.3 twist case. 50

4.1 Description of a rotating structure having a general boundary, $B(x, y, z)$, and a general cross-section, $C(z)$. 53

4.2 General schematic diagram of a rotating/spinning parallelepiped. 62

4.3 General schematic diagram of a rotating thin plate. 63

4.4 Change in the non-dimensional natural frequencies of a rotating thin cantilevered plate with non-dimensional rotation speed. Solid and dashed lines are the data calculated using 3D-ST approach and ANSYS®, respectively, and the square markers are the data presented in [5], respectively. 64

4.5 The first five mode shapes of a thin rotating cantilevered plate having the geometric properties as $L_x/L_z = 1$, $L_y/L_z = 0.01$, and non-dimensional hub radius of 1. The red lines indicate the undeflected geometries. 65

4.6 **(a)** Spinning and **(b)** rotating beams having a rectangular cross-section. . . 66

4.7 The effect of coriolis, spin-softening, and nonlinear (stress-stiffening) terms on the dynamics of cantilevered **(a)** spinning and **(b)** rotating beams. (Dotted (black) lines show the results for stationary cases. The results after including the *coriolis* terms are shown by the dashed dotted (green) lines. Then, the *spin softening* terms are also included to the simulation and the results are shown by dashed (red) lines. And lastly, solid (blue) lines represent the simulation results including all the terms. Similarly, square and circle markers represent the non-dimensional natural frequencies calculated using ANSYS® with and without nonlinear (stress-stiffening) effects, respectively). 67

4.8 Change of non-dimensional natural frequencies of an unconstrained spinning beam with non-dimensional rotation speed. The solid and dashed lines represent the bending and torsional/axial modes, respectively, and the (black) square markers are the results obtained from the ANSYS®. 69

4.9 The first seven mode shapes of an unconstrained spinning beam with non-dimensional rotation speed. The red lines indicate the undeflected geometries. 70

4.10 Effect of alignment errors on the dynamics of spinning beams: **(a)** pure spinning case, **(b)** comparison of pure spinning case with small alignment errors case and **(c)** comparison of pure spinning case with large alignment errors case (Blue solid and red dashed lines represent the non-dimensional natural frequencies corresponding to pure spinning and spinning with alignment errors cases, respectively). 70

4.11 **(a)** Rotating blade having an airfoil cross-section, and **(b)** the corresponding mapping procedure. 71

4.12 **(a)** Rotating blade having an airfoil cross-section, and **(b)** the corresponding mapping procedure. 73

4.13 The variation of 2nd, 3rd, and 4th mode shapes of the cantilevered rotating blade having aspect ratio of 3 and non-dimensional hub radius of 1 with rotation speed (The rows and columns corresponds to the mode shapes and to the non-dimensional rotation speeds of 0.005, 0.01, 0.015, 0.02, and 0.025 in ascending order from up to down and left to right, respectively). The red lines indicate the undeflected geometries. 73

4.14 Effect of aspect ratio on the non-dimensional natural frequencies of a rotating cantilevered beam having an airfoil geometry where the non-dimensional hub ratio and twist rate are 1 and 0.02, respectively (the solid and dashed lines represent the bending and torsional-axial dominant modes, respectively). . . 74

5.1 Micro endmill geometry and parameters for geometric description. 77

5.2 Micro-endmill with setup (attachment) errors. 78

5.3 Moving frame and rotating tool frame related through bending (ψ_x and ψ_y) and torsion (ψ_z) angles. 80

5.4 SEM images of micro-tools: **(a)** two-fluted endmill and **(b)** four-fluted endmill. 85

5.5 Change of damped natural frequencies with rotational speed for **(a)** ME-1 and **(b)** ME-3. 88

5.6 The first seven mode shapes of an unconstrained rotating tool for $\Omega = 5000$ Hz (upper row) and $\Omega = 10000$ Hz (lower row). 89

5.7 Schematics depicting the motion of the tool-tip. 90

5.8 Orbital vibrations for the steady-state harmonic response. Dashed black, dashed dotted blue, and solid red lines show the static and dynamic tool-tip runout, and orbital motions, respectively.. 91

6.1 CAD model of the impact excitation system. 95

6.2 **(a)** The impact excitation system (in the deflected position) and **(b)** an illustrative time response of the impact head. 98

6.3 Three phases of motion experienced by the IES during modal testing: **(a)** motion before impact, **(b)** motion during impact, **(c)** motion after impact. 100

6.4 **(a)**Substructures (I:XIII) and **(b)** geometric properties of the IES. 102

6.5 **(a)** Experimental setup for determining the pull-force profile, **(b)** measured pull force profiles by the dynamometer, and **(c)** fitted decaying pull force profile exerted by the electromagnet after it is shut off (when the electromagnet is connected to a 6V DC supply). 104

6.6 **(a)** Experimental setup for determining the (decaying) magnetic damping and **(b)** decaying damping profile exerted by the electromagnet after it is shut off (when the electromagnet is connected to a 6V DC supply). 105
6.7 Selection of control parameters. 107
6.8 FRF measurement of the flexure-based body and impact load cell system. . 108
6.9 Comparison of FRFs obtained from the experiment and from the model. . . 109
6.10 Comparison of measured (dashed) and simulated impact head (solid) velocities. 110
6.11 Impact testing on a cast iron block. 111
6.12 **(a)** Process maps and **(b)** impact force profiles and corresponding input spectra for the selected parameters (solid lines - experimental data, red (dotted) line - simulation data). 112
6.13 The effect of flexure geometry on process maps and excitation bandwidth contour plots: **(a)** Flexure 1, **(b)** Flexure 2, **(c)** Flexure 3. 114
6.14 Effect of extender mass on process maps and excitation bandwidth contour plots: **(a)** with no extender mass, **(b)** with an extender mass of 0.5 g, **(c)** with an extender mass of 1.0 g. 115
6.15 Effect of impact tip radius on process maps and excitation bandwidth contour plots: **(a)** r = 0.3 mm, **(b)** r = 1.2 mm. 116
6.16 Impact location variability obtained **(a)** using the designed IES, **(b)** with manual hits using a miniature impact hammer. 117
6.17 Impact force amplitude and excitation bandwidth variability obtained **(a)** using the designed IES, **(b)** with manual hits. 117
6.18 Coherence plots calculated using **(a)** the designed IES and **(b)** manual hits (obtained only averaging the test in which single-hits are obtained). 118
6.19 Modal testing of a miniature contact probe using the IES. 119
6.20 **(a-c)** Contour plots generated for control parameter selection for experimentation on the contact probe. **(d-f)** Comparison of simulation and experimental results for the selected control parameter sets (solid lines: experimental results, dashed line: simulation result). 120
6.21 FRFs and corresponding coherence plots obtained using the designed IES (solid lines) and manual hits (dashed lines). 121

7.1 The experimental setup for obtaining speed-dependent dynamics of miniature UHS spindles. 124
7.2 Excitation force applied at the tip of the cylindrical artifact in time (top) and frequency (bottom) domain (for a 5 mm overhang length and 50,000 rpm spindle speed). 125
7.3 Alignment of laser beams: **(a)** coarse alignment, **(b)** fine alignment. 127
7.4 Experimental procedure: **(a)** CAD Models showing the spindle, cylindrical artifact, and the IES, **(b)** Schematic diagram indicating the impact and measurement locations. 129
7.5 Steps of frequency domain filtering approach: **(a)** Raw displacement data, **(b)** IR sensor data, **(c)** Response of the spindle due to the impact (filtered data). 131

7.6 Frequency spectrum of: **(a)** Range 1 that includes both the dynamic response and the unwanted spindle motions, **(b)** Range 2 that includes only the unwanted spindle motions, and **(c)** filtered data that include only the dynamic response. 132

7.7 **(a)** Direct (H_{AA}^{yy}), and **(b)** cross (H_{AA}^{xy}) FRFs calculated at point A for the spindle speed of 50,000 rpm. 134

7.8 Magnitudes (in logarithmic scale) of the FRF matrix at point A for the spindle speed of 50,000 rpm. 135

7.9 Uncertainty analysis for three different spindle speeds. 137

7.10 Effect of spindle speed on the amplitude of direct receptance (H_{AA}^{xx}) in the horizontal (x) direction at point A. 139

7.11 Effect of spindle speed on the coherence of direct receptance (H_{AA}^{xx}) in the horizontal (x) direction at point A. 140

7.12 Effect of spindle speed on natural frequencies and associated damping ratios of the spindle. The dashed red line shows the 1X-synchronous line. 141

7.13 Change of runout measured from the cylindrical artifact surface at point A as a function of spindle speed. 141

7.14 Effect of collet pressure on the H_{AA}^{xx} element of the FRF matrix for 110,000 rpm spindle speed. 142

8.1 Macro-endmill geometry. 145

8.2 THSM assembly and coordinates. 146

8.3 RCSA components with coordinates. 146

8.4 Component coordinates for flexible coupling. 146

8.5 Cross-section of **a)** endmills 1-3 (coordinates are provided in mm), **b)** endmill 4. 148

8.6 Impact hammer experimentation setup: **a)** Direct FRF measurement at the endmill shank end **b)** Torsional measurement. 149

8.7 Experimental setup for endmill 4 (carbide endmill). 150

8.8 Absolute percent errors of the approximate methods for **a)** Endmill 1; **b)** Endmill 2; **c)** Endmill 3; **d)** Endmill 4. 155

8.9 Holder and blank dimensions for 127.68 mm overhang length (All dimensions are in mm). 157

8.10 Blank-holder model components. 157

8.11 Measured (solid line) and predicted (dotted line) tool point FRFs for the carbide tool blank with overhang lengths of: **a)** 127.68 mm; **b)** 124.35 mm; and **c)** 118.62 mm (rigid connection). 158

8.12 Component coordinates for flexible coupling in case of blank. 159

8.13 Measured (solid line) and predicted (dotted line) tool point FRFs for the carbide tool blank with overhang lengths of: **a)** 127.68 mm; **b)** 124.35 mm; and **c)** 118.62 mm (flexible connection). 161

8.14 Measured (solid line) and predicted (dotted line) tool point FRFs for the carbide endmill with overhang lengths of: **a)** 127.59 mm; **b)** 124.78 mm; and **c)** 118.7 mm (flexible connection). 162

List of Tables

3.1 Convergence of the 3D-ST solution for the unconstrained pretwisted rectangle beam having the properties $width/height = 2$, $length/height = 5$ and a Poisson's ratio of 0.3, and comparison with results from the 3D-FEM simulations based on the non-dimensional natural frequencies. 37

3.2 Mapping coefficients for the mapping of the two-fluted geometry in Fig. 3.9 (calculated through Eqs. (3.10)-(3.11)). 43

3.3 Convergence of the 3D-ST solution for the unconstrained pretwisted 2-fluted cutting-tool geometry having the properties $diameter/length = 4$ and a Poisson's ratio of 0.3, and comparison with results from 3D-FEM simulations based on the non-dimensional natural frequencies. 44

3.4 Convergence of the 3D-ST solution for the unconstrained pretwisted airfoil geometry with length-to-breadth ratio of 3 and a Poisson's ratio of 0.3, and comparison with results from 3D-FEM simulations. 48

5.1 Geometric properties of the micro-endmills used for comparison study. . . . 86

5.2 Comparison of natural frequencies (in Hz) obtained by 3D-ST and FEM approaches for micro-endmills listed in Table 5.1. 87

5.3 Tool attachment values used in this study. 91

6.1 Geometric properties of the IES. 101

6.2 Material properties of the IES. 101

6.3 Comparison of natural frequencies of the IES. 109

7.1 Natural frequencies and associated damping ratios of the FRF matrix given in Fig. 7.8. 137

8.1 Properties of the endmills used for validation experiments (all parameters except the helix angle were measured using digital calipers with a resolution of 0.01 mm). 148

8.2 Endmill material properties. 151

8.3 Convergence study for endmill 1 from Table 8.1. 152

8.4 Equivalent diameter of endmills. 153

8.5 Comparison of the experimental and predicted natural frequencies 154

8.6 Carbide endmill/blank and holder material properties. 156

8.7 Component dimensions for 127.68 mm overhang length. 157

8.10 Percent error between measurement and prediction for the carbide endmill. 160

8.8 Stiffness matrix values. 160

8.9 Percent error between measurement and prediction. 160

Chapter 1

Introduction

"If you want to find the secrets of the universe, think in terms of energy, frequency, and vibration."

-Nikola Tesla

1.1 Motivation

In the past few decades, there has been an increasing demand for three-dimensional (3D) micro-scale complex products (see Fig. 1.1 for examples of micro-scale feature and devices) from various industries (e.g., medical devices, energy conversion devices, aerospace applications, etc.) to use the advantages of miniaturization such as functionality due to small size, and space and material savings [6, 7]. To address this demand, new micro-manufacturing techniques have been investigated. However, fabricating such complex 3D features using micro-manufacturing techniques such as photo-lithography (used for MEMS devices), focused ion beam machining (FIB), femtosecond laser micro-machining (FLM), selective laser sintering (SLS), electro-chemical machining (ECM), and electro-discharge machining (EDM), on different materials has been either impractical and costly, or simply impossible.

In recent years, to overcome the geometric and material limitations, mechanical micro-machining (e.g., micromilling, microdrilling, etc.) became a promising emerging technique for fabricating micro-scale features and small parts. Although, it has come a long way in the last few years and does not have the limitations as other micro-fabrication techniques, its full potential cannot be realized without a thorough understanding of micromachining processes [8]; and thus, effective means to correlate process parameters with performance

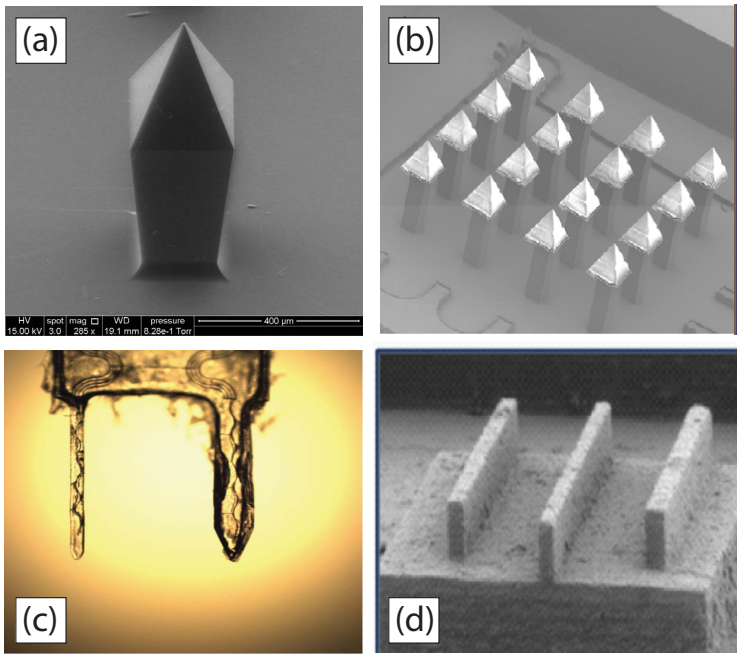

Figure 1.1: Examples of micro-scale complex features: **(a)** Poly-methyl methacrylate (PMMA) bevel shape microneedle [1], **(b)** polylactide (PLA) microbarbs [2], **(c)** carboxymethyl cellulose (CMC) brain probe [3], and **(d)** Green state ceramic wall.

metrics, such as dimensional and surface quality and process throughput (chatter avoidance), are direly needed.

Mechanical micromachining is basically the scaled down version of macro-scale (conventional) mechanical machining processes. Figure 1.2 shows an example of micro-machine-tools (μMT) designed and constructed in Multi-scale Manufacturing and Dynamics Laboratory (MMDL) at Carnegie Mellon University (CMU). In order to attain high material removal rates while using micro-scale cutting tools (whose diameters can go down to 25 μm in diameter), miniature ultra-high-speed (UHS) spindles (that can rotate at speeds above 60,000 rpm) are used in micromachining operations [6]. For instance, Fig. 1.2 shows a μMT which includes a 160,000 rpm air turbine, air bearing miniature UHS spindle equipped with a 3.125 mm (1/8 inch) precision collet. The feed motions are provided by three-axis precision slides (Aerotech ALS130-XYZ) with a 10 nm resolution and a maximum linear (feed) speed of 250 mm/sec. In the μMT shown in Fig. 1.2, the UHS spindle is stationary and the relative motion between the cutting tool and the workpiece is provided by the precision slides that are programmed with G-codes. To facilitate the measurement of micromachining forces, the workpiece is mounted on a dynamometer (Kistler 9256C1), which in turn is attached to the three-axis slides. A stereo microscope with 95X magnification is used to view the workpiece surface during the initial tool approach.

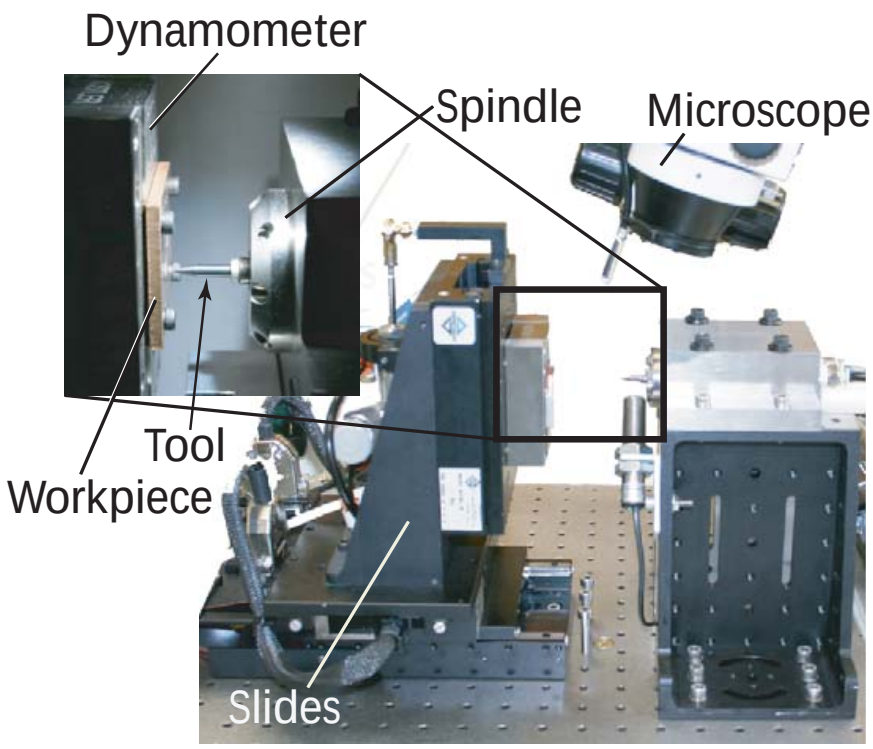

Figure 1.2: Three-axis micro-machine-tool (μMT) designed and constructed in Multi-scale Manufacturing and Dynamics Laboratory (MMDL) at Carnegie Mellon University (CMU).

As in the macro-scale machining, the dynamic response in the micro-scale is controlled by the interaction between the cutting mechanics and the structural dynamics. The cutting mechanics determines the machining forces based on the selected machining conditions (depth of cut, feed rate, etc.), tool geometry, and relative tool-workpiece vibrations. The relative tool-workpiece vibrations arise from the dynamic response of the machining-system structure, as reflected at the cutting points, due to the excitation from (micro) machining forces [9, 10]. The dynamics of the machining-system structure include the dynamic behavior of the entire structural assembly, including the micro-tool, collet[1], spindle, and the machine. Due to potential process instability, the mechanics-dynamics interaction can cause unstable cutting conditions, leading to dimensional and surface inaccuracies if the cutting conditions and tool geometry are not selected carefully (see Figure 1.3 that shows examples of micro channels machined with two different cutting conditions). Even under stable cutting conditions, forced vibrations of the flexible tool can lead to errors in the location of the machined surface (in milling). Thus, accurate prediction of the dynamic response of the entire structural assembly reflected at the micro-tool tip is central to identifying fa-

[1]the holding device, that exerts a strong clamping force, used to attach the micro-tools to the UHS spindle.

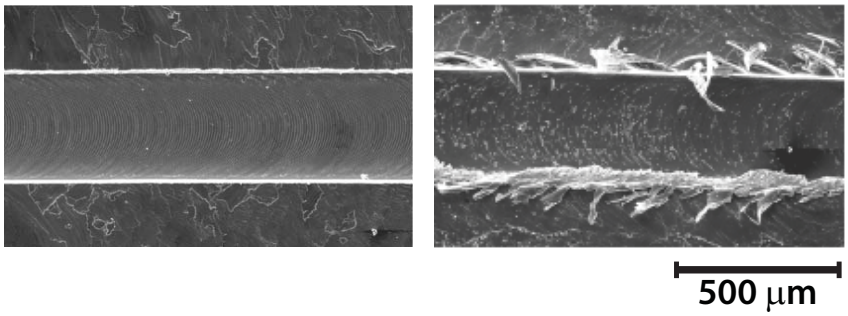

Figure 1.3: Micromachining of a channel with two different cutting conditions [4].

vorable cutting conditions that will simultaneously satisfy process quality and throughput requirements during micromachining.

As a result, to accurately predict the 3D dynamic response of the entire structural assembly reflected at the micro-tool tip, high-fidelity dynamic models for the constituent parts (micro-tool, collet, spindle, and the machine) of the machining-system structure should be constructed and assembled/coupled. However, note that, since the UHS spindles and micro-scale cutting tools are rotated at ultra high rotational speeds, gyroscopic forces have a significant effect on the dynamics of the machining-system structure; and thus cannot be neglected.

1.2 Literature Review

The thesis mainly focuses on obtaining high-fidelity dynamic models to understand and predict the (rotational) vibrational behavior of (micro) cutting tools and (miniature) UHS spindles used in micromachining processes. Thus, only the literature on these fields is presented in this chapter; and the literature reviews and background information of other related work are provided in the associated chapters. First, a brief overview of the mechanical micromachining processes is summarized. Next, the state of the art approaches/techniques on obtaining cutting tool and spindle dynamics are discussed in detail. Since a new 3D elasticity based approach that uses Tchebychev[1] polynomials is developed to accurately predict the rotational 3D coupled dynamics of the micro-tools in this thesis, an extensive background information is given on modeling techniques (especially on modeling the dynamics of pretwisted and rotating structures).

[1] *Pafnuty Lvovich Tchebyshev* is a Russian mathematician who is known for Tchebychev polynomials. Depending on the transliteration, his name can be written as Chebychev, Chebysheff, Chebyshov, or Tchebychev. In this thesis, '*Tchebychev*' is used.

1.2.1 Dynamics of mechanical micromachining processes

Micromachining is the process of manufacturing miniature features by physically (mechanically) removing material (in the form of chips) from a larger body (called as workpiece) to achieve a desired geometry. Although micromachining is the scaled down version of its macro-scale counterpart, the individual mechanisms governing these processes are considerably different. The main difference is the comparable edge radius of the micro-tool to chip thickness. In micromachining, the assumption of sharp cutting edge that holds for macro-scale machining processes, is not valid anymore, and thus results in two different cutting processes [11]: when the uncut chip thickness is greater than the *minimum chip thickness*[2], a chip formation occurs (referred as *shearing*, see Fig. 1.4(a)), however if the uncut chip thickness is below the *minimum chip thickness*, no chip is formed during the cutting operations (referred as *plowing*, see Fig. 1.4(b)). In plowing, the material is plastically deformed and there will be some amount of elastic recovery of the material after the tool pass, which causes increased cutting forces and poor surface quality at low feed rates [12].

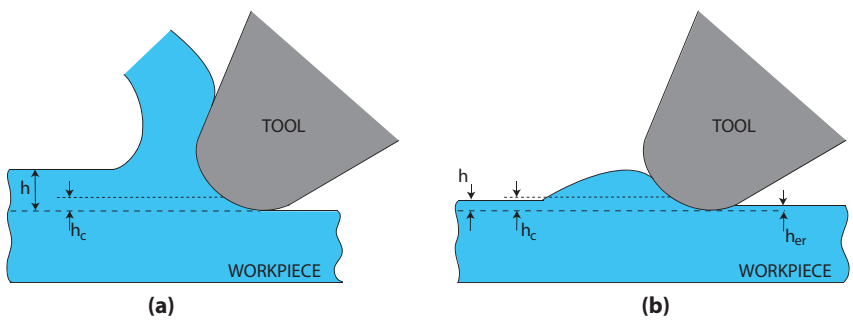

Figure 1.4: Schematic views of **(a)** shearing and **(b)** plowing mechanisms.

Over the past few years, there has been many studies that attempted to develop a model to predict the micromachining forces (i.e., cutting mechanics). The developed mechanistic models for micromachining so far can be classified mainly into three categories: **(1)** analytical approach where the effects such as the minimum chip thickness or built-up edge effects are modeled analytically [12–14], **(2)** mechanistic approach [15] and **(3)** finite-element (FE) approach [16].

Although, a fairly large body of literature has been devoted to understand the dynamics of macro scale machining processes [17–19], there are only a few attempts to truly garner a comprehensive understanding of the micromachining dynamics. This is mainly due to the significant challenges that the micromachining process poses such as imperfections in

[2] *Minimum chip thickness* is a critical limit that depends on the material and the edge radius of the tool.

tooling, relative tool-workpiece vibrations, uncertainties in workpiece microstructure.

One of the most significant challenges in (micro)machining is the unwanted vibrations, that bring important limitations to satisfying accuracy and material removal rate requirements, arising from the interaction between the cutting mechanics and the structural dynamics [9, 10]. As mentioned earlier, mechanical forces are generated during the machining process, which act on the cutting tool and cause the system (spindle-holder/collet-tool system) to deflect/vibrate. Furthermore, even in the absence of micromachining forces, due to the high rotational speeds and the attachment errors (eccentricity and tilt errors occur while attaching the tool to the UHS spindle), the tool tip follows a circular path that varies strongly with spindle speed [20]. Therefore, the dynamic behavior of the spindle-holder/collet-tool system at the cutting edge—commonly referred as the tool tip dynamics—must be well-characterized.

1.2.2 Modeling three-dimensional dynamics of cutting tools

For a given UHS spindle/collet combinations, a wide selection of micro-tool geometries can be used which necessitates a modeling approach to accurately and efficiently predict the (rotational) dynamics of arbitrary cutting tool geometries. Most of the recent models for dynamics of drilling and milling tools included beam-based models (The Euler-Bernouilli [21, 22] and Timoshenko [23] beam models) to overcome the shortcomings of the lumped parameter models in predicting the tool dynamics. Although significant improvements have been observed, the beam models still could not capture the 3D (coupled torsional-axial and non-symmetric bending) dynamic behavior of the tools due to the complex geometry arising from the pretwisted fluted sections [24–26]. This is especially true for micro-tools, where a set of different sections ranging from 3 mm (shank) to the tip diameter (e.g., 50 μm) and fluted (pretwisted) section with its 3D nature bring further complexities to dynamic response, rendering it fully three-dimensional. Furthermore, the UHS spindle speeds make the rotational effects significant in micro-tool dynamics.

In this thesis, a unified modeling approach (see Fig. 1.5) is used: **(a)** having circular cross-sections, the dynamic behavior of the sections other than the fluted section is simplified, resulting in uncoupled axial, torsional, and bending motions; and thus, 1D beam equations can accurately capture the dynamic behavior of these sections [27, 28]; however, **(b)** the fluted section has a (complex) curved cross-section and pretwisted geometry resulting in coupled axial-torsional-bending-bending motions, which necessitates a 3D modeling approach.

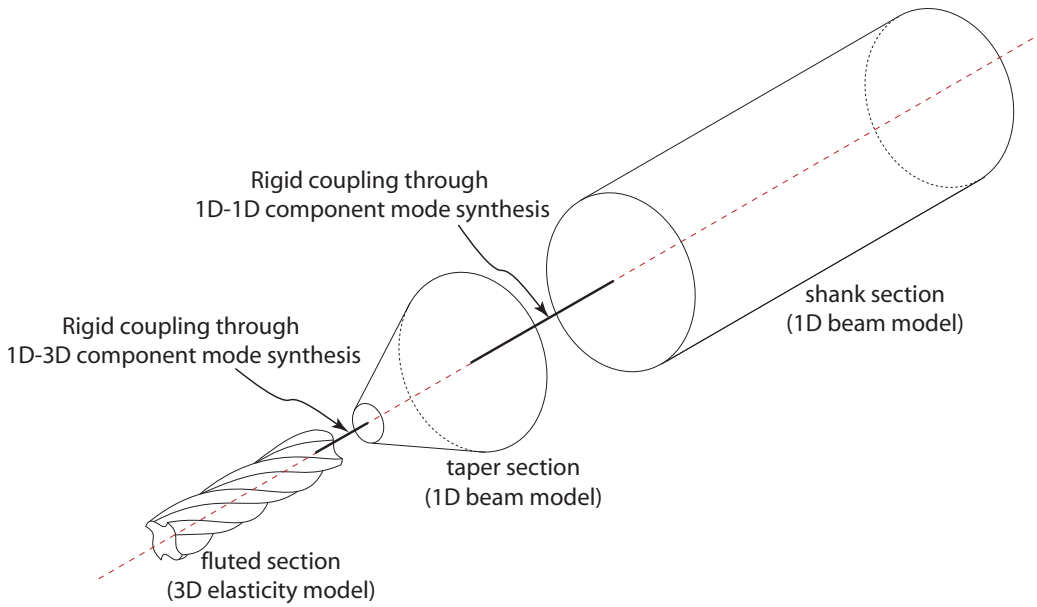

Figure 1.5: Schematic showing the unified modeling approach for a micro endmill.

The 1D-beam based models (that use spectral-Tchebychev polynomials) were already derived in the literature [29, 30]; thus within the scope of this thesis, 3D linear elasticity based dynamic models are derived, especially to capture the dynamics of pretwisted and rotating 3D structures. Therefore, here only the literature reviews on the numerical solution of pretwisted and rotating structures are covered.

1.2.2.1 Modeling three-dimensional dynamics of pretwisted beams

Pretwisted beams[3] with general cross-section[4] are seen in many engineering applications, such as turbine, compressor and propeller blades, helicopter rotor blades, wind-turbine blades, and drilling and milling tools. Since most such applications involve moving components, the dynamic behavior of pretwisted beams are critical to the functional and failure characteristics of a myriad of systems. The importance of pretwisted beams in many applications highlights the need for understanding of, and developing high-fidelity models for, dynamic response of pretwisted beams [31, 32].

In contrast to those of beams with no pretwist, the vibrational (dynamic) characteristics of pretwisted beams are 3D in nature [32]. Due to the interaction between pretwist and lateral contraction, pretwisted beams—even with doubly-symmetric cross-sections—

[3]Note that the classifications made here as beams merely represent the general characteristics of the geometry.

[4]In this thesis, '*general cross-section*' term is used to include any kind of cross-section (including cross-sections composed of straight lines or curved lines or both).

exhibit coupled bending deformations, usually referred to as bending-bending vibrations. Furthermore, arising from the warping of cross-sections, pretwisted beams wind/unwind under axial compression/tension. This indicates that their torsional and axial deformations are also coupled. In addition to the bending-bending and torsional-axial coupling, when the cross-sectional center of mass and the shear center are not coincident (i.e., the cross-section is asymmetric about the principal axes), the bending and torsional/axial deformations also become coupled, leading to bending-bending-torsional-axial deformations. Although its effect is relatively small at low twist rates, the pretwist changes the dynamic behavior considerably at high twist rates and for curved cross-sections.

A large body of literature has been devoted to modeling and analysis of pretwisted beam vibrations. A through review of the works until the early 1990s is provided by Rosen [32], with a particular emphasis on one-dimensional rod-based methods. In general, the approaches to modeling pretwisted beam dynamics can be broadly classified into two categories: **(1)** the use of classical beam, plate, and shell theories with and without modifications to account for different effects arising due to the pretwist, and **(2)** the use of three-dimensional linear elasticity theories. Many researchers modeled the *bending-bending* vibrations of the pretwisted beams using the Euler-Bernoulli [22, 33–41] and Timoshenko [11, 42–46] beam theories. Although the application of classical beam theories captured the basic characteristics of the coupling between the bending modes due to the pretwist for simple cross-sections, large deviations were observed between the experimental and theoretical calculations. It was realized that the pretwist-induced in-plane deformations causes non-uniform stress distributions, resulting in reductions in bending stiffness and changes in natural frequencies and mode shapes [47]. To address this, attempts were made to modify the classical beam theories to capture the bending motions of pretwisted beams [47,48]. Although those modifications enabled better prediction of (only) the first few natural frequencies for low twist rates, the modes shapes were not predicted accurately [41].

Coupled *axial-torsional* deformations of the pretwisted beams have also been the subject of many works. Experimental observations indicated that the pretwist causes increased (apparent) torsional stiffness and reduced (apparent) axial stiffness [47, 49]. This phenomenon is a result of the coupling between the torsional and axial deformations, and it was discovered early on that the warping of the cross-section is the main reason behind this coupling effect [49–51]. An approach to model the coupled axial-torsional deformations is to incorporate the warping through the use of Saint-Venant's warping function [25, 50–52]. Liu et al. [53] demonstrated that, to improve the prediction of axial modes, the warping function must be derived specifically for the pretwisted beam and no terms should be neglected.

As an alternative, nonlinear beam models that incorporate warping were derived [47, 48]. While those model enhancements resulted in improved prediction of axial-torsional motions, inaccuracies were still significant for larger pretwist rates and higher modes.

Another approach for modeling pretwisted beam dynamics is to use 3D linear elasticity theories [49, 54, 55]. Both the natural frequencies and the mode shapes can be predicted accurately even for high twist rates and higher modes of vibration. Although derivation of the 3D models for pretwist beam dynamics is quite straightforward, the solution of the models are more involved and demands the use of numerical techniques.

To this end, many researchers used finite-element [11,22,39,40,42,43] and finite-difference [34] techniques to solve dynamics of pretwisted beams. Obtaining accurate solutions using these techniques for higher modes and at high twist rates imposes significant computational burden. Albeit, when converged, the finite-elements solutions provide accurate predictions for natural frequencies and modes shapes of pretwisted beam.

Alternatively, series-based solution approaches such as Rayleigh-Ritz [31, 35, 56] method or Galerkin's [33, 41] method may be used to solve the 3D problems, even though their usage is far more common for 1D and 2D problems [29]. Series-based solutions are commonly preferred to the finite-element and finite-difference solutions due to their simplicity, resulting in orders of magnitude reduction in computation time. The main issue with many of the existing series-based solution techniques is the need for identifying basis/trial functions that are fast converging. Furthermore, the basis functions are required to satisfy the boundary conditions, which necessitates a new set of basis functions for each different boundary condition.

A recent approach within the series-based methods is the spectral-Tchebychev (ST) technique, which uses Tchebychev polynomials as the basis for discretizing the boundary-value problem in either the differential or the integral form [27–29, 45, 46, 57–60]. The solution can be formulated to incorporate the boundary conditions into the solution directly, therefore eliminating the need for using different basis functions for different boundary conditions [28, 29, 45, 46, 59]. It was shown that the ST technique can be used to obtain dynamics of linear and nonlinear beams with varying boundary and forcing conditions in an accurate and rapid fashion [29]. This technique was used to model the pretwisted beam dynamics using 1D and 1D/2D Timoshenko beam equations [30, 45] and was validated experimentally [46]. More recently, a 3D-ST solution was derived for solving the 3D dynamics of parallelepipeds under various boundary conditions [59]. It was demonstrated that the convergence is very rapid, and the solution is as accurate as that obtained from finite-element

techniques, yet at a fraction of the computational time.

1.2.2.2 Modeling three-dimensional dynamics of rotating structures

The motion of rotating structures can be described as large overall motions (the dictated rotational motion) accompanied by small elastic deformations (the dynamic response); and both the large overall motions and the elastic deformations (i.e., the dynamics of rotating structures) change significantly with rotation speed due to the *coriolis*, *centrifugal softening*, and *stress-stiffening* effects [61,62]. As a result of coriolis forces (that are proportional to the rotation velocity), it was shown that the axial and transverse motions become coupled and also complex vibration modes occur [61]. Besides the coriolis forces, the rotating structure experiences centrifugal forces (that are proportional to the square of rotation velocity) that are trying to destabilize the structure; thus results in a decrease in the stiffness of the structure called centrifugal (spin) softening. Lastly, due to the large overall motions, a stationary stress field is created, resulting in a strengthening effect (or weakening effect depending on the created stress-field) called the stress-stiffening effect which is simply the coupling effect between the stretching and bending deformations [63]. To capture the effect of stress-stiffening, second order-displacement terms (that are nonlinear) need to be included in the derivation of the governing boundary value problem describing the motion of rotating structures [62].

Over the last few decades, there are a lot of studies that attempted to model the dynamics of rotating structures, which can be classified into two categories: **(1)** one-dimensional beam based modeling approaches (which is the classical approach to rotordynamics) [63] or **(2)** plate/shell based modeling approaches (that are used generally to model the dynamics of rotating blades) [62,64]. The one-dimensional methods such as Euler-Bernoulli [32,65,66] and Timoshenko beam theories [67–69] or dynamic stiffness matrix technique [70], yield accurate results for simple geometries and low rotational speeds; however as the geometry becomes complex (or even for rotating stubby beams) and/or as the rotation speed increases, large deviations in natural frequencies and mode shapes are observed between the experimental and theoretical calculations [47,71]. Moreover, the beam-based approaches does not enable to investigate the cross-sectional deformations (i.e., warping effects). Although, there were attempts to modify the classical beam theories to overcome this challenge [47,48], they only improved the prediction of the first few modes. Furthermore, as mentioned in the previous section, the prediction accuracy reduced sharply even for the lower modes in the case of high twist rates [41] and rotation speeds [62]. Although, the plate/shell based approaches (the

classical plate theory [72] or Mindlin plate theory [62]) give better results for rotating blade type of structures, their accuracy also reduces as the boundary becomes more complex or warping effects become important.

A majority of the researchers [65, 73, 74] use finite element (FE) techniques to model the dynamics of rotating structures. The FE techniques enable accurate prediction of dynamics for stationary structures. However, in the case of rotating structures, including the additional terms such as gyroscopic, spin softening, and centrifugal stiffening effects to the element formulations is challenging [61]. Although, with the recent developments in the element formulations, several commercial FE software become able to capture the linear dynamics of rotating systems accurately [63,75], as the rotational speed increases and the stress-stiffening effects are included, deviations in natural frequencies and mode shapes are observed compared to experimental and analytical results. Furthermore, note that the computational burden increases as the structure becomes complex.

1.2.3 Identification and modeling of miniature UHS spindles

Dynamics of the UHS spindles critically affect the tool-tip dynamics, and thus, the vibrations generated during the micromachining operations [46, 76, 77]. Therefore, the quality and throughput of the micromachining processes are strongly correlated with the dynamic behavior of the (miniature) UHS spindles.

The dynamics of the conventional and high-speed spindles that are used in macro-scale machining operations has been well-studied in the literature. Some works have attempted to model the spindle dynamics analytically, e.g., [17, 78]. Although analytical models provided promising results, accurately capturing spindle dynamics using analytical techniques has been challenging due to the large level of uncertainties arising from the spindle characteristics (e.g., bearings) and the lack of accurate models for damping behavior. For these reasons, *experimental modal analysis* is generally considered as the prevailing approach for modeling spindle dynamics. In this experimental modeling approach, either a tool [79] or a cylindrical artifact [21, 77] is attached to the spindle. An excitation force is then applied to the tool/artifact, commonly using an instrumented impact hammer, and the ensuing dynamic response is measured using a motion sensor (e.g., an accelerometer). If desired, the dynamics of the cylindrical artifact can be removed from the overall response to determine only the spindle dynamics [23]. The dynamic behavior is then represented in the frequency domain in the form of frequency response functions (FRFs). Curve fitting techniques can then be used to identify the dynamic (modal) parameters from the FRFs. In

general, the impact tests are performed on a non-rotating spindle [21, 80, 81]. However, it has been shown that the dynamic behavior of spindles may change significantly with spindle speed [19, 82–84]. In addition, spindle dynamics may vary with collet pressure and/or with the tool overhang length [20, 77, 85].

Applying traditional modal testing techniques to modeling the dynamics of miniature UHS spindles poses significant challenges: *First*, non-contact measurement techniques, such as Laser Doppler Vibrometry (LDV), are required since the contact-based measurement methods cannot be applied due to relatively large size and weight of the transducers (e.g., accelerometers) and the associated adverse effects to dynamic behavior of the spindle [86,87]. Further complications arise in using contact-based sensors when the spindle is rotating at ultra-high speeds. *Second*, the frequency bandwidth of the excitation and measurement methods must cover the bandwidth of micromachining forces, which can reach up to 20 kHz [88]. Current dynamic excitation methods are commonly limited to a 10 kHz bandwidth. This necessitates development and use of techniques that provide dynamic excitations with a broad frequency bandwidth. *Third*, the excitation force exerted to the miniature spindle system should not exceed limiting force for the bearings (preferably $\leq$20 N) to prevent damage. Even with miniature hammer systems, impact force amplitudes can be as high as 200 N during a manual impact, and can cause significant damage to the bearings of miniature spindles. *Fourth*, obtaining highly repeatable excitations and measurements (i.e., with high coherence) becomes especially difficult when testing miniature spindles, which necessitates excitations on and measurements from small artifacts (e.g., a 3 mm diameter cylindrical artifact). And *fifth*, since the measurements need to be performed on a rotating spindle to capture the rotational effects, the *unwanted spindle motions*, which arise from the tool-spindle centering errors and spindle error motions, are also measured together with the dynamic response. Thus, an effective approach for removal of unwanted spindle motion data from the measurements is needed to isolate the dynamic response to the provided excitation.

To date, only a few works investigated the dynamics of miniature UHS spindles. For instance, Park and Rahnama [89] determined the dynamics of a *non-rotating* miniature spindle through modal testing within a 10 kHz bandwidth. A short cylindrical artifact attached to the spindle was instrumented with an accelerometer, and the excitation was provided manually using an impact hammer. The repeatability of the obtained FRFs and associated uncertainties have not been discussed in the paper since no coherence data was provided. Later, Aran and Budak [90] obtained the tool-tip dynamics from a miniature endmill attached to a *non-rotating* UHS spindle using modal testing. Due to the manual

impact excitation, the bandwidth of the excitation was limited to 10 kHz, and low coherence values were observed above 10 kHz and below 3 kHz. More recently, Jin and Altintas [91] used a piezoelectric actuator to excite the micro-endmill attached to a non-rotating high-speed spindle to obtain the tool tip dynamics. The dynamic motions were measured using an LDV system. Although this method enabled obtaining the dynamic behavior at high frequencies, it cannot be applied for modal testing from a rotating spindle due to contact-based excitation approach.

In the aforementioned studies on UHS spindle dynamics, the experiments were all performed on non-rotating spindles and only along one direction, and thus, the gyroscopic effects that have strong effect at ultra-high rotational speeds and the effect of cross FRFs have not been captured. Furthermore, UHS spindles that use aerodynamic bearings do not allow performing modal tests from non-rotating spindles, as the bearings cannot carry any load when not being rotated at high speeds. Therefore, the modal tests need to be performed at operational speeds to accurately identify the speed-dependent dynamics of the spindle.

1.3 Research Objectives

The mechanical micromachining possesses the basic capability to meet the need for fabricating 3D complex micro-scale features and small parts on a variety of materials. However, to realize the full potential of mechanical micromachining, the dynamics of the process needs to be well-understood. Therefore, the **overarching objective of this Ph.D. research** is to model and experimentally analyze the rotational dynamics of micro scale cutting tools and miniature UHS spindles, both of which are central to understanding the process stability. Figure 1.6 shows the overall theme of this study to address the overarching objective. Accordingly, the specific objectives are:

1. **To develop a unified spectral-Tchebychev (ST) technique to model the rotational dynamics of cutting tools:** Cutting tools are generally the most flexible parts of the micro-tool/collet/UHS spindle/machine assembly. Thus, the 3D dynamic behavior of rotating micro-tools with their complex geometry, and their coupling with the spindle dynamics, are critical for determining the dynamic response at the tool tip. Since a wide selection of cutting tool geometries are commercially available, accurate and numerically efficient dynamic models of realistic tool geometries that can capture the non-symmetric bending and coupled torsional/axial dynamics are highly needed.

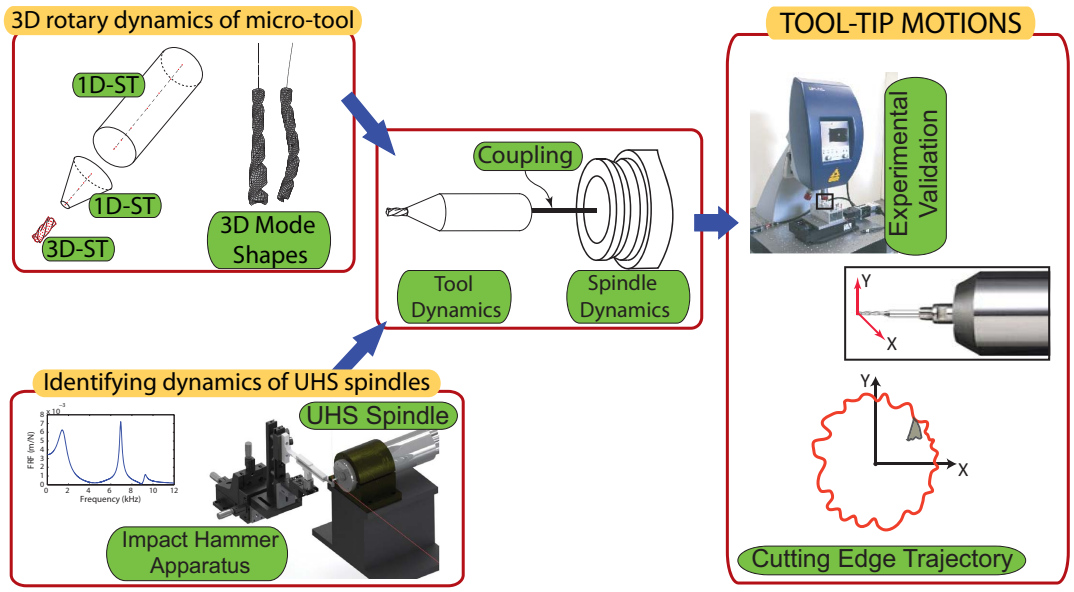

Figure 1.6: Overall theme describing the research objectives.

The simple beam-based models (such as Euler-Bernoulli or Timoshenko beam models) of the micro-tool dynamics cannot fully capture 3D dynamic behavior of micro-tools. Furthermore, the ultra-high spindle speeds make the rotational effects significant in micro-tool dynamics. Therefore, **to address this objective**, a 3D-ST technique, that uses 3D elasticity based models, is derived to model the rotational (coupled) 3D dynamics of cutting tools.

2. **To identify and model the coupled 3D dynamics of miniature UHS spindles at varying spindle speeds:** To have an effective material removal rate when using micro-scale cutting tools, UHS spindles, having rotational speeds above 60,000 rpm (up to 400,000 rpm), are generally utilized in mechanical micromachining. To attain high accuracy on the fabricated features, the dynamics of the system at the cutting edge (commonly referred as the tool tip dynamics) must be well-understood. Although modal testing could be used to characterize spindle dynamics, the conventional modal testing methods are not suitable for the experiments on miniature UHS spindles due to various challenges: First, the dynamic response of UHS spindles (contact or air bearing type) depends strongly on the spindle speed. Hence, the measurement and the identification should be performed at different spindle speeds. Second, the frequency bandwidth of the measurements should be wider than the excitation bandwidth of micromachining forces that can reach above 20 kHz [92–94]. Third, the force exerted to the system during excitation should be kept as small as possible (preferably $\leq$

20 N) to prevent any possible damage to the miniature UHS spindle. And fourth, since the characterization must be performed when the spindle is rotating, the non-ideal motions arising from spindle and centering errors (tool-attachment errors) that confound the modal response should be removed from the measured data.

To address this objective, an experimentally-based approach is developed to obtain high-fidelity frequency response function (FRFs) (both direct and cross terms) in two-mutually orthogonal directions. The obtained FRFs can then be used to derive an experimental model of the miniature UHS spindle dynamics. A novel IES is designed and constructed to excite the system in a repeatable fashion upto 20 kHz excitation bandwidth with controlled impact force amplitudes (to prevent any damage to the UHS spindle). Simultaneous measurements in two-mutually orthogonal directions are performed using two fiber-optic laser Doppler vibrometry (LDV) systems from a short precision artifact attached to the spindle. A frequency-domain filtering approach is developed to isolate the response of the system from the non-ideal motions of the spindle. The described method is used to identify the dynamics of a miniature UHS spindle (ASC 200 Fisher Precise air-bearing spindle) at different spindle speeds and collet pressures.

1.4 Research Contributions

The fundamental contributions of this Ph.D. research are focused on modeling and experimentally analyzing the rotational dynamics of micro scale cutting tools and miniature UHS spindles. Specific contributions include;

1. Development of a three-dimensional (3D) spectral-Tchebychev (ST) modeling approach to predict
   (a) the dynamics of pretwisted structures,
   (b) the rotational 3D dynamics of structures, and
   (c) the 3D dynamics of rotating micro-tools.
2. Development of a novel impact excitation system (IES) that enables repeatable, high-bandwidth impacts with controlled impact force amplitudes for modal testing of (miniature and compliant) structures.

3. Development of a systematic experimental approach to identify and understand the coupled two-dimensional speed-dependent dynamics of miniature UHS spindles.

1.5 Thesis Organization

The outline of the thesis is as follows:

- Although a 3D solution approach is needed to accurately solve the dynamics of the fluted section (since it presents 3D coupled motions such as coupled bending-bending-torsional-axial motions), having circular sections, the dynamic behavior of the other sections (i.e., shank and taper sections of micro-tools) are uncoupled; thus 1D solution approaches can accurately predict the dynamics of these section. Therefore, for the sake of completeness, in Chapter 2, a brief summary of the 1D-ST originally developed by Yagci *et al.* [29] is given.

- In Chapter 3, a new series-based spectral approach, that uses Tchebychev polynomials as the spatial basis function, to obtain efficient and high-fidelity 3D dynamic models for pretwisted structures is presented. The developed solution approach is described in detail through three sample pretwisted beam problems with rectangular, curved, and airfoil cross-sections having different pretwist amounts.

- Next, the developed 3D-ST technique is advanced to solve the dynamics of rotating/spinning structures with mixed boundary conditions. The details of the derivation are presented in Chapter 4. To show the effectiveness of the solution approach, various case studies are investigated and the results are compared to those found from literature and to those calculated from FE simulations.

- Chapter 5 describes the application of the developed solution technique to solve the dynamics of rotating micro-cutting tools in the presence of attachment errors.

- In Chapter 6, the design and evaluation of a novel custom made impact excitation system (IES) is explained in detail. The constructed IES enables repeatable and high-bandwidth modal testing of (miniature and compliant) structures; thereby plays a key role in addressing the challenges in modal testing of miniature UHS spindles.

- Subsequently, Chapter 7 presents the experimental methodology to obtain the speed-dependent dynamics of miniature UHS spindles using the constructed IES. The developed experimental methodology is used to characterize the two-dimensional speed-

dependent dynamics of an air bearing electric turbine miniature spindle (ASC 200 Fisher Precise air-bearing spindle).

- As a last study, to show the broad impact of the develop modeling approach, a macro-scale endmill is modeled using the 3D-ST technique and coupled to the (experimentally obtained) dynamics of the spindle to predict the tool-point dynamics. The study presented in this chapter is performed together with Prof. Tony. L. Schmitz (Professor of Mechanical Engineering and Engineering Science Department at University of North Carolina Charlotte) and his Ph.D. student Uttara Kumar (currently works as a Mechanical Engineer at General Electric Global Research) as a collaborative research.

- Lastly, Chapter 9 and Chapter 10 summarize the conclusions deduced from the presented research, and discuss the future work to obtain the dynamics of the micro machine tool at the tool tip (merging the cutting tool and the spindle dynamics) and the extension of the conducted fundamental research, respectively.

Chapter 2

One-Dimensional Spectral-Tchebychev Technique

"Practice makes the master."

-Patrick Rothfuss (The Name of the Wind)

This chapter summarizes the application of ST technique, that was developed by Yagci *et al.* [29], to solve the dynamics of 1D beam problems and the general properties of Tchebychev polynomials. To insure the accuracy of the dynamic model, particularly for higher modes, the Timoshenko beam model (instead of Euler-Bernoulli beam model), which includes the shear and rotary inertia effects, is used in this thesis.

2.1 Timoshenko Beam Model

The boundary value problem (BVP) governing the dynamics of the structures can be derived using the extended Hamilton's principle [95], which is expressed as

$$\int_{t_1}^{t_2} (\delta E_K - \delta E_S + \delta W_{nc}) dt = 0, \quad \delta q_i = 0 \quad \text{at} \quad t = t_1, t_2. \tag{2.1}$$

The terms E_K, E_S, and W_{nc} represent the kinetic energy, strain (potential) energy, and the work done by non-conservative forces, respectively, t_1 and t_2 are two instants of time, q_i represents the generalized coordinate, which corresponds to the ith term of the deflection vector $\mathbf{q}$ (in this case $\mathbf{q} = \{\mathbf{u}; \psi\}$ where $\mathbf{u}$ is the flexural displacement and ψ is the slope), and δ is the variational operator.

For a Timoshenko beam, the terms of kinetic energy, strain energy, and the work done by non-conservative forces can be expressed as

$$E_K = \frac{1}{2}\int_0^L \rho A(z)\left(\frac{\partial \mathbf{u}}{\partial t}\right)^2 dz, \tag{2.2}$$

$$E_S = \frac{1}{2}\int_0^L \left\{EI(z)\left(\frac{\partial \psi}{\partial z}\right)^2 + k_s GA(z)\left(\frac{\partial \mathbf{u}}{\partial z} - \psi\right)^2\right\} dz, \tag{2.3}$$

$$W_{nc} = \int_0^L {\mathbf{f_q}}^T \mathbf{q}\, dz \tag{2.4}$$

where L is the length of the beam, ρ is the density, $A(z)$ is the cross-sectional area, E is the Young's modulus, G is the shear modulus, $I(z)$ is the second area moment, k_s is the shear constant, and $\mathbf{f_q}$ is the forcing vector (note here that $\mathbf{f_q}$ includes both forces and moments acting on the beam).

Inserting Eqs. (2.2)-(2.4) into the Hamilton's equation, Eq. (2.1), and applying integration by parts, the integral boundary value problem (IBVP) can be obtained as

$$\begin{aligned}\int_0^L \Bigg\{&\rho A(z)\frac{\partial^2 \mathbf{u}}{\partial t^2}\,\delta\mathbf{u} + \rho I(z)\frac{\partial^2 \psi}{\partial t^2}\,\delta\psi + EI(z)\frac{\partial \psi}{\partial z}\,\frac{\partial \delta\psi}{\partial z}\\ &+ k_s GA(z)\left(\frac{\partial \mathbf{u}}{\partial z} - \psi\right)\left(\frac{\partial \delta\mathbf{u}}{\partial z} - \delta\psi_y\right)\Bigg\} dz = \int_0^L {\mathbf{f_q}}^T \{\delta q\} dz,\end{aligned} \tag{2.5}$$

where $\delta\mathbf{q} = \{\delta\mathbf{u};\, \delta\psi\}$ are the functions representing the variation of the deflection terms.

2.2 Spectral-Tchebychev Technique

To solve the derived IBVP, Eq. (2.5), a discretization procedure is applied through the use of Tchebychev series expansion, including expressing the derivatives and inner products as Tchebychev matrices. A brief overview of the Tchebychev approach is given in the following sections; however, the reader is referred to [29, 96, 97] for detailed characteristics of Tchebychev polynomial and derivation of the Tchebychev matrices.

2.2.1 Tchebychev polynomials and expansion

Tchebychev polynomials are a set of recursive and orthogonal polynomials that can be described as

$$\mathtt{T}_k(x) = \cos\left(k\,\cos^{-1}(x)\right) \quad \text{for} \quad k = 0, 1, 2, \cdots \tag{2.6}$$

where k is an integer [97]. Since Tchebychev polynomials form a complete set only on the $(-1, 1)$ interval (which indicates that any square-integrable function can be represented exactly by an infinite series expansion using the Tchebychev polynomials as the basis), a linear mapping is applied between $x \in (l_1, l_2)$ and $\xi \in (-1, 1)$ to obtain the scaled Tchebychev polynomials $\mathbb{T}_k(x) = T_k(\xi(x))$ for the interval (l_1, l_2).

The convergence behavior of Tchebychev polynomials is exponential (i.e., the coefficients of expansion decays exponentially with increasing number of polynomials used) [96, 97]. Thus, a function can be expressed accurately with low polynomial numbers. Considering the numerical calculations, one can use the truncated series expansion as

$$f_N(x) = \sum_{k=0}^{N-1} a_k \mathbb{T}_k(x) \tag{2.7}$$

where a_k's are the coefficients of the expansion, and N is the number of polynomials used in the expansion.

2.2.2 Gauss-Lobatto sampling

Although a function can be sampled at N arbitrary spatial points within the domain, there are two sampling options that work perfectly with the Tchebychev polynomials: **(a)** Gauss-Tchebychev sampling and **(b)** Gauss-Lobatto sampling [96]. In this study, Gauss-Lobatto sampling is used; thus the sampling points, p_k, can be calculated as

$$p_k = \cos\left(\frac{(k-1)\pi}{N-1}\right) \quad , \quad k = 1, 2, 3, \cdots, N \tag{2.8}$$

Using the Gauss-Lobatto sampling, the relationship between the coefficients of expansion (a_k)'s and the sampled function can be written as

$$\begin{Bmatrix} y_0 \\ y_1 \\ \vdots \\ y_{N-1} \end{Bmatrix} = \begin{bmatrix} \mathbb{T}_0(x_0) & \mathbb{T}_1(x_0) & \cdots & \mathbb{T}_{N-1}(x_0) \\ \mathbb{T}_0(x_1) & \mathbb{T}_1(x_1) & \cdots & \mathbb{T}_{N-1}(x_1) \\ \vdots & \vdots & \ddots & \vdots \\ \mathbb{T}_0(x_{N-1}) & \mathbb{T}_1(x_{N-1}) & \cdots & \mathbb{T}_{N-1}(x_{N-1}) \end{bmatrix} \begin{Bmatrix} a_0 \\ a_1 \\ \vdots \\ a_{N-1} \end{Bmatrix}. \tag{2.9}$$

or in matrix form as

$$\mathbf{a} = \mathbf{\Gamma_F f} \quad \text{and} \quad \mathbf{f} = \mathbf{\Gamma_B a} \tag{2.10}$$

where $\mathbf{a}$, $\mathbf{f}$, $\mathbf{\Gamma_F}$, and $\mathbf{\Gamma_B}$ are the vectors of expansion coefficients and sampled function, and the forward and backward transformation matrices, respectively [29] (note that $\mathbf{\Gamma_F} = \mathbf{\Gamma_B}^{-1}$).

2.2.3 Differentiation and integration in Tchebychev domain

Since the IBVP is discretized using Tchebychev polynomials, the derivative and integral operations should also be performed in this domain. The nth spatial derivative $\partial f^{(n)}/\partial x_i^{(n)}$ can be written using the Tchebychev expansion in Eq. (2.7) by replacing coefficients $\mathbf{a}$ with coefficients $\mathbf{b}^{(n)}$. That is, the derivative of a function is itself another function, which can be expanded using Tchebychev polynomials. The coefficients $\mathbf{a}$ and $\mathbf{b}^{(n)}$ of the nth spatial derivative of $\mathbf{f}$ with respect to coordinate x can be found using the recursive nature of the Tchebychev polynomials as

$$\mathbf{b}^{(n)} = \mathbf{D}_x^n \, \mathbf{a}. \tag{2.11}$$

Using the differentiation and transformation matrices, the derivative of the function f can be computed as

$$\mathbf{f}^{(n)} = \mathbf{\Gamma_B} \, \mathbf{b}^{(n)} = \mathbf{\Gamma_B} \, \mathbf{D}_x^n \, \mathbf{\Gamma_F} \, \mathbf{f} = \mathbf{Q}_x^n \, \mathbf{f}, \tag{2.12}$$

where $\mathbf{f}^{(n)}$ is the sampled vector for the nth derivative of $\mathbf{f}$, and $\mathbf{Q}_x^n$ is the nth derivative matrix for the x direction.

To perform the integral operations, first the definite integral vector, $\mathbf{v}$, necessary to perform the integral operation

$$\int_{l_1}^{l_2} f(x) dx = \mathbf{v}^T \, \mathbf{a} \tag{2.13}$$

must be calculated. Using the truncated series expansion, the definite integral vector can be found as $v_k = \int_{l_1}^{l_2} \mathbb{T}_k dx$. Similarly, the inner product of two functions $\mathbf{f}$ and $\mathbf{g}$ can be expressed by Tchebychev polynomials as

$$\int_{l_1}^{l_2} f(x) \, g(x) \, dx = \int_{l_1}^{l_2} h(x) \, dx. \tag{2.14}$$

Note that, the multiplication of two functions, $f(x)$ and $g(x)$, that are defined in the N dimensional space, will result a function, $h(x)$ in $2\,N$ dimensional space. Thus, first the

functions, $f(x)$ and $g(x)$, should be interpolated to be defined in the $2\,N$ dimensional space as

$$\begin{aligned}\mathbf{f_{2N}} &= \mathbf{\Gamma_{B_{2N}}}[\mathbb{I}_N;\, \mathbb{O}_N]\mathbf{\Gamma_{F_N}}\mathbf{f_N} \\ &= \mathbf{S_2}\mathbf{f_N}\,, \end{aligned} \tag{2.15}$$

where $\mathbf{S_2}$ is the N-to-$2\,N$ interpolating matrix, $\mathbf{\Gamma_{B_{2N}}}$ is the $2\,N \times 2\,N$ dimensional backward transformation matrix, and $\mathbb{I}_N$ and $\mathbb{O}_N$ are the $N \times N$ dimensional identity and zero matrices, respectively. Thus,

$$\int_{l_1}^{l_2} h(x)\,dx = \mathbf{v}_{2N}^T\,\mathbf{a}^h = \mathbf{f}_N^T\mathbf{V}\mathbf{g}_N, \tag{2.16}$$

where $\mathbf{v}_{2N}$ is the definite integral vector for a function defined in the $2\,N$ dimensional space, and $\mathbf{a}^h$ is the expansion coefficients for the function, $h(x)$. Using the forward and backward transformation matrices, the inner product matrix, $\mathbf{V}$, for the multiplication of two functions can be found as $\mathbf{V} = \mathbf{S}_2^T\mathbf{v}_{d,2N}S_2$, where $\mathbf{v}_{d,2N}$ is the diagonal matrix whose diagonal elements are the values of $\mathbf{v}_{2N}$.

However, if the differential equation has variable coefficients (referred as weighting functions, $w(x)$) such as $A(z)$ or $I(z)$, their effect should be imposed to the inner product matrix. Note that, in this case, three functions are multiplied; and thus, the resulting function will be in $3\,N$ dimensional space. Following the derivation for the multiplication of two functions described above, the inner product matrix for the multiplication of three functions ($f(x)$, $g(x)$, $w(x)$) can be found as $\mathbf{V}^w = \mathbf{S_3}^T\mathbf{v}_{d,3N}\mathbf{w}_{d,3N}\mathbf{S_3}$ [29].

2.3 Obtaining the Discretized Equations of Motion

Using the Tchebychev expansion, the deflection terms in Eq. (2.5) can now be written as

$$q_i(x,\psi,t) = \sum_{k=1}^{N_\xi} a_{qi}(t)T_{k-1}(x). \tag{2.17}$$

The discretized deflection terms in x and ψ directions can be expressed as

$$\mathbf{u} = \begin{bmatrix} \mathbb{I} & \mathbb{O} \end{bmatrix}\mathbf{q} = \mathbb{I}_u\mathbf{q}\,, \tag{2.18}$$

$$\psi = \begin{bmatrix} \mathbb{O} & \mathbb{I} \end{bmatrix}\mathbf{q} = \mathbb{I}_\psi\mathbf{q}, \tag{2.19}$$

where $\mathbb{I}$ and $\mathbb{O}$ are $(N_x \times N_x)$ identity and zero matrices, respectively, and $\mathbf{q} = \{\mathbf{u};\ \psi\}$ represents the sampled deflections. Substituting Eqs. (2.12)- (2.18) in Eq. (2.5), the mass, stiffness and forcing matrices can be obtained as

$$M = \rho A \mathbb{I}_u^T \mathbf{V} \mathbb{I}_u + \rho I \mathbb{I}_\psi^T \mathbf{V} \mathbb{I}_\psi \ , \tag{2.20}$$

$$K = EI \mathbb{Q}_\psi^T \mathbf{V} \mathbb{Q}_\psi + k_s G A (\mathbb{Q}_u - \mathbb{I}_\psi)^T \mathbf{V} (\mathbb{Q}_u - \mathbb{I}_\psi) \ , \tag{2.21}$$

$$F = V \mathbf{f_q} \ . \tag{2.22}$$

Chapter 3

Modeling the Three-Dimensional Dynamics of Pretwisted Beams

"Numerical precision is the very soul of science."

-Sir D'Arcy Wentworth Thompson

This chapter presents the application of the ST technique to solve 3D dynamics of unconstrained pretwisted beams with general cross-section (including both straight and curved cross-sections). In general, the dynamic response of pretwisted beams presents 3D motions, including coupled bending-bending-torsional-axial motions. As such, accurately solving pretwisted beam dynamics requires a 3D solution approach. In this work, the IBVP based on the 3D linear elasticity equations is solved numerically using the 3D-ST approach. To simplify evaluation of the volume integrals, the boundaries are simplified applying two coordinate transformations to render the pretwisted beam with curved cross-section into an equivalent straight beam with rectangular cross-section. Three sample pretwisted beam problems with rectangular, curved, and airfoil cross-sections at different twist rates are solved using the presented approach.

3.1 Boundary-Value Problem for Three-Dimensional Beams

The geometry of a pretwisted beam having a general cross-section and uniform twist rate is illustrated in Fig. 3.1. The function $B(x, y, z)$ is used to describe the 3D boundary. The twist rate is quantified by the number (or fraction) of full twists within the length of the beam. For instance, a twist rate of 0.5, or half twist per length, indicates that the total

twist is 180 degrees within the length of the beam (i.e., the pitch is equal to twice the beam length).

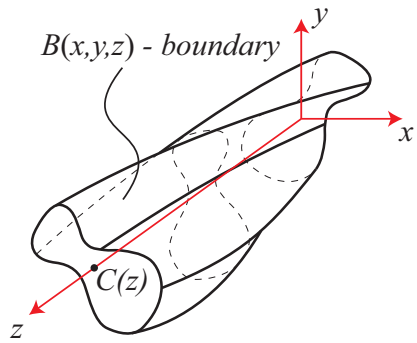

Figure 3.1: Description of a pretwisted beam having a general cross-section.

The boundary value problem (BVP) governing the dynamics of the structures can be derived using the extended Hamilton's principle [95] (as described before), which is expressed as

$$\int_{t_1}^{t_2} (\delta E_K - \delta E_S + \delta W_{nc}) dt = 0, \qquad \delta \mathbf{q_i}(x, y, z, t) = 0 \quad \text{at} \quad t = t_1, t_2. \tag{3.1}$$

The terms E_K, E_S, and W_{nc} represent the kinetic energy, strain (potential) energy, and the work done by nonconservative forces, respectively, t_1 and t_2 are two instants of time, x, y, z are the spatial variables, $\mathbf{q_i}$ represents the generalized coordinate, which corresponds to the ith term of the deflection vector $\mathbf{q} = \{\mathbf{u}; \mathbf{v}; \mathbf{w}\}$, and δ is the variational operator.

For linear elastic behavior, the strain, stress, and displacement relationships can be used to express the strain energy as

$$E_S = \frac{1}{2} \int_V \mathbf{q}^T \mathbf{B}^T \mathbf{C} \mathbf{B} \mathbf{q} \, dx \, dy \, dz. \tag{3.2}$$

Here, V represents the volume domain of the BVP, $\mathbf{C}$ is the constitutive matrix ($\sigma = \mathbf{C}\epsilon$) and $\mathbf{B}$ is the differential operator matrix ($\epsilon = \mathbf{B}\mathbf{q}$) that relates the strains to the displacements. The kinetic energy and the work done by non-conservative forces for a structure are written as

$$E_K = \frac{1}{2} \int_V \rho \, \dot{\mathbf{q}}^T \dot{\mathbf{q}} \, dx \, dy \, dz, \tag{3.3}$$

$$W_{nc} = \int_V \mathbf{f_q}^T \mathbf{q} \, dx \, dy \, dz + \mathbf{f_b}^T \, \mathbf{q_b}, \tag{3.4}$$

respectively, where $\mathbf{f_q} = \{\mathbf{f_x}; \mathbf{f_y}; \mathbf{f_z}\}^T$ represents the forces in the domain, $\mathbf{f_b}$ represents the forces on the boundary and $\mathbf{q_b}$ represents the deflection terms on the boundary.

Inserting Eqs. (3.2) and (3.3) into the extended Hamilton's principle described in Eq. (3.1) leads to

$$\int_{t_1}^{t_2} \int_V \left\{ \left[\rho\, \ddot{\mathbf{q}}^T \delta\mathbf{q} - \mathbf{q}^T \mathbf{B}^T \mathbf{C} \mathbf{B} \delta\mathbf{q} + \mathbf{f_q}^T \delta\mathbf{q} \right] dx\, dy\, dz + \mathbf{f_b}^T\, \delta\mathbf{q}_b \right\} dt = 0, \tag{3.5}$$

In this variational approach, the variation defining the deflection vector is imposed as

$$\mathbf{q} = \bar{\mathbf{q}} + \hat{\mathbf{q}}, \tag{3.6}$$

where $\mathbf{q}$ is the solution of the boundary value problem, $\bar{\mathbf{q}}$ represents a family of trial functions satisfying the displacement (essential) boundary conditions, and $\hat{\mathbf{q}}$ is the variation (from the true solution $\mathbf{q}$) in the form of time-invariant arbitrary test functions that satisfy the homogeneous displacement boundary conditions [95]. Using Eq. (3.6), the variation of the displacement terms can be expressed as $\delta\,\mathbf{q} = \hat{\mathbf{q}}$, which is inserted into Eq. (3.5) resulting in the IBVP as

$$\int_V \left[\rho\, \ddot{\mathbf{q}}^T \hat{\mathbf{q}} + \mathbf{q}^T \mathbf{B}^T \mathbf{C} \mathbf{B} \hat{\mathbf{q}} \right] dx\, dy\, dz = \int_V \mathbf{f_q}^T \hat{\mathbf{q}}\, dx\, dy\, dz + \mathbf{f_b}^T\, \hat{\mathbf{q}}_\mathbf{b}. \tag{3.7}$$

For generality and numerical efficiency, the IBVP is non-dimensionalized using the reference length L_r such that $x = x^* L_r$, $y = y^* L_r$, $z = z^* L_r$, $\mathbf{q} = \mathbf{q}^* L_r$, $\hat{\mathbf{q}} = \hat{\mathbf{q}}^* L_r$, $L = L^* L_r$, $A = A^* L_r^2$, and $\mathbf{B} = \mathbf{B}^*/L_r$. Here, $\mathbb{A}$ represents the area and the * subscript indicates the non-dimensional parameter. The constitutive matrix $\mathbf{C}$ is non-dimensionalized as $\mathbf{C} = \mathbf{C}^* E$, where E is the Young's modulus of the material. Substituting non-dimensionalized variables, the IBVP becomes

$$\int_V \left[\frac{\rho L_r^2}{E}\, \ddot{\mathbf{q}}^T \hat{\mathbf{q}} + \mathbf{q}^T \mathbf{B}^T \mathbf{C} \mathbf{B} \hat{\mathbf{q}} \right] dx\, dy\, dz = \int_V \frac{L_r}{E} \mathbf{f_q}^T \hat{\mathbf{q}}\, dx\, dy\, dz, + \frac{1}{E\, L_r^2} \mathbf{f_b}^T \hat{\mathbf{q}}_\mathbf{b}\,, \tag{3.8}$$

where the superscripts are omitted for simplicity.

3.2 Formulation of the Boundary-Value Problem for Pretwisted Beams

For pretwisted beams having general cross-sections, solving the IBVP given in Eq. (3.8) poses significant challenges due to the complicated domain on which the volume integrals

must be evaluated. To address this challenge, the domain of the problem should be simplified using coordinate transformations. First, a local reference frame ($\bar{x}$, $\bar{y}$, $\bar{z}$) that rotates with the pretwist is defined (see Fig. 3.2(b)). In this domain, the original pretwist beam is represented as a straight beam with the same cross-sectional geometry as that of the pretwisted beam. This transformation is achieved by using a rotational transformation matrix that imposes a right-hand rotation of $2\pi\alpha z/L$ about the z axis as

$$\begin{Bmatrix} \bar{x} \\ \bar{y} \\ \bar{z} \end{Bmatrix} = \begin{bmatrix} \cos(2\pi\alpha\frac{z}{L}) & \sin(2\pi\alpha\frac{z}{L}) & 0 \\ -\sin(2\pi\alpha\frac{z}{L}) & \cos(2\pi\alpha\frac{z}{L} & 0 \\ 0 & 0 & 1 \end{bmatrix} \begin{Bmatrix} x \\ y \\ z \end{Bmatrix}. \tag{3.9}$$

where α is the twist rate, and L is the total length of the beam [39, 44, 49].

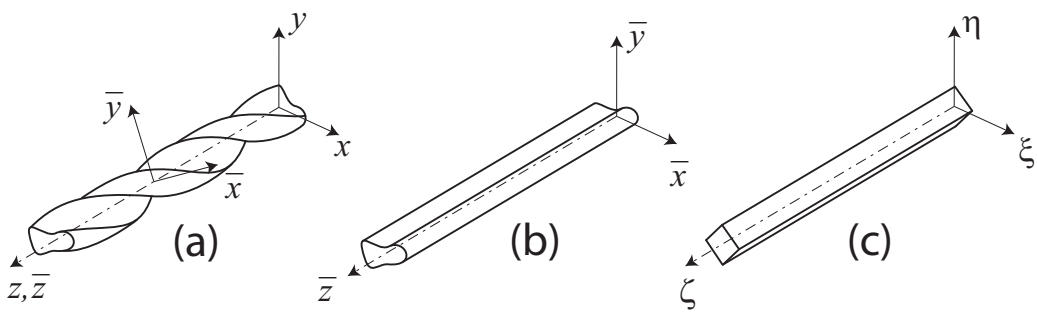

Figure 3.2: **(a)** The pretwisted beam in the physical domain, **(b)** the straight beam with curved cross-section obtained after the first transformation, **(c)** the straight beam with rectangular cross-section obtained after the cross-sectional mapping.

Second, a one-to-one mapping approach is used to transform the curved cross-section (if present) from $\bar{x}$, $\bar{y}$, and $\bar{z}$ coordinates onto a rectangular cross-section defined by ξ, η, and ζ coordinates (see Fig. 3.3) [98]. In this study, a polynomial mapping is used to express the physical coordinates in terms of a set of mapping points and mapping polynomials as

$$\bar{x}(\xi,\eta) = \sum_{i=1}^{(m+1)(n+1)} \bar{x}_i\phi_i(\xi,\eta), \qquad \bar{y}(\xi,\eta) = \sum_{i=1}^{(m+1)(n+1)} \bar{y}_i\phi_i(\xi,\eta), \tag{3.10}$$

where $\bar{x}_i$ and $\bar{y}_i$ are mapping points, and m and n are the polynomial orders along the ξ and η directions, respectively. Corresponding to each mapping point, a mapping polynomial

(shape function) ϕ_i is defined as

$$\phi_i(\xi,\eta) = A_0\left(\prod_{k=1,k\neq m_i}^{m+1}(\xi-\xi_k)\right)\left(\prod_{l=1,l\neq n_i}^{n+1}(\eta-\eta_l)\right), \tag{3.11}$$

where i lies at the intersection of lines m_i and n_i on the rectangular mapping. This definition ensures that the shape function for a mapping point i is unity for point i and zero for all other mapping points. To ensure the unity condition, A_0 is determined from $A_0 = 1/(\phi_i(\xi_i,\eta_i)$.

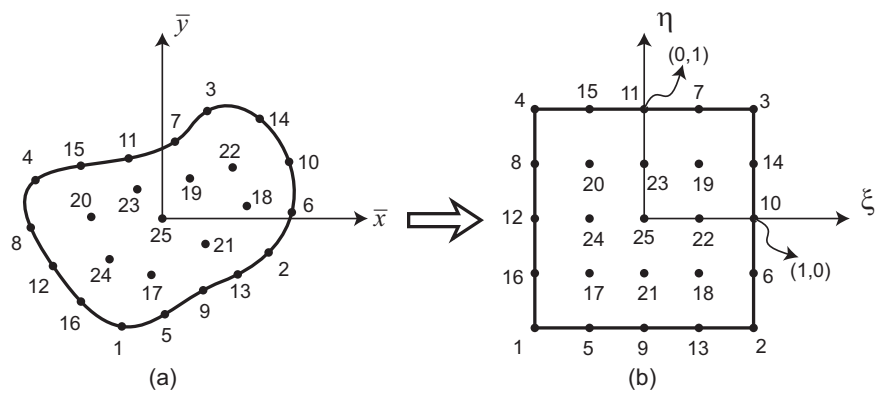

Figure 3.3: A fourth-order polynomial mapping of the curved cross-section to a rectangular domain. The cross-section in **(a)** the physical domain and **(b)** the mapped rectangular domain.

The accuracy of the mapping depends on the selection of the mapping points and the type and the order of the mapping polynomials [98]. In this work, no attempt has been made to optimize the mapping approach. A fourth order mapping with $m = n = 4$ lines (rectangular mapping) is used in this analysis (see Fig. 3.3), leading to 25 mapping polynomials. The minimum number of required mapping points, which is $(m+1)(n+1) = 25$ for this case, is used to capture the complicated cross-sectional geometry. This results in $m+1 = 5$ and $n+1 = 5$ lines in ξ and η coordinates, respectively.

The presented approach relies on the use of a one-to-one mapping, and therefore requires the Jacobian of mapping to be positive for all sampling points. This brings some limitations in terms of the geometries that can be mapped to a rectangular shape, and necessitates careful choice of mapping points. For instance, it is not possible to obtain a one-to-one mapping for geometries that cross-section mapping leads to either discontinuous edges or obtuse angles for the corner mapping points. Therefore, the choice of mapping points should be validated by checking the determinant of the Jacobian.

Through the two transformations, the curved pretwisted beam in the physical domain becomes a straight rectangular beam in the transformed domain. However, the IBVP defined by Eq. (3.8) should be modified to complete the transformations. For this purpose, the derivative operators in the physical (x,y,z) domain are transformed onto the mapped domain (ξ, η, ζ) using Jacobian matrices as

$$\frac{\partial}{\partial \varepsilon_i} = \sum_{j=1}^{3}\sum_{k=1}^{3} J_{jk}^{\bar{q}q} J_{ki}^{\epsilon\bar{q}} \frac{\partial}{\partial q_j} \quad \text{and} \quad \frac{\partial}{\partial q_j} = \sum_{i=1}^{3} (J^{-1})_{ij} \frac{\partial}{\partial \varepsilon_i} \ , \tag{3.12}$$

where $J_{jk}^{\bar{x}x}$ and $J_{ki}^{\epsilon\bar{x}}$ are the elements of the Jacobian matrices. Here, q and ε represent the physical domain and mapped domain coordinates, respectively. Using the differential operators in Eq. (3.12) along with $dx\,dy\,dz = |\mathbf{J}|\,d\xi\,d\eta\,d\zeta$, the functions in Eq. (3.8) can be expressed in the mapped coordinates ξ, η, and ζ. Therefore, while simplifying the problem boundaries, the transformations increased the complexity of the boundary-value problem.

3.3 Three-Dimensional Spectral-Tchebychev Technique

The solution approach entails discretizing the (transformed) boundary value problem through the use of Tchebychev series expansion, including expressing the derivatives and inner products as Tchebychev matrices. Since the Tchebychev expansion converges exponentially [97], a finite number of terms is sufficient to describe a function $f(\xi, \eta, \zeta)$ in the (x,y,z) domain as

$$f(\xi, \eta, \zeta) = \sum_{k=1}^{N_\xi}\sum_{l=1}^{N_\eta}\sum_{m=1}^{N_\zeta} a_{klm}\, T_{k-1}(\xi)\, T_{l-1}(\eta)\, T_{m-1}(\zeta), \tag{3.13}$$

where a's are the polynomial coefficients and N_j is the number of polynomials associated with the coordinate $j = \xi, \eta, \zeta$.

Any continuous function in the (transformed) domain is discretized through sampling at the Gauss-Lobatto points [29, 59] in all three directions. The sampling and computations are conducted in the matrix-vector domain (rather than in the tensor domain) as

$$f_c = f(\xi(k), \eta(l), \zeta(m)), \qquad c = (k-1)N_\eta N_\zeta + (l-1)N_\zeta + m. \tag{3.14}$$

Vector mapping is also applied to the coefficients of the Tchebychev polynomials a_{klm} in Eq. (3.13). Thus, the size of the vectors $\mathbf{f}$ and $\mathbf{a}$ are ($N_\xi N_\eta N_\zeta \times 1$). The vector of the

sampled function $\mathbf{f}$ and the Tchebychev coefficient vector $\mathbf{a}$ are related as

$$\mathbf{a} = \mathbf{\Gamma_F}\,\mathbf{f} \quad \text{and} \quad \mathbf{f} = \mathbf{\Gamma_B}\,\mathbf{a}, \tag{3.15}$$

where $\mathbf{\Gamma_F}$ and $\mathbf{\Gamma_B}$ are $(N_\xi N_\eta N_\zeta \times N_\xi N_\eta N_\zeta)$ global (extended) forward and backward transformation matrices, respectively. To find the global transformation matrices, a similar vector mapping procedure described in Eq. (3.14) is followed. For instance, the global backward transformation matrix is computed as

$$\begin{gathered}
\Gamma_{B_{c_1 c_2}} = \Gamma^x_{B_{k_1 k_2}}\,\Gamma^y_{B_{l_1 l_2}}\,\Gamma^z_{B_{m_1 m_2}} \\
k_1 = 1,\ldots,N_x\,,\;\; k_2 = 1,\ldots,N_x\,,\;\; l_1 = 1,\ldots,N_y\,,\;\; l_2 = 1,\ldots,N_y\,, \\
m_1 = 1,\ldots,N_z\,,\;\; m_2 = 1,\ldots,N_z\,, \\
c_1 = (k_1 - 1)\,Ny\,N_z + (l_1 - 1)\,N_z + m_1\,, \\
c_2 = (k_2 - 1)\,Ny\,N_z + (l_2 - 1)\,N_z + m_2\,.
\end{gathered} \tag{3.16}$$

The nth spatial derivative $\partial^{(n)} f / \partial {\xi_i}^{(n)}$ can be written using the Tchebychev expansion in Eq. (3.13) by replacing coefficients a with coefficients $b^{(n)}$. That is, the derivative of a function is itself another function, which can be expanded using Tchebychev polynomials. The coefficients $\mathbf{a}$ and $\mathbf{b}^{(n)}$ of the nth spatial derivative of f with respect to coordinate x_i can be given as

$$\mathbf{b}^{(n)} = D^n_{\xi_i}\,\mathbf{a}. \tag{3.17}$$

Using the differentiation and transformation matrices, the derivative of the function f can be computed as

$$\mathbf{f}^{(n)} = \mathbf{\Gamma_B}\,\mathbf{b}^{(n)} = \mathbf{\Gamma_B}\,D^n_{\xi_i}\,\mathbf{\Gamma_F}\,\mathbf{f} = \mathbf{Q^n_{\xi_i}}\,\mathbf{f}, \tag{3.18}$$

where $\mathbf{f}^{(n)}$ is the sampled vector for the nth derivative of f, and $\mathbf{Q^n_{\xi_i}}$ is the nth derivative matrix for the ξ_i direction and is extended as

$$\begin{gathered}
\mathbb{Q}_{x_{c_1 c_2}} = Q_{x_{k_1 k_2}} \\
k_1 = 1,\ldots,N_x\,,\;\; k_2 = 1,\ldots,N_x\,,\;\; l = 1,\ldots,N_y\,,\;\; m = 1,\ldots,N_z\,, \\
c_1 = (k_1 - 1)\,Ny\,N_z + (l - 1)\,N_z + m\,, \\
c_2 = (k_2 - 1)\,Ny\,N_z + (l - 1)\,N_z + m\,.
\end{gathered} \tag{3.19}$$

$$\mathbb{Q}_{y_{c_1 c_2}} = Q_{y_{l_1 l_2}} \tag{3.20}$$
$$k = 1, \ldots, N_x\,, \;\; l_1 = 1, \ldots, N_y\,, \;\; l_2 = 1, \ldots, N_y\,, \;\; m = 1, \ldots, N_z\,,$$
$$c_1 = (k-1)\, Ny\, N_z + (l_1 - 1)\, N_z + m\,,$$
$$c_2 = (k-1)\, Ny\, N_z + (l_2 - 1)\, N_z + m\,.$$

$$\mathbb{Q}_{z_{c_1 c_2}} = Q_{z_{m_1 m_2}} \tag{3.21}$$
$$k = 1, \ldots, N_x\,, \;\; l = 1, \ldots, N_y\,, \;\; m_1 = 1, \ldots, N_z\,, \;\; m_2 = 1, \ldots, N_z\,,$$
$$c_1 = (k-1)\, Ny\, N_z + (l - 1)\, N_z + m_1\,,$$
$$c_2 = (k-1)\, Ny\, N_z + (l - 1)\, N_z + m_2\,.$$

for x, y, and z directions, respectively.

The inner product matrix calculations for one-dimensional problems are described in the previous chapter. However, the global inner product matrix calculation for the pretwisted geometries is slightly different since the differential equation has a variable coefficient (weighting function) that is the Jacobian of mapping ($\mathbf{J}$).

$$\int_{I_x}\int_{I_y}\int_{I_z} f(x,y,z)g(x,y,z)A(x,y,z)dxdydz = \mathbf{f}^T\mathbf{V}^{\mathbf{A}}\mathbf{g}, \tag{3.22}$$

where I_x, I_y, and I_z defines the domain for each dimension. Similarly as in one-dimensional case, the product of Tchebychev expansion of three functions has an order of $3N_x 3N_y 3N_z$ in 3D domain. Therefore, the values of the functions at $N_x N_y N_z$ Gauss-Lobatto points are extrapolated to $3N_x 3N_y 3N_z$ points to better approximate the inner product such that

$$\mathbf{f}_{3N_x 3N_y 3N_z} = \mathbf{S^{x_3}}\mathbf{S^{y_3}}\mathbf{S^{z_3}}\mathbf{f}_{N_x N_y N_z}\,. \tag{3.23}$$

Here $\mathbf{S^{x_3}}$, $\mathbf{S^{y_3}}$, and $\mathbf{S^{z_3}}$ are calculated in the same procedure as $\mathbf{S_3}$ in one-dimensional domain [29]. Therefore, Eq. (3.22) can be written as using the summation notation,

$$\int_v f(x,y,z)g(x,y,z)A(x,y,z)dv = \tag{3.24}$$
$$\sum_{i,j,k}^{3N_x,3N_y,3N_z} \mathbf{v_i^{3N_x}}\mathbf{v_j^{3N_y}}\mathbf{v_k^{3N_z}}(\mathbf{S_{ia}^{x_3}}\mathbf{S_{jb}^{y_3}}\mathbf{S_{kc}^{z_3}}\mathbf{S_{id}^{x_3}}\mathbf{S_{je}^{y_3}}\mathbf{S_{kf}^{z_3}}\mathbf{S_{il}^{x_3}}\mathbf{S_{jm}^{y_3}}\mathbf{S_{kn}^{z_3}}A_{lmn}).$$

Therefore, the global inner product matrix is,

$$\mathbf{V^A_{abcdef}} = \sum_{i,j,k}^{3N_x,3N_y,3N_z} \sum_{l,m,n}^{3N_x,3N_y,3N_z} \mathbf{v_i^{3N_x} v_j^{3N_y} v_k^{3N_z}} \tag{3.25}$$

$$(\mathbf{S^{x_3}_{ia} S^{y_3}_{jb} S^{z_3}_{kc} S^{x_3}_{id} S^{y_3}_{je} S^{z_3}_{kf} S^{x_3}_{il} S^{y_3}_{jm} S^{z_3}_{kn}} A_{lmn}).$$

Here, $\mathbf{V^A_{abcdef}}$ is a 6D tensor. To transform it into a global inner product matrix, same mapping frame is used as described in Eq (3.3).

3.4 Obtaining the Discretized Equations of Motion

Using the Tchebychev expansion, the deflection terms, $\mathbf{q}$, in Eq. (3.8) can now be written in the form of Eq. (3.13) as a finite summation of Tchebychev polynomials. The discretized deflection terms in ξ, η, and ζ directions can be expressed as

$$\mathbf{u} = \mathbf{I_u q} = \big[\mathbf{I\,0\,0}\big]\mathbf{q}, \qquad \mathbf{v} = \mathbf{I_v q} = \big[\mathbf{0\,I\,0}\big]\mathbf{q}, \qquad \mathbf{w} = \mathbf{I_w q} = \big[\mathbf{0\,0\,I}\big]\mathbf{q}, \tag{3.26}$$

where $\mathbf{I}$ and $\mathbf{0}$ are $(N_\xi N_\eta N_\zeta \times N_\xi N_\eta N_\zeta)$ identity and zero matrices, respectively, and $\mathbf{q} = \{\mathbf{u};\ \mathbf{v};\ \mathbf{w}\}^T$ represents the sampled deflections.

For the unconstrained pretwisted beams, the integral form of the boundary value problem given in Eq. (3.8) directly incorporates the natural (traction) boundary conditions; that is, no additional boundary conditions are required to be imposed. Applying the derivative operations described in $\mathbf{B}$ (the differential operator matrix) on the discretized deflections, and applying the inner-product operation, the boundary-value problem given in Eq. (3.8) can be expressed in a discretized form as

$$\hat{\mathbf{q}}^T(\mathbf{M}\ddot{\mathbf{q}} + \mathbf{K}\mathbf{q} - \mathbf{f}) = 0, \tag{3.27}$$

where $\mathbf{M}$, $\mathbf{K}$, and $\mathbf{f}$ are mass, stiffness matrices and forcing vector, respectively, and can be expressed as

$$\mathbf{M} = \frac{\rho L_r^2}{E}\,\rho(\mathbf{I_u}^T\mathbf{V}\mathbf{I_u} + \mathbf{I_v}^T\mathbf{V}\mathbf{I_v} + \mathbf{I_w}^T\mathbf{V}\mathbf{I_w}), \tag{3.28}$$

$$\mathbf{K} = \mathbf{B}^T\mathbf{V}\mathbf{B_C}, \tag{3.29}$$

$$\mathbf{f} = \frac{1}{E}\,\mathbf{V}\Big(\mathbf{f_q} + \frac{1}{L_r^2}\mathbf{f_b}\Big). \tag{3.30}$$

In the above equation, $\mathbf{f_q}$ and $\mathbf{f_b}$ are discretized force vectors in the domain and on the boundary, respectively.

The eigenvalue problem can now be obtained by assuming a solution in the form of $\mathbf{q_d} = \bar{\mathbf{q}}_\mathbf{d}\, e^{i\omega\, t}$. Solution of the eigenvalue problem provides the natural frequencies and mode-shapes of the structure, which can be written in terms of the non-dimensional mass and stiffness matrices as $(\mathbf{K} - \lambda^2\overline{\mathbf{M}}\ )\mathbf{q_d}\, e^{i\omega\, t} = 0$, where $\overline{\mathbf{M}} = \mathbf{M}E/(\rho L_r^2)$ and λ is the non-dimensional natural frequency. The relationship between the non-dimensional natural frequency and the natural frequency of the structure is $\lambda = \omega L_r(\rho/E)^{1/2}$. Furthermore, if addition of (proportional) damping is desired, Eq. (3.27) is transformed into the modal domain, where an experimentally-extracted (or modeled) damping matrix is added to the system.

3.5 Model Application

In this section, the application of the 3D-ST method for solving pretwisted beam problems by considering 3D dynamics of pretwisted rectangular beams and beams with curved cross-sections is described. A two-fluted drill-bit and an airfoil were selected as the curved beam examples. In each case, the convergence of the solution was studied by varying the number of polynomials in each of the three directions. To investigate the change of natural frequencies as the twist rate increases, the twist rate was varied at several levels, starting from the no-twist case.

3.5.1 Convergence study

3.5.1.1 Convergence of spectral Tchebychev approach

An important advantage of the Tchebychev polynomials is their fast-converging nature, which is especially advantageous for structural dynamics problems with mixed boundary conditions [96]. As such, only a relatively small number of polynomials is sufficient to accurately model the system behavior. Furthermore, numerically efficient solutions obtained by the 3D-ST method enable effectively studying the convergence characteristics, and thereby identifying the minimum number of polynomials (N_x-N_y-N_z)[5] needed to achieve a specific level of convergence.

[5]This triplet-number notation is used to indicate the number of polynomials (N_x, N_y and N_z) used in x, y, and z directions, respectively.

To identify the optimum convergence behavior, a reference solution that uses a large number of polynomials is selected first, and the associated non-dimensional natural frequencies λ_r^i are calculated for all the modes within the frequency bandwidth of interest. Then, for a selected set of triplet polynomials, the natural frequencies $\lambda_{Nx,Ny,Nz}^i$ are determined. A logarithmic convergence value is then calculated for each mode as

$$C_{Nx.Ny.Nz}^i = \log\left(\frac{|\lambda_{Nx.Ny.Nz}^i - \lambda_r^i|}{\lambda_r^i}\right). \tag{3.31}$$

To exemplify the convergence study, a pretwisted rectangular beam having a width-to-depth ratio of 2, a length-to-depth ratio of 5, and a twist rate of 2 is analyzed. Poisson's ratio is set to 0.3. A 3D-ST model with 15-15-20 polynomials is used as the reference to calculate the logarithmic convergence. Although this convergence value ($C_{Nx,Ny,Nz}^i$) is calculated for each individual mode, in this study an averaged convergence value is also calculated considering the first nine modes of the structure. An approach to guide the selection of the number of polynomials, that will result in the most efficient and accurate solution, may be realized using the convergence maps. Note that, the convergence data spans a three dimensional grid. Thus, convergence values corresponding to the number of polynomial, $N_x - N_y - N_z$, ranging from $3 - 15$, $3 - 15$, and $11 - 19$, respectively, are calculated. To help with the visualization of convergence, rather than plotting the convergence in 3D plots, for each N_z, a 2D plot of convergence value for increasing N_x and N_y values is given. Furthermore, to present the convergence values using continuous contours, a linear interpolation is used. Clearly, the convergence values are only meaningful for integer numbers of polynomials. Figure 3.4 shows the corresponding convergence plots.

Important observations can be made from Fig. 3.4 regarding the convergence characteristics. First, it is seen that, beyond a point, increased number of polynomials in a particular direction does not improve the convergence. This is visible from the straight lines in the vertical (for N_y) and horizontal (for N_x) directions. Considering this convergence behavior, an optimum convergence line is drawn (see the thick red lines in Fig. 3.4). To create the optimum convergence lines, the horizontal and vertical straight portions of convergence for a given convergence level was extrapolated to meet at an intersection point. Subsequently, the optimum convergence line is determined through a linear fit to the intersection points. For a given convergence value, the optimum convergence line indicates the number of polynomials that would yield the convergence value with the smallest number of polynomials. Second, islands of higher convergence are observed. This is due to the effect of the cross-sectional mapping and pretwist on the derivative matrices at high pretwist rates. However,

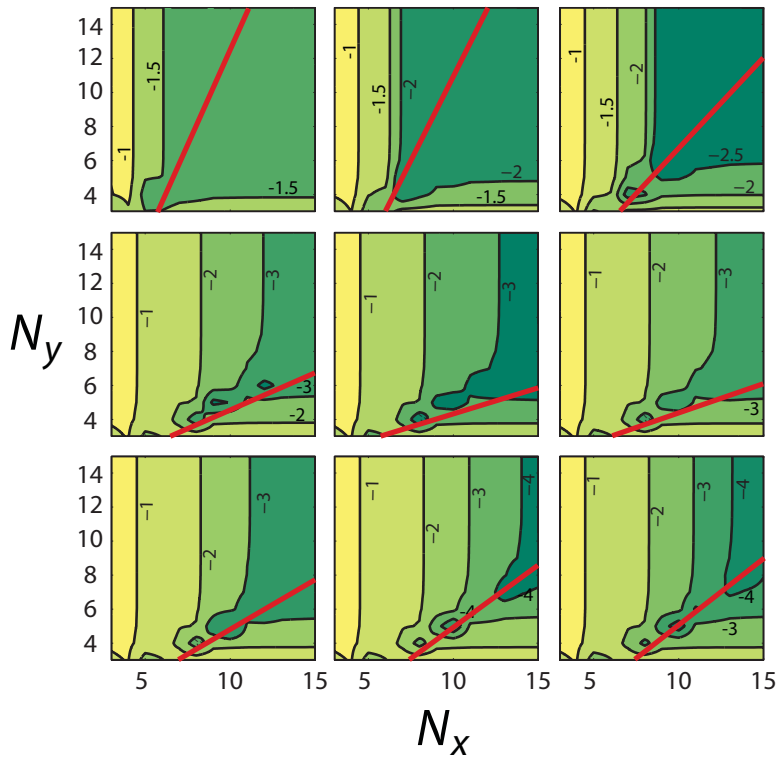

Figure 3.4: Convergence study for pretwisted beam with rectangular cross-section for a twist rate of 2. First row is for $N_z = 11, 12, 13$ (from left to right), middle row is for $N_z = 14, 15, 16$ (from left to right), last row is for $N_z = 17, 18, 19$ (from left to right).

it is not realistic to utilize those regions in calculations, since small changes in parameters or numerical noise could eliminate these islands of high convergence.

Furthermore, to determine the triplet polynomial numbers more robustly, a methodology is developed. Accordingly, the triplet polynomial number that has a minimum value for the product of polynomial numbers (i.e., $N_x.N_y.N_z$) and satisfies an averaged converge value of $\overline{C}^i_{Nx.Ny.Nz} < -\epsilon_a$ for the first nine modes, and a convergence value of $C^i_{Nx.Ny.Nz} < -\epsilon_i$ for any individual mode, is determined.

3.5.1.2 Convergence of finite element simulations

The precision of the solution was assessed by comparing the non-dimensional natural frequencies λ and the mode shapes Φ_i obtained from the 3D-ST method to those from a commercial FE solver (ANSYS® version 12.0 with SOLID187 3D 10-node tetrahedral structural solid elements with linear shape functions). To ensure the accuracy of the FE solutions, a convergence study was performed for each FE model to select the sufficient number of elements. For this purpose, FE simulations were performed with increased number of elements

(in each subsequent simulation, the number of elements are doubled); the convergence is considered to be reached when the maximum difference in nondimensional natural frequencies (in the first nine modes) is less than 0.1% in two consecutive simulations.

3.5.2 Dynamics of a pretwisted rectangular beam

To demonstrate the application of the 3D-ST solution, the dynamics of an unconstrained pretwisted beam with rectangular cross-section was analyzed. Due to its rectangular cross section, 3D-ST solution of this pretwisted beam does not require a cross-sectional mapping, but only requires transformation of twisting coordinate frame to a straight coordinate frame. Furthermore, since the cross-sectional geometry is symmetric about the principal axes, the bending modes are not coupled with the torsional-axial modes. In this analysis, the beam geometry is selected to have a width-to-depth ratio of 2 and a length-to-depth ratio of 5. The Poisson's ratio was set to 0.3. Five pretwisted cases with the twist rates of 0 (no twist), 0.25 (total twist is 90 degrees), 0.5 (total twist is 180 degrees), 1 (total twist is 360 degrees), and 2 (total twist is 720 degrees) were studied.

Table 3.1 provides the non-dimensional natural frequencies calculated for each of the first nine modes for the twist rates of 0, 0.25, 0.5, 1, and 2 at different number of polynomials. The specific polynomial numbers chosen for this calculations were identified using the convergence plots and the optimum convergence lines described above. The convergence characteristics could also be analyzed from this table. It is observed that the convergence rate decreases as the pretwist rate increases. This is due to the fact that the stress distributions and warping of the cross-section becomes more complicated at increased pretwist rates. Indeed, the case shown in Fig. 3.4 demonstrates the worst-case scenario for convergence among all the studied cases. Natural frequencies obtained from the 3D-FEM solution were also included in Table 3.1, where 40,000 elements were used based on the FEM convergence study.

In Table 3.1, the deformation mechanism for each mode (other than rigid body modes) is identified using the mode shapes of the pretwisted beam (see Fig. 3.5). The bending modes are represented with B_{ij} where i is the mode number and j (either 1 or 2) is the principal direction of deformation. The coupled torsional-axial modes are represented with TA_i where i is the mode number. Since rectangular cross-section is asymmetric, B_{i1} and B_{i2} are different. The torsional and axial deflections of a pretwisted beam are coupled since the beam untwists under tensile axial loading, or twists under compressive axial loading. However, the modes are commonly dominated by either the torsional (T) or axial (A)

Table 3.1: Convergence of the 3D-ST solution for the unconstrained pretwisted rectangle beam having the properties $width/height = 2$, $length/height = 5$ and a Poisson's ratio of 0.3, and comparison with results from the 3D-FEM simulations based on the non-dimensional natural frequencies.

Twist: 0.00	B_{11}	$\underline{T}A_1$	B_{12}	B_{21}	$\underline{T}A_2$	$T\underline{A}_3$	B_{22}	$\underline{T}A_4$	B_{31}
6-5-9	0.2294	0.2881	0.3660	0.5382	0.5754	0.6231	0.6987	0.8684	0.8905
7-6-11	0.2293	0.2880	0.3660	0.5381	0.5753	0.6231	0.6987	0.8680	0.8897
9-7-13	0.2293	0.2880	0.3660	0.5381	0.5753	0.6231	0.6987	0.8679	0.8897
11-9-16	0.2293	0.2880	0.3660	0.5381	0.5753	0.6231	0.6987	0.8679	0.8897
3D-FEM	0.2293	0.2880	0.3660	0.5381	0.5753	0.6231	0.6987	0.8680	0.8897

Twist: 0.25	B_{11}	$\underline{T}A_1$	B_{12}	B_{21}	$\underline{T}A_2$	$T\underline{A}_3$	B_{22}	$\underline{T}A_4$	B_{31}
6-5-9	0.2183	0.2921	0.3523	0.5402	0.5772	0.6111	0.6825	0.8571	0.8815
7-6-11	0.2184	0.2921	0.3523	0.5403	0.5771	0.6112	0.6826	0.8566	0.8808
9-7-13	0.2184	0.2921	0.3523	0.5403	0.5770	0.6112	0.6826	0.8565	0.8808
11-9-16	0.2184	0.2921	0.3523	0.5403	0.5770	0.6112	0.6826	0.8565	0.8808
3D-FEM	0.2183	0.2920	0.3522	0.5402	0.5770	0.6112	0.6825	0.8565	0.8807

Twist: 0.50	B_{11}	$\underline{T}A_1$	B_{12}	B_{21}	$T\underline{A}_2$	$\underline{T}A_3$	B_{22}	$\underline{T}A_4$	B_{31}
6-5-9	0.1995	0.2990	0.3060	0.5709	0.5791	0.5797	0.5986	0.8302	0.9032
7-6-11	0.1997	0.2998	0.3064	0.5716	0.5797	0.5798	0.5983	0.8325	0.9017
9-7-13	0.1997	0.2999	0.3064	0.5716	0.5797	0.5799	0.5985	0.8326	0.9018
11-9-16	0.1997	0.2999	0.3064	0.5716	0.5797	0.5799	0.5985	0.8326	0.9018
3D-FEM	0.1995	0.2998	0.3062	0.5715	0.5798	0.5798	0.5983	0.8326	0.9020

Twist: 1.00	B_{11}	B_{12}	$\underline{T}A_1$	B_{21}	$T\underline{A}_2$	$\underline{T}A_3$	B_{22}	B_{31}	$\underline{T}A_4$
6-5-9	0.1886	0.2058	0.2914	0.4012	0.4946	0.5557	0.5927	0.7796	0.7856
7-6-11	0.1913	0.2071	0.3042	0.3979	0.5028	0.5737	0.5785	0.7808	0.7852
9-7-13	0.1920	0.2081	0.3048	0.3983	0.5036	0.5773	0.5776	0.7887	0.7899
11-9-16	0.1921	0.2083	0.3049	0.3989	0.5036	0.5778	0.5785	0.7891	0.7915
3D-FEM	0.1918	0.2080	0.3049	0.3986	0.5039	0.5779	0.5785	0.7892	0.7920

Twist: 2.00	B_{11}	B_{12}	$\underline{T}A_1$	B_{21}	B_{22}	$T\underline{A}_2$	B_{31}	$\underline{T}A_3$	B_{32}
7-5-11	0.1600	0.1636	0.2588	0.3597	0.3687	0.4306	0.5043	0.5234	0.6383
9-7-13	0.1625	0.1631	0.2481	0.3526	0.3573	0.4349	0.4996	0.5183	0.5806
12-8-17	0.1629	0.1632	0.2632	0.3527	0.3585	0.4375	0.5095	0.5112	0.5615
14-10-19	0.1630	0.1633	0.2640	0.3529	0.3585	0.4383	0.5101	0.5151	0.5603
3D-FEM	0.1631	0.1634	0.2644	0.3529	0.3586	0.4388	0.5100	0.5165	0.5603

deformations. To identify the dominant deformation mechanism, the amount of strain imposed by each deformation mechanism is determined, and the mechanism that yielded the larger strain is considered as the dominant mechanism (identified by an underline in Table 3.1). For instance, the $\underline{T}A_1$ mode is the first torsional-axial mode dominated by torsional deformations, and $T\underline{A}_2$ is the second torsional-axial mode dominated by axial deformations.

From Table 3.1, it is seen that the non-dimensional natural frequencies from the 3D-ST and 3D-FEM solutions converge to approximately the same values for all the nine deflection modes. The maximum difference between the 3D-FEM and 3D-ST solutions were found to be 0.27 % (taking the FEM solution as reference) over the first nine natural frequencies. The convergence of both solutions depends on the twist rate and the mode number. However, the convergence of the 3D-ST method is observed to be very rapid with increasing polynomial

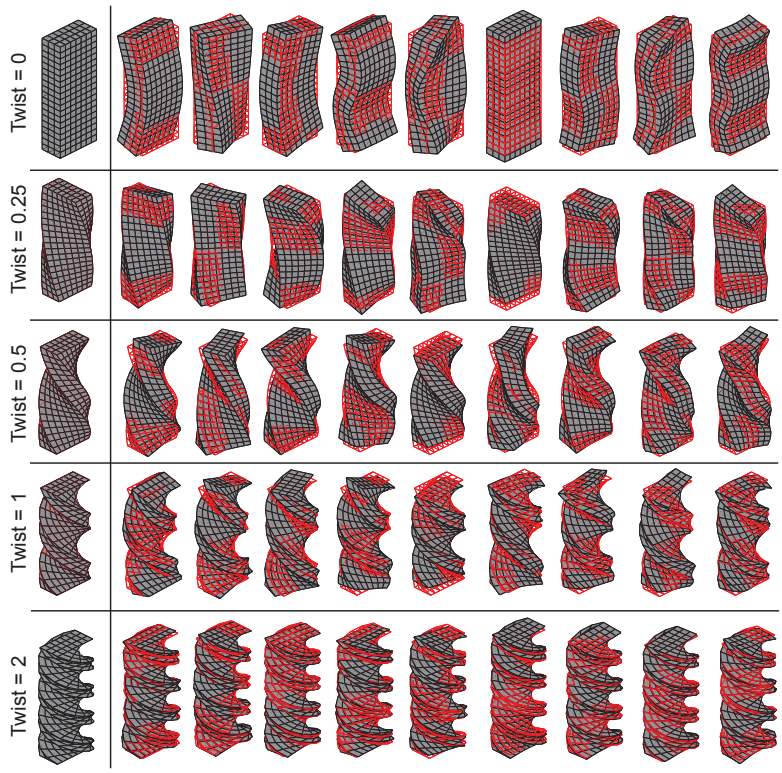

Figure 3.5: The mode shapes of an unconstrained pretwisted beam. The undeflected geometries of the beams are provided on the left column. The first nine mode shapes are given on the right column where the red lines indicate the undeflected geometries.

numbers.

The undeflected geometry of the beams and mode shapes for the unconstrained case are presented in Fig. 3.5. It is seen from the figure that the first deflection mode is the bending mode for all twist cases studied. However, other modes shift order as the pretwist rate increases. For instance, the first torsion dominated torsional-axial mode is the second mode for the twist rates of 0, 0.25, and 0.5, and is the third mode for total twists of 1 and 2. Another example is the axial dominated torsional-axial mode, which is the sixth mode for the twist rates of 0, 0.25, and 2, and is the fifth mode for the twist rates of 0.5 and 1.

To qualitatively compare the mode shapes obtained from the 3D-ST and 3D-FEM solutions, a modal assurance criterion (MAC) analysis was performed. The MAC is a measure of consistency of the modal vectors obtained from two different solution methods [99, 100]. The MAC number is calculated as

$$\mathrm{MAC} = \frac{\left|\mathbf{\Phi_{FEM}}^T \mathbf{\Phi_{3D-ST}}\right|^2}{\left(\mathbf{\Phi_{FEM}}^T \mathbf{\Phi_{FEM}}\right)\left(\mathbf{\Phi_{3D-ST}}^T \mathbf{\Phi_{3D-ST}}\right)} \ , \tag{3.32}$$

where $\mathbf{\Phi_{FEM}}$ and $\mathbf{\Phi_{3D-ST}}$ are the modal matrices obtained from the 3D-FEM and 3D-ST solutions, respectively. In the literature, the consistency between two mode shapes is considered to be satisfactory if the MAC value along the diagonal is above 0.8 [100]. Clearly, a higher MAC number indicates better consistency between the mode shapes. In calculating the MAC values for this work, first, the nodal displacements were extracted from ANSYS® for each mode. Next, the displacement values corresponding to the position of each node was obtained from the 3D-ST solution. The two sets of values were then placed in a matrix form in $\mathbf{\Phi_{FEM}}$ and $\mathbf{\Phi_{3D-ST}}$ matrices, and the MAC values were calculated from Eq. (3.32). As seen in Fig. 3.6, the MAC values for all the cases are very close to unity for different modes and twist rates. Minimum MAC values of 0.9987, 0.9990, 0.9990, 0.9991, and 0.9679 and average MAC values of 0.9993, 0.9993, 0.9992, 0.9992, and 0.9914 were obtained for twist rates of 0, 0.25, 0.5, 1, and 2, respectively. Therefore, the mode shapes from the 3D-ST and 3D-FEM solutions are in excellent agreement.

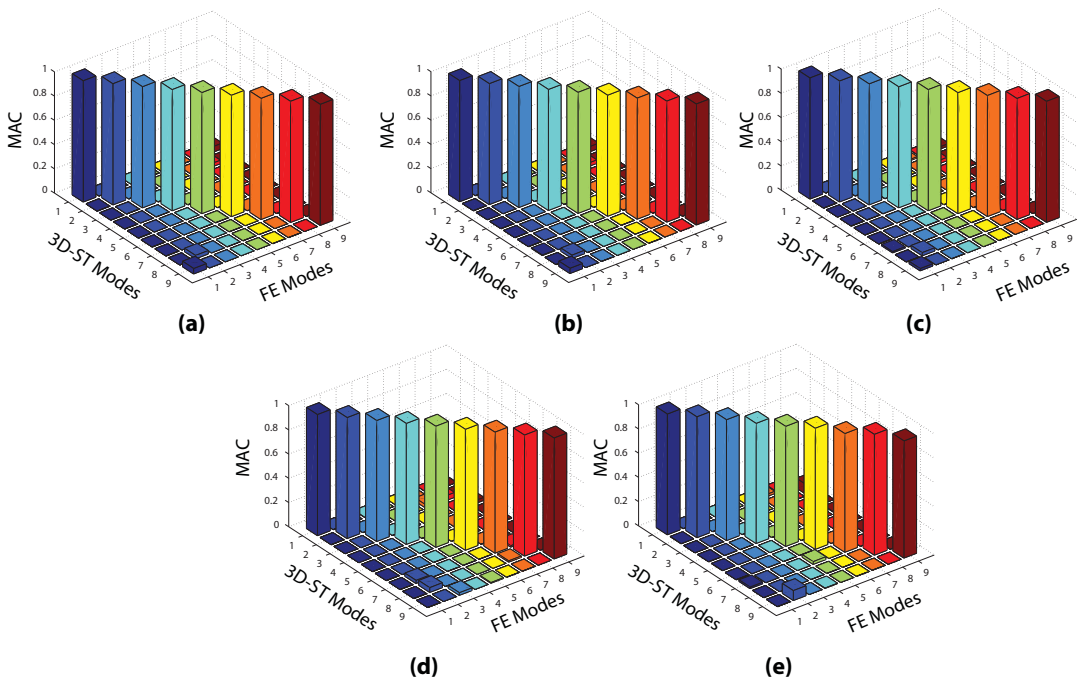

Figure 3.6: Modal Assurance Criteria (MAC) analysis of the pretwisted beam with rectangular cross-section for the twist rates of **(a)** 0, **(b)** 0.25, **(c)** 0.5, **(d)** 1, and **(e)** 2.

In addition to natural frequencies and mode shapes, internal displacements, strains, and stresses can be straightforwardly obtained from the 3D-ST solution. Figure 3.7 provides two examples. The normal stress experienced during the first bending mode and the axial deflection for the first torsion dominated torsional-axial mode are plotted over the cross-

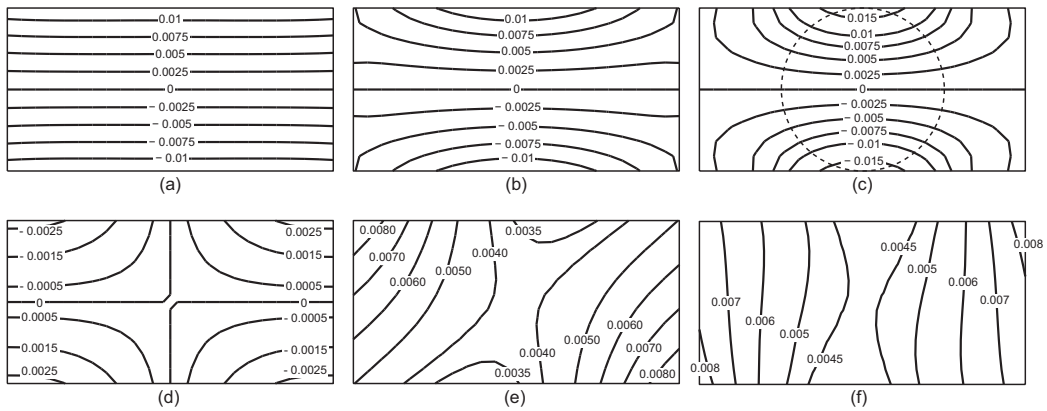

Figure 3.7: **(a)-(c)** Normal stresses due to bending (σ_z) for the first bending mode computed on the cross-section (z=2.5). **(d)-(f)** Axial displacement (w) for the first torsional-axial mode on the bottom cross-section (z=0). The left column is for no twist, the middle column is for a twist rate of 0.5, and the right column is for a twist rate of 1.

section at three different twist rates. For calculating the strains and displacements, the deflection values were first obtained from the normalized mode shapes. Next, the strains are calculated using the Tchebychev derivative matrices from $\epsilon = \mathbf{Bq}$. Stresses were then obtained from the constitutive relationships between the stresses and strains ($\sigma = \mathbf{C}\epsilon$).

Although an in-depth discussion of stress and strain distributions in pretwisted beams is beyond the scope of this work, a brief consideration is provided here since the presented stresses and displacements give important insights about the changes in dynamic behavior of pretwisted beams with increased twist rates. As seen in Fig. 3.7, considering the first bending mode, when the twist rate is zero, the normal stresses due to bending vary linearly along the cross-section. As the twist rate increases, the stress isolines start curving towards the narrower side. As a result, a large portion of the cross-section, including the edges of the longer dimension, exhibit very low stresses. It is also seen that the stresses within the core of the beam, which is indicated by the dashed circle in Fig. 3.7, are not affected significantly by the pretwist. In other words, the portion of the beam that are outside the core gets thinner with increasing twist amount. This phenomenon can be visualized by considering a beam with infinite twist where thickness of the portions outside the core region approach to zero due to very high twist rate. When the twist amount is increased, the amount of the normal stresses due to bending that the outer portions can carry reduces, and the stress is concentrated at the core of the beam, causing the bending stiffness of the beam to decrease with increasing twist amount (Fig. 3.8). These changes in stress distribution is responsible for the variation in natural frequencies and mode shapes due to increased twist rate.

The second row of figures in Fig. 3.7 represents the change in axial deflection with

increasing twist rate. For zero twist, torsional and axial deformations are not coupled; hence, the axial deflection of the cross-section for the torsional mode is solely due to the warping of the rectangular cross-section [101]. When the twist rate is non-zero, the axial deformation of the cross-section arises from the untwisting and warping of the cross-section due to the coupled axial-torsion deflections. Interestingly, at increased twist rates, the axial deflection at the portions outside the core region become considerably larger than those in the core region.

3.5.2.1 Comparison to 1D/2D solution

The demonstrate the utility of the 3D-ST solution, the natural frequencies from the 3D-ST solution with varying twist rate are compared to those from the 1D/2D beam solution used in the literature for pretwisted beam problems [47,57,95]. For this comparison, the pretwisted beam with rectangular cross-section is considered. It is noted that the numerically-efficient nature of the 3D-ST solution facilitates rapidly performing such detailed analyses with changing twist rates (with a 0.005 incremental twist rate for this study).

The non-dimensional natural frequencies obtained from the 3D-ST model are given in Fig. 3.8, where the bending modes are indicated by solid lines and the torsional-axial modes are given by dashed lines. While the values fluctuate, overall, the increased twist rate was seen to reduce the frequency of bending modes. Furthermore, as expected, increased twist rate renders the structure more symmetric, and causes bending mode pairs in two principal directions to approach each other. The torsion-dominated axial-torsional modes were seen to change only by a small amount with increasing twist rate. It is also observed that the bending natural frequencies decrease due to decreasing bending stiffness with increasing twist amount.

The 1D/2D model considers the bending and torsional/axial deformations independently. The Timoshenko beam model, which includes rotary inertia and shear deformation, was used for modeling the bending vibrations [95]. The beam bending model incorporates the pretwist effect in the varying second area moments [11,34,35,37,40,42,45]. For the torsional-axial vibrations, the coupled torsional/axial pretwisted beam model proposed by Rosen *et al.* was used [47]. This model superposes the axial deflection with the Saint-Venant torsion (a 2D solution for the warping function). The cross-sectional deformation and constants for the torsional/axial deformation model were computed using a closed form series solution based on [101]. The solution of the system is obtained using 1D-ST for each of bending and axial/torsional deformations [29].

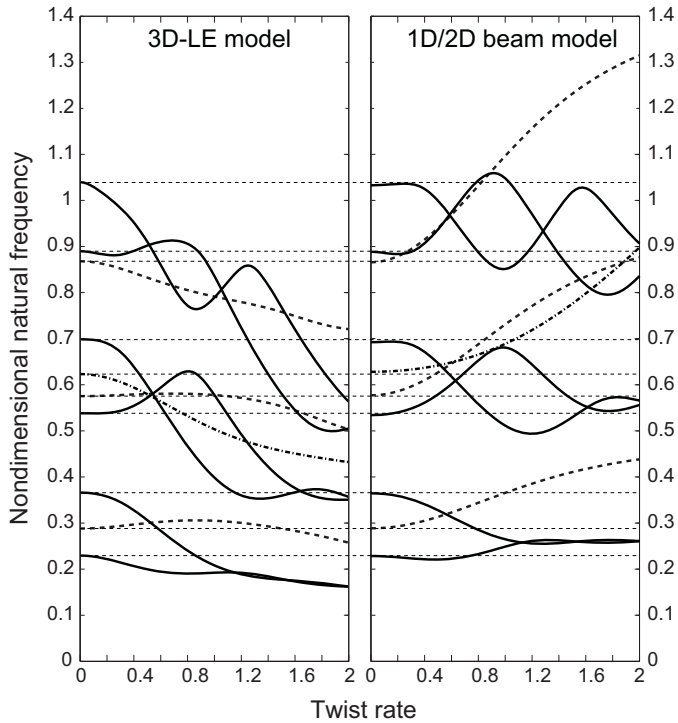

Figure 3.8: Natural frequencies from the 3D linear elasticity based solutions (on the left) and beam (1D/2D) solutions (on the right). Solid lines - bending modes, dashed lines - torsion dominated torsional-axial modes, dashed dotted lines - axial dominated torsional-axial mode.

The non-dimensional natural frequencies obtained from 1D/2D solution are given in Fig. 3.8. In comparing two solutions, the model predictions were seen to match closely in the absence of twist. However, as the twist rate increases, significant differences are observed. Although both models capture the convergence of the bending mode pairs to one another with increasing twist rate, the reduction of bending natural frequencies at increased twist rates (due to the reduced bending stiffness) is not captured by the 1D/2D solution. As such, the 1D/2D predictions result in errors reaching 100% for the bending modes. Similarly, at increased twist rates, the torsional/axial modes are not well captured using the 1D/2D solution. While the 3D-ST solution indicates a general reduction in torsional-axial modes with increasing twist rate, the 1D/2D solution shows a significant increase in those modes. As such, again, the errors could reach 100% at high twist rates.

Although a closed form series solution for warping function and torsional/axial cross-sectional constants exists for a rectangular cross-section, such a closed-form solution does not exist for more complicated geometries such as the two-fluted cutting tool and airfoil geometries studied in this study. For the curved cross-sections, a two-dimensional numerical

solution is required to obtain the warping function and cross-sectional constants [52] used in the torsional/axial beam models. Cross-sectional constants in the beam models are not straightforward to obtain, and beam models do not give accurate results for highly pretwisted beams. Therefore, 3D solutions should be preferred.

3.5.3 Dynamics of a pretwisted beam with curved cross-section

As another example, the dynamics of an unconstrained beam with curved cross-section that resembles the fluted region of a cutting tool (2-fluted end mill) was studied. The diameter-to-height ratio was set to 4, and the Poisson's ratio was set to 0.3. First, the cross-section of the cutting tool was measured optically, and the measured cross-section was mapped onto a rectangular domain (see Fig. 3.9). The specific mapping coefficients for this example are given in Table 3.2. Next, a rotating coordinate frame was used to transform the rectangular pretwisted beam into a straight rectangular beam. The cases with the twist rates of 0, 0.25, 0.5, 1, and 2 were analyzed.

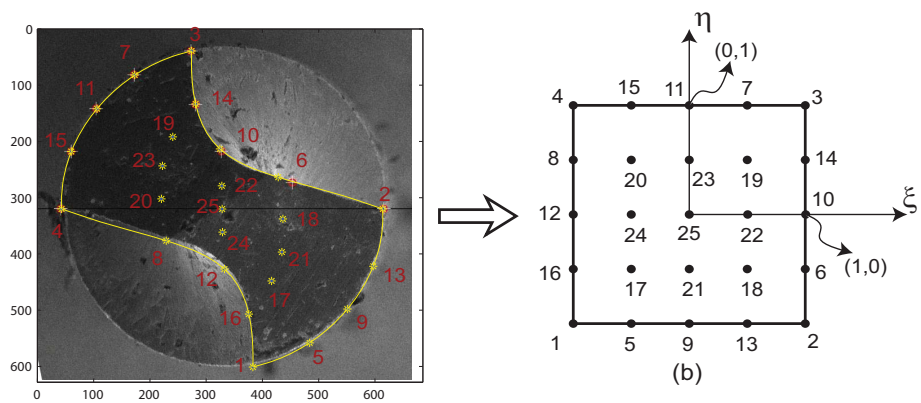

Figure 3.9: The cross-sectional mapping for the two fluted cutting tool geometry.

Table 3.2: Mapping coefficients for the mapping of the two-fluted geometry in Fig. 3.9 (calculated through Eqs. (3.10)-(3.11)).

	ξ^4	ξ^3	ξ^2	ξ^1	ξ^0
η^4	0	0.035	0	−0.010	0
η^3	−0.092	0	0.104	0	−0.007
η^2	0	−0.065	0	0.132	0
η^1	0.090	0	0.107	0	0
η^0	0	−0.024	0	−0.366	0

	ξ^4	ξ^3	ξ^2	ξ^1	ξ^0
η^4	0	−0.037	0	0.024	0
η^3	0.099	0	−0.145	0	0.057
η^2	0	0.003	0	−0.056	0
η^1	−0.159	0	0.265	0	0.130
η^0	0	0.058	0	0.254	0

In order to determine the number of polynomials to be used in the 3D-ST formulation, a convergence study similar to that presented above was conducted. Table 3.3 shows the

Table 3.3: Convergence of the 3D-ST solution for the unconstrained pretwisted 2-fluted cutting-tool geometry having the properties $diameter/length = 4$ and a Poisson's ratio of 0.3, and comparison with results from 3D-FEM simulations based on the non-dimensional natural frequencies.

Twist: 0.00	B_{11}	$\underline{T}A_1$	B_{12}	B_{21}	$\underline{T}A_2$	B_{22}	$T\underline{A}_3$	$\underline{T}A_4$	B_{31}
6-7-9	0.1820	0.2756	0.3433	0.4663	0.5654	0.7383	0.7828	0.8373	0.8848
8-9-11	0.1820	0.2756	0.3433	0.4663	0.5655	0.7382	0.7829	0.8363	0.8848
10-12-13	0.1820	0.2756	0.3433	0.4662	0.5656	0.7382	0.7829	0.8363	0.8847
12-14-16	0.1820	0.2756	0.3433	0.4662	0.5656	0.7382	0.7829	0.8363	0.8847
3D-FEM	0.1818	0.2764	0.3430	0.4657	0.5671	0.7383	0.7829	0.8356	0.8865

Twist: 0.25	B_{11}	$\underline{T}A_1$	B_{12}	B_{21}	$\underline{T}A_2$	B_{22}	$T\underline{A}_3$	$\underline{T}A_4$	B_{31}
6-7-9	0.1779	0.2775	0.3140	0.5013	0.5672	0.6641	0.7744	0.8820	0.9084
8-9-11	0.1778	0.2775	0.3139	0.5013	0.5672	0.6642	0.7745	0.8818	0.9067
10-12-13	0.1778	0.2776	0.3139	0.5013	0.5673	0.6641	0.7745	0.8819	0.9067
12-14-16	0.1778	0.2776	0.3139	0.5013	0.5673	0.6641	0.7745	0.8819	0.9067
3D-FEM	0.1775	0.2783	0.3137	0.5007	0.5686	0.6639	0.7745	0.8835	0.9062

Twist: 0.50	B_{11}	B_{12}	$\underline{T}A_1$	B_{21}	$\underline{T}A_2$	B_{22}	$T\underline{A}_3$	$\underline{T}A_4$	B_{31}
6-7-9	0.1698	0.2611	0.2825	0.5514	0.5708	0.5727	0.7501	0.8733	0.8882
8-9-11	0.1698	0.2614	0.2826	0.5504	0.5714	0.5737	0.7503	0.8740	0.9054
10-12-13	0.1698	0.2614	0.2827	0.5514	0.5715	0.5738	0.7503	0.8741	0.9112
12-14-16	0.1698	0.2614	0.2827	0.5514	0.5715	0.5739	0.7503	0.8741	0.9118
3D-FEM	0.1695	0.2611	0.2833	0.5510	0.5726	0.5733	0.7504	0.8755	0.9114

Twist: 1.00	B_{11}	B_{12}	$\underline{T}A_1$	B_{21}	B_{22}	$\underline{T}A_2$	$T\underline{A}_3$	B_{31}	$\underline{T}A_4$
8-9-11	0.1605	0.1750	0.2954	0.3603	0.5372	0.5788	0.6679	0.8398	0.8625
10-12-13	0.1612	0.1760	0.2956	0.3612	0.5376	0.5809	0.6683	0.8361	0.8500
12-14-16	0.1614	0.1764	0.2956	0.3629	0.5419	0.5811	0.6683	0.8387	0.8518
13-15-17	0.1614	0.1764	0.2956	0.3630	0.5424	0.5811	0.6683	0.8407	0.8519
3D-FEM	0.1612	0.1762	0.2960	0.3628	0.5425	0.5821	0.6689	0.8424	0.8535

Twist: 2.00	B_{11}	B_{12}	B_{21}	B_{22}	$T\underline{A}_1$	B_{31}	$T\underline{A}_2$	B_{32}	$\underline{T}A_3$
10-12-13	0.1179	0.1182	0.2811	0.2837	0.2839	0.4048	0.4848	0.5425	0.5816
12-14-16	0.1170	0.1174	0.2753	0.2825	0.2991	0.4145	0.4976	0.5010	0.5690
13-15-17	0.1169	0.1172	0.2769	0.2846	0.3008	0.4154	0.4992	0.5007	0.5738
15-17-19	0.1167	0.1171	0.2782	0.2862	0.3016	0.4168	0.4999	0.5048	0.5785
3D-FEM	0.1174	0.1177	0.2785	0.2866	0.3022	0.4174	0.5014	0.5070	0.5806

non-dimensional natural frequencies obtained for different numbers of polynomials for the first nine modes. The results from a 3D-FEM study (with 80,000 elements) are also included in this table. The non-dimensional natural frequencies obtained from the 3D-ST solution match those from the 3D-FEM closely, where the maximum difference is below 0.6% for any mode and twist rate. Generally, the convergence of the 3D-ST solution becomes somewhat slower with increasing twist rate.

Figure 3.10 gives the mode shapes of the corresponding geometry from the 3D-ST solution while using 15-17-19 polynomials. The MAC values between the mode shapes from the 3D-ST and 3D-FEM solutions is calculated using Eq. (3.32). Minimum MAC values of 0.9986, 0.9278, 0.9989, 0.9984, and 0.9939 and average MAC values of 0.9993 ,0.9600, 0.9993, 0.9991, and 0.9973 were obtained for twist rates of 0, 0.25, 0.5 , 1, and 2, respectively.

A plot showing the change of first nine non-dimensional natural frequencies at increasing

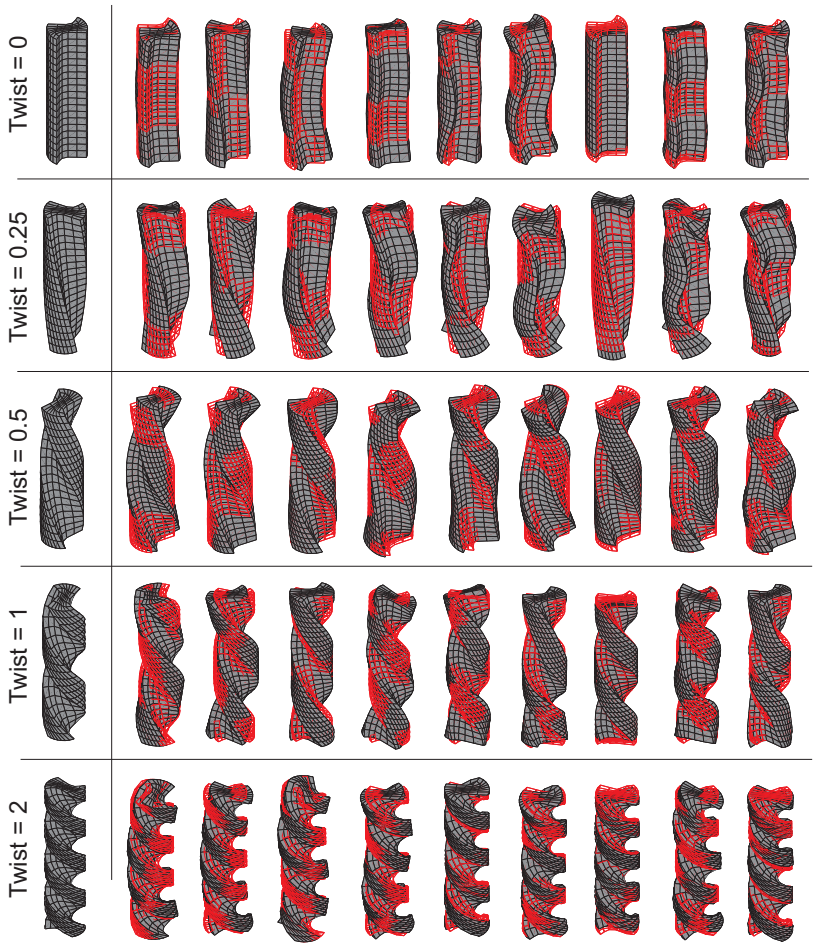

Figure 3.10: The mode shapes of an unconstrained pretwisted beam with cutting tool geometry. The undeflected geometries of the beams are provided on the left column. The first nine mode shapes are given on the right column where the red lines indicate the undeflected geometries.

twist rates is given in Fig. 3.11. As expected, this plot resembles that given for the rectangular cross-section beam in Fig. 3.8. As such, it can again be concluded that the bending mode pairs are strongly affected by the twist rate. At high twist rates, the bending-mode pairs merge together, indicating increased symmetry for bending motions due to increased twist rate. After the initial cyclic-like behavior, bending frequencies reduce with increased twist rate. The twist rate has very little impact on the torsion dominated torsional-axial modes. On the other hand, the axial dominated torsional-axial mode is affected significantly, where the natural frequency decreases with increasing twist rate.

Figure 3.12 gives the normal stresses (for the first bending mode) and axial deflections (for the first axial-torsional mode) of the curved cross-section beam at the middle of the beam, where z is equal to twice the diameter. Similar to those for the rectangular cross-

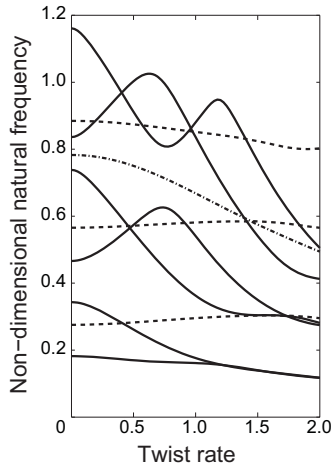

Figure 3.11: Change in the natural frequencies of an unconstrained pretwisted beam with two fluted cutting tool geometry. Solid lines - bending modes, dashed lines - torsion dominated torsional-axial modes, dashed dotted lines - axial dominated torsional-axial mode.

sectioned beam, it is seen that the stresses concentrate towards the center (core) section as the twist rate increases. The axial deflection of the cross-section for the first torsion dominated torsional-axial mode increase with increasing twist amount (see Figs. 3.12(d)-(f)). For zero twist, axial deflections arise from the warping of the cross-section due to torsion. With increasing twist rate, the axial untwisting of the beam impose further axial deflections on the cross-section.

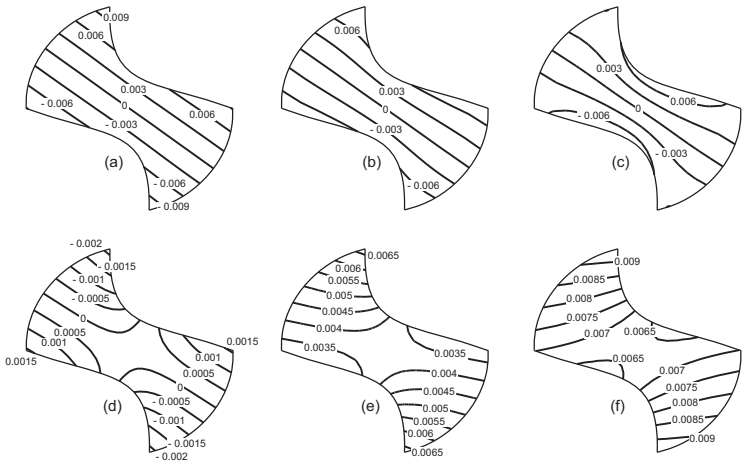

Figure 3.12: **(a)-(c)** Normal stresses due to bending (σ_z) for the first bending mode computed on the cross-section (z=2). **(d)-(f)** Axial displacement (w) for the first torsional-axial mode on the bottom cross-section (z=0). Left column is for no twist, middle column is for half twist, and right column is for full twist.

3.5.4 Dynamics of a pretwisted airfoil

Both the rectangular and curved (cutting-tool) cross-sectioned beam examples given above had their shear center coincident with their geometric center. As such, bending and torsional/axial motions were uncoupled. In this section, the dynamics of an unconstrained pretwisted airfoil, which exhibits coupled bending-bending-torsional-axial motions, was analyzed. For this study, the aspect ratio of the airfoil (the ratio of the length-to-breadth) is set to 3 and the Poisson's ratio was selected to be 0.3. As before, a cross-sectional mapping (to a rectangular cross section, see Fig. 3.13) and a coordinate transformation from the rotating to the straight coordinates were applied to simplify the domain of the problem. The twist rates of 0, 0.1, 0.3, and 0.5 were studied.

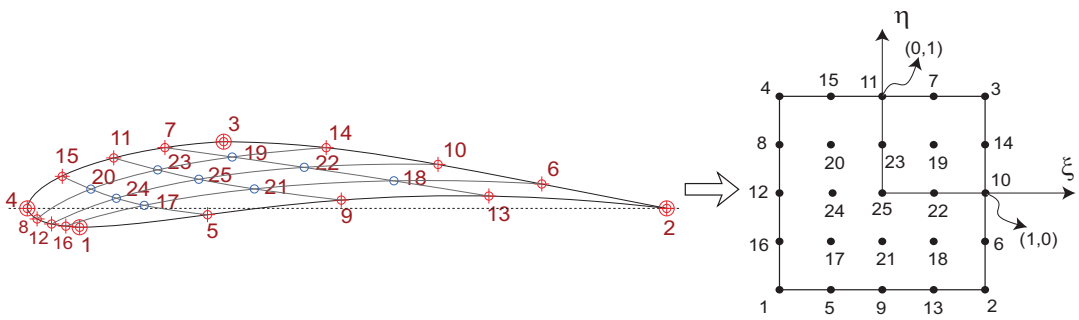

Figure 3.13: Mapping procedure for airfoil geometry cross-section.

As before, a convergence study was performed to guide the selection of number of polynomials to be used in the 3D-ST solution. Convergence of the first nine non-dimensional natural frequencies is given in Table 3.4 for the selected twist rates. Furthermore, the non-dimensional natural frequencies from the 3D-FEM solution were also included in Table 3.4. It is noted that the FEM solution required 130,000 elements to attain a convergence of 0.4% on the natural frequencies. It is seen that the results from the 3D-ST solution and those from the 3D-FEM solution are in very good agreement. As before, the difference between the natural frequencies from the two solutions increase with increased twist rate. However, largest difference is below 0.89%, which is observed for the eighth mode in the highest twist rate case.

The mode shapes for the unconstrained airfoil are given in Fig. 3.14. Since the bending and axial/torsional modes are coupled, a visual assessment of mode shapes becomes more important in this case. For the lower modes and lower twist rates, a dominant mechanism is easily identified. However, at higher modes, such an identification becomes quite difficult.

Table 3.4: Convergence of the 3D-ST solution for the unconstrained pretwisted airfoil geometry with length-to-breadth ratio of 3 and a Poisson's ratio of 0.3, and comparison with results from 3D-FEM simulations.

Twist: 0.0	$Mode_1$	$Mode_2$	$Mode_3$	$Mode_4$	$Mode_5$	$Mode_6$	$Mode_7$	$Mode_8$	$Mode_9$
6-7-9	0.0717	0.1549	0.1910	0.2916	0.3491	0.4123	0.4483	0.5313	0.5317
8-9-11	0.0716	0.1543	0.1906	0.2862	0.3432	0.3909	0.4481	0.4591	0.4861
9-10-13	0.0716	0.1543	0.1905	0.2861	0.3430	0.3904	0.4481	0.4561	0.4845
11-12-15	0.0716	0.1543	0.1905	0.2861	0.3430	0.3904	0.4481	0.4559	0.4843
3D-FEM	0.0716	0.1541	0.1904	0.2858	0.3432	0.3911	0.4483	0.4599	0.4882

Twist: 0.1	$Mode_1$	$Mode_2$	$Mode_3$	$Mode_4$	$Mode_5$	$Mode_6$	$Mode_7$	$Mode_8$	$Mode_9$
6-7-9	0.0706	0.1617	0.1840	0.3046	0.3467	0.4295	0.4601	0.5276	0.5533
8-9-11	0.0705	0.1611	0.1837	0.2990	0.3396	0.4069	0.4589	0.4663	0.4987
9-10-13	0.0705	0.1611	0.1837	0.2989	0.3395	0.4064	0.4586	0.4644	0.4959
11-12-15	0.0705	0.1611	0.1837	0.2989	0.3395	0.4063	0.4585	0.4643	0.4957
3D-FEM	0.0705	0.1610	0.1835	0.2988	0.3394	0.4071	0.4590	0.4668	0.4992

Twist: 0.3	$Mode_1$	$Mode_2$	$Mode_3$	$Mode_4$	$Mode_5$	$Mode_6$	$Mode_7$	$Mode_8$	$Mode_9$
6-7-9	0.0662	0.1470	0.2080	0.3087	0.3937	0.4989	0.5366	0.5558	0.6380
8-9-11	0.0661	0.1467	0.2076	0.2981	0.3856	0.4632	0.5068	0.5317	0.5342
9-10-13	0.0661	0.1467	0.2076	0.2978	0.3852	0.4614	0.5047	0.5300	0.5311
11-12-15	0.0661	0.1467	0.2078	0.2978	0.3852	0.4613	0.5045	0.5296	0.5308
3D-FEM	0.0661	0.1465	0.2075	0.2975	0.3854	0.4620	0.5071	0.5317	0.5337

Twist: 0.5	$Mode_1$	$Mode_2$	$Mode_3$	$Mode_4$	$Mode_5$	$Mode_6$	$Mode_7$	$Mode_8$	$Mode_9$
6-7-9	0.0639	0.1164	0.2481	0.2747	0.4729	0.5120	0.6292	0.6434	0.6530
8-9-11	0.0638	0.1152	0.2404	0.2657	0.4222	0.4723	0.5228	0.5512	0.5813
9-10-13	0.0638	0.1152	0.2399	0.2653	0.4132	0.4701	0.5184	0.5463	0.5734
11-12-15	0.0638	0.1152	0.2399	0.2653	0.4127	0.4699	0.5176	0.5453	0.5718
3D-FEM	0.0637	0.1151	0.2397	0.2651	0.4125	0.4710	0.5221	0.5502	0.5769

The MAC values between the mode shapes from the 3D-ST and 3D-FEM solutions is calculated using Eq. (3.32). It is seen that the MAC values for all the modes are close to unity for all cases. Minimum MAC values of 0.9849, 0.8920, 0.9900, and 0.8978 and average MAC values of 0.9956, 0.9787, 0.9958, and 0.9839 were obtained for twist rates of 0, 0.1, 0.3, and 0.5, respectively.

A plot showing the change in non-dimensional natural frequencies with continuous change in twist rate is given in Fig. 3.15. An important difference here is that there is no cross-over of the natural frequencies as observed in the two examples above (see Figs. 3.8 and 3.11). Instead, a smooth transition occurs between bending-dominated and torsion dominated modes (the torsion dominated motions are outlined with grey regions). This phenomenon is referred to as *curve veering* and has been extensively studied in rotor-blade systems (e.g., [102, 103]). It was shown that the *frequency crossing* and *curve veering* depend on the symmetry of the investigated geometry [103]. Therefore, whereas frequency cross-overs were observed in the cases of pretwisted rectangular beam and pretwisted beam with the cutting tool cross-section due to the symmetry of these geometries, in the case of pretwisted beam with the airfoil cross-section the curve veering phenomenon was observed.

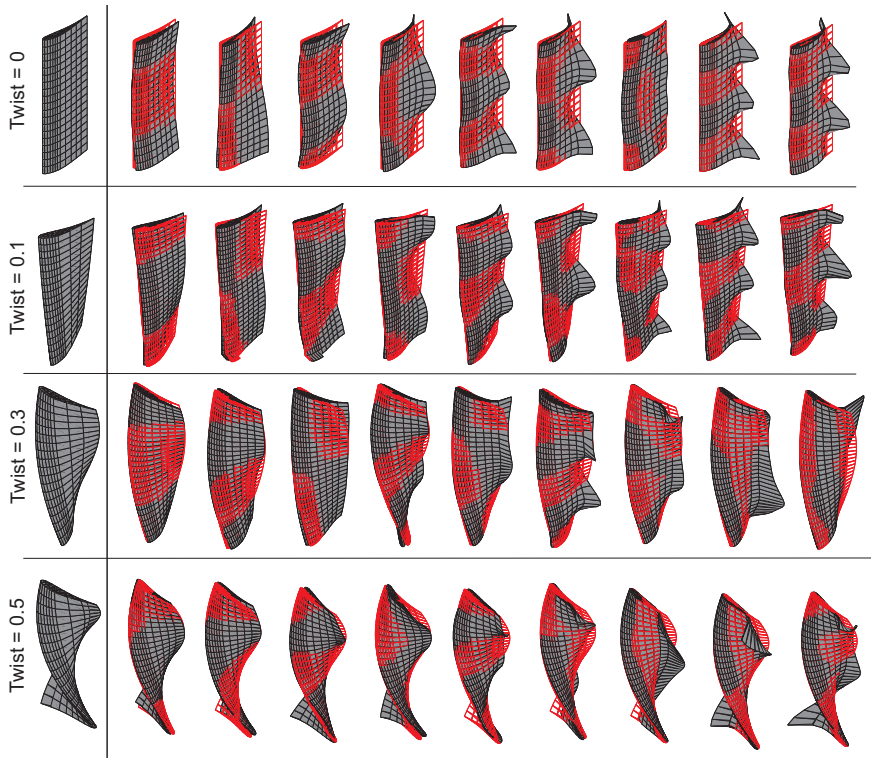

Figure 3.14: The mode shapes of an unconstrained pretwisted beam with airfoil geometry. The undeflected geometries of the beams are provided on the left column. The first nine mode shapes are given on the right column where the red lines indicate the undeflected geometries.

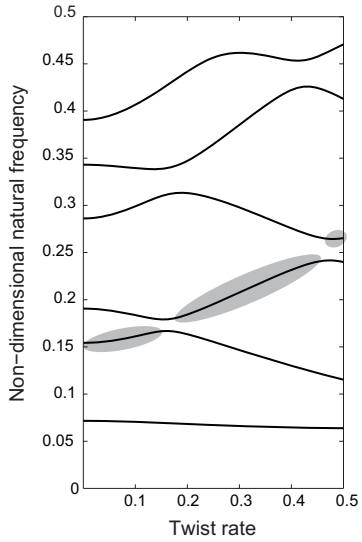

Figure 3.15: Change in the natural frequencies of an unconstrained pretwisted beam with airfoil geometry.

The normal stresses due to bending for the first bending mode is plotted in Figs. 3.16(a)-(b) for twist rates of 0 and 0.3. A small difference is observed between the two cases due to small twist amount. The normal stress due to bending follow the expected pattern, being zero on the neutral axis, negative on the side under compression and positive on the side under tension. Axial deformations of the cross-section for the torsion dominated mode are shown in Fig. 3.16(c)-(d).

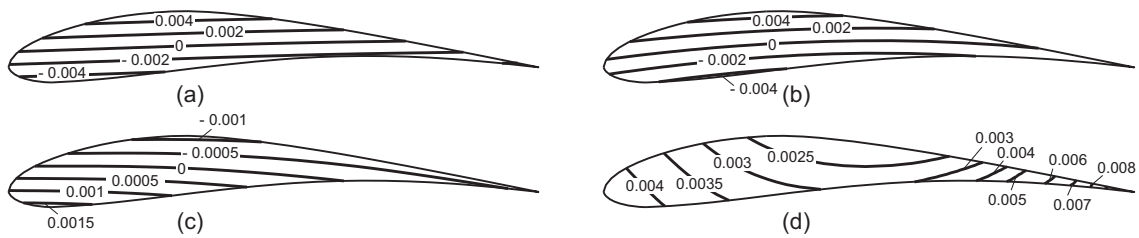

Figure 3.16: **(a)-(b)** Normal stresses due to bending (σ_z) for the first bending mode computed on the cross-section (z=1.5). **(c)-(d)** Axial displacement (w) for the first torsional-axial mode on the bottom cross-section (z=0). Left column is for no twist, and right column is for the 0.3 twist case.

3.6 Summary and Conclusions

This chapter presented a series based solution approach, the three-dimensional spectral-Tchebychev (3D-ST) technique, for the dynamics of unconstrained pretwisted beams with general cross-section (including both straight and curved cross-sections). After a brief overview of the derivation of the integral boundary value problem and the 3D-ST technique, three sample problems including pretwisted beams with rectangular, curved (two-fluted cutting tool) and airfoil cross-sections at different twist rates were solved. The convergence of the 3D-ST solution was studied, and the non-dimensional natural frequencies and mode shapes were compared to those from a finite-elements solution. The natural frequencies from the 3D-ST solution were also compared with those from a 1D/2D solution at different twist rates. The following specific conclusions are drawn from this work:

- The presented 3D-ST approach enables computational efficient solutions for the three dimensional dynamics of pretwisted beams with general cross-section. The numerically efficient nature of the 3D-ST solution also facilitates rapidly studying the of numerical convergence behavior.

- The non-dimensional natural frequencies and mode shapes from the 3D-ST solution

are in excellent agreement with those from the 3D-FEM solution for different cross-sectional shapes and twist rates. However, the computational cost of the 3D-ST solution is one-to-two order of magnitude less than that of the 3D-FEM solution.

- The cross-sectional stress, strain, and deformation distributions for a given operational deflection shape can be obtained from the 3D-ST solution. The nature of those distributions provides important insights into the vibrational characteristics of pretwisted beams.

- For beams with symmetric cross-sections, each of the pairs of bending natural frequencies merges towards a single frequency at high twist rates. This is due to the increased symmetry in bending arising from the pretwist. Furthermore, after an initial cyclic behavior, the frequency of bending modes reduce significantly with increasing twists rates due to the reduction in the effective bending stiffness. Whereas the pretwist has only a small effect on torsion-dominated torsional-axial modes, the axial-dominated torsional-axial mode reduces sharply with increasing twist rates.

- For the airfoil cross-section, when coupled bending-bending-torsional-axial motions are observed, the frequency cross-overs are not seen between different mode shapes. Rather, the curve-veering phenomenon is observed.

- The 1D/2D solution for the pretwisted beam dynamics result in very large errors in natural frequencies when the twist rates are increased. Instead, the 3D-ST solution can be used to obtain accurate solutions without appreciable increase in computational cost.

Chapter 4

Modeling Three-Dimensional Dynamics of Rotating Structures under Mixed Boundary Bonditions

"Everything should be made as simple as possible, but not simpler."

-Albert Einstein

This chapter presents the derivation of a general modeling approach that uses the ST technique to determine the 3D dynamic response of rotating structures (including complex structures having pretwisted boundaries with curved cross-sections). In general, the dynamic response of rotating structures presents coupled 3D motions. To accurately capture the coupled dynamics, a 3D solution approach is needed. The presented solution technique is applied to a rotating/spinning parallelepiped (including rotating plates and rotating/spinning beams) under free and mixed boundary conditions, and a rotating cantilevered pretwisted beam with an airfoil geometry.

4.1 Model Development

A rotating structure with a general geometry is depicted in Fig. 4.1. A frame of reference xyz, the structural frame, is attached to the structure. Note that the structural frame rotates with the structure. The function $B(x, y, z)$ is used to describe the 3D (undeformed) boundary, and $C(z)$ is used to describe the cross-section, which is defined to be perpendicular to the z axis. An arbitrary rotational vector $\mathbf{\Omega}$ acting on structure is defined arbitrarily

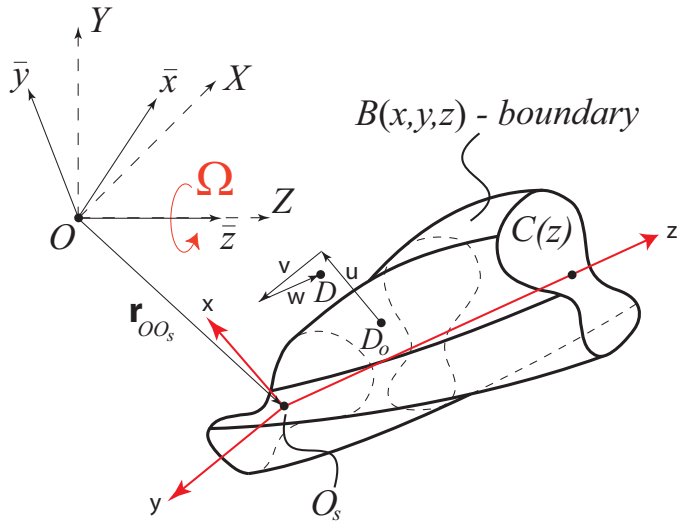

Figure 4.1: Description of a rotating structure having a general boundary, $B(x, y, z)$, and a general cross-section, $C(z)$.

in the 3D space. A stationary (fixed) reference frame (XYZ) is defined at point O where the Z axis is aligned with the rotation vector, $\mathbf{\Omega}$. Then, a rotating coordinate frame ($\bar{x}\bar{y}\bar{z}$), where $\bar{z}$ axis is aligned with the rotation axis, is introduced (see Fig. 4.1). The rotating coordinate frame rotates with the rotation speed (Ω) about the $\bar{z}$ (or Z) axis in counter-clockwise direction. Therefore, to express the relationship between the stationary coordinate frame (XYZ) and the rotating coordinate frame ($\bar{x}\bar{y}\bar{z}$), a rotation transformation matrix can be written as

$$\begin{Bmatrix} X \\ Y \\ Z \end{Bmatrix} = \begin{bmatrix} \cos(\Omega t) & -\sin(\Omega t) & 0 \\ \sin(\Omega t) & \cos(\Omega t) & 0 \\ 0 & 0 & 1 \end{bmatrix} \begin{Bmatrix} \bar{x} \\ \bar{y} \\ \bar{z} \end{Bmatrix}, \tag{4.1}$$

where Ω is the rotation speed of the structure around Z (or $\bar{z}$) axis, and t is the time. Note that the orientation of the (undeformed) structure can be arbitrary with respect to the rotation axis. To describe the structure's orientation with respect to the rotation axis, three (constant/time invariant) Euler angles (ψ_x, ψ_y, and ψ_z), that represent the three consecutive rotations, are defined. In this study, 3-2-1 set of Euler angles are considered [104]. Therefore, the transformation matrices between the rotating coordinate frame ($\bar{x}\bar{y}\bar{z}$) and the rotational structure frame (xyz) can be written as

$$\left\{\begin{array}{c}\bar{x}\\ \bar{y}\\ \bar{z}\end{array}\right\} = \begin{bmatrix}\cos(\psi_z) & -\sin(\psi_z) & 0\\ \sin(\psi_z) & \cos(\psi_z) & 0\\ 0 & 0 & 1\end{bmatrix}\begin{bmatrix}\cos(\psi_y) & 0 & \sin(\psi_y)\\ 0 & 1 & 0\\ -\sin(\psi_y) & 0 & \cos(\psi_y)\end{bmatrix}\begin{bmatrix}1 & 0 & 0\\ 0 & \cos(\psi_x) & -\sin(\psi_x)\\ 0 & \sin(\psi_x) & \cos(\psi_x)\end{bmatrix}\left\{\begin{array}{c}x\\ y\\ z\end{array}\right\}. \tag{4.2}$$

The following section explains the formulation of the boundary value problem. In deriving the IBVP, the following assumptions are made:

- The structural frame (xyz) attached to the structure is straight (see Fig. 4.1).
- The cross-sectional geometry is assumed to be uniform along the z axis, but it is allowed to be reoriented about the z axis (e.g., such as pretwisted structures with constant twist rate).
- The material properties are assumed to be uniform throughout the structure.

4.1.1 Formulation of the boundary value problem

The IBVP governing the dynamics of the rotating structures can be derived using the extended Hamilton's principle as in Chapter 3. However, in this case, 3D nonlinear elasticity equations are used in deriving the IBVP to capture the effect due to the stress-stiffening terms (as described in Chapter 1). Accordinlgy, the strains can be expressed in terms of displacements as

$$\epsilon_{ij} = \frac{1}{2}\left\{\frac{\partial q_i}{\partial x_j} + \frac{\partial q_j}{\partial x_i} + \sum_{k=1}^{3}\frac{\partial q_k}{\partial x_i}\frac{\partial q_k}{\partial x_j}\right\}, \quad i,\, j = 1,\, 2,\, 3 \;\; (q_1 = u, q_2 = v, q_3 = w)\,, \tag{4.3}$$

where the first two terms are the linear part of the strain and the summation term is the nonlinear part of the strain. Thus, the strains can be written as

$$\epsilon = \epsilon_{\mathbf{l}} + \epsilon_{\mathbf{nl}}\,, \tag{4.4}$$

where the strain vector is $\epsilon = \{\epsilon_{\mathbf{xx}}; \epsilon_{\mathbf{yy}}; \epsilon_{\mathbf{zz}}; \gamma_{\mathbf{yz}}; \gamma_{\mathbf{xz}}; \gamma_{\mathbf{xy}}\}$, and $\gamma_{ij} = 2\,\epsilon_{ij}$ are the shear strains experienced by the structure. Thus, the strain energy can be written as

$$E_S = \frac{1}{2}\int_V \Big(\epsilon_{\mathbf{l}} + \epsilon_{\mathbf{nl}}\Big)^T \mathbf{C}\Big(\epsilon_{\mathbf{l}} + \epsilon_{\mathbf{nl}}\Big) dV \tag{4.5}$$

$$= \frac{1}{2}\int_V {\epsilon_{\mathbf{l}}}^T \mathbf{C}\epsilon_{\mathbf{l}}\, dV + \frac{1}{2}\int_V {\epsilon_{\mathbf{nl}}}^T \mathbf{C}\epsilon_{\mathbf{nl}}\, dV + \frac{1}{2}\int_V {\epsilon_{\mathbf{nl}}}^T \mathbf{C}\epsilon_{\mathbf{l}}\, dV + \frac{1}{2}\int_V {\epsilon_{\mathbf{l}}}^T \mathbf{C}\epsilon_{\mathbf{nl}}\, dV \tag{4.6}$$

Using the constitutive matrix, the stress vector can be expressed in terms of strains as $\sigma = \mathbf{C}\epsilon$. Furthermore, the relation between the linear part of the strain and the displacement can be expressed as $\epsilon_l = \mathbf{Bq}$, where $\mathbf{B}$ is the differential operator matrix. Therefore, the linear part of the strain energy becomes $E_{S_l} = \frac{1}{2}\int_V \mathbf{q^T B^T C B q}\, dV$. The remaining terms in Eq. (4.6), that constitute, $\mathbf{E_{S_{nl}}}$, include either second or third order deflection components. The methodology to linearize these higher order terms is given below. For instance, Eq. (4.6) includes terms similar to

$$E^i_{S_{nl}} = \frac{1}{4}\int_V \frac{\partial u}{\partial x}(\lambda + 2\mu)\Big(\frac{\partial v}{\partial x}\Big)^2 dV\,. \tag{4.7}$$

Applying the Hamilton's principle, Eq. (4.7) becomes,

$$\delta E^i_{S_{nl}} = \frac{1}{4}\int_V \frac{\partial}{\partial x}\delta u(\lambda + 2\mu)\Big(\frac{\partial v}{\partial x}\Big)^2 dV + \frac{1}{2}\int_V \frac{\partial u}{\partial x}(\lambda + 2\mu)\frac{\partial v}{\partial x}\frac{\partial}{\partial x}\delta v\, dV\,. \tag{4.8}$$

Thus, each term can be linearized around the equilibrium solution as

$$\begin{aligned}\delta E^i_{S_{nl}} = {} & \frac{1}{4}\int_V (\lambda + 2\mu)\frac{\partial}{\partial x}\delta u\Big[\Big(\frac{\partial v^o}{\partial x}\Big)\Big(\frac{\partial v}{\partial x}\Big) + \Big(\frac{\partial v}{\partial x}\Big)\Big(\frac{\partial v^o}{\partial x}\Big)\Big]dV \\ & + \frac{1}{2}\int_V (\lambda + 2\mu)\Big[\frac{\partial u^o}{\partial x}\frac{\partial v}{\partial x} + \frac{\partial u}{\partial x}\frac{\partial v^o}{\partial x}\Big]\frac{\partial}{\partial x}\delta v\, dV\,,\end{aligned} \tag{4.9}$$

where superscript 'o' represents the equilibrium solution.

The kinetic energy and the work done by non-conservative forces for a structure are expressed as in Eqs. (3.3) and (3.4) in Chapter 3. To derive the velocity vector $\dot{\mathbf{q}}$ for any point within the rotating 3D structure, first, the position vector for any point should be written with respect to the origin (point O in Fig. 4.1). For instance, the position vector for point D can be expressed as

$$\begin{aligned}\mathbf{r}_{OD} &= \mathbf{r}_{OO_s} + \mathbf{r}_{O_sD_o} + \mathbf{r}_{D_oD} \\ &= (e_{\bar{x}}\,\mathbf{i}_{\bar{x}} + e_{\bar{y}}\,\mathbf{i}_{\bar{y}} + e_{\bar{z}}\,\mathbf{i}_{\bar{z}}) + (x_D\,\mathbf{i}_x + y_D\,\mathbf{i}_y + z_D\,\mathbf{i}_z) + (u_D\,\mathbf{i}_x + v_D\,\mathbf{i}_y + w_D\,\mathbf{i}_z),\end{aligned} \tag{4.10}$$

where $\mathbf{i}_j$ is the unit vector associated with the j direction, $e_{\bar{x}}$, $e_{\bar{y}}$, and $e_{\bar{z}}$ are the (constant) offsets of the origin of the rotating structure frame (O_s) from point O (origin of the rotating (or fixed) coordinate frame) in $\bar{x}$, $\bar{y}$, and $\bar{z}$ directions, respectively, x_D, y_D, and z_D are the (initial) geometric locations of point D within the structure with respect to the rotating structural frame (xyz), and u_D, v_D, and w_D are the deflections of point D from the initial locations in the rotating structural frame (xyz). Then, the velocity of point D can be

expressed as follows

$$\mathbf{v}_D = \dot{\mathbf{r}}_{OD} + \mathbf{\Omega} \times \mathbf{r}_{OD} = \dot{\mathbf{r}}_{OD} + (\Omega\, \mathbf{i}_{\bar{z}}) \times \mathbf{r}_{OD} \ , \tag{4.11}$$

$$= (\dot{u}_D\, \mathbf{i}_x + \dot{v}_D\, \mathbf{i}_y + \dot{w}_D\, \mathbf{i}_z) + (\Omega\, \mathbf{i}_{\bar{z}}) \times \Big\{ (e_{\bar{x}}\, \mathbf{i}_{\bar{x}} + e_{\bar{y}}\, \mathbf{i}_{\bar{y}} + e_{\bar{z}}\, \mathbf{i}_{\bar{z}}) + \big[(x_D + u_D)\, \mathbf{i}_x + (y_D + v_D)\, \mathbf{i}_y + (z_D + w_D)\, \mathbf{i}_z \big] \Big\}, \tag{4.12}$$

or, in matrix form as

$$\mathbf{v}_D = \dot{\mathbf{r}}_{OD} + \Big[\mathbf{\Omega} \Big]_{\times} \mathbf{r}_{OD} \ , \tag{4.13}$$

through conversion of the cross product into matrix multiplication [105], which will yield the individual velocity elements as

$$\mathbf{v}_{D_{\mathbf{i}_x}} = \dot{u} - \Omega \cos\psi_y \Big[e_y \cos\psi_z - e_x \sin\psi_z + (v + y) \cos\psi_x - (w + z) \sin\psi_x \Big] \ , \tag{4.14}$$

$$\mathbf{v}_{D_{\mathbf{i}_y}} = \dot{v} + \Omega \Big[(w + z) \sin\psi_y + e_x \cos\psi_x \cos\psi_z + (u + x) \cos\psi_x \cos\psi_y + e_y \cos\psi_x \sin\psi_z - e_y \cos\psi_z \sin\psi_x \sin\psi_y + e_x \sin\psi_x \sin\psi_y \sin\psi_z \Big] \ , \tag{4.15}$$

$$\mathbf{v}_{D_{\mathbf{i}_z}} = \dot{w} - \Omega \Big[(v + y) \sin\psi_y + e_x \cos\psi_z \sin\psi_x + (u + x) \cos\psi_y \sin\psi_x + e_y \sin\psi_x \sin\psi_z + e_y \cos\psi_x \cos\psi_z \sin\psi_y - e_x \cos\psi_x \sin\psi_y \sin\psi_z \Big] \ . \tag{4.16}$$

Applying the extended Hamilton's principle using the derived kinetic enegry, potential energy, and the work done by non-conservative forces, the integral boundary value problem (IBVP) can be expressed as

$$\int_{t_1}^{t_2} \Bigg\{ \int_{\mathbb{V}} \Big\{ \Big[\rho \ddot{\mathbf{q}}^T \delta\mathbf{q} + 2\rho\Omega \dot{\mathbf{q}}^T \mathbf{N}_{\mathbf{C_{cor}}} \delta\mathbf{q} + \mathbf{q}^T \mathbf{B}^T \mathbf{C} \mathbf{B} \delta\mathbf{q} - \rho\Omega^2 \mathbf{q}^T \mathbf{N}_{\mathbf{K_{spin}}} \delta\mathbf{q} + \delta\mathbf{E}_{\mathbf{S_{nl}}} - \rho\Omega^2 \mathbf{q_{ip}}^T \mathbf{N}_{\mathbf{F_c}} \delta\mathbf{q} - \mathbf{n_{F_c}}^T \delta\mathbf{q} \Big\} d\mathbf{V} - \mathbf{f_b}^T \delta\mathbf{q_b} \Bigg\} dt = 0. \tag{4.17}$$

where $\mathbf{N}_{\mathbf{C_{cor}}}$, $\mathbf{N}_{\mathbf{K_{spin}}}$, $\mathbf{N}_{\mathbf{F_c}}$, and $\mathbf{n}_{\mathbf{F_c}}$ are the operator system matrices for coriolis and spin-softening matrices, and centrifugal and external forcing vectors, respectively, and $\mathbf{q_{ip}} = \{\mathbf{x}; \mathbf{y}; \mathbf{z}\}$ is the vector of the initial (geometric) positions for each point within the structure. The operator system matrices given in Eq. (4.17) can be expressed as

$$\mathbf{N_{C_{cor}}} = \begin{bmatrix} \mathbf{0} & -\cos\psi_x\cos\psi_y\,\mathbf{I} & \sin\psi_x\cos\psi_y\,\mathbf{I} \\ \cos\psi_x\cos\psi_y\,\mathbf{I} & \mathbf{0} & \sin\psi_y\,\mathbf{I} \\ -\sin\psi_x\cos\psi_y\,\mathbf{I} & -\sin\psi_y\,\mathbf{I} & \mathbf{0} \end{bmatrix} , \tag{4.18}$$

$$\mathbf{N_{K_{spin}}} = \begin{bmatrix} \cos^2\psi_y\,\mathbf{I} & \frac{1}{2}\sin\psi_x\sin 2\psi_y\,\mathbf{I} & \frac{1}{2}\cos\psi_x\sin 2\psi_y\,\mathbf{I} \\ \frac{1}{2}\sin\psi_x\sin 2\psi_y\,\mathbf{I} & \cos^2\psi_x\cos^2\psi_y+\sin^2\psi_y\,\mathbf{I} & \frac{1}{2}\sin 2\psi_x\cos^2\psi_y\,\mathbf{I} \\ \frac{1}{2}\cos\psi_x\sin 2\psi_y\,\mathbf{I} & \frac{1}{2}\sin 2\psi_x\cos^2\psi_y\,\mathbf{I} & \sin^2\psi_x\cos^2\psi_y+\sin^2\psi_y\,\mathbf{I} \end{bmatrix} , \tag{4.19}$$

$$\mathbf{N_{F_c}} = \begin{bmatrix} \cos^2\psi_y\,\mathbf{I} & \frac{1}{2}\sin\psi_x\sin 2\psi_y\,\mathbf{I} & \frac{1}{2}\cos\psi_x\sin 2\psi_y\,\mathbf{I} \\ \frac{1}{2}\sin\psi_x\sin 2\psi_y\,\mathbf{I} & \cos^2\psi_x\cos^2\psi_y+\sin^2\psi_y\,\mathbf{I} & \frac{1}{2}\sin 2\psi_x\cos^2\psi_y\,\mathbf{I} \\ \frac{1}{2}\cos\psi_x\sin 2\psi_y\,\mathbf{I} & \frac{1}{2}\sin 2\psi_x\cos^2\psi_y\,\mathbf{I} & \sin^2\psi_x\cos^2\psi_y+\sin^2\psi_y\,\mathbf{I} \end{bmatrix} , \tag{4.20}$$

$$\mathbf{n_{F_c}} = \begin{Bmatrix} \rho\Omega^2 e_x\cos\psi_y\cos\psi_z\,\mathbb{i}+\rho\Omega^2 e_y\cos\psi_y\sin\psi_z\,\mathbb{i} \\ -\rho\Omega^2 e_x(\cos\psi_x\sin\psi_z-\sin\psi_x\sin\psi_y\cos\psi_z)\,\mathbb{i}+\rho\Omega^2 e_y(\cos\psi_x\cos\psi_z+\sin\psi_x\sin\psi_y\sin\psi_z)\,\mathbb{i} \\ \rho\Omega^2 e_x(\sin\psi_x\sin\psi_z+\cos\psi_x\sin\psi_y\cos\psi_z)\,\mathbb{i}-\rho\Omega^2 e_y(\sin\psi_x\cos\psi_z-\cos\psi_x\sin\psi_y\sin\psi_z)\,\mathbb{i} \end{Bmatrix} . \tag{4.21}$$

Here, $\mathbf{I}$ and $\mathbf{0}$ are $(N_xN_yN_z \times N_xN_yN_z)$ identity and zero matrices, respectively; and $\mathbb{i}$ is a $(N_xN_yN_z \times 1)$ vector whose elements are 1.

For numerical efficiency, the IBVP given in Eq. (4.17) is non-dimensionalized where the domain of the integrals and the coordinates are scaled by a reference length L_r. Thus, the non-dimensional parameters are $x = x^*L_r$, $y = y^*L_r$, $z = z^*L_r$, $q = q^*L_r$, and $\mathbf{B} = \mathbf{B}^*/L_r$ where the '$*$' superscript indicates the non-dimensional variables. The constitutive matrix is non-dimensionalized as $\mathbf{C} = \mathbf{C}^*E$. Therefore, the non-dimensional rotational speed is expressed as $\gamma = \Omega L_r(\rho/E)^{1/2}$. Similarly, the non-dimensional natural frequency is expressed as $\lambda = \omega L_r(\rho/E)^{1/2}$ where λ is the non-dimensional natural frequency. For the sake of simplicity, the '$*$' superscript on the non-dimensional terms are omitted hereafter.

4.1.2 Solution of the boundary value problem

The IBVP given in Eq. (4.17) is discretized through the developed ST technique as described in Chapter 3. The only difference in this case is that, when the dynamics of rotating structures having pretwisted geometries and curved cross-sections are investigated, the inner product matrix should be calculated considering two variable coefficients (weighting functions); which can be calculated following the same derivation procedure.

$$\int_{I_x}\int_{I_y}\int_{I_z} \mathbf{r}(x,y,z)\mathbf{s}(x,y,z)\mathbf{f}(x,y,z)\mathbf{g}(x,y,z)\,dx\,dy\,dz = \mathbf{f}^T\mathbf{V}^{\mathbf{r},\mathbf{s}}\mathbf{g} . \tag{4.22}$$

Here, I_x, I_y, and I_z defines the domain of the integral operation for each dimension. Since, Eq. (4.22) includes the multiplication of four functions, the product will have an order of $4N_x\,4N_y\,4N_z$. Thus, similar to the derivation given for stationary three-dimensional problems, the values of each function at $N_x\,N_y\,N_z$ Gauss-Lobatto points are interpolated to $4N_x\,4N_y\,4N_z$ as

$$\mathbf{f_{4N_x\,4N_y\,4N_z}} = \mathbf{S^{x_4}\,S^{y_4}\,S^{z_4}\,f_{N_x\,N_y\,N_z}}\,, \tag{4.23}$$

where the matrices $\mathbf{S^{x_4}}$, $\mathbf{S^{y_4}}$, and $\mathbf{S^{x_4}}$ are calculated following the same derivation procedure given in [29]. So, the integral given in Eq. (4.22) can be written as

$$\int_V \mathbf{r}(x,y,z)\mathbf{s}(x,y,z)\mathbf{f}(x,y,z)\mathbf{g}(x,y,z)dV = \tag{4.24}$$
$$\sum_{i,j,k}^{4N_x,4N_y,4N_z} \mathbf{v_i^{4N_x}v_j^{4N_y}v_k^{4N_z}}\left[\left(\mathbf{S_{ia}^{x_4}S_{jb}^{y_4}S_{kc}^{z_4}}\right)\left(\mathbf{S_{id}^{x_4}S_{je}^{y_4}S_{kf}^{z_4}}\right)\left(\mathbf{S_{il}^{x_4}S_{jm}^{y_4}S_{kn}^{z_4}r_{lmn}}\right)\left(\mathbf{S_{io}^{x_4}S_{jp}^{y_4}S_{kr}^{z_4}s_{opr}}\right)\right].$$

using the summation notation. Therefore, the inner product matrix can be found as

$$\mathbf{V_{abcdef}^{r,s}} = \sum_{i,j,k}^{4N_x,4N_y,4N_z}\ \sum_{l,m,n}^{4N_x,4N_y,4N_z}\ \sum_{o,p,r}^{4N_x,4N_y,4N_z} \mathbf{v_i^{4N_x}v_j^{4N_y}v_k^{4N_z}} \tag{4.25}$$
$$\left[\left(\mathbf{S_{ia}^{x_4}S_{jb}^{y_4}S_{kc}^{z_4}}\right)\left(\mathbf{S_{id}^{x_4}S_{je}^{y_4}S_{kf}^{z_4}}\right)\left(\mathbf{S_{il}^{x_4}S_{jm}^{y_4}S_{kn}^{z_4}r_{lmn}}\right)\left(\mathbf{S_{io}^{x_4}S_{jp}^{y_4}S_{kr}^{z_4}s_{opr}}\right)\right].$$

To efficiently calculate the calculate the inner product matrix, the matrices and vectors given in Eq. (4.25) are transformed into tensors and multiplied using the MATLAB Tensor Toolbox Version 2.5 (developed by Sandia National Laboratories). Therefore, the inner product matrix, $\mathbf{V_{abcdef}^{r,s}}$, is obtained as 6D tensor. To transform it into a global inner product matrix, the vector mapping procedure is applied as described in Chapter 3.

The deflection terms, $\mathbf{q}$, in the transformed domain can be discretized as

$$\mathbf{u} = \begin{bmatrix}\ \mathbf{I\,0\,0}\ \end{bmatrix}\mathbf{q} = \mathbf{I_u q},\ \ \mathbf{v} = \begin{bmatrix}\ \mathbf{0\,I\,0}\ \end{bmatrix}\mathbf{q} = \mathbf{I_v q},\ \ \mathbf{w} = \begin{bmatrix}\ \mathbf{0\,0\,I}\ \end{bmatrix}\mathbf{q} = \mathbf{I_w q}, \tag{4.26}$$

where $\mathbf{I}$ and $\mathbf{0}$ are $(N_\xi N_\eta N_\zeta \times N_\xi N_\eta N_\zeta)$ identity and zero matrices, respectively. Furthermore, the variation is imposed on the deflection vector as $\mathbf{q} = \bar{\mathbf{q}} + \hat{\mathbf{q}}$ where $\mathbf{q}$ is the (true) solution of the boundary value problem, $\bar{\mathbf{q}}$ is a family of trial functions satisfying the displacement (essential) boundary conditions, and $\hat{\mathbf{q}}$ is the variation from the true solution $\mathbf{q}$ in the form of time-invariant arbitrary test functions that satisfy the homogeneous displacement boundary conditions.

Therefore, after dicretizing the deflections and applying the derivative and inner-product operations, the IBVP given in Eq. (4.17) can be written in matrix form as

$$\mathbf{M}\,\ddot{\mathbf{q}} + (\mathbf{C} + \mathbf{C_{cor}})\dot{\mathbf{q}} + (\mathbf{K} - \mathbf{K_{spin}} + \mathbf{K_{nl}})\mathbf{q} - \mathbf{f_s} - \mathbf{f_d} = 0\,, \tag{4.27}$$

where $\mathbf{M}$, $\mathbf{C}$, $\mathbf{C_{cor}}$, $\mathbf{K}$, $\mathbf{K_{spin}}$, $\mathbf{K_{nl}}$, $\mathbf{f_s}$, and $\mathbf{f_d}$ are the mass, damping, coriolis, stiffness, spin-softening, and nonlinear stiffness matrices, and static and dynamic forcing vectors, respectively. Since the IBVP is written in the rotating frame of reference, instead of the gyroscopic and rotating damping matrices, Eq. (4.27) includes the coriolis and spin-softening matrices.

To find the equilibrium solution, a quasi-static approach is used. The deflection vector is expressed as a summation of the equilibrium deflection vector ($\mathbf{q_s}$) and the dynamic deflection vector ($\mathbf{q_d}$) as

$$\mathbf{q} = \mathbf{q_s} + \mathbf{q_d}\ . \tag{4.28}$$

The static part of the solution ($\mathbf{q_s}$) should satify the matrix form of the IBVP. Thus inserting ($\mathbf{q_s}$) to Eq. (4.27) yields

$$\mathbf{q_s} = \Big(\mathbf{K} - \mathbf{K_{spin}} + \mathbf{K_{nl}}\Big)^{-1}\mathbf{f_s}\ . \tag{4.29}$$

Since the nonlinear stiffness matrix includes terms that depend on equilibrium solution ($\mathbf{q_s}$), the above equation is solved iteratively until the equilibrium deflection vector ($\mathbf{q_s}$) converges. For the first step of this iterative solution, the nonlinear stiffness terms are taken as zero and are subsequently updated at each step until a converged solution for the equilibrium deflection vector is obtained.

After finding the equilibrium solution, the equation of motion becomes,

$$\mathbf{M}\,\ddot{\mathbf{q}}_\mathbf{d} + \Big(\mathbf{C} + \mathbf{C_{cor}}\Big)\dot{\mathbf{q}}_\mathbf{d} + \Big(\mathbf{K} - \mathbf{K_{spin}} + \overline{\mathbf{K}}_\mathbf{nl}\Big)\mathbf{q_d} = \mathbf{f_d}\,. \tag{4.30}$$

Here, $\overline{\mathbf{K}}_\mathbf{nl}$ represents the terms arising from the linearization of the nonliner stress-stiffening terms. Although, the IBVP approach eliminates the necessity to impose natural boundary conditions, the essential boundary conditions are still required to be imposed explicitly. To impose the essential boundary conditions, basis recombination (projection matrices ap-

proach) [29] is used as

$$\mathbf{q_d} = \mathbf{P}\,\mathbf{q_{d_h}} + \mathbf{R}\,\mathbf{q_{d_b}}\,. \tag{4.31}$$

Here, $\mathbf{P}$ and $\mathbf{R}$ are the projection matrices, $\mathbf{q_{d_h}}$ are the deflection terms within the domain, and $\mathbf{q_{d_b}}$ are the deflection terms on the boundary. After applying the projection matrices, the IBVP for a rotating structure can be expressed as

$$\mathbb{M}\ddot{\mathbf{q}}_{\mathbf{d_h}} + \Big(\mathbf{C} + \mathbb{C}_{\mathbf{cor}}\Big)\dot{\mathbf{q}}_{\mathbf{d_h}} + \Big(\mathbb{K} - \mathbb{K}_{\mathbf{spin}} + \overline{\mathbb{K}}_{\mathbf{nl}}\Big)\mathbf{q_{d_h}} = \mathbb{f}_{\mathbf{d}}\ , \tag{4.32}$$

where $\mathbb{M}$, $\mathbb{C}$, $\mathbb{C}_{\mathbf{cor}}$, $\mathbb{K}$, $\mathbb{K}_{\mathbf{spin}}$, $\overline{\mathbb{K}}_{\mathbf{nl}}$, and $\mathbb{f}_{\mathbf{d}}$ are the global mass, damping, coriolis, linear stiffness, spin-softening, and nonlinear stiffness matrices, and forcing vector respectively, and can be expressed as

$$\mathbb{\Lambda}_i = \mathbf{P}^T\mathbf{\Lambda_i}\mathbf{P} \ \text{ and } \ \mathbb{f} = \mathbf{P}^T\mathbf{f}\ . \tag{4.33}$$

Here, $\mathbf{\Lambda}_i = \mathbf{M}$, $\mathbf{C}$, $\mathbf{C_{cor}}$, $\mathbf{K}$, $\mathbf{K_{spin}}$, or $\overline{\mathbf{K}}_{\mathbf{nl}}$. In the presented 3D-ST solution approach, the non-dimensionalization approach described in the previous chapter is used, by selecting a reference length L_r. Thus, the (non-dimensional) system matrices can be expressed as

$$\mathbf{M} = \frac{\rho L_r^2}{E}\Big(\mathbf{I_u}^T\mathbf{V}\mathbf{I_u} + \mathbf{I_v}^T\mathbf{V}\mathbf{I_v} + \mathbf{I_w}^T\mathbf{V}\mathbf{I_w}\Big)\,, \tag{4.34}$$

$$\begin{aligned}\mathbf{C_{cor}} = &-2\gamma L_r\sqrt{\frac{\rho}{E}}\Bigg[\cos\psi_x\cos\psi_y\Big(\mathbf{I_v}^T\mathbf{V}\mathbf{I_u} - \mathbf{I_u}^T\mathbf{V}\mathbf{I_v}\Big)\\ &-\sin\psi_x\cos\psi_y\Big(\mathbf{I_w}^T\mathbf{V}\mathbf{I_u} - \mathbf{I_u}^T\mathbf{V}\mathbf{I_w}\Big) - \sin\psi_y\Big(\mathbf{I_w}^T V\mathbf{I_v} - \mathbf{I_v}^T\mathbf{V}\mathbf{I_w}\Big)\Bigg]\,,\end{aligned} \tag{4.35}$$

$$\mathbf{K} = \mathbf{B}^T\mathbf{V}\mathbf{B_C}\,, \tag{4.36}$$

$$\begin{aligned}\mathbf{K_{spin}} = &\gamma^2\Bigg[\cos^2\psi_y\mathbf{I_u}^T\mathbf{V}\mathbf{I_u} + \Big(\cos^2\psi_y\cos^2\psi_x + \sin^2\psi_y\Big)\mathbf{I_v}^T\mathbf{V}\mathbf{I_v}\\ &+\Big(\sin^2\psi_x\cos^2\psi_y + \sin^2\psi_y\Big)\mathbf{I_w}^T\mathbf{V}\mathbf{I_w} + \frac{1}{2}\sin 2\psi_y\sin\psi_x\Big(\mathbf{I_v}^T\mathbf{V}\mathbf{I_u} + \mathbf{I_u}^T\mathbf{V}\mathbf{I_v}\Big)\\ &+\frac{1}{2}\sin 2\psi_y\cos\psi_x\Big(\mathbf{I_w}^T\mathbf{V}\mathbf{I_u} + \mathbf{I_u}^T\mathbf{V}\mathbf{I_w}\Big) - \frac{1}{2}\sin 2\psi_x\cos^2\psi_y\Big(\mathbf{I_w}^T\mathbf{V}\mathbf{I_v} + \mathbf{I_v}^T\mathbf{V}\mathbf{I_w}\Big)\Bigg]\,,\end{aligned} \tag{4.37}$$

$$\mathbf{F_d} = \frac{L_r}{E}\mathbf{V}\Big(\mathbf{f_q} + \frac{1}{L_r^3}\mathbf{f_b}\Big)\,. \tag{4.38}$$

It is noted that $\mathbf{C}$ represents the damping arising from the structural configuration (i.e., due to energy dissipation through joints, internal structural damping, etc.); as such, $\mathbf{C}$ is

generally determined through modal testing. Due to the space considerations, the closed form of the nonlinear stiffness matrix ($\overline{\mathbf{K}}_{\mathbf{nl}}$) is not given here; however the derivation given in Section 4.1.1 can be followed to obtain this matrix. Once the (global) system matrices are found, the natural frequencies and mode shapes of a rotating structure can be found in the state space, since the coriolis matrix causes a non-proportional damping, and thus, prevents solving the system in the configuration space [95]. Furthermore, the system matrices can be used to model the dynamic behavior in response to arbitrary force inputs in numerical simulation studies. Note also that here, the derivation of the boundary value problem for a single rotation axis is presented; however using the following presented derivation approach the boundary value problem of a structure can be found when more than one rotational axis is defined.

4.2 Model Application

In this section, the application of the 3D-ST method for solving the dynamics of rotating 3D structures is described and demonstrated. Two case studies were investigated: **(1)** rotating/spinning parallelepipeds with free and mixed boundary conditions and **(2)** a rotating cantilevered pretwisted blade with airfoil cross-section. The natural frequencies were obtained from the eigensolution using the global system matrices. To ensure the accuracy of the 3D-ST solutions and to select the optimum number of polynomials, a convergence study was performed in each case. Furthermore, in each case study, the change of natural frequencies with rotational speed was investigated.

To the best of the author's knowledge, there is no study investigating the 3D dynamics of rotating structures. Previous studies were mainly focused on the dynamics of rotating/spinning beams (1D models) or plates (2D models). Therefore, to assess the precision of the presented solution technique, within the first case study, the non-dimensional natural frequencies, λ, of a rotating cantilevered plate obtained from the 3D-ST method were compared to those found in the literature (that were obtained using plate models) as well as to those found by a commercial FE solver.

4.2.1 Dynamics of rotating/spinning parallelepipeds

To demonstrate and evaluate the application of the presented 3D-ST solution, the dynamics of rotating/spinning parallelepipeds, as depicted in Fig. 4.2, were analyzed and compared with the results presented in the literature. Note that, since the geometry in this case

study is straight with rectangular cross-section, there is no need to apply rotational or cross-sectional mapping. The rotating coordinate frame ($\bar{x}\bar{y}\bar{z}$) and the rotating structure frame (xyz) are defined as described in section 4.1.

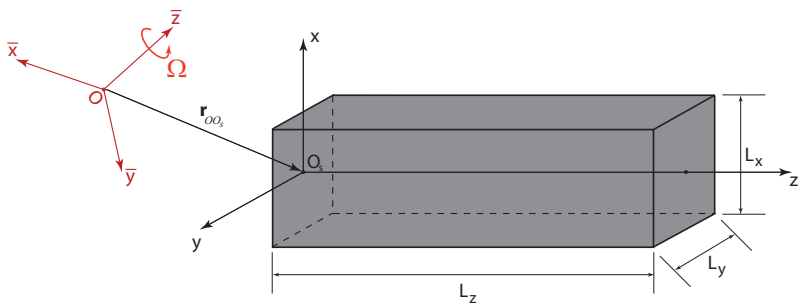

Figure 4.2: General schematic diagram of a rotating/spinning parallelepiped.

Depending on the orientation and the location of the structure with respect to the rotation axis, the structure either rotates about an axis or spins[6] around an axis, or both. For instance, when the rotating coordinate frame ($\bar{x}\bar{y}\bar{z}$) and the rotating structural frame (xyz) are aligned (i.e., $\bar{x}$ and $\bar{y}$ components of r_{OO_s} and the three constant Euler angles ϕ_x, ϕ_y, and ϕ_z are zero), the structure is in pure-spin configuration. In this section, the non-dimensional natural frequencies and mode shapes of rotating/spinning parallelepipeds (such as rotating beams and plates or spinning beams) were calculated by the presented 3D-ST approach and compared with those found in the literature (when exist) or obtained using a commercial FE solver. Note that the classifications made here such as beams and plates merely represents the general characteristics of the geometry.

4.2.1.1 Rotating thin plates

In this case study, the 3D dynamics of a rotating cantilevered (at $z = 0$ face of the geometry) square thin plate (see Fig. 4.3) having geometric properties as $L_x/L_z = 1$ and $L_y/L_z = 0.01$, offsets as $e_{\bar{x}}/L_z = 0$, $e_{\bar{z}}/L_z = 0$ and $e_{\bar{y}}/L_z = R_h/L_z = 1$, and Euler angles as $\psi_x = 0^o$, $\psi_y = -90^o$, and $\psi_z = 0$, was analyzed. Poisson's ratio was set to 0.3. To assess the precision of the presented solution approach, the non-dimensional natural frequencies found from the 3D-ST solution were compared to those presented in [5] and also to those found by a commercial finite element solver (ANSYS® version 14.5 with SOLID187 3D 10-node tetrahedral structural solid elements).

[6] *Spinning* is a special case of rotation where the rotation axis passes through the structure's center of mass.

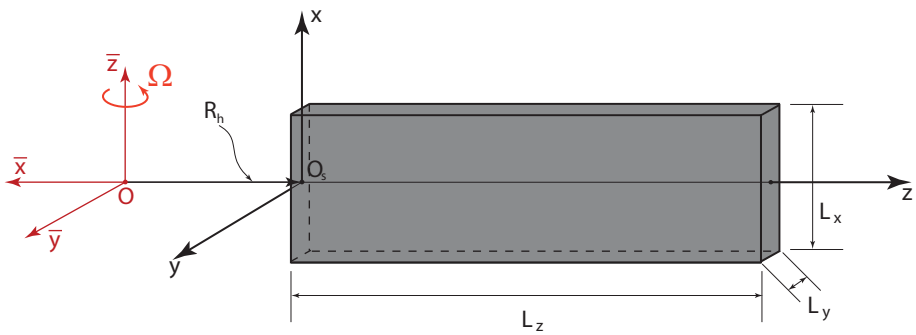

Figure 4.3: General schematic diagram of a rotating thin plate.

Following the presented model derivation, the non-dimensional system matrices defined in Eqs. (4.34)-(4.38) reduce to

$$\mathbf{M} = \frac{\rho L_r^2}{E}\Big(\mathbf{I_u}^T\mathbf{V}\mathbf{I_u} + \mathbf{I_v}^T\mathbf{V}\mathbf{I_v} + \mathbf{I_w}^T V\mathbf{I_w}\Big)\,, \tag{4.39}$$

$$\mathbf{C_{cor}} = -\,2\gamma L_r\sqrt{\frac{\rho}{E}}\Big(\mathbf{I_w}^T\mathbf{V}\mathbf{I_v} - \mathbf{I_v}^T\mathbf{V}\mathbf{I_w}\Big)\,, \tag{4.40}$$

$$\mathbf{K_{spin}} = \gamma^2\Big(\mathbf{I_v}^T\mathbf{V}\mathbf{I_v} + \mathbf{I_w}^T\mathbf{V}\mathbf{I_w}\Big)\,, \tag{4.41}$$

$$\mathbf{K} = \mathbf{B}^T\mathbf{V}\mathbf{B_C}\,, \tag{4.42}$$

$$\mathbf{f} = \gamma^2\Big[\mathbf{y}\mathbf{V}\mathbf{I_v} + \Big(\mathbf{z} + \beta\Big)\mathbf{V}\mathbf{I_w}\Big]\,, \tag{4.43}$$

and the stress-stiffening matrix ($\overline{\mathbf{K_{nl}}}$) can be obtained following the derivation given in Section 4.1.1. Here, the reference length L_r is chosen to the length (L_z) of the rectangular plate, and $\beta = R_h/L_r$ is the non-dimensional hub radius. Then, the global system matrices were obtained by inserting Eqs. (4.39)-(4.43) into Eq. (4.33). Subsequently, the natural frequencies and mode shapes were calculated using the state-space formulation [100]. However, the non-dimensionalization approach that is traditionally used for the plate models is different from the 3D models. And thus, to enable comparison of our results with those in literature, the non-dimensionalization approach[7] given in [5] was adopted for this case.

To determine the required number of polynomials used in each direction for the 3D-ST solution, a convergence study described in the previous section was performed using $\epsilon_a = -3$, $\epsilon_i = -2$, and a reference solution that uses 14-7-14 polynomials. Based on the convergence studies, 3D-ST models with 11-5-12 polynomials was used to model the rotating thin cantilevered square plate. Similarly, a priori convergence study was performed for the

[7]In plate models, the non-dimensionalization is performed using the flexural rigidity of the plate as $\lambda = \omega T$ where $T = \sqrt{\rho L_y L_z^4/D}$. Here, D is the flexural rigidity calculated as $D = EL_y^3/(12(1-\nu^2))$.

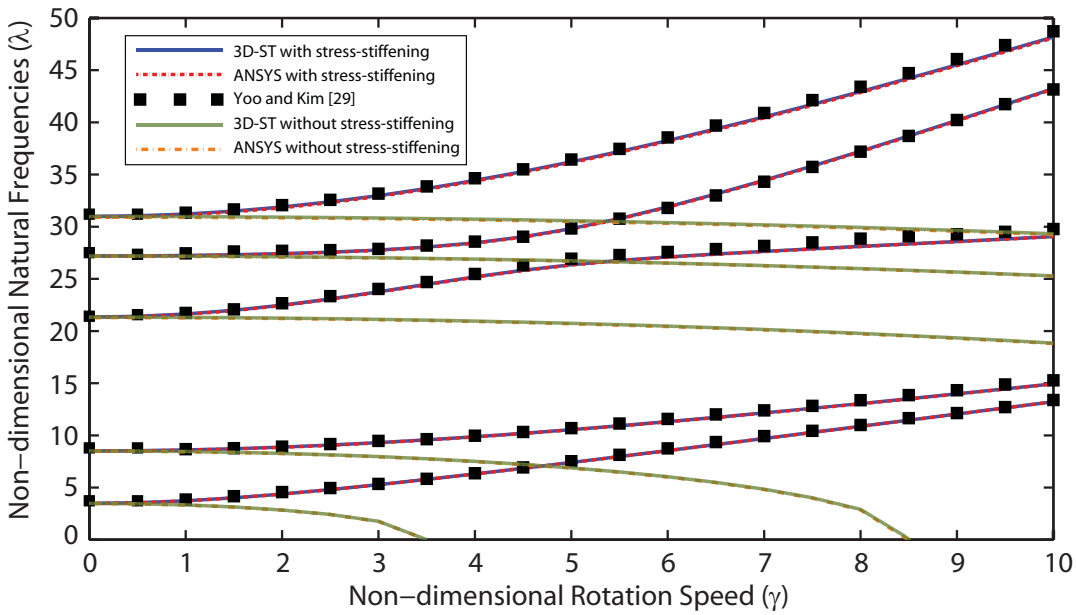

Figure 4.4: Change in the non-dimensional natural frequencies of a rotating thin cantilevered plate with non-dimensional rotation speed. Solid and dashed lines are the data calculated using 3D-ST approach and ANSYS®, respectively, and the square markers are the data presented in [5], respectively.

FEM solution, and the results were obtained using 40,000 elements. Figure 4.4 shows the comparison of the first five non-dimensional natural frequencies calculated with the presented 3D-ST technique, ANSYS®, and those presented by Yoo and Pierre [5] (that used *Kirchhoff-Love* plate theory). Furthermore, to demonstrate the importance of nonlinear effects, the non-dimensional natural frequencies were also calculated without including the nonlinear (stress-stiffening) terms and the results were also given in Fig. 4.4.

Important observations can be made from Fig. 4.4. First, the natural frequencies obtained from the 3D-ST solution are in very good agreement with those from [5] and the ANSYS® results. The maximum difference between the 3D-ST and ANSYS® results are less than 0.5% for any mode and at any non-dimensional rotation speed. Although the differences in non-dimensional natural frequencies between the 3D-ST and plate models show a slight increase with increasing rotational speeds, possibly due to the assumptions used in the plate modeling techniques [106], the maximum difference is less than 1%. Second, the effect of rotation speed on each mode is not similar (i.e., some modes are affected more than the others). To explain this phenomenon, a mode-shape analysis was performed using the developed 3D-ST solution. The corresponding five mode shapes for the rotating rectangular cantilevered plate are given in Fig. 4.5 for six different non-dimensional rotational speeds ($\gamma = 0, 2, 4, 6, 8$, and 10). As observed, a transition occurs between the third (bending mode

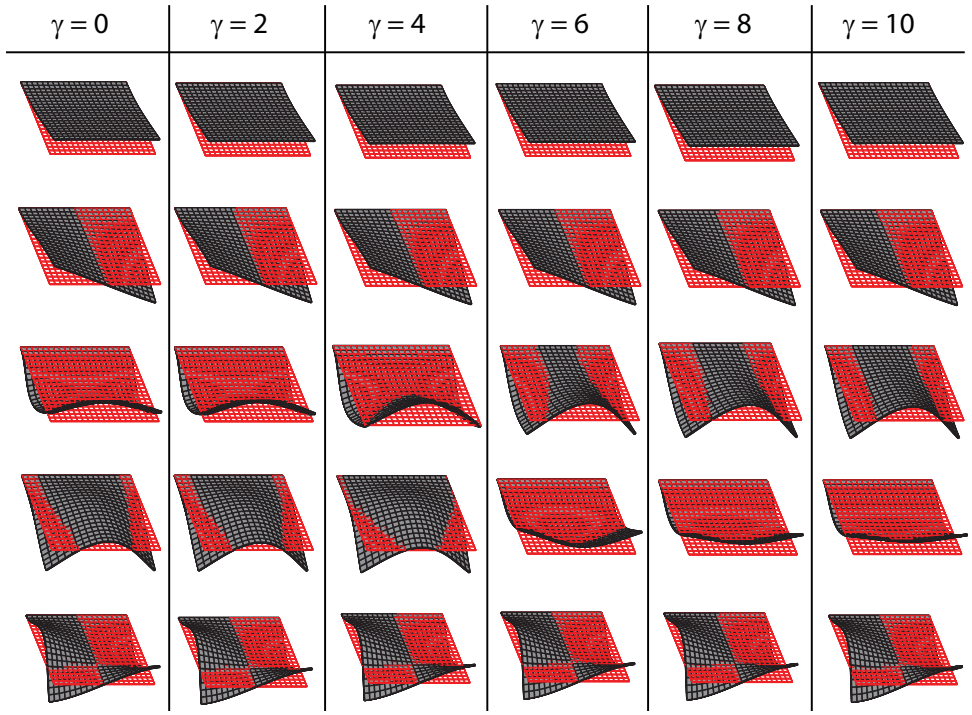

Figure 4.5: The first five mode shapes of a thin rotating cantilevered plate having the geometric properties as $L_x/L_z = 1$, $L_y/L_z = 0.01$, and non-dimensional hub radius of 1. The red lines indicate the undeflected geometries.

around the y axis) and fourth mode (bending mode around the z axis) shapes, which is a phenomenon referred to as *curve veering* in the literature [102]. This happens due to the fact that the stationary stress-field created by the nonlinear (stress-stiffening) effects increases the stiffness of the bending modes around the y axis more than the bending modes around the z axis.

In addition to the comparison of non-dimensional natural frequencies, in this example, the mode shapes obtained from the 3D-ST and 3D-FEM solutions through a modal assurance criterion (MAC) analysis were quantitatively compared. The modal assurance criterion is a measure of consistency of the modal vectors obtained from two different approaches. A MAC value of unity between two mode shapes indicates that the two mode shapes are identical. In the literature, the threshold MAC value of 0.8 is considered as a satisfactory consistency between the mode shapes found by two different approaches [100]. Here, to calculate the MAC values, the modal vector calculated in ANSYS® solution was extracted for each mode. The modal vector is composed of the nodal displacements. Therefore, using the 3D-ST solution, the modal vector was obtained by determining the displacement values corresponding to the position of each node. Finally, using the modal vectors obtained from

the two different solution techniques, MAC values for each mode were calculated. According to this analysis, minimum MAC values of 0.9995, 0.9993, 0.9991, 0.9954, 0.9877, and 0.9917, and average MAC values of 0.9997, 0.9995 ,0.9911, 0.9982, 0.9973, and 0.9973 were obtained for non-dimensional rotation speeds of 0, 2, 4, 6, 8, and 10, respectively. Therefore, it is concluded that the mode shapes obtained from the 3D-ST and 3D-FEM solutions are in excellent agreement.

4.2.1.2 Rotating/spinning beams

The next case study is a rotating/spinning beam with rectangular cross-section geometry as depicted in Fig. 4.6. The beam has the geometric properties of $L_x/L_z = 0.3$ and $L_y/L_z = 0.2$, and zero offsets (i.e., $e_{\bar{x}}/L_z = 0$, $e_{\bar{z}}/L_z = 0$ and $e_{\bar{y}}/L_z = R_h/L_z = 0$). The Poisson's ratio was set to 0.3. Similar to the previous examples, the geometry has a straight, rectangular, non-changing cross-section; thus, there is no need to apply rotational and cross-sectional mapping procedures. The rotating coordinate frame ($\bar{x}\bar{y}\bar{z}$) and the rotating structural frame (xyz) are defined as described in Section 4.1.

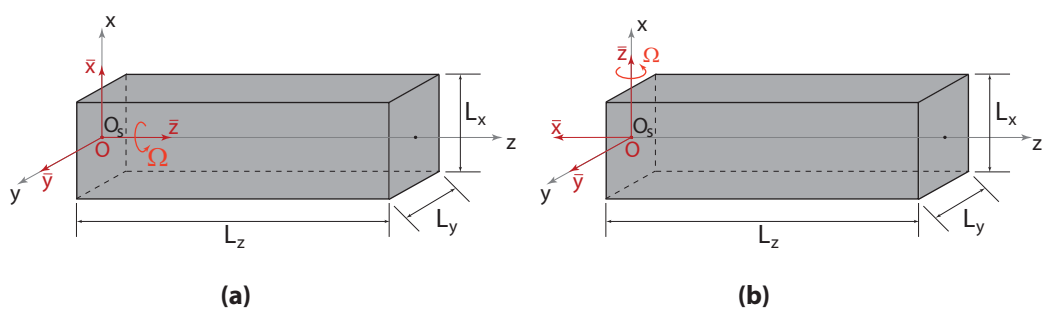

Figure 4.6: **(a)** Spinning and **(b)** rotating beams having a rectangular cross-section.

Depending on the orientation of the beam with respect to the rotation vector (or to the rotating coordinate frame, $\bar{x}\bar{y}\bar{z}$), the physics of the problem changes. As seen from Fig. 4.6, two different cases were studied here: **(1)** when the rotating coordinate frame ($\bar{x}\bar{y}\bar{z}$) and the rotating structural frame (xyz) are aligned (i.e., the three constant Euler angles ψ_x, ψ_y, and ψ_z are zeros, the problem becomes a purely spinning beam (see Fig. 4.6(a)), and **(2)** when $\psi_y = -90^o$ while the other Euler angles are zeros, the problem becomes a purely rotating beam (see Fig. 4.6(c)). The non-dimensional system matrices for both cases can be found using Eqs. (4.34)-(4.38) considering the orientation of the structure. As in the previous example, to determine the required number of polynomials used in each direction, a convergence study was performed using $\epsilon_a = -3$, $\epsilon_i = -2$, and a reference solution that

uses 11-11-15 polynomials. Based on the convergence study, the spinning/rotating beam with a rectangular cross-section was modeled with $N_x - N_y - N_z = 8 - 7 - 11$ polynomials.

The non-dimensional natural frequencies of cantilevered beams (where the $z = 0$ plane is fixed) in each case depicted in Fig. 4.6 were analyzed as a function of non-dimensional rotational speed. In this analysis, to determine the effect of coriolis, spin-softening, and nonlinear stiffness (stress-stiffening) matrices in the BVP problem, the non-dimensional natural frequencies were calculated with and without the contribution of those components (see Fig. 4.7). Furthermore, the non-dimensional natural frequencies calculated from the 3D-FEM solution were also included in Fig. 4.7 for the cases with and without the nonlinear (stress-stiffening) terms. As in the previous cases, a priori convergence study was performed for the FEM solution, and the results were obtained using 60,000 elements.

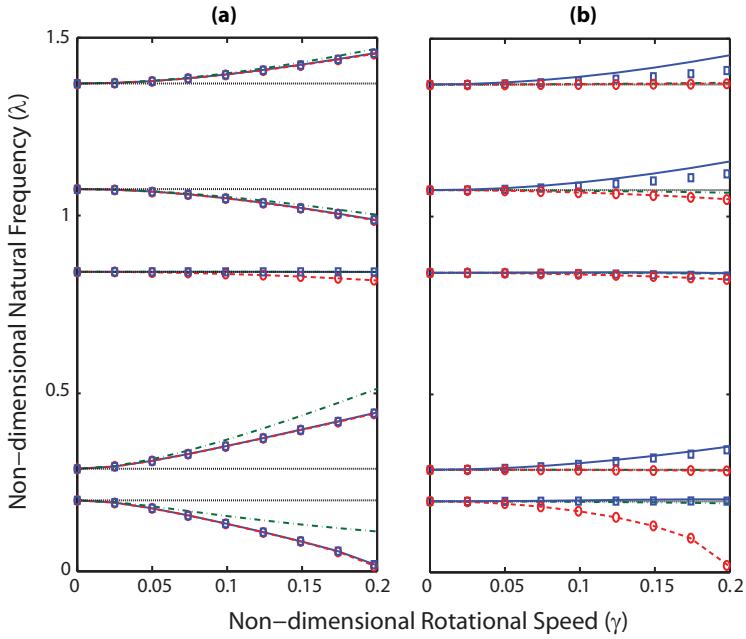

Figure 4.7: The effect of coriolis, spin-softening, and nonlinear (stress-stiffening) terms on the dynamics of cantilevered **(a)** spinning and **(b)** rotating beams. (Dotted (black) lines show the results for stationary cases. The results after including the *coriolis* terms are shown by the dashed dotted (green) lines. Then, the *spin softening* terms are also included to the simulation and the results are shown by dashed (red) lines. And lastly, solid (blue) lines represent the simulation results including all the terms. Similarly, square and circle markers represent the non-dimensional natural frequencies calculated using ANSYS® with and without nonlinear (stress-stiffening) effects, respectively).

Important observations can be made from Fig. 4.7. *First*, the effect of each term in

the BVP given in Eq. (4.30) is different and can be seen clearly. For the spinning beam case, the addition of *coriolis* terms (that are skew-symmetric terms) causes the natural frequencies of bending-mode pairs to split. After adding the *spin softening* terms, a decrease in the stiffness of the structure (thus, in the natural frequencies) occurs. After including the *nonlinear stiffness (stress-stiffening)* terms, the natural frequencies increases; however this is very small (less than 1%) for the cantilevered spinning beam; and thus, the nonlinear effects may be neglected (especially for computational efficiency). On the other hand, for the rotating beam case, the effect of *coriolis* and *spin softening* is minimal; however after including the *nonlinear stiffness (stress-stiffening)* terms, the stiffness of the structure increases significantly (due to the created stationary stress field), and thus, causes an increase in natural frequencies (see Fig. 4.7). *Second*, the results obtained from the 3D-ST and the 3D-FEM approaches are in excellent agreement (the maximum difference in non-dimensional frequencies is less than 1%) for the spinning beam case (see Fig. 4.7(a)). However, for the rotating beam case, although the results are in very good agreement at low rotational speeds, as the rotation speed increases, the differences for fourth and fifth modes becomes larger due to the approximations made in calculating the nonlinear effects in 3D-FEM solution. It was stated in the literature that ANSYS® can only predict the dynamics of spinning axially symmetric structures accurately [63]. *Lastly*, for the rotating cantilevered beam case, the first and fourth modes (which are the bending modes around the y axes) are affected by the nonlinear terms (stress-stiffening terms) more than the other modes are, as described in the previous example.

Next, to analyze the effect of boundary conditions, the non-dimensional natural frequencies and mode shapes of an unconstrained spinning beam were calculated (see Figs. 4.8 and 4.9). Note that although the boundary conditions are different, the basis recombination approach enables using the same set of Tchebychev polynomials as basis functions, and thus, the presented 3D-ST approach can be used directly for problems with different boundary conditions. Similar to the previous cases, the results (both natural frequencies and mode shapes) were compared with those found using ANSYS®. As observed from Fig. 4.8, the natural frequencies obtained from the 3D-ST solution closely match those from the 3D-FEM closely. The difference between the non-dimensional natural frequencies from the two solutions increases with increasing rotation speed; however the maximum difference is less than 1% for any mode and rotational speed. However, note that the computational cost of the 3D-ST solution is three-to-four times less than that of the 3D-FEM solution. Furthermore, as observed from Fig. 4.9, curve veering occurs between the second and third mode shapes, and sixth and seventh mode shapes as the rotational speed increases. The minimum MAC

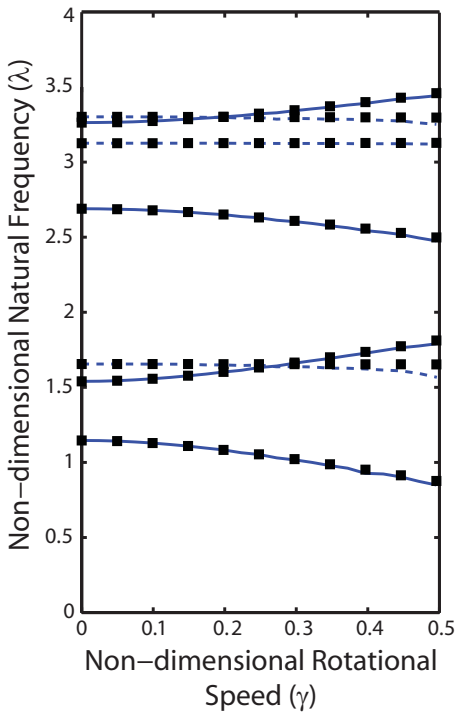

Figure 4.8: Change of non-dimensional natural frequencies of an unconstrained spinning beam with non-dimensional rotation speed. The solid and dashed lines represent the bending and torsional/axial modes, respectively, and the (black) square markers are the results obtained from the ANSYS®.

value between the mode shapes found by 3D-ST approach and ANSYS® was calculated as 0.9738 considering first seven mode shapes at any rotational speed.

Finally, to investigate the effect of alignment errors, three different cases were analyzed: **(1)** with no alignment errors (i.e., pure spinning), **(2)** with small alignment errors ($e_{\bar{x}}/L_z = 0.003$, $e_{\bar{y}}/L_z = 0.004$, $\psi_x = 0.2^o$, and $\psi_y = 0.5^o$), and **(3)** with large alignment errors ($e_{\bar{x}}/L_z = 0.15$, $e_{\bar{y}}/L_z = 0.02$, $\psi_x = 3^o$, and $\psi_y = 1^o$). Figure 4.10(a)-(c) shows the calculated non-dimensional natural frequencies as a function of non-dimensional rotation speed. As the alignment errors increase, the (centrifugal) forces acting on the structure also increase. Thus, the structure exhibits large overall motions that change the apparent stiffness of the structure. However, in this case, due to the orientation and position of the structure with respect to the rotation axis, the nonlinear terms (arising from the created stationary stress field) decrease the stiffness of the structure (i.e, weaken the structure) [63]. Therefore, as seen in Figs.4.10(b)-4.10(c), this change in apparent stiffness destabilizes the structure, leading to the observed differences in non-dimensional natural frequencies. Furthermore, the maximum rotational speed that the structure can experience reduce sharply as the alignment errors increases.

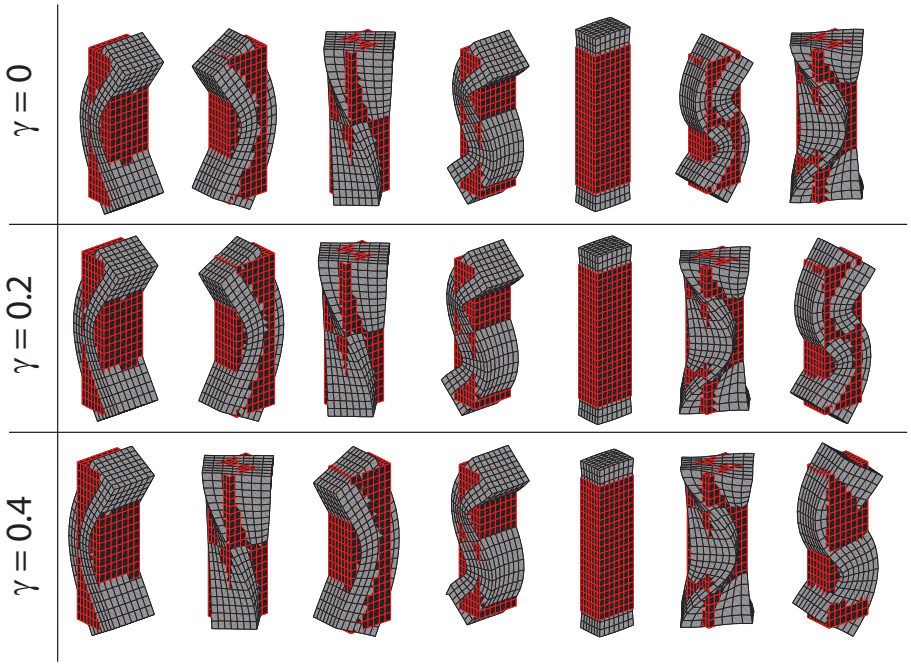

Figure 4.9: The first seven mode shapes of an unconstrained spinning beam with non-dimensional rotation speed. The red lines indicate the undeflected geometries.

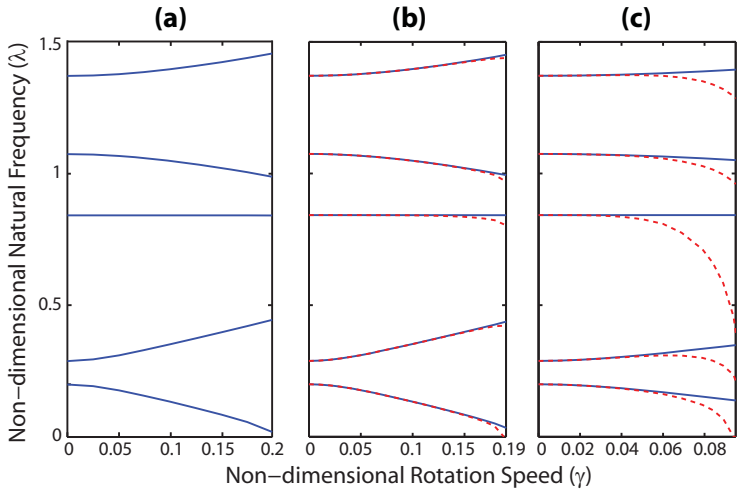

Figure 4.10: Effect of alignment errors on the dynamics of spinning beams: **(a)** pure spinning case, **(b)** comparison of pure spinning case with small alignment errors case and **(c)** comparison of pure spinning case with large alignment errors case (Blue solid and red dashed lines represent the non-dimensional natural frequencies corresponding to pure spinning and spinning with alignment errors cases, respectively).

4.2.2 Dynamics of a rotating pretwisted blade with airfoil cross-section

The spinning/rotating parallelepiped examples given in the previous section do not require any rotational and cross-sectional mapping procedures. In this last example, the dynamics of a rotating cantilevered pretwisted beam having an airfoil cross-section (that resembles a rotating blade) that is attached to a rigid rotor was investigated. Figure 4.11(a) illustrates the geometry of the rotating structure, which has an aspect ratio (length-to-chord-length[8]) of 3. Furthermore, the structure has a pretwist dictated by the twist rate[9]. The Poisson's ratio was set to 0.3.

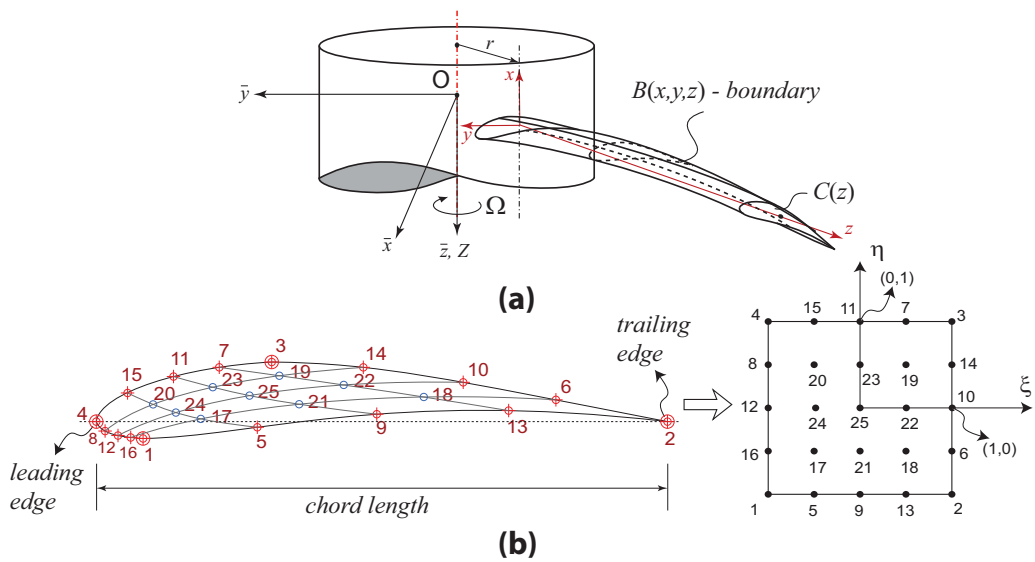

Figure 4.11: **(a)** Rotating blade having an airfoil cross-section, and **(b)** the corresponding mapping procedure.

As mentioned, the analyzed structure is a pretwisted beam with a curved cross-section; thus, first, a rotational transformation was applied to obtain a straight beam with the airfoil geometry, and then the airfoil cross-section was mapped onto a rectangular domain. The former transformation was achieved by using a rotational transformation around the z axis imposing a right hand rotation of $2\pi\alpha z/L_z$ where α is the twist rate. For the latter transformation (see Fig. 4.11(b)), a one-to-one mapping approach was used to map the airfoil cross-section onto a rectangular cross-section (defined in $\xi\eta\zeta$ frame). In the cross-section mapping procedure, a fourth order polynomial mapping (leading to 25 mapping polynomi-

[8]The chord length is the length of the straight line connecting leading and trailing edges of an airfoil cross-section (see Fig. 4.11(b)).

[9]The twist rate is quantified by the number (or fraction) of total twist within the length of the beam. For instance, a twist rate of 0.5 indicates that the total twist is 180 degrees within the length of the beam, i.e., the pitch is equal to twice the beam length.

als) described in [71, 98] was used. For more detailed information about the rotational and cross-section mapping procedures, the reader is referred to [71].

After applying the two coordinate transformations and using Eqs. (4.34)-(4.38), the global system matrices can be obtained. As in the previous examples, a convergence study was preformed to determine the required number of polynomial necessary for each direction using $\epsilon_a = -3$, $\epsilon_i = -2$, and a reference solution that uses 11-11-15 polynomials. Based on the convergence study, the rotating cantilevered pretwisted beam with airfoil cross-section was modeled with $N_x - N_y - N_z = 8 - 9 - 11$ polynomials.

The simplicity, numerical efficiency, and completely parameterized nature of the solution afforded by the 3D-ST approach enabled effective analysis of the effects of different parameters on the dynamics of rotating blades. As an example, Fig. 4.12(a)-(b) shows the effect of nonlinear (stress-stiffening) terms, and the variation of non-dimensional natural frequencies with non-dimensional rotation speed for different hub-radius ratios ($\beta = R_h/L_z$) for a straight blade geometry (i.e., no pretwist). First, it is clearly seen that the thin geometry of the beam causes string nonlinear effects, and thus, the nonlinear terms cannot be neglected (see Fig. 4.12(a)). Next, the effect of hub radius ratio on the non-dimensional natural frequencies are investigated. As the hub radius ratio increases, the centrifugal forces also increase; resulting in the stationary stress field that creates larger overall motions, which increase the stiffening effect (see Fig. 4.12(b)). Furthermore, as observed in the thin plate analysis, curve veering phenomenon can also be observed in this case study between the 2nd, 3rd, and 4th modes of the blade structure. The mode shapes are given in Fig. 4.13 for a hub radius ratio of 1. As seen, the second mode shape, which is the bending dominant mode[10], becomes the third and fourth mode shape as the rotational speed is increased.

The effect of aspect ratio on the dynamics of a rotating cantilevered beam with an airfoil ratio was also investigated. For this analysis, the non-dimensional hub ratio and twist rate were selected as 1 and 0.02, respectively. Figure 4.14 shows the variation of non-dimensional frequencies as a function of aspect ratio. As expected, as the aspect ratio increases, all the non-dimensional natural frequencies decrease. However, the aspect ratio has a more significant effect on the bending dominant modes (see Fig. 4.14).

[10]Since the shear center and the geometric center is not coincident for the investigated airfoil geometry, it exhibits coupled bending-bending-torsional-axial motions. Therefore, the mode shapes are identified based on the dominant motion [71].

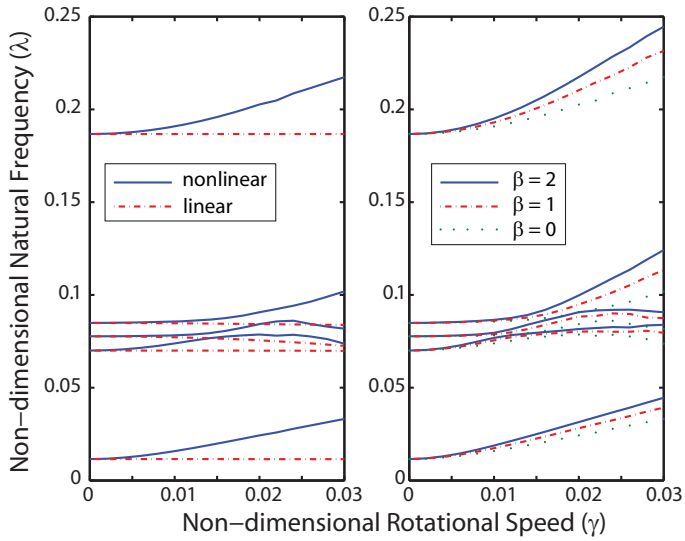

Figure 4.12: **(a)** Rotating blade having an airfoil cross-section, and **(b)** the corresponding mapping procedure.

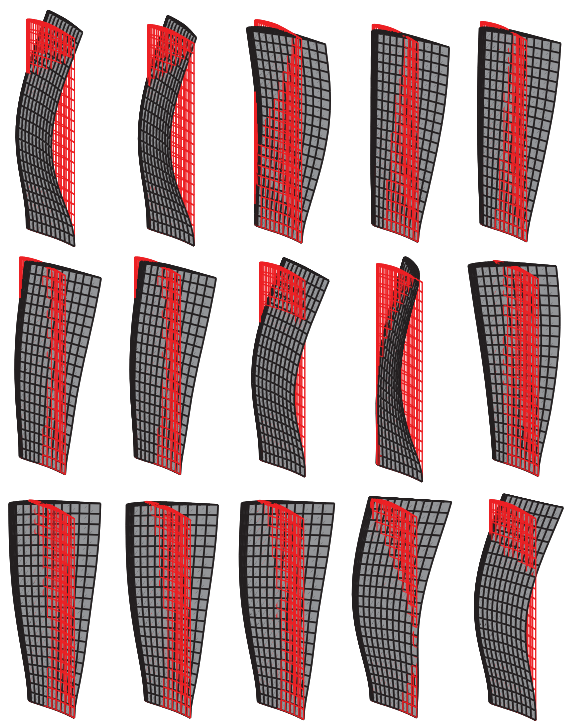

Figure 4.13: The variation of 2nd, 3rd, and 4th mode shapes of the cantilevered rotating blade having aspect ratio of 3 and non-dimensional hub radius of 1 with rotation speed (The rows and columns corresponds to the mode shapes and to the non-dimensional rotation speeds of 0.005, 0.01, 0.015, 0.02, and 0.025 in ascending order from up to down and left to right, respectively). The red lines indicate the undeflected geometries.

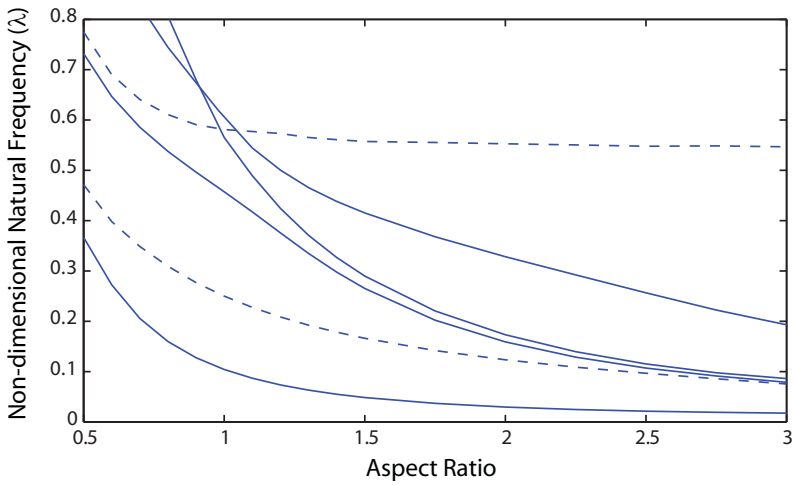

Figure 4.14: Effect of aspect ratio on the non-dimensional natural frequencies of a rotating cantilevered beam having an airfoil geometry where the non-dimensional hub ratio and twist rate are 1 and 0.02, respectively (the solid and dashed lines represent the bending and torsional-axial dominant modes, respectively).

4.3 Summary and Conclusions

This chapter presented the 3D-ST technique to determine the dynamics of rotating structures with general cross-section (including both straight and curved cross-sections) and under mixed boundary conditions. Following the derivation of the IBVP using the 3D-ST technique, two sample case studies were investigated: **(a)** a rotating/spinning parallelepiped having mixed boundary conditions, and **(b)** a rotating cantilevered pretwisted beam with an airfoil geometry. In each case, the convergence of the 3D-ST solution, and the effect of rotational speed on the non-dimensional natural frequencies were studied. Furthermore, the non-dimensional natural frequencies of the rotating/spinning parallelepiped were compared to those obtained from literature or finite elements solution. It is concluded that the presented 3D-ST approach enables accurate and computationally efficient solutions for the three dimensional dynamics of rotating structures with general cross-section under mixed boundary conditions. Due to the completely parameterized and efficient nature of the solution approach, various parametric analysis, which can be a powerful tool in the design stage of rotating structures, can easily be conducted. The 3D-ST approach also enables calculation of the mode shapes that provide important insights into the vibrational characteristics of rotational systems.

The following specific conclusions are drawn from this work:

- The non-dimensional natural frequencies and mode shapes obtained from the presented 3D-ST solution were in excellent agreement with those obtained from literature and finite elements (differences are less than 1%). Although the FEM can accurately predict the dynamics of rotating thin plates and spinning structures, due to the approximation in the calculation of the nonlinear stiffness terms, as the structure gets complex, differences in non-dimensional natural frequencies were observed between the 3D-ST and 3D-FEM approaches for the rotating beam case at high rotational speeds. Furthermore, the computational cost of the 3D-FEM approach is three-to-four times higher than that of the 3D-ST approach.

- The effect of rotation speed on each mode is different: Some modes are affected more than the others and therefore, as the rotation speed increases, frequency crossing or curve veering phenomena where a transition between the mode shapes, are observed.

- The effect of nonlinear (stress-stiffening) terms has a higher impact on the rotating structures than the spinning structures. This is due to the fact that the centrifugal forces create a high stress field along the axial direction of the rotating structures that leads to increase in the bending stiffness of the structure.

- Although the nonlinear terms has a small effect on the dynamics of spinning beams, in the case of spinning beams with alignment errors, the nonlinear terms weaken the structure and try to destabilize it; thereby reducing the maximum rotational speed that the structure can experience.

Chapter 5

Modeling Three-Dimensional Rotational Dynamics of Endmills

"Divide and conquer."

-Philip II, King of Macedon

This chapter presents an analytical modeling approach (the application of the developed 3D-ST technique in Chapters 3 and 4) to predict the 3D dynamics of rotating micro endmill dynamics considering the setup (attachment) errors. Since the fluted section of the cutting tools presents 3D coupled motions such as coupled bending-bending-torsional-axial motions, a 3D solution approach is needed to accurately solve the dynamics of (rotating) micro-tool. However, to simultaneously attain numerical efficiency and modeling accuracy, a unified approach is followed where the circular sections of the tools are modeled using 1D-ST approach (as described in Chapter 2; however adding the effects of the rotational terms) and the fluted section is modeled using 3D-ST approach.

5.1 Model Development

This section describes the derivation of the dynamic model for rotating micro endmills including setup (attachment) errors. Figure 5.1 shows a traditional micro endmill geometry: The overall geometry of a micro endmill include a macro-scale cylindrical shank section, a micro-scale fluted section, and a taper section that connects the macro-scale shank to the micro-scale fluted section.

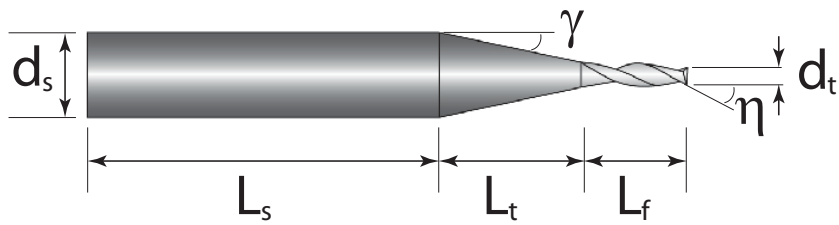

Figure 5.1: Micro endmill geometry and parameters for geometric description.

Having circular cross-sections, the dynamic behavior of the sections other than the fluted section is simplified, resulting in uncoupled axial, torsional, and bending motions. Therefore, one-dimensional (1D) beam equations can accurately capture the dynamic behavior of these sections [27,28]. However, the fluted section has a (complex) curved cross-section and pretwisted geometry resulting in coupled axial-torsional-bending-bending motions, which necessitates a 3D modeling approach [71]. However, in order to simultaneously attain numerical efficiency and modeling accuracy, a unified approach is utilized. In this approach, the fluted section is modeled using a 3D model, whereas 1D models are used for the other sections of the micro endmills. The complete dynamic model for the micro endmill is then obtained through coupling of the individual sections using a component mode synthesis (CMS) approach.

5.1.1 Geometry of micro-endmill including setup errors

While attaching a micro endmill to a spindle, a number of unavoidable (attachment or setup) errors arise due to the imperfections in spindle-collet assembly and manufacturing inaccuracies of the collet or the micro-tool. Figure 5.2 shows the geometry of a commonly used micro-endmill including the attachment errors. These setup errors can be defined as an axial error (spindle axis offset, e) along the spindle axis and two tilts in two perpendicular (xz and xy) planes defined by the angles α (tool tilt angle) and ϕ (tool plane angle). As seen from Fig. 5.2, these errors lead to a static tool-tip runout (r_{ts}).

In deriving the boundary value problem for the presented micro-endmill geometry including setup errors, three reference (coordinate) frames are defined to simplify the problem domain. *First*, a stationary reference frame (XYZ) is defined at point O, where Z axis is aligned with the spindle axis. *Second*, a rotating spindle frame ($\bar{x}\bar{y}\bar{z}$) that rotates with the spindle speed (Ω) about $\bar{z}$ (or Z) axis is introduced. A counter-clockwise rotation matrix around Z axis can be written to describe the relationship between the stationary reference

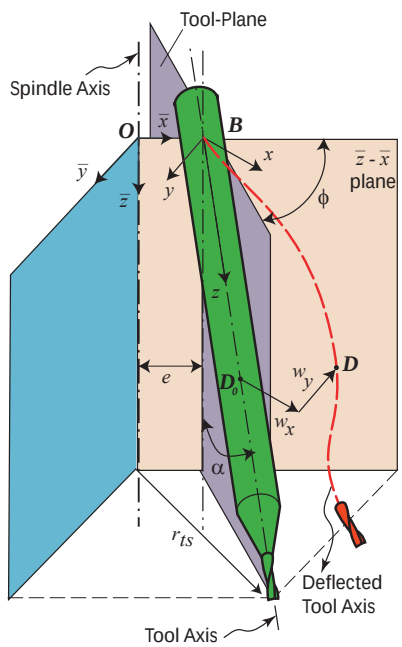

Figure 5.2: Micro-endmill with setup (attachment) errors.

frame and the rotating spindle frame. *Third*, a rotating tool frame (xyz), where z axis is aligned with the micro-endmill axis, is defined. The spindle axis offset (e) is assumed to be along the $\bar{x}$ axis (see Fig. 5.2). To express the relationship between the rotating tool frame and the rotating spindle frame, two consecutive counter-clockwise rotations can be defined using the tool tilt (α) and tool plane angles (ϕ) [30].

5.1.2 Formulation of the boundary value problem

The IBVP governing the dynamics of the structures can be derived using the extended Hamiltons principle [95], which is expressed as

$$\int_{t_1}^{t_2} (\delta E_K - \delta E_S + \delta W_{nc}) dt = 0, \;\; \delta q_i(x, y, z, t) = 0 \;\; \text{at} \;\; t = t_1, t_2. \tag{5.1}$$

Here, E_K, E_S, and W_{nc} represent the kinetic energy, the strain (potential) energy, and the work done by nonconservative forces, respectively, t_1 and t_2 are the two instants of time where the variation is zero (stationary points), x, y, and z are the spatial variables, $\mathbf{q}_i$ represents the generalized coordinate, which corresponds to the ith term of the deflection vector ($\mathbf{q} = \{\mathbf{w_x}; \mathbf{w_y}; \mathbf{w_z}; \psi_\mathbf{x}; \psi_\mathbf{y}; \psi_\mathbf{z}\}$ for the 1D models and $\mathbf{q} = \{\mathbf{u}; \mathbf{v}; \mathbf{w}\}$ for the 3D model), and δ is the variational operator.

To simplify the problem domain, as described earlier a unified modeling approach is

utilized to simultaneously achieve numerical efficiency and modeling accuracy. The regions having circular cross-sections are modeled using Timoshenko beam equations and the fluted section is model using 3D elasticity equations. The following sections describe the modeling approaches for 1D-ST and 3D-ST approaches for rotating micro-endmills.

5.1.2.1 Derivation of the one-dimensional model

Although Chapter 2 presents the derivation of a simple Timoshenko beam, here to be compatible with the 3D model of the fluted section, each point in the cylindrical sections (that are modeled using 1D-ST) needs to have six degrees of freedom. Therefore, to derive the IBVP for 1D models, Timoshenko beam equations are used together with the strain and kinetic energy equations for axial and torsional motions [27, 28]. Accordingly, the potential energy of an axisymmetric beam can be written as

$$\begin{aligned} V =& \frac{1}{2}\int_0^L \Bigg\{ EI(z)\left(\frac{\partial \psi_x}{\partial z}\right)^2 + EI(z)\left(\frac{\partial \psi_y}{\partial z}\right)^2 + EA(z)\left(\frac{\partial w_z}{\partial z}\right)^2 + GJ(z)\left(\frac{\partial \psi_z}{\partial z}\right)^2 \\ &+ k_s GA(z)\left[\left(\frac{dw_x}{dz} - \psi_y\right)^2 + \left(\frac{dw_y}{dz} + \psi_x\right)^2\right]\Bigg\} dz, \end{aligned} \tag{5.2}$$

where $\mathbf{q} = \{\mathbf{w_x}\,;\mathbf{w_y}\,;\mathbf{w_z}\,;\psi_\mathbf{x}\,;\psi_\mathbf{y}\,;\psi_\mathbf{z}\}$ are the deflections corresponding to six degrees of freedom (three displacements and three rotations about the axis of the cross-section), L is the length of the beam, E is the Young's modulus, $I(z)$ is the second area moment, $A(z)$ is the area of the beam along the z axis, G is the shear modulus, $J(z)$ is the polar moment of inertia, and k_s is the shear constant.

The kinetic energy of a beam is the combination of translational (T_t) and rotational (T_r) kinetic energies and can be expressed as

$$\begin{aligned} T &= T_t + T_r \\ &= \frac{1}{2}\int_0^L m(\mathbf{v}_D \cdot \mathbf{v}_D)dz + \frac{1}{2}\int_0^L \rho(I\omega_1^2 + I\omega_2^2 + J\omega_3^2)dz\,. \end{aligned} \tag{5.3}$$

Here, m is the mass per unit length (i.e., $m = \rho\, A$), ρ is the density of the beam, $\mathbf{v}_D$ is the velocity of any point along the beam length, and w_1, w_2, and w_3 are the components of the rotational velocity vector, w_r, that is applied to the center of the tool cross-section on the $t_1t_2t_3$ frame subjected to rotary vibrations (see Fig. 5.3) [30].

To find the velocity vector (in Eq. (5.3)), $\mathbf{v}_D$, the position vector for any point in the deflected micro-endmill should be written with respect to the origin of the spindle frame,

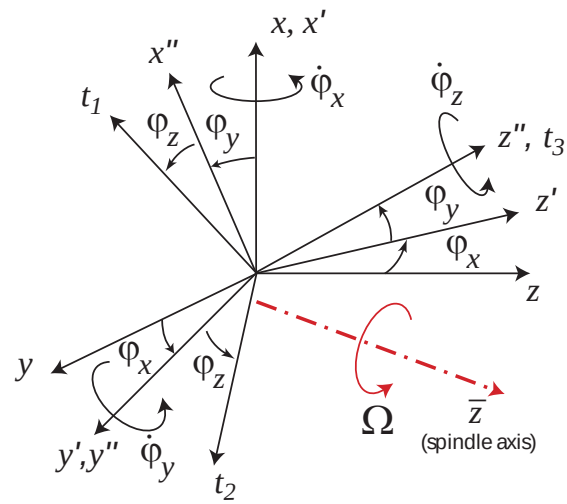

Figure 5.3: Moving frame and rotating tool frame related through bending (ψ_x and ψ_y) and torsion (ψ_z) angles.

O. For instance, the position vector of point D (see Fig. 5.2) can be defined as,

$$\mathbf{r}_{OD} = e\,\mathbf{i}_{\overline{x}} + w_{x_D}\,\mathbf{i}_x + w_{y_D}\,\mathbf{i}_y + (z_D + w_{z_D})\,\mathbf{i}_z, \tag{5.4}$$

where $\mathbf{i_j}$ is the unit vector associated with the j direction, z_D is the (initial) geometric location of point D along the beam length, and w_{x_D}, w_{y_D}, and w_{z_D} are the deflection amounts of point D in the rotating tool (or xyz coordinate) frame. Then, the velocity of point D can be found following same derivation as given in Eqs. (4.11)-(4.13).

For the second part of Eq. (5.3), the components of the rotational velocity (w_1, w_2, and w_3) can be found from three consecutive coordinate transformations relating the xyz coordinate frame to $t_1t_2t_3$ coordinate frame. Thus, the rotational vector can be expressed as

$$\omega_{\mathbf{r}} = \dot{\psi}_x\mathbf{i}_x + \dot{\psi}_y\mathbf{i}_{y'} + \dot{\psi}_z\mathbf{i}_{t_3} + \Omega\mathbf{i}_{\overline{z}} = \omega_1\mathbf{i}_{t_1} + \omega_2\mathbf{i}_{t_2} + \omega_3\mathbf{i}_{t_3}. \tag{5.5}$$

The transformation matrix relating the xyz coordinate frame to $t_1t_2t_3$ coordinate frame can be written as

$$\begin{Bmatrix} i_{i_{t_1}} \\ i_{i_{t_2}} \\ i_{i_{t_3}} \end{Bmatrix} = \begin{bmatrix} \cos(\psi_z) & \sin(\psi_z) & 0 \\ -\sin(\psi_z) & \cos(\psi_z) & 0 \\ 0 & 0 & 1 \end{bmatrix} \begin{bmatrix} \cos(\psi_y) & 0 & -\sin(\psi_y) \\ 0 & 1 & 0 \\ \sin(\psi_y) & 0 & \cos(\psi_y) \end{bmatrix} \begin{bmatrix} 1 & 0 & 0 \\ 0 & \cos(\psi_x) & \sin(\psi_x) \\ 0 & -\sin(\psi_x) & \cos(\psi_x) \end{bmatrix} \begin{Bmatrix} i_x \\ i_y \\ i_z \end{Bmatrix}. \tag{5.6}$$

Here, three axis body-fixed Eulerian angles are used to describe rotation of the micro-endmill

about two orthogonal directions —bending rotation, ψ_x, around x axis that transforms the xyz frame to the $x'y'z'$ frame and bending rotation, ψ_y, around y' axis that transforms the $x'y'z'$ frame to the $x''y''z''$ frame—and a torsional rotation, ψ_z, around z'' axis that transforms the $x''y''z''$ frame to the $t_1t_2t_3$ frame (see Fig. 5.3). Using the coordinate transformation matrix defined in Eqs. (5.5) and (5.6), the rotational speeds ω_1, ω_2, and ω_3 can be expressed as

$$\begin{aligned} w_1 =& \dot{\psi}_x \cos\psi_y \cos\psi_z + \dot{\psi}_y \sin\psi_z - \Omega \sin\alpha \cos\psi_y \cos\psi_z \\ &+ \Omega \cos\alpha (\sin\psi_x \sin\psi_z - \cos\psi_x \cos\psi_z \sin\psi_y)\,, \end{aligned} \tag{5.7}$$

$$\begin{aligned} w_2 =& -\dot{\psi}_x \cos\psi_y \sin\psi_z + \dot{\psi}_y \cos\psi_z + \Omega \sin\alpha \cos\psi_y \sin\psi_z \\ &+ \Omega \cos\alpha (\cos\psi_z \sin\psi_x + \cos\psi_x \sin\psi_y \sin\psi_z)\,, \end{aligned} \tag{5.8}$$

$$w_3 = \dot{\psi}_x \sin\psi_y + \dot{\psi}_z - \Omega \sin\alpha \sin\psi_y + \Omega \cos\alpha \cos\psi_x \cos\psi_y\,. \tag{5.9}$$

Lastly, the work done by non-conservative forces can be given as

$$W_{nc} = \int_0^L \left(\mathbf{f_x}^T \mathbf{w_x} + \mathbf{f_y}^T \mathbf{w_y} + \mathbf{f_z}^T \mathbf{w_z} \right) dz\,, \tag{5.10}$$

where $\mathbf{f_x}$, $\mathbf{f_y}$, and $\mathbf{f_z}$ are the external forces in the x, y, and z directions, respectively.

After deriving the energy terms and the work done by non-conservative forces, the extended Hamilton's principle is used to obtain the integral boundary value problem (IBVP) for rotating micro-endmill dynamics as

$$\begin{aligned} \int_{t_1}^{t_2} \Bigg\{ \int \Big\{ & \rho \ddot{\mathbf{q}}^T \mathbf{N_M^{1D}} \delta\mathbf{q} + 2\rho\Omega \dot{\mathbf{q}}^T \mathbf{N_{C_{cor}}^{1D}} \delta\mathbf{q} + \mathbf{q}^T \mathbf{N_K^{1D}} \delta\mathbf{q} - \rho\Omega^2 \mathbf{q}^T \mathbf{N_{K_{spin}}^{1D}} \delta\mathbf{q} \\ & - \rho\Omega^2 \mathbf{q_{ip}}^T \mathbf{N_{F_c}^{1D}} \delta\mathbf{q} - \mathbf{n_{F_c}^{1D}}^T \delta\mathbf{q} \Big\} dz - \mathbf{f_b}^T \delta\mathbf{q_b} \Bigg\} dt = 0. \end{aligned} \tag{5.11}$$

where $\mathbf{N_M^{1D}}$, $\mathbf{N_{C_{cor}}^{1D}}$, $\mathbf{N_{K_{spin}}^{1D}}$, $\mathbf{N_{K_{spin}}^{1D}}$, $\mathbf{N_{F_c}^{1D}}$, and $\mathbf{n_{F_c}^{1D}}$ are the operator system matrices for mass, coriolis, stiffness, and spin-softening matrices, and centrifugal and external forcing vectors for the 1D case, respectively, and $\mathbf{q_{ip}} = \{\mathbf{0}; \mathbf{0}; \mathbf{z}; \mathbf{0}; \mathbf{0}; \mathbf{0}\}$ is the vector of the initial (geometric) positions for each point within the structure. The operator system matrices given in Eq. (5.11) can be expressed as

$$\mathbf{N_M^{1D}} = \begin{bmatrix} A\mathbf{I} & \mathbf{0} & \mathbf{0} & \mathbf{0} & \mathbf{0} & \mathbf{0} \\ \mathbf{0} & A\mathbf{I} & \mathbf{0} & \mathbf{0} & \mathbf{0} & \mathbf{0} \\ \mathbf{0} & \mathbf{0} & A\mathbf{I} & \mathbf{0} & \mathbf{0} & \mathbf{0} \\ \mathbf{0} & \mathbf{0} & \mathbf{0} & I\mathbf{I} & \mathbf{0} & \mathbf{0} \\ \mathbf{0} & \mathbf{0} & \mathbf{0} & \mathbf{0} & I\mathbf{I} & \mathbf{0} \\ \mathbf{0} & \mathbf{0} & \mathbf{0} & \mathbf{0} & \mathbf{0} & J\mathbf{I} \end{bmatrix}, \tag{5.12}$$

$$\mathbf{N_{C_{cor}}^{1D}} = \begin{bmatrix} \mathbf{0} & -A\cos(\alpha)\mathbf{I} & \mathbf{0} & \mathbf{0} & \mathbf{0} & \mathbf{0} \\ A\cos(\alpha)\mathbf{I} & \mathbf{0} & A\sin(\alpha)\mathbf{I} & \mathbf{0} & \mathbf{0} & \mathbf{0} \\ \mathbf{0} & -A\sin(\alpha)\mathbf{I} & \mathbf{0} & \mathbf{0} & \mathbf{0} & \mathbf{0} \\ \mathbf{0} & \mathbf{0} & \mathbf{0} & \mathbf{0} & \mathbf{0} & \mathbf{0} \\ \mathbf{0} & \mathbf{0} & \mathbf{0} & \mathbf{0} & \mathbf{0} & I\sin(\alpha)\mathbf{I} \\ \mathbf{0} & \mathbf{0} & \mathbf{0} & \mathbf{0} & -I\sin(\alpha)\mathbf{I} & \mathbf{0} \end{bmatrix}, \tag{5.13}$$

$$\mathbf{N_K^{1D}} = \begin{bmatrix} k_s GA\mathbf{Q_1}^T\mathbf{Q_1} & \mathbf{0} & \mathbf{0} & \mathbf{0} & -k_s GA\mathbf{Q_1} & \mathbf{0} \\ \mathbf{0} & k_s GA\mathbf{Q_1}^T\mathbf{Q_1} & \mathbf{0} & k_s GA\mathbf{Q_1} & \mathbf{0} & \mathbf{0} \\ \mathbf{0} & \mathbf{0} & EA\mathbf{Q_1}^T\mathbf{Q_1} & \mathbf{0} & \mathbf{0} & \mathbf{0} \\ \mathbf{0} & k_s GA\mathbf{Q_1} & \mathbf{0} & k_s GA\mathbf{I} + EI\mathbf{Q_1}^T\mathbf{Q_1} & \mathbf{0} & \mathbf{0} \\ -k_s GA\mathbf{Q_1} & \mathbf{0} & \mathbf{0} & \mathbf{0} & k_s GA\mathbf{I} + EI\mathbf{Q_1}^T\mathbf{Q_1} & \mathbf{0} \\ \mathbf{0} & \mathbf{0} & \mathbf{0} & \mathbf{0} & \mathbf{0} & GJ\mathbf{Q_1}^T\mathbf{Q_1} \end{bmatrix}, \tag{5.14}$$

$$\mathbf{N_{K_{spin}}^{1D}} = \begin{bmatrix} A\cos^2(\alpha)\mathbf{I} & \mathbf{0} & \frac{1}{2}\sin 2\alpha\mathbf{I} & \mathbf{0} & \mathbf{0} & \mathbf{0} \\ \mathbf{0} & A\mathbf{I} & \mathbf{0} & \mathbf{0} & \mathbf{0} & \mathbf{0} \\ \frac{1}{2}\sin 2\alpha\mathbf{I} & \mathbf{0} & A\sin^2(\alpha)\mathbf{I} & \mathbf{0} & \mathbf{0} & \mathbf{0} \\ \mathbf{0} & \mathbf{0} & \mathbf{0} & -I\cos^2(\alpha)\mathbf{I} & \mathbf{0} & \mathbf{0} \\ \mathbf{0} & \mathbf{0} & \mathbf{0} & \mathbf{0} & I\left[\sin^2(\alpha) - \cos^2(\alpha)\right]\mathbf{I} & \mathbf{0} \\ \mathbf{0} & \mathbf{0} & \mathbf{0} & \mathbf{0} & \mathbf{0} & J\sin(\alpha)\mathbf{I} \end{bmatrix}, \tag{5.15}$$

$$\mathbf{N}_{\mathbf{F_c}}^{\mathbf{1D}} = \begin{bmatrix} \mathbf{0} & \mathbf{0} & \mathbf{0} & \mathbf{0} & \mathbf{0} & \mathbf{0} \\ \mathbf{0} & \mathbf{0} & \mathbf{0} & \mathbf{0} & \mathbf{0} & \mathbf{0} \\ \mathbf{0} & \mathbf{0} & A\sin^2(\alpha)\mathbf{I} & \mathbf{0} & \mathbf{0} & \mathbf{0} \\ \mathbf{0} & \mathbf{0} & \mathbf{0} & \mathbf{0} & \mathbf{0} & \mathbf{0} \\ \mathbf{0} & \mathbf{0} & \mathbf{0} & \mathbf{0} & \mathbf{0} & \mathbf{0} \\ \mathbf{0} & \mathbf{0} & \mathbf{0} & \mathbf{0} & \mathbf{0} & \mathbf{0} \end{bmatrix}, \tag{5.16}$$

$$\mathbf{n}_{\mathbf{F_c}}^{\mathbf{1D}} = \begin{Bmatrix} \rho A\Omega^2 e\cos\alpha\cos\phi\,\mathbb{i} \\ -\rho A\Omega^2 e\sin\phi\,\mathbb{i} \\ \rho A\Omega^2 e\sin\alpha\cos\phi\,\mathbb{i} \\ \mathbb{0} \\ -\frac{1}{2}\rho I\sin 2\alpha\,\mathbb{i} \\ \mathbb{0} \end{Bmatrix}. \tag{5.17}$$

5.1.2.2 Derivation of the three-dimensional model

In deriving the IBVP for the 3D case, 3D elasticity equations are used. The details of the derivation procedure is given in Chapter 4.

5.1.3 Solution of the integral boundary value problem

To solve the dynamics of the rotating micro-endmill, first, the boundary value problems given in Eq. (5.11) for the 1D case and Eq. (4.17) for the 3D case are discretized through the ST technique. For the circular sections (that are modeled using Timoshenko beam equations), the 1D-ST approach described in Chapter 2 and for the fluted section (that is modeled using 3D elasticity equations), the 3D-ST approach described in Chapter 3 is used.

5.1.4 System matrices for the entire micro-endmill

To obtain the complete model for the micro-endmill, a component mode synthesis technique is used to combine the dynamics of each individual section. Note that the cylindrical sections are modeled using 1D-ST approach; thus to express a three dimensional behavior, each point along the tool length has six degrees of freedom (three displacements and three angles). However, the 3D-ST technique provides three deflection components for each sampling point distributed within the cross-section. The component mode synthesis technique equates the

shared boundary through compatibility equations (i.e., displacement and slope compatibility conditions).

The compatibility equations for the boundaries between the 1D models are written simplify by equating the degrees of freedom at the connection boundaries of the coupled sections. However, to relate the three displacement degrees of freedom, $\{\mathbf{u};\ \mathbf{v};\ \mathbf{w}\}$, coming from the 3D-ST approach to the six degrees of freedom, $\{\mathbf{w_x};\ \mathbf{w_y};\ \mathbf{w_z};\ \phi_\mathbf{x};\ \phi_\mathbf{y};\ \phi_\mathbf{z}\}$, coming from the 1D-ST approach for each point (x, y) within the cross-section (at the shared boundary), compatibility equations can be written as

$$\{\mathbf{u};\ \mathbf{v};\ \mathbf{w}\} = \{\mathbf{w_x} - y\phi_\mathbf{z};\ \mathbf{w_y} + x\phi_\mathbf{z};\ \mathbf{w_z} + x\phi_\mathbf{y} + y\phi_\mathbf{x}\} \tag{5.18}$$

by assuming small angle assumption.

The IBVP approach eliminates the necessity to impose natural boundary conditions; however, the essential boundary conditions should be imposed to the combined system equations. To impose the essential boundary conditions, basis recombination [29] approach is used as described in the previous chapter:

$$\mathbf{q} = \mathbf{P}\mathbf{q_d} + \mathbf{R}\mathbf{q_b}\,. \tag{5.19}$$

Here, $\mathbf{P}$ and $\mathbf{R}$ are the projection matrices, $\mathbf{q_d}$ is the deflection vector within the domain, and $\mathbf{q_b}$ is the deflection vector on the boundary.

After applying the projection matrices to the combined system equations, the system equations for the complete micro-endmill can be found. For instance, for a micro-endmill, the system equations are expressed as

$$\mathbb{M}\{\ddot{q}_d\} + (\mathbb{C} + \mathbb{C}_{\mathbb{cor}})\{\dot{q}_d\} + (\mathbb{K} - \mathbb{K}_{\mathbb{spin}})\{q_d\} = \mathbb{F} \tag{5.20}$$

where $\mathbb{M}$, $\mathbb{C}$, $\mathbb{C}_{\mathbb{cor}}$, $\mathbb{K}$, $\mathbb{K}_{\mathbb{spin}}$, and $\mathbb{F}$ are the global mass, damping, coriolis, stiffness, and spin-softening matrices, and force vector, respectively, and can be expressed as

$$\mathbb{\Lambda}_i = \mathbf{P}^T \begin{bmatrix} \Lambda_{i_{shank}} & 0 & 0 \\ 0 & \Lambda_{i_{taper}} & 0 \\ 0 & 0 & \Lambda_{i_{flute}} \end{bmatrix} \mathbf{P} \tag{5.21}$$

$$\mathbb{F} = \mathbf{P}^T \begin{Bmatrix} F_1 \\ F_2 \\ F_3 \end{Bmatrix} \tag{5.22}$$

where $\mathbb{A}_i = \mathbb{M}, \mathbb{C}, \mathbb{G}, \mathbb{K}$, or $\mathbb{B}$. Once the global system matrices are found, the natural frequencies of a rotating micro-endmill can be found using state-space formulation.

5.2 Model Application

In this section, the application of the described technique for solving rotating micro-endmills including setup (attachment) errors is described. To this end, both two-fluted and four-fluted micro-endmills, were considered. To get the actual cross-section geometry for the fluted regions —that is needed to accurately model the micro-endmills—, the micro-endmills were cut by electron discharge machining (EDM) along several locations along the fluted section and then cross-section of each section is measured by scanning electron microscopy (SEM). The SEM images were then analyzed by MATLAB® image-processing toolbox to identify the boundaries (periphery of the cross-section), and sample points along the periphery were extracted to define the (curved) cross-section [27, 107]. Figure 5.4 shows sample SEM images of two-fluted and four-fluted micro-endmills.

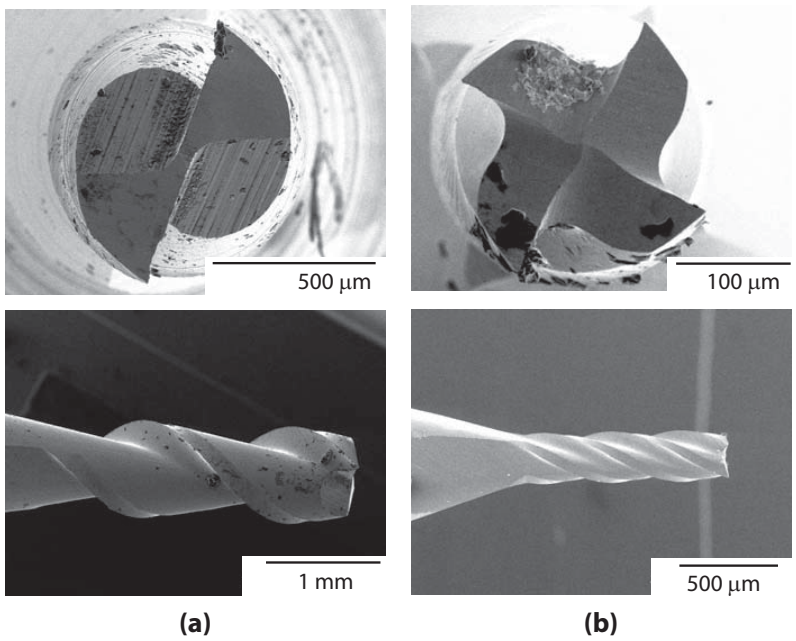

Figure 5.4: SEM images of micro-tools: **(a)** two-fluted endmill and **(b)** four-fluted endmill.

The natural frequencies and mode shapes were calculated using the global system matrices. For each tool, *first*, a convergence study was performed by varying the number of polynomials as described in detail in Section 3.5.1. *Second*, to assess the precision of the presented solution technique, the natural frequencies and mode shapes were compared to

those found from a commercial finite element (FE) solver (in this study, ANSYS® version 14.5 is used). To ensure the accuracy of the FE solutions (and also to determine the sufficient element number), a convergence study was also performed with increased number of elements. The convergence is considered to be reached when the maximum difference in natural frequencies for the first ten modes is less than 0.1% in two consecutive simulations. *Third*, the effect of rotational speed on the dynamics of micro-endmills was investigated. And *lastly*, the response of micro-endmills to harmonic forces was studied under various attachment conditions.

5.2.1 Comparison with finite element method

In this section, the presented solution technique is applied to predict the natural frequencies and mode shapes of of rotating micro-endmills having different geometries. Table 5.1 shows the geometric parameters of the micro-endmills used for the comparison study. The natural frequencies are obtained using the global system matrices. To ensure the accuracy of the 3D-ST solutions and to select the optimum number of polynomials, a convergence study is performed and the polynomial numbers for the shank, taper, and fluted sections are selected as $N_z = 19$, $N_z = 21$, and N_x-N_y-$N_z = 7 - 7 - 13$, respectively.

Table 5.1: Geometric properties of the micro-endmills used for comparison study.

Tool	Number of Flutes	d_s (mm)	L_s (mm)	γ (deg.)	d_t (μm)	L_f (mm)	η (deg.)
ME-1	2	3.175	30.83	12.3	811	2.7	46.8
ME-2	2	3.175	29.75	11.5	544	1.8	30.0
ME-3	4	3.175	30.80	13.6	245	1.0	28.0

To assess the precision of the presented solution approach, first, the natural frequencies and then the mode shapes found from the 3D-ST solution were compared to those found by a commercial FE solver (ANSYS® version 14.5 with SOLID187 3D 10-node tetrahedral structural solid elements). Based on the FEM convergence study, 60,000 elements were used in modeling the micro-endmills.

Table 5.2 shows the first ten natural frequencies found using the 3D-ST approach and the percent differences between the 3D-ST and FEM results for the micro-endmills listed in Table 5.1. The maximum difference is 1.1 % (taking the FEM solution as reference) for the 6th (torsional-axial[11]) mode for ME-1. The average difference over the first ten modes

[11]Due to the pretwisted nature of the fluted section, the torsional and axial modes are coupled. In other

Table 5.2: Comparison of natural frequencies (in Hz) obtained by 3D-ST and FEM approaches for micro-endmills listed in Table 5.1.

	ME-1		ME-2		ME-3	
Tool	ST	FEM	ST	FEM	ST	FEM
1	15300	15302	16151	16150	15618	15740
2	15306	15305	16255	16151	15814	15740
3	38908	38843	41612	41613	40877	41174
4	39171	39116	41637	41647	41355	41175
5	53121	52624	65308	65301	63561	63683
6	57402	56782	70343	70024	74995	75487
7	63547	63359	72535	72369	75802	75488
8	76248	76232	83742	83366	95859	95859
9	77262	77170	90452	89711	113540	113830
10	94938	94947	97634	97636	114647	113870

for all five micro-endmills is 0.3%. Note that the computational cost of the 3D-ST solution is one-to-two orders of magnitude less than that of the FEM solution.

Next, to qualitatively compare the mode shapes obtained from the 3D-ST solution and FEM solutions, a modal assurance criterion (MAC) analysis was performed. The MAC is a measure of consistency of the modal vectors calculated from two different approaches. In literature, the threshold for MAC value is 0.8 to consider a satisfactory consistency between the mode shapes [100]. Clearly, a higher MAC number indicates better consistency between the mode shapes, and when the two mode shapes (obtained from two different solution approaches) are identical, a MAC value of unity is obtained. In this study, to calculate the MAC values, the modal matrices calculated in ANSYS® and in 3D-ST solutions were extracted. Then, using the obtained modal vectors, MAC values for each mode was calculated (for the details of this analysis, the reader is referred to [71]). According to this analysis, an average MAC value of 0.9977 and a minimum MAC value of 0.9927 were obtained for the modeled micro-endmills. Therefore, it can be concluded that the mode shapes obtained from the 3D-ST and FEM solutions are in excellent agreement.

5.2.2 Effect of rotational speed

To investigate the effect of rotational speed on the dynamics of micro-endmills, the natural frequencies and mode shapes were calculated at nine different spindle speeds ranging from 1 kHz to 10 kHz. Furthermore, the results were compared to those found from ANSYS®. The FE model of micro-endmills were constructed using solid elements (SOLID187) that

words, the beam untwists under tensile axial loading, or twists under compressive axial loading

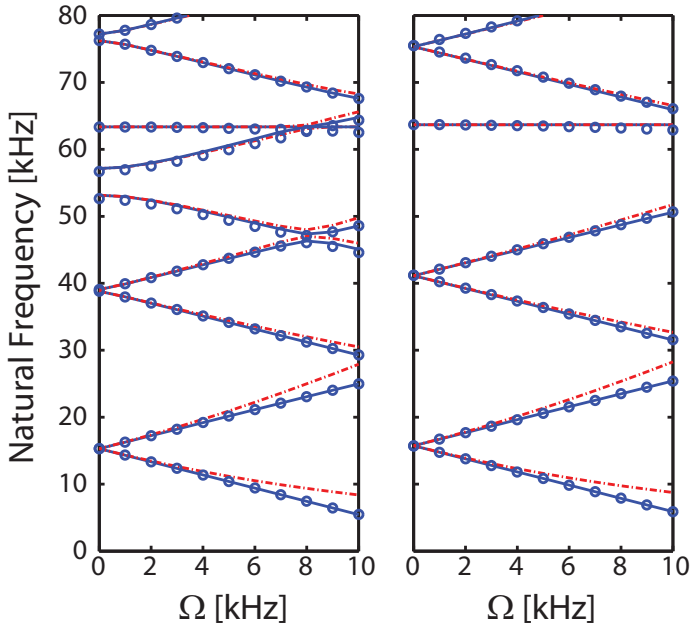

Figure 5.5: Change of damped natural frequencies with rotational speed for **(a)** ME-1 and **(b)** ME-3.

can incorporate the coriolis and centrifugal softening effects in rotating tool frame. For this analysis, two micro-endmills (ME-1 and ME-3 listed in Table 5.1) were used. Figure 5.5 shows the (damped) natural frequencies of micro-endmills with increasing spindle speed.

Important observations can be made from Fig. 5.5. *First*, the calculated natural frequencies are in excellent agreement with ANSYS® results. *Second*, as a result of coriolis forces (that are proportional to the rotation velocity and results in a skew symmetric damping matrix), the undamped natural frequencies split into two: forward and backward modes. As the natural frequencies of the forward modes increase, the natural frequencies of the backward modes decrease with increasing rotational speed. *Third*, since the rotating micro-endmills experience centrifugal forces (that are proportional to the square of rotation velocity) that are trying to destabilize the structure, the apparent stiffness decreases; thus results in a decrease in natural frequencies. And *lastly*, a frequency crossing phenomena is observed where transitions of mode shapes occurs between the third and fourth modes and sixth and seventh modes. To illustrate this phenomenon explicitly, first seven mode shapes were calculated and plotted as shown in Fig. 5.6. As observed, two transitions occur between the fourth and fifth mode shapes and between the sixth and seventh mode shapes.

In addition to the comparison of natural frequencies, the mode shapes obtained from the presented solution approach and FEM solutions were compared qualitatively through MAC analysis and a minimum MAC value of 0.9895 for torsional-axial dominant mode and

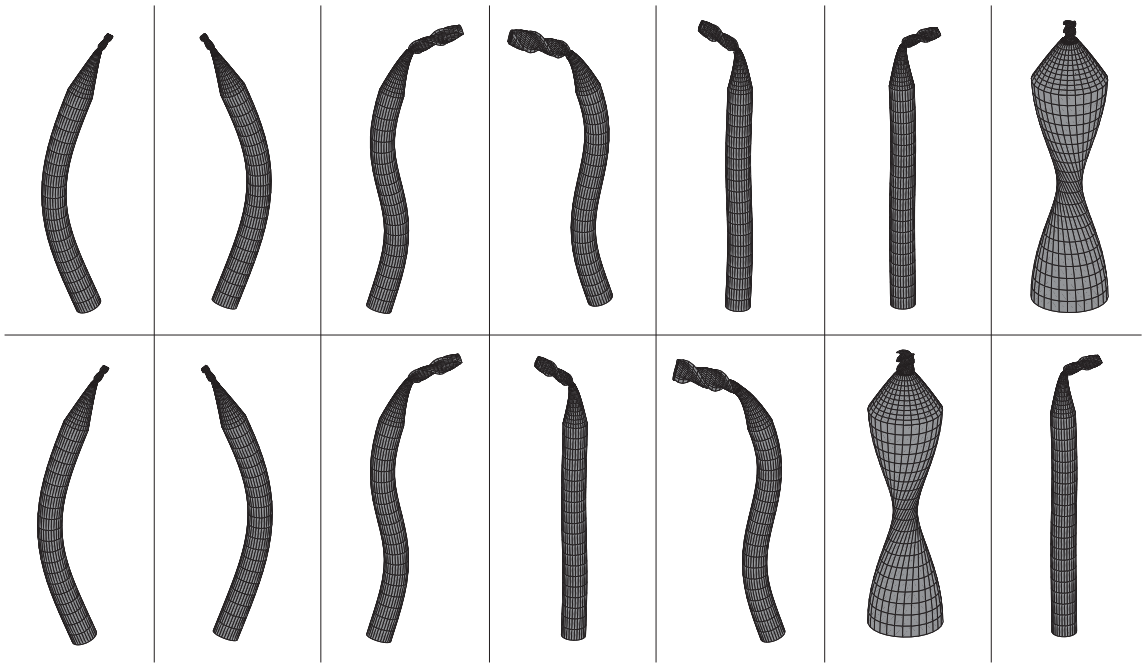

Figure 5.6: The first seven mode shapes of an unconstrained rotating tool for $\Omega = 5000$ Hz (upper row) and $\Omega = 10000$ Hz (lower row).

an average MAC value of 0.9997 was obtained. As a result, it can be concluded that the mode shapes obtained from the 3D-ST and FEM solutions are in excellent agreement.

5.2.3 Effect of attachment(setup) errors and response of micro-endmills

In reality, due to the tool-spindle centering errors (tool attachment errors), tool-tip trajectory deviates from the ideal trajectory. This deviation is commonly referred as tool-tip runout [20]. As shown in Fig. 5.2, the tool attachment errors can be defined by an eccentricity (spindle axis offset, e) and two tilt angles (α, tool tilt angle, and ϕ, tool plane angle). It has been shown in literature that tool attachment errors have a profound effect on the dynamics of the micro-endmills [20, 30].

The motion of the tool-tip is illustrated in Fig. 5.7 and can be decomposed into three parts:

1. Due to the attachment errors (eccentricity and tilt errors - also referred as the *centering errors* [20]), the geometric axis of the tool is displaced from the axis average line. From a quasi-static point of view (i.e., when the spindle is rotated at very low speeds), this alteration in axis average line causes the tool tip to rotate in a circular path, whose diameter is larger than the diameter of the tool. This motion is described as the static

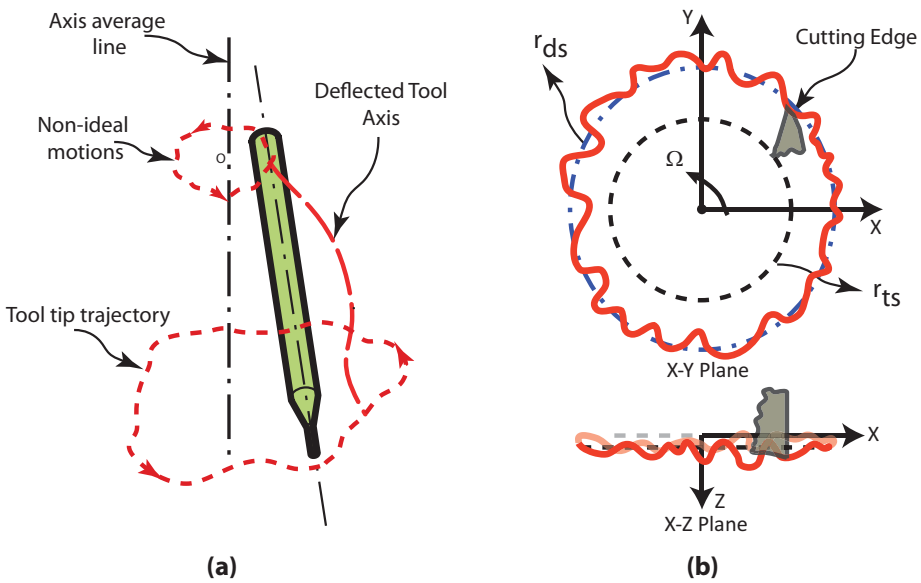

Figure 5.7: Schematics depicting the motion of the tool-tip.

tool-tip runout (r_{ts}).

2. As the spindle (rotation) speed increases (i.e., from a dynamic point of view), the centrifugal forces start to act on the micro-tool, creating a rotating unbalance phenomenon. Since these centrifugal forces are static (time invariant), they shift the equilibrium position of the micro-tool; thereby resulting in a circular motion with a larger diameter than the quasi-static case, which is described as the dynamic tool-tip runout (r_{td}) as shown in Fig. 5.7(b). Note that here the radial stiffness of the spindle is assumed to be uniform circumferentially.

3. Lastly, when the micro-tool is subjected to external (cutting) forces, it starts to oscillate around the dynamic tool-tip runout as shown by the solid red line in Fig. 5.7.

To investigate the effect of tool attachment errors on the motion/response of tool tip, the motion of the tool tip point was calculated for various eccentricity, tool tilt angle, and tool plane angle values (see Table 5.3 due to a harmonic forcing. Although, in reality this harmonic force is a combination of spindle frequency, tooth passing frequency and its harmonics, here only the response due to a single frequency harmonic force was investigated. Thus, the harmonic force assumed to be acting on the tip point of the micro-tool, and have an amplitude, F_0, and a frequency, f, acting of the x and y directions simultaneously (with a phase difference of 90°).

Table 5.3: Tool attachment values used in this study.

Case No.	Eccentricity (e) [μm]	Tool tilt angle (α) [$deg.$]	Tool plane angle (ϕ) [$deg.$]	Spindle speed [Hz]	Forcing frequency [Hz]
1	0.75	0.005	90	2000	4000
2	0.75	0.005	90	4000	8000
3	1.5	0.0025	90	2000	4000
4	1.5	0.0025	90	2000	8000
5	0.5	0.001	90	2000	4000
6	1.0	0.001	90	2000	4000

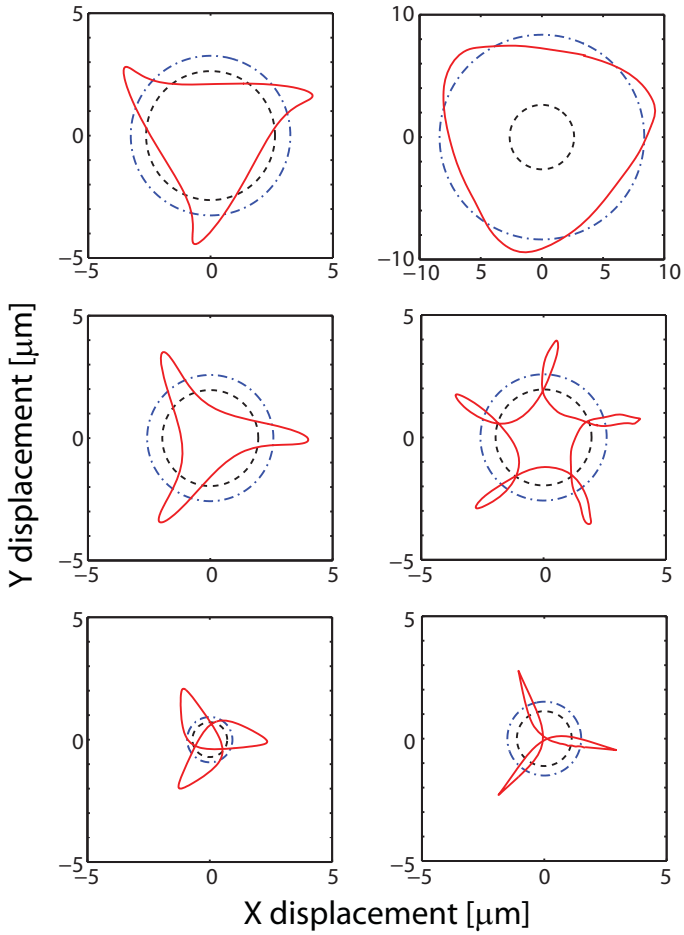

Figure 5.8: Orbital vibrations for the steady-state harmonic response. Dashed black, dashed dotted blue, and solid red lines show the static and dynamic tool-tip runout, and orbital motions, respectively..

In this preliminary analysis, six different cases were considered (see Table 5.3). As seen, four different tool attachment cases at different spindle speeds and tooth-passing frequencies (i.e., forcing frequencies) were investigated. Figure 5.8 shows the static tool-tip

runout, dynamic tool-tip runout, and orbital motions of the tool tip. As observed, quite interesting orbital motions were observed arising from the coupling between the rotational and forcing frequencies. However, note that these orbital shapes may be different during an actual machining operation due to the coupling between the dynamics of the system and mechanistic of the machining process.

5.3 Summary and Conclusions

This chapter presented the application of the analytical (unified) modeling approach developed in Chapters 3 and 4 and in [29,30] to predict the 3D dynamics of rotating micro tools considering the attachment errors. The natural frequencies of a micro endmill were investigated as a function of spindle speed and the results are found to be in excellent agreement to those obtained from a FE solver (maximum difference is less than 1% in any mode at any spindle speed). Furthermore, the system matrices obtained using the presented approach were used to model the dynamic behavior in response to arbitrary force inputs, and thus, orbital motions of the micro endmill tip was investigated for different tool attachment configurations and at different spindle speeds and tooth-passing frequencies.

Chapter 6

An Impact Excitation System for Repeatable, High Bandwidth Modal Testing of Miniature Structures

"If you can not do great things, do small things in a great way."

-Napoleon Hill

This chapter presents the design and evaluation of an impact excitation system (IES) for repeatable, high-bandwidth, and controlled-force modal testing of miniature structures. The technical contribution of the work presented in this chapter, is the tailored-made impact excitation system that enables repeatable (in terms of the impact bandwidth, location, and force magnitude) modal testing of (miniature and compliant) structures, while providing a high excitation-bandwidth and excellent coherence values, which constitutes the experimental foundation for the further research on the characterization of the speed-dependent dynamics of miniature UHS spindles.

6.1 Introduction

Miniature components and devices have been utilized increasingly in many fields to realize the advantages of miniaturization [6, 88]. Some current applications for miniature devices

include miniature turbines and motors, miniature molds and dies, miniature robots, miniature unmanned aerial vehicles, and miniature sensors. In this work, the miniature systems refer to those that are of small size, and more specifically, those that exhibit high natural frequencies (commonly first dominant mode above 1 kHz) and that are fragile in nature. For instance, to characterize the dynamics of miniature UHS spindles used in mechanical micromachining, the bandwidth of the dynamic excitation is required to reach 25 kHz, and the excitation amplitude should be limited (e.g., $\leq 20N$) to prevent damage to the bearings [77]. Since the structural dynamics behavior of miniature structures is critical to the functionality and performance of many systems, experimental techniques for accurate characterization of the dynamics of miniature structures are important for reliable design and performance evaluation, as well as to verify numerical and analytical models [93, 100, 108–110].

In the last few decades, expansive efforts have been devoted to developing modal testing techniques for larger structures. Modal testing involves exciting the structure with a known (or measured) force and measuring the ensuing response. One of the most common modal testing techniques involves exciting the structure by applying an impulsive force using an instrumented impact hammer [100, 111]. The ensuing transient response is then recorded using accelerometers or non-contact methods such as LDV [100, 109, 110]. Processing of excitation force and response signals in the frequency domain yields the complex FRFs, which describe the structural dynamics behavior within a range of frequencies. An accurate description requires the use of repeatable excitation and measurement approaches within the frequency range of interest. This entails providing an excitation force with sufficient energy within the frequency bandwidth of interest.

Applying traditional modal testing techniques to miniature structures poses significant challenges: First, the small size and mass of miniature structures necessitate application of excitation/measurement techniques and instrumentation that do not alter the dynamic characteristics of the structure. In terms of measurements, this requirement is satisfied by the use of non-contact techniques, such as LDV. Second, since scaling effects can cause miniature structures to exhibit modes at high frequencies, the excitation and measurement methods must provide sufficient bandwidth to fully characterize the modal behavior. Third, due to the fragility and high-compliance of miniature structures, the excitation method should enable applying well-controlled force magnitudes to prevent damage. And fourth, the repeatability of impact location and orientation becomes more critical due to the small size of the structure.

To address the aforementioned challenges, miniature impact hammers have been employed in the modal testing of miniature structures. Although miniature impact hammers

are capable of exciting structures within a broad frequency range, when applied manually, they do not allow controlling the impact force amplitude and obtaining impacts with repeatable force magnitude, bandwidth, location, and orientation [46, 87, 93, 112, 113]. As a result, miniature impact hammers do not provide an efficient and effective approach to modal excitation for miniature structures. Therefore, there is a strong need for repeatable and high bandwidth impact excitation systems to enable accurate modal characterization of miniature structures. The system should be inherently capable of providing controlled-force single-impact excitations with a high frequency-bandwidth in a repeatable fashion.

This chapter presents a novel impact excitation system (IES) for repeatable and high-bandwidth modal testing of miniature structures. The system includes a miniature force sensor with an impact tip attached to a custom designed flexure-based body (see Fig. 6.1).

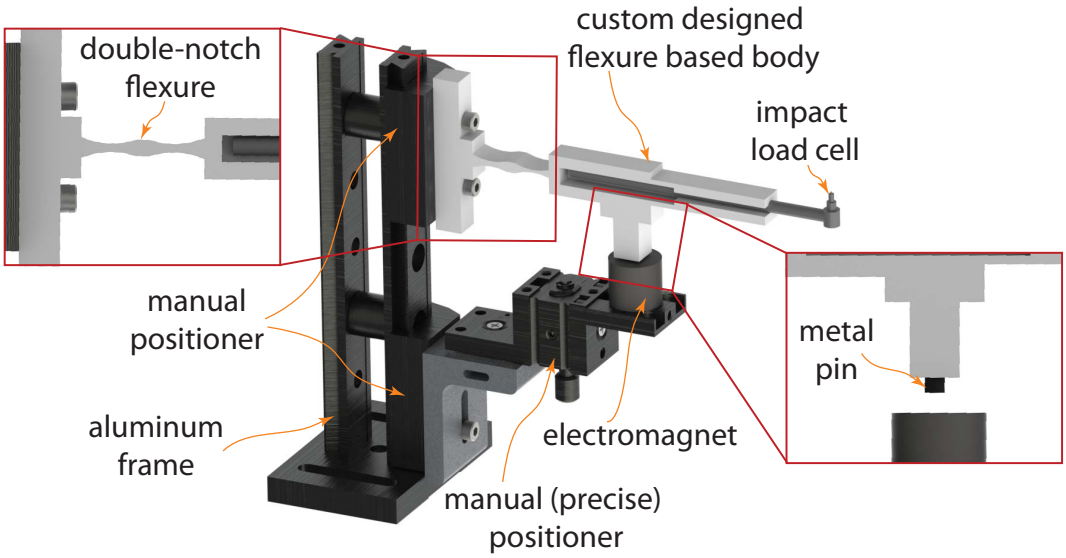

Figure 6.1: CAD model of the impact excitation system.

The system functions by releasing the flexure from a specified initial deflection. An automated release mechanism driven by an electromagnet is designed for repeatable release of the flexure from the initial deflection. Upon release, the impact tip hits the test structure, which is placed at a specified distance away from the neutral (undeflected) position of the tip. The IES allows controlling the impact force and the excitation bandwidth by providing capability to modify **(1)** the flexure geometry and dimensions; **(2)** added mass to the impact tip; **(3)** the initial displacement amplitude; and **(4)** the initial gap between the tip and the test sample. To assist in determining the IES parameters for single impact hits within a specified force limit, a model of the IES including a dynamic model of the

flexure-based body, an empirical model of the electromagnetic force and damping, as well as a Hertzian model of the impact event, is developed and experimentally validated. The excitation bandwidth, impact force, and impact location repeatability of the IES are then compared to those obtained through manual application of a miniature impact hammer. Lastly, the application of the IES is demonstrated through modal testing of a miniature contact probe system.

6.2 Impact Excitation System

This section describes the design and components of the IES. The IES is designed to obtain repeatable, high-bandwidth, single-hit impacts while controlling the impact force amplitude. In addition to material properties and geometries of the impact tip and the test surface, the impact force and bandwidth are strongly correlated with the momentum of the impact [114–117]. Since the impact momentum depends on the impact velocity and impact mass, for a given impact mass, obtaining repeatable impacts with limited force necessitates providing an accurate and repeatable impact velocity. Furthermore, to conduct modal tests with high repeatability and reliability, the variability in impact location and orientation should be minimized. It is also critical to determine sets of parameters that will enable single-impact excitations as required by modal testing.

The designed IES system is illustrated in Fig. 6.1. The general characteristics of IES design can be described considering its three subsystems, including **(1)** a flexure-based spring that provides controlled dynamic stiffness and motion to the impact mass, **(2)** an automated release mechanism to provide reproducible initial deflection and rapid release of the flexure system from its initial deflection, and **(3)** a load cell attached to the impact mass to measure the excitation force applied to the test structure. For the IES design described here, the release mechanism is an electromagnet. Manual positioners are used to host the IES system, and to allow a prescription of the initial deflection and the initial gap between the impact tip and the sample surface. As such, depending on the test structure and test requirements, the design enables changing the dynamic stiffness, the initial displacement amplitude and the initial gap between the impact tip and the test sample, so that the desired impact type (single vs. multiple), force, and bandwidth can be obtained.

The operation of the system designed can be visualized by considering the response of the IES and the associated time response given in Fig. 6.2. When turned on, the electromagnet pulls the magnetic pin, thereby providing an initial deflection to the flexure-based body, as seen in Fig. 6.2(a). When turned off, the electromagnet releases the body and causes it to

move along a well-described trajectory. This trajectory continues until the impact tip hits the sample surface (see Fig. 6.2(b)). Depending on the dynamics of the IES, the impact, and the test sample, single or multiple impacts would occur.

The impact head includes a stainless steel impact tip and a load cell (PCB, Model 086E80) that measures the impact force with a sensitivity of 22.5 mV/N and a frequency bandwidth of 100 kHz [118]. Extender masses can be attached to the back side of the impact head to change the impact mass, and thus, the impact momentum, for a given impact velocity. The impact head is screwed onto a plastic shank that is attached to the holder portion of the IES body. During the tests presented here, the impact signals are acquired using a signal conditioner (PCB, Model 480E09) that is connected to a data acquisition system consisting of a National Instruments PXI-1033 chassis with a PXI-6259 data acquisition board. A LabView^{TM}-based code is written to acquire the excitation force signals and to generate the control signal for the electromagnet.

To provide smooth, repeatable and uni-directional motions, a double-notch type flexure that connects the holder portion of the body to the base is included in the design (see Fig. 6.1). The flexure-based body is fabricated from acrylonitrile butadiene styrene (ABS) using a 3D printer (Dimension Elite 3D). In this fabrication process, the constructed CAD model of the flexure-based body is given to the 3D printer software (CatalystEX Software). The software breaks down the CAD model into (0.2 mm thick) slices which are sent to the 3D printer. The ABS filament is fed through a nozzle that is heated to melt the thermoplastic. After the extrusion, the material immediately hardens. The 3D printed flexure portions are then finish-machined to ensure accurate geometric dimensions and uniformity. The selection of the flexure type design is motivated by smooth, continuous, repeatable, and predictable displacement behavior of flexures [119]. More importantly, flexures have significantly higher compliance along a single axis, thereby limiting the motions along the other axes (e.g., bending motions in other directions). Furthermore, as compared to spring- and bearing-type connectors, flexures move without friction, hysteresis, and backlash [120]. Considering the space limitations, a double-notched flexure geometry is selected from various flexure designs. Since the flexibility of the system is concentrated in local areas (the neck regions), the double-notched flexure design enables changing the overall stiffness of the entire flexure based body by simply changing the notch geometry. The range of impact force magnitudes with single-hit impacts can be widened by using different flexure geometries (single vs. double, flexure thickness, neck shape, etc.). In this study, three different double-notch flexure geometries (with rectangular cross-sections and different neck thicknesses) were fabricated and tested.

For a given structure and impact head/mass, the impact velocity is controlled by the initial deflection and initial gap between the impact tip and the sample surface. In addition to providing means to prescribe initial deflection and initial gap precisely and repeatably, it is critical to release the system from its initial deflected position in a repeatable manner. To provide initial deflection to the flexure based body, a tubular electromagnet (ELMATU019017) is used. When turned on, the electromagnet deflects the IES body by pulling a small magnetic pin glued onto the holder portion until contact between the electromagnet surface and the magnetic pin is established. The initial deflection is controlled by prescribing the initial separation between the electromagnet and the magnetic pin by using a precision slide. The flexure based body is released by cutting off the voltage applied to the electromagnet. A relay (GR12V10ABL, Futurlec) is used to minimize the variability in switching durations. A set of tests performed on the relay indicated that the average switching duration is below 1 ms. This is sufficiently fast and repeatable that it does not affect the performance of the IES or the modeling procedure described in the following sections. Since the electromagnet is a large inductor itself, it resists changes in electrical current. Due to this behavior inductive voltage spikes occur when the electromagnet is switched off. Therefore, to prevent this, a flyback diode is also included in the system.

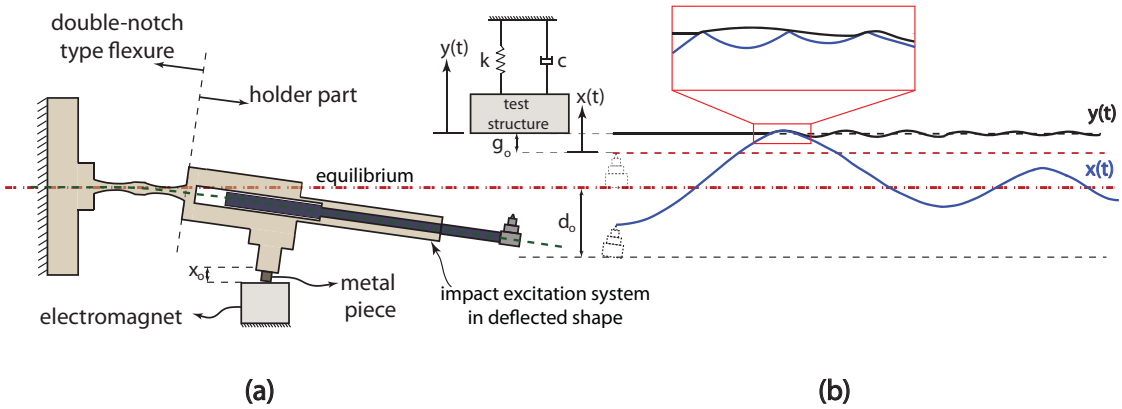

Figure 6.2: **(a)** The impact excitation system (in the deflected position) and **(b)** an illustrative time response of the impact head.

6.3 Model Development

The purpose of the IES is to enable providing high-bandwidth, controlled-force, and single-hit impact excitations to miniature structures in a repeatable fashion. Although the IES design has this basic capability, only certain combinations of system parameters, including

initial displacement (as dictated by x_0), initial gap (g_0), impact head mass (m_t), and flexure geometry, will deliver the required performance. Traditionally, identification of an appropriate impact mass, hammer type, tip material, etc., is done through a time-consuming trial-and-error approach. However, a high-fidelity model of the IES can enable identifying favorable sets of system parameters and associated impact characteristics (force, bandwidth, single or multiple impacts) without resorting to extensive experimentations.

To construct this model, the motion of the IES during modal testing should be well understood. As depicted in Fig. 6.3, the motion of IES during modal testing can be decomposed into three phases: **(1)** Motion before impact, **(2)** motion during impact, and **(3)** motion after impact. In the first phase, a voltage supplied to the electromagnet provides an initial deflection to the IES body (see Fig. 6.2(a)). When the voltage to the electromagnet is cut off, the potential energy stored in the flexure due to initial deflection causes it to move towards the test sample. However, the electromagnet (being an inductor itself) resists the changes in the electric current passing through the circuit, resulting in a time delay for the magnetic field to collapse fully [121]. Due to this time delay, the electromagnet continues to apply a (decaying) pull force to the flexure-based body until the magnetic field collapses completely. This pull force is a function of time and the separation ($x_o(t)$) between the electromagnet and the magnetic pin. In addition, the motion of the flexure within the collapsing (changing) magnetic field induces an eddy current that results in a (decaying) magnetic damping [121]. This energy dissipation can be modeled as viscous damping and added to the system's inherit damping characteristics. Thus, the behavior of the IES (and thus, the trajectory of the impact tip) can be modeled by considering the response of the (time-varying) damped structural dynamics of the flexure-based body due to the initial deflection and the (time- and space-varying) pull force from the electromagnet. In this work, the structural dynamics of the flexure-based body is modeled using beam and 3D linear-elasticity equations using the ST technique [29, 59]. The damping and the varying force arising from the electromagnet are determined using an empirical approach. Given all the parameters, the purpose of this portion of the model is to determine the initial impact velocity at the instant of the impact.

The second phase involves the impact event. This phase is composed of deformation and restitution sub-phases, where the impact tip and the test surface move together. As a result of the initial impact velocity, an elastic indentation is initiated on the sample surface. As the indentation progresses, the force arising from the indentation is applied to the impact tip, exciting the dynamics of the IES. At a certain indentation depth, the initial impulse provided by the impact tip is matched by the indentation force, which marks the peak of the

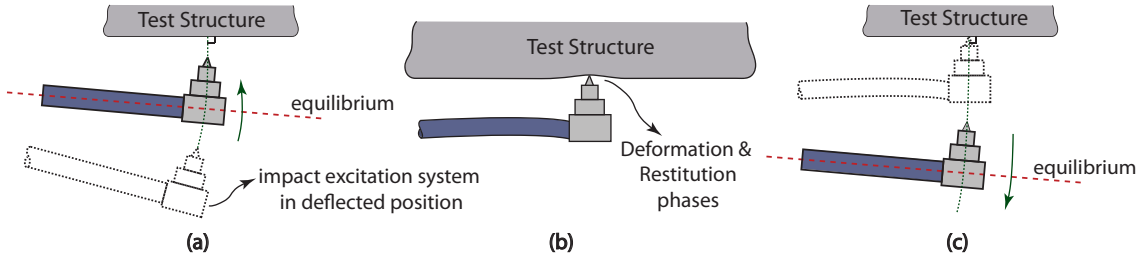

Figure 6.3: Three phases of motion experienced by the IES during modal testing: **(a)** motion before impact, **(b)** motion during impact, **(c)** motion after impact.

impact force. Subsequently, the restitution sub-phase ensues by the reversal of tip motion and the elastic recovery of the sample surface. Eventually, the contact between the impact tip and the sample surface is lost, marking the end of the impact event. In this work, the impact force is modeled using the Hertz theory considering the tip and sample materials, tip- and sample-surface curvatures, and the coefficient of restitution of the impact. The impact force is input into the structural dynamics model of the IES at every instant.

The third phase begins with the separation of the impact tip from the sample surface. This phase involves free-response of the flexure-based body (and the impact head) as a response to an initial displacement (where the impact tip loses contact with the sample surface) and an initial velocity (which is the exit velocity at the end of the impact event). Under the ideal case of single-impact excitations, the impact tip would not contact the sample surface again, and thus, modeling the motion during the third phase is of no interest. However, in practice, depending on the system dynamics and the choice of system parameters, multiple impacts could occur. Since one of the goals of the model is to predict the occurrence of multiple impacts (and thus to determine conditions to avoid them), this phase also becomes critical to modeling the IES behavior.

The rest of this section describes the individual models required to model each of the three phases of the motion. This includes **(1)** an analytical model of the structural dynamics of the flexure based body (with the attached impact head); **(2)** an empirical model of the electromagnetic force and damping; and **(3)** a Hertzian model for the impact force.

6.3.1 Analytical model of the flexure and the impact load cell system

The analytical model of the flexure based body and impact load cell system is constructed using the ST approach [29, 59]. To reduce the numerical inefficiency arising from the discontinuities in the cross-section, the flexure based body and impact load cell system are

divided into substructures (see Fig. 6.4), geometric and material parameters (cross-section area, moment of inertia, etc. - see Table 6.1 and Table 6.2 for geometric and material properties, respectively) of which are either uniform or can be expressed as continuous functions. Furthermore, to achieve simultaneous numerical efficiency and modeling accuracy, 1D-ST models for the holder substructures (V through XIII) and 3D-ST models for the base and flexure sections (I through IV) are used. This modeling approach involves deriving the IBVP for each section using the extended Hamilton's principle. The IBVP is selected since it describes the system dynamics in a compact form and simplifies the solution approach by eliminating the necessity of imposing natural boundary conditions to the IBVP. The model for each substructure is then combined using the CMS approach to obtain the dynamic model for the entire system.

Table 6.1: Geometric properties of the IES.

	Flexure 1	Flexure 2	Flexure 3
L_f (mm)	120		
L_T (mm)	143		
L_{EM} (mm)	65		
L_h (mm)	6.3		
w (mm)	10		
t_n (mm)	2.0	2.5	3.0
r (deg)	19	23	31

Table 6.2: Material properties of the IES.

		Elastic Modulus E (GPa)	Density ρ (kg/m^3)	Possion's Ratio ν
Flexure based body:	ABS	2.25	1080	0.39
Impact head shank:	Polypropylene	2	1000	0.45
Impact head:	Stainless Steel	220	8000	0.27

For the 1D model, the Timoshenko beam approach, that includes the shear and rotary inertia effects, is used to insure the accuracy of the dynamic model. For this model, the holder portion is assumed to behave as a stubby beam, and modeled using a 1D model that includes bending, axial, and torsional motions. To obtain an accurate model, the shear and rotary inertia effects are captured by following the Timoshenko beam approach described in Chapters 2 and 5. For the 3D model, the IBVP is obtained using 3D linear elasticity

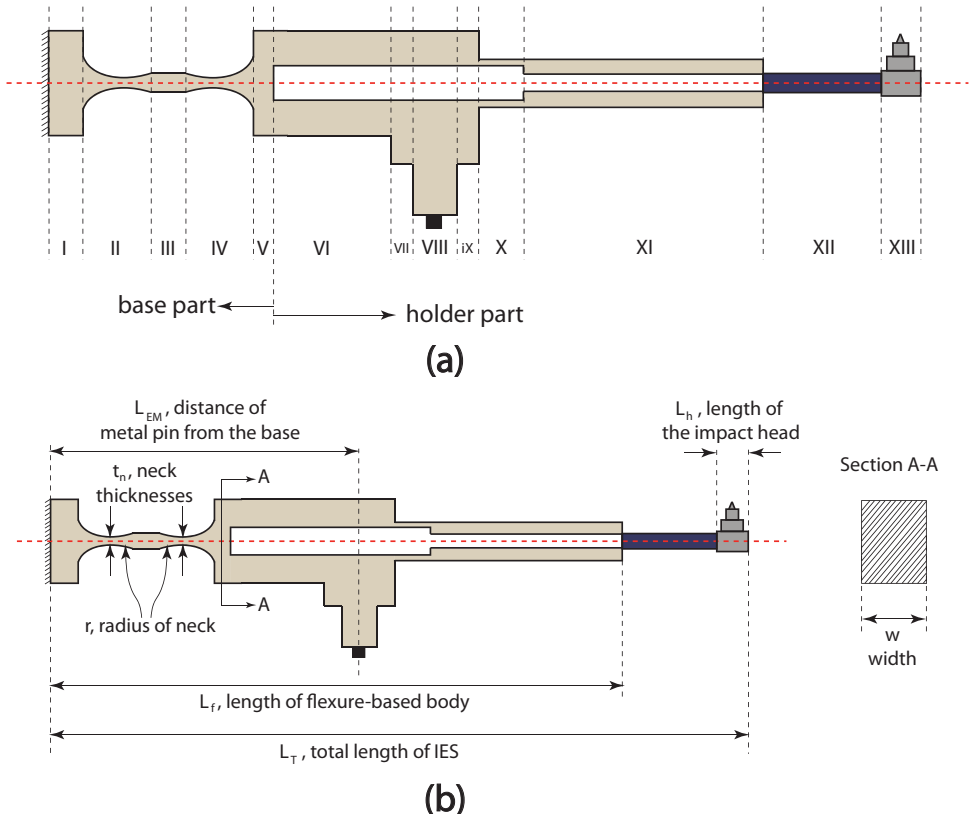

Figure 6.4: **(a)**Substructures (I:XIII) and **(b)** geometric properties of the IES.

equations through extendend Hamiton's principle as shown in Chapter 3.

Next, the 1D-ST and 3D-ST techniques are used to discretize the IBVPs to obtain the mass and stiffness matrices, and the forcing vector. The pull force applied by the electromagnet is introduced to the model as an external forcing vector, $\mathbf{f}$.

The modeling approach does not include damping. For the IES, the damping arises from two sources: the structure (including the joints and the material), and the decaying electromagnetic (eddy-current) damping. The former is obtained from modal testing of the IES body itself. The latter is obtained using an empirical model derived here (see below for details). To incorporate damping into the model, the extracted damping ratios are added into the constructed model in the modal domain.

6.3.2 An empirical model for electromagnetic pull force and damping

To model the pull force and the damping arising from the electromagnet, an empirical approach is followed. The experimental setup depicted in Figure 6.5(a) is used to measure the pull force from the electromagnet after cutting off the voltage to the magnet. In this

setup, a magnetic pin (identical to the one used in the IES) is glued onto a plastic holder, which, in turn, was attached to a force dynamometer (Kistler, 9256C1). Since the motion of the IES starts after the voltage is cut off, the forces acted upon the IES body by the electromagnet should be determined as a function of both time and distance between the pin and the electromagnet. To extract the spatial dependence of the electromagnetic force, a manual positioner (having a resolution of 1 μm) is used to prescribe different spatial separations between the electromagnet and the pin. Starting from when the pin is in contact with the electromagnet, a total of 20 experiments were conducted at every 100 μm of incremental distance. In the experiments, while measuring the pull force of the electromagnet, the voltage is first supplied to the electromagnet and then it is cut off. The forces through this entire event are continuously measured to determine the transient characteristics of the pull force and the time it takes for electromagnetic force to collapse completely. Therefore, at each separation distance, the pull force is measured (in time) using the force dynamometer right before and after discontinuing the voltage supplied to the electromagnet, until the force decays to zero.

The measured pull-force profiles at different separation distances, x_0, are plotted in Fig. 6.5(b). As expected, the larger the separation distance, the lower the pull force at time $t = 0$, which is the instant the voltage to the electromagnet is discontinued. At a given x_0, the pull force decays in time in an (approximately) exponential manner. Since the goal of this exercise is to form an empirical model as a function of both time and separation distance, a two-level curve fitting algorithm is used. First, the time-dependent decaying force at each set distance is curve-fitted using an exponential form $F_{x_0}(t) = A\mathrm{e}^{Bt}$, determining the coefficients A and B for each x_0 (see Fig. 6.5(b)). For all 20 experiments, the mean goodness of fit (r^2) value is calculated as 0.9932 (with a standard deviation of 0.0073). Subsequently, both A and B are plotted as a function of x_0. Curve fitting each of those as a function of $A(x_0) = 0.0634 \ + \ 1.1978 \ e^{(-0.0435 \ x_0)}$ and $B(x_0) = -775$ resulted in an empirical function of pull force F as $F(x_0, t) = A(x_0)\,\mathrm{e}^{B(x_0)\,t}$ (see Fig. 6.5(c)). This pull-force function is used during the IES modal testing simulations.

Another empirical model is developed for the time-dependent damping arising from the electromagnet. For this purpose, a simulation framework that includes the structural dynamics model of the flexure-based body and the pull force is developed. A modal test on the flexure-based body itself is used to extract the damping ratio from the system structure (see below). The time-dependent damping ratio arising from the electromagnet is added to the structural damping ratio. The approach followed here involves measuring (from experiments) the velocity of the impact head along its trajectory after the release, then

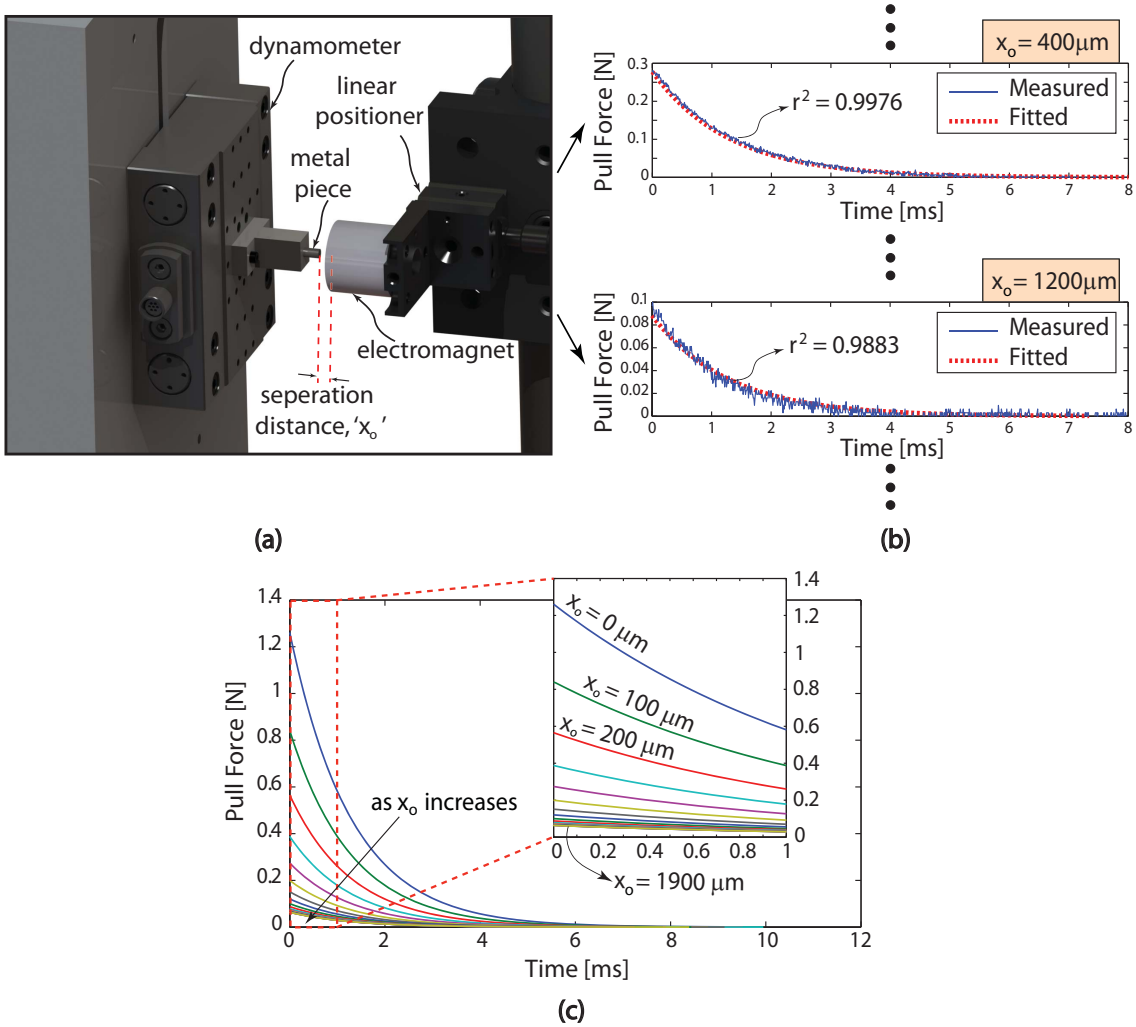

Figure 6.5: **(a)** Experimental setup for determining the pull-force profile, **(b)** measured pull force profiles by the dynamometer, and **(c)** fitted decaying pull force profile exerted by the electromagnet after it is shut off (when the electromagnet is connected to a 6V DC supply).

comparing the velocity to that from the simulation framework, where an empirical model of the time-dependent damping ratio is included. Since electromagnets act as inductors, and since the decaying energy profile of an inductor shows an exponential behavior [121], an exponential model $\xi = a\,e^{bt}$ is chosen, where ξ is the decaying electromagnetic damping ratio, t is time, and a and b are calibration constants. An optimization algorithm (from the optimization toolbox of MATLAB®) is used to determine the calibration coefficients as those that result in the closest fit between the measured and simulated trajectory of the impact head.

The experimental setup given in Fig. 6.6(a) is used to measure the velocity of the impact

head along the trajectory after release. The electromagnet is turned on to pull and hold the flexure based body in the deflected shape. The voltage to the electromagnet is then cut off, and the (time-dependent) trajectory of the impact head is measured using an LDV that is shone onto the back side of the impact head.

Although small, the initial separation x_0 also has an effect on the time-dependent damping coefficient. To ensure the model is applicable for a range of initial separation distances, two tests, one at $x_0 = 2$ mm and another at $x_0 = 3$ mm were conducted. The results from these two tests are used to determine the calibration coefficients for the time-dependent damping ratio a and b as 0.57 and 0.6, respectively. Figure 6.6(b) shows the time-dependent damping profile.

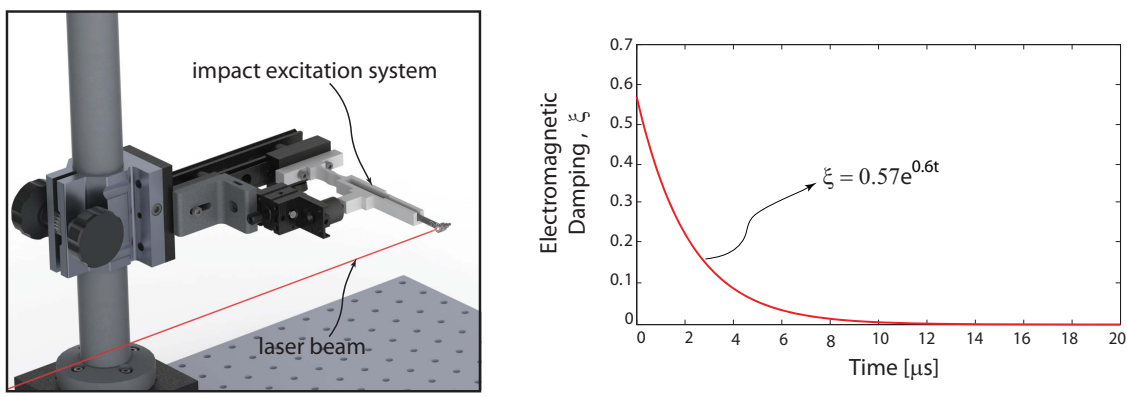

(a) (b)

Figure 6.6: **(a)** Experimental setup for determining the (decaying) magnetic damping and **(b)** decaying damping profile exerted by the electromagnet after it is shut off (when the electromagnet is connected to a 6V DC supply).

6.3.3 Impact dynamics model

The impact dynamics model is constructed based on the Hertz theory of contact [114–116]. Following the Hertz theory, the impact (contact) force including the hysteresis damping can be expressed as [122],

$$F_{impact} = K\,\delta^n \left\{ 1 + \frac{3(1-e^2)}{4}\,\frac{\dot{\delta}}{U_o} \right\}, \tag{6.1}$$

where

$$K = \frac{4}{3\pi(k_i + k_j)} \left\{ \frac{r_i\, r_j}{r_i + r_j} \right\}^{\frac{1}{2}} . \tag{6.2}$$

Here, K represents the contact stiffness, e represents the coefficient of restitution, U_o represents the impact velocity, δ and $\dot{\delta}$ represents the indentation amount and velocity, respectively, and r_i and r_j represents the radius of the colliding bodies at the impact region. Note that if one of the surfaces is flat, the quantity in the bracket becomes equal to the radius of curvature of the non-flat colliding body, i.e., the radius of the impact tip. The non-linearity coefficient of the impact, n, taken as 1.5 according to the Hertz theory [116, 122]. The material properties of the colliding bodies, k_i and k_j, are expressed as

$$k_l = \frac{1 - v_l^2}{\pi E_l} \quad , \quad k = i, j \quad , \tag{6.3}$$

where ν is the Poisson's ratio and E is the modulus of elasticity of the colliding bodies. Note that the coefficient of restitution is dependent on the materials and geometries of the colliding bodies, and the impact velocity [116]. For several material types and geometries (such as colliding spheres), the value of the coefficient of restitution can be found from the literature. However, for complex geometries, it needs to be determined from experimentation.

6.3.4 Selection of control parameters

Although the IES has the basic capability of providing repeatable single-hit impacts with controlled force and high bandwidth, identification of proper control parameters is needed to achieve a satisfactory performance. In other words, appropriate flexure geometry, initial displacement (x_0), initial gap (g_0) and the impact head mass (m_t) should be selected.

An approach to guide the selection of proper process conditions may be realized using simulation-based process maps that indicate no-, single-, and multiple-hit regions superposed on contour plots of impact forces. The required inputs to the simulation include geometric and material properties of the flexure-based body, the coefficient of restitution (e), and curvatures of the impact tip and sample-surface. It is noted that the simulation framework also allows variation of those parameters to simulate different impact tip and sample materials, flexure geometries, etc. For those input parameters, and for each impact-head mass, a range of x_o and g_o values can be simulated. As a result, no-, single-, and multi-hit regions would be identified. In addition, the impact-force contours are determined. For the single-hit region, the frequency bandwidth can also be calculated. Furthermore, as seen

below, the effect of adding an extended mass to the impact head can be investigated.

Such a process map is given in Fig. 6.7(a). Figure 6.7(b) shows a sample force measurement and the associated frequency spectra, which allows identification of the frequency bandwidth for the impact. Figure 6.7(c) shows a sample contour map for the bandwidth within the single-hit region.

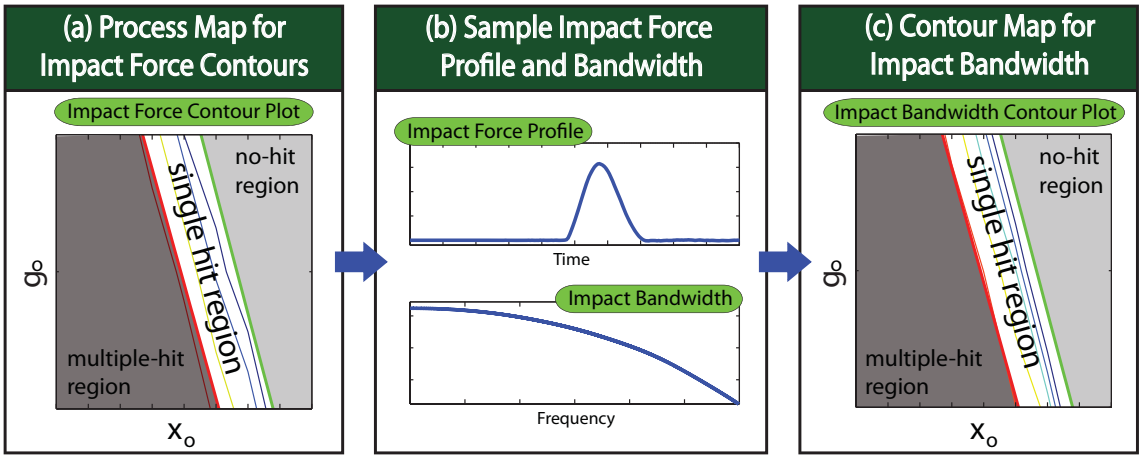

Figure 6.7: Selection of control parameters.

It is important to note here that, when creating the process maps, the dynamic response of the sample is neglected by considering the sample as a rigid structure. This is due to the fact that the sample dynamics is not known *a priori*. However, the proposed framework can be extended to include a (non-exact) sample dynamics, which may be obtained after (a non-ideal) first hit with a set of control parameters obtained from the process map that considers a rigid sample. Using the updated simulation in an iterative fashion could produce the ideal impact conditions. A thorough treatment of this approach is beyond the scope of the current work.

6.4 Modal Validation

In this section, experimental validation for the structural dynamics model of the flexure-based IES body and the electromagnetic damping model are presented. Subsequently, the entire model is validated by comparing hit types (no-, single-, and multiple-hit), force magnitudes, and frequency bandwidths.

6.4.1 Experimental validation of the structural dynamics model for the IES body

Predicting the structural dynamics behavior of the IES body, including the impact head, is critical to a successful simulation of the impact tests. In particular, the bending modes, which are the dominant modes affecting the motion of the IES during modal testing, should be predicted accurately. To evaluate the presented ST-based structural model, a set of modal tests of the IES body itself was performed.

The experimental setup used for this validation study is given in Fig. 6.8. The impact excitations to the IES were provided with another (yet identical) impact excitation system. The response to impact excitations was measured using an LDV (Polytec 300) system, by shining the laser onto a reflective tape attached directly to the IES body. The tests were conducted for three different flexure geometries (see Fig. 6.4 for flexure geometries and associated dimensions). The mass of the impact head was measured as 1.8 *grams*.

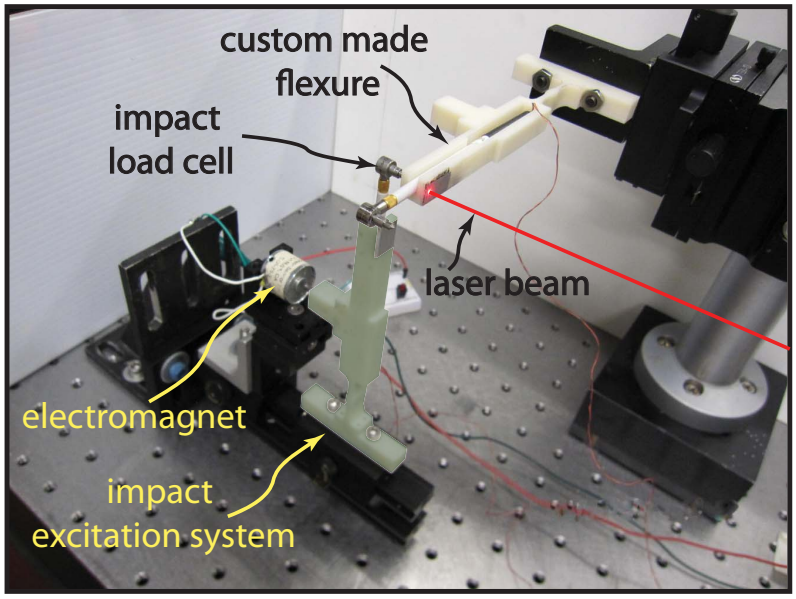

Figure 6.8: FRF measurement of the flexure-based body and impact load cell system.

The FRF obtained from the experiments when using Flexure 3 is given in Fig. 6.9 as an example. For each case, a complex curve-fit (rational fractional polynomial method) was applied to extract the modal parameters of the system within a bandwidth that includes the third bending mode. The damping ratios extracted from this procedure were incorporated into the ST model. Using the model, model-based FRFs were created and compared to the experimental FRFs. An example is given in Fig. 6.9, where the FRFs from the experiments

and the model are compared when using Flexure 3. A good match between the model and the experiments is observed. A further evaluation is completed by comparing the modal parameters from the experiments (through curve-fitting) and the ST model, as seen in Table 6.3. Table 6.3 also presents the damping ratios extracted from the curve-fitting of the experimental data. The average difference in natural frequencies from the experiments and the model was seen to be 0.61 %, with a maximum difference of 1.56 % for the 3rd mode of Flexure 2. Therefore, it can be concluded that the presented ST-based model can accurately capture the dynamic behavior of the flexure-based IES body (including the impact head).

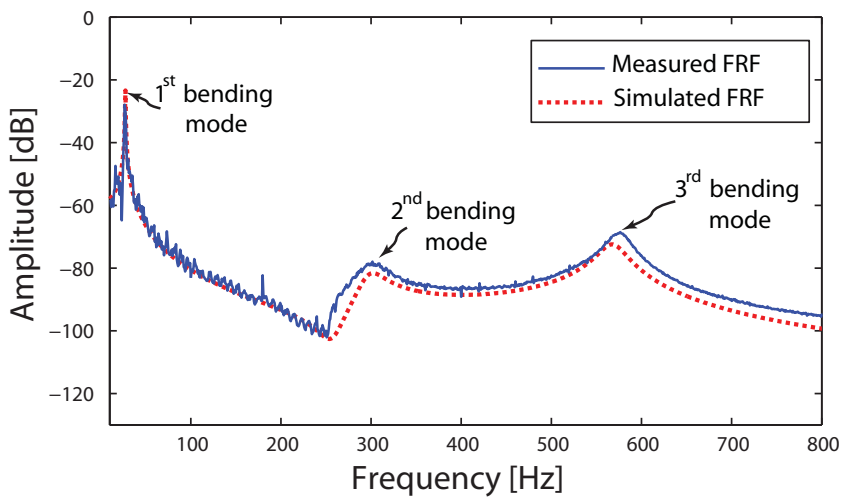

Figure 6.9: Comparison of FRFs obtained from the experiment and from the model.

Table 6.3: Comparison of natural frequencies of the IES.

	1st flexure: 2 mm neck thickness			
Mode	ST model (Hz)	Experiments (Hz)	% Diff.	Damping ratio (ζ)
1	20.9	20.8	-0.60	0.0070
2	269.5	273.4	1.43	0.0466
3	497.7	500.9	0.64	0.0257
	2nd flexure: 2.5 mm neck thickness			
Mode	ST model (Hz)	Experiments (Hz)	% Diff.	Damping ratio (ζ)
1	23.0	23.1	0.64	0.0086
2	287.5	284.4	-1.09	0.0411
3	532.0	523.7	-1.56	0.0217
	3rd flexure: 3 mm neck thickness			
Mode	ST model (Hz)	Experiments (Hz)	% Diff.	Damping ratio (ζ)
1	27.3	27.4	0.50	0.0090
2	301.6	298.5	-1.03	0.0470
3	576.6	568.0	-1.49	0.0223

6.4.2 Validation of the electromagnetic damping model

To validate the empirical electromagnetic damping model, two experiments (using the setup shown in Fig. 6.6(a)) with initial separation distances of $x_0 = 1.5$ mm and $x_0 = 2.5$ mm were conducted. The velocity profile of the impact head along its trajectory between its release and impact was measured and compared with the velocity profile obtained from the model simulations (see Fig. 6.10). For quantitative evaluation, the goodness of fit (r^2) was calculated between the velocities from the experiment and the model: The cases with separation distances of $x_0 = 1.5$ mm and $x_0 = 2.5$ mm yield r^2 values of 0.9926 and 0.9862, respectively. Therefore, the constructed empirical model captures the electromagnetic damping effectively and can be used to predict the motions of the IES.

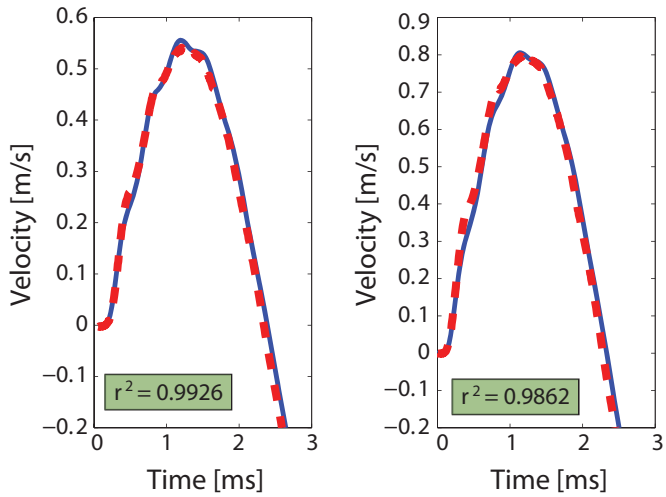

Figure 6.10: Comparison of measured (dashed) and simulated impact head (solid) velocities.

6.4.3 Validation of overall model of impact excitation system

To validate the overall IES model, impact tests were performed on a rigid (anodized) cast iron block using the IES with the Flexure 2 geometry and an impact head mass of 1.8 g. Figure 6.11 shows the experimental setup used for this validation study. The cast iron block is fixed to the vibration isolation table. A process map is created using the developed model, and compared to the experimental results in terms of number of hits (no-, single-, or multiple-hit), impact force magnitude, and frequency bandwidth.

Figure 6.12(a) shows the process map generated for this case. For these simulations, a coefficient of restitution value of $e = 0.85$ is selected for the stainless steel-cast iron impact based on [116]. Although the value of e changes with velocity, a mean value is used for the

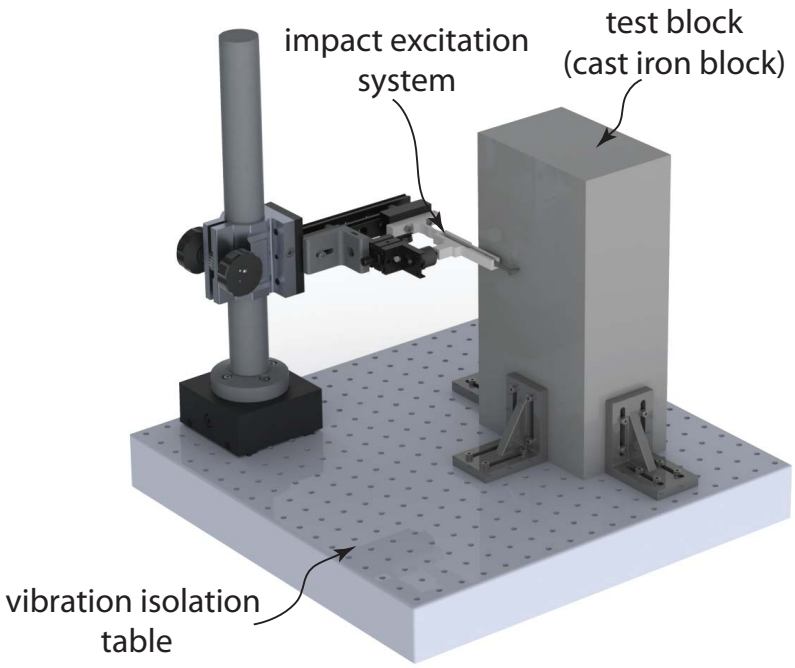

Figure 6.11: Impact testing on a cast iron block.

range of impact velocities that are seen when using the IES. The no-hit (gray), multiple-hit (black), and single-hit (white) regions are identified, and impact force magnitudes are indicated using contour lines. Validation tests were conducted for a range of parameters spanning the no-, single-, and multiple-hit regions (as indicated by the markers on the process map in Fig. 6.12(a)). It is seen that the simulation successfully predicted no-hit, single-hit and multiple-hit cases every time. For two of the single-hit cases, the force profiles and associated impact spectra (that is used for determining the bandwidth) from the experiments and the model are also given in Fig. 6.12(b). Again, a very good agreement is observed on both the force profiles and frequency bandwidth. For the 19 data points that are within the single-hit region, a statistical analysis of the differences of force magnitude and bandwidth between the experiments and simulations are performed. The bandwidth comparison indicated an average difference of 1.81 kHz (< 5 % of any bandwidth), with a standard deviation of 0.94 kHz. The average difference in force magnitudes were 0.90 N, with a standard deviation of 0.72 N. Therefore, it can be concluded that the simulation results are in excellent agreement with those obtained from the experiments: The derived model accurately represents the dynamics of impact excitations when using the IES, and can be used to select control parameters for single-hit, wide-bandwidth impacts with controlled impact force magnitudes.

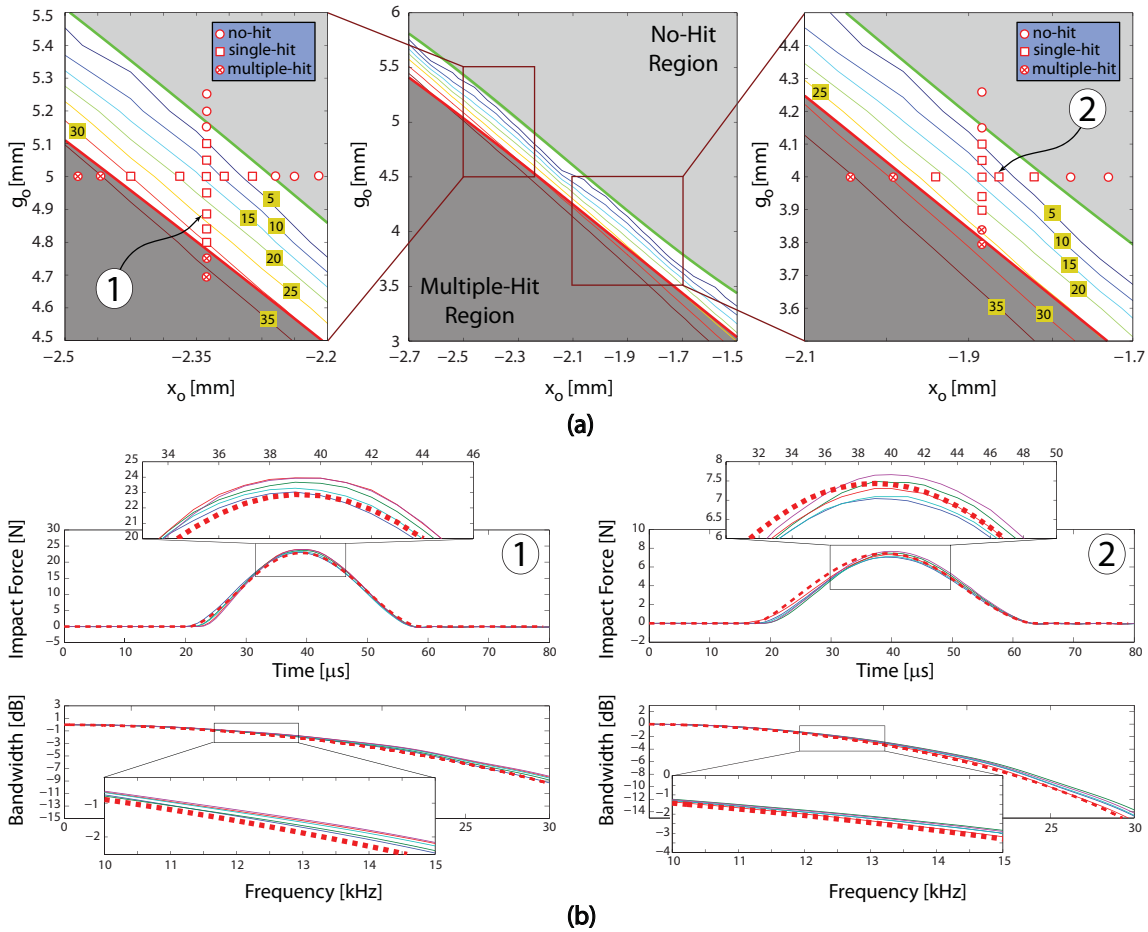

Figure 6.12: **(a)** Process maps and **(b)** impact force profiles and corresponding input spectra for the selected parameters (solid lines - experimental data, red (dotted) line - simulation data).

6.5 The Effect of Control Parameters on the IES Performance

Using the constructed simulation framework, a parametric study was performed to investigate the effect of control parameters on impact force magnitudes and excitation bandwidths. The goal of this exercise is to show that the IES allows controlling the impact-force magnitude and bandwidth, and the parameters for required magnitudes and bandwidth can be obtained by using the derived model. It is noted that only a small range of parameters are considered here, but the model can be easily extended to simulate different parameters. For this study, the analyzed control parameters included the initial displacement given to the flexure based body (x_o), the initial gap between the impact tip and the test sample (g_o), the extender mass attached to the impact tip, and the impact tip geometry. The changes

in impact force magnitudes and excitation bandwidths were investigated through process maps (impact force magnitude contour plots) and bandwidth contour plots, respectively. In the simulations, a coefficient of restitution of $e = 0.95$ was used.

6.5.1 The effect of flexure geometry

The effect of flexure geometry was investigated by varying the neck thickness ($t_n = 2$ mm, 2.5 mm, and 3 mm) of the flexure (see Table 6.1). Figure 6.13 shows the process maps for impact forces and excitation bandwidths. As expected, the range of control parameters, g_o and x_o, resulting in single-hits are different for each flexure geometry, where increased neck thickness (and thus, increased flexure stiffness) shifts the single-impact region towards lower values of initial displacements. This is expected since a larger amount of potential energy is stored in a stiffer flexure, resulting in obtaining similar impact-speed regimes for smaller initial deflections. Furthermore, the single-impact region is widened with increase flexure thickness, and a wider range of impact force magnitudes (up to 19 N) can be realized within this region. Similarly, the use of thicker flexure allows a broader range of impact bandwidths (from 10 kHz to 43 kHz) to be realized within the single-impact region. However, an increased sensitivity to initial conditions (as seen by more closely spaced contour lines) is seen for both impact force magnitudes and (especially) the impact bandwidth. It is interesting to note that an impact bandwidth of above 40 kHz can be obtained when using Flexure 3. A similar analysis can be performed to characterize the effect of other flexure types, geometries, and materials.

6.5.2 The effect of impact mass

Next, the effect of extender (added) mass was analyzed. Three simulations were performed using Flexure 2 for three different extender mass values: $m_a = 0$ g (no extender mass), $m_a = 0.5$ g and $m_a = 1$ g (the impact mass without the added mass is $m = 1.8$ g). Figure 6.14 shows the obtained process maps and excitation bandwidth contour plots. It is seen that increased impact mass shifts the single-impact region slightly toward larger initial displacements (x_o). As expected, larger impact force magnitudes are seen within the single-impact region. It is noted that this effect is not due to a simple increase in momentum from increased mass value, since the impact mass also affects the velocity profile (and thus the impact velocity and single vs. multiple hit regions). Similarly, increased impact mass changes the impact bandwidth within the single-hit region, but the effect is considerably smaller than that on the impact force magnitude.

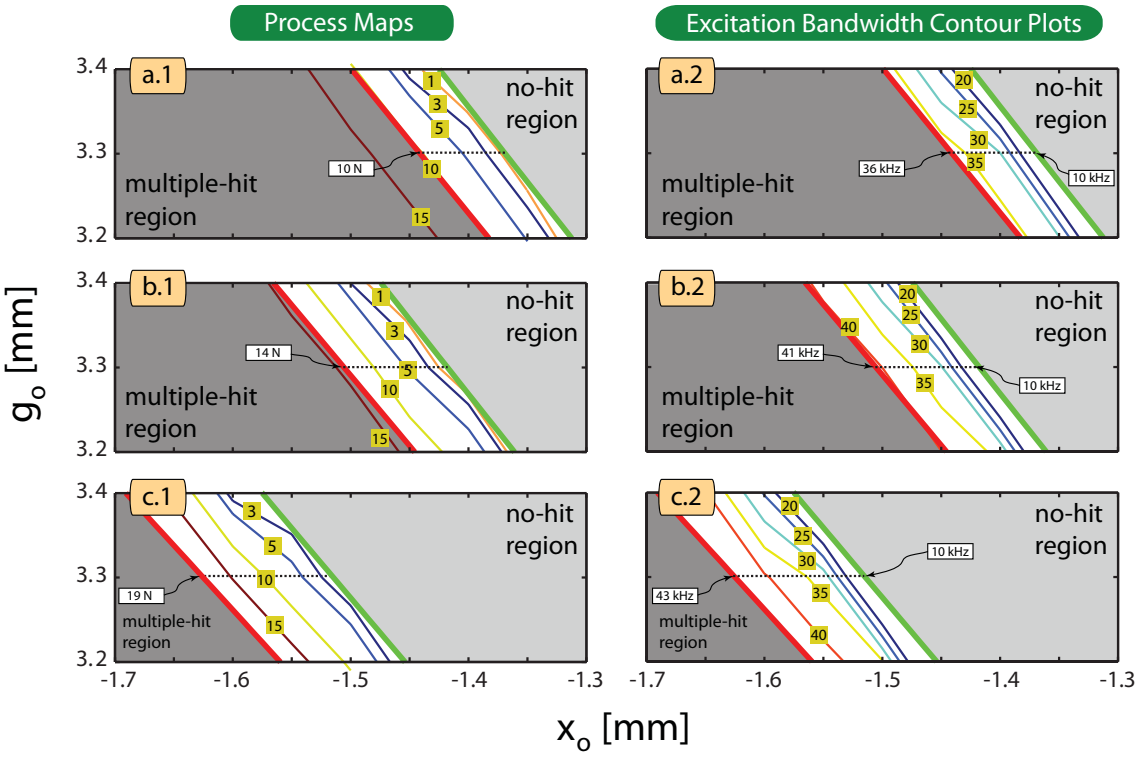

Figure 6.13: The effect of flexure geometry on process maps and excitation bandwidth contour plots: **(a)** Flexure 1, **(b)** Flexure 2, **(c)** Flexure 3.

6.5.3 The effect of impact-tip radius

The effect of impact tip radius was also investigated using Flexure 2 for two different impact head radii: 0.3 mm and 1.2 mm. Figure 6.15 shows the calculated process maps and excitation bandwidth contour plots. It is seen that the impact-tip radius does not affect the position of single-hit region with respect to the initial conditions. However, as expected, increased tip radius leads to reduced bandwidths within the single-hit region, while not varying impact force magnitudes significantly. On the other hand, smaller tip radii increases the sensitivity of bandwidths to initial conditions.

6.6 System Evaluation and Comparisons with a Miniature Impact Hammer

The repeatability of the IES in terms of impact force magnitude, frequency bandwidth, and impact location is critical. In this section, the repeatability of the IES is evaluated. Furthermore, the IES performance is compared to that obtained when using a miniature

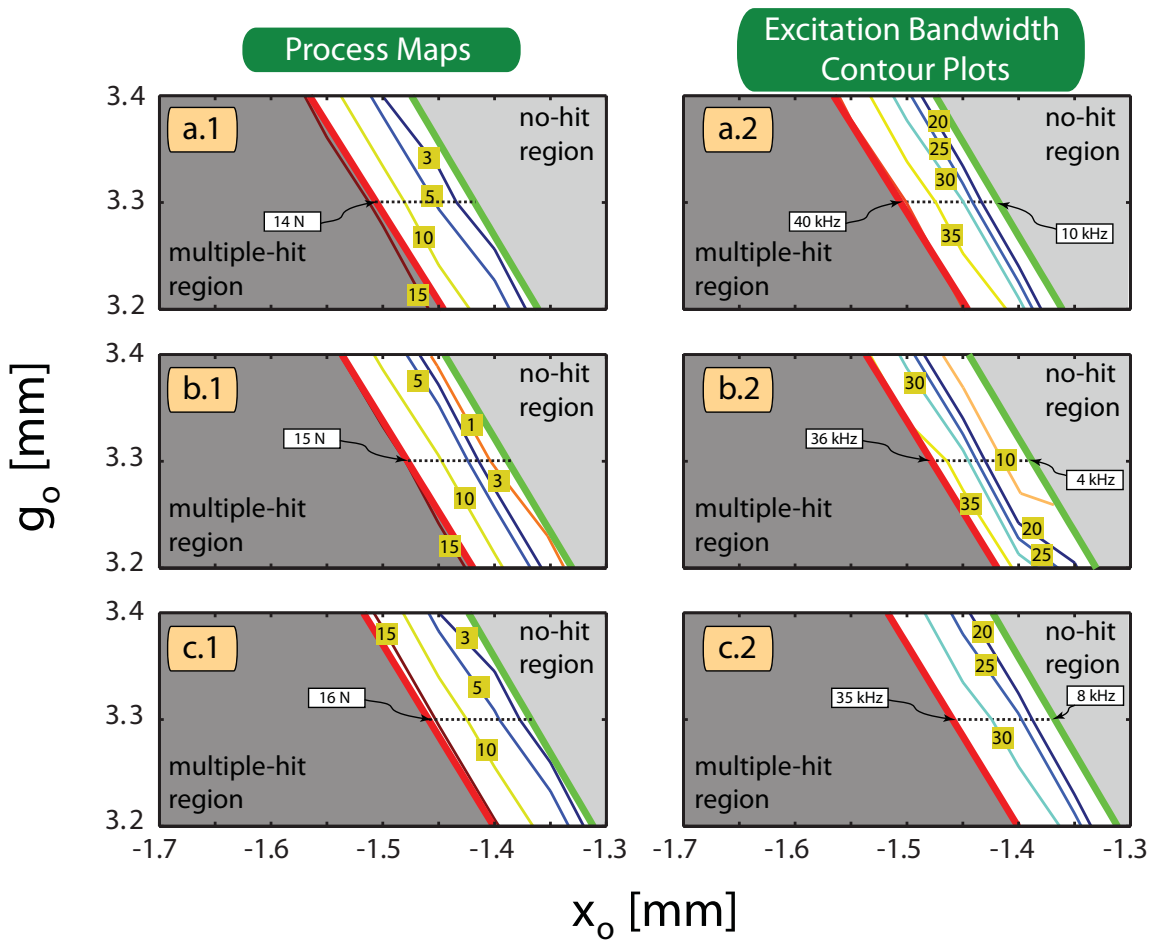

Figure 6.14: Effect of extender mass on process maps and excitation bandwidth contour plots: **(a)** with no extender mass, **(b)** with an extender mass of 0.5 g, **(c)** with an extender mass of 1.0 g.

impact hammer (PCB - Model 086E80) manually. The evaluation and comparison tests were all conducted using the experimental setup given in Fig. 6.11. For the IES impacts, x_o= 1.9 mm and g_o= 4 mm values are used, as identified from the simulations presented in Sec. 6.4.3 as a single hit case with an impact force magnitude of 15.5 N.

To determine the variability in impact location, a pressure paper that changes color at locations where pressure is applied is attached to the hitting region on the surface of the test block. Each of the IES and miniature impact hammer is used to apply 50 consecutive hits. The traces in the pressure paper are captured using a microscope with an attached digital camera. Figure 6.16 shows the results from both approaches. To quantify the hit regions, an image processing algorithm is used to calculate the impact area that encloses all the impact points. As seen in Fig. 6.16, the designed IES enables delivering impact excitations with a high level of repeatability in impact location, with a resulting impact area of 0.25 mm^2.

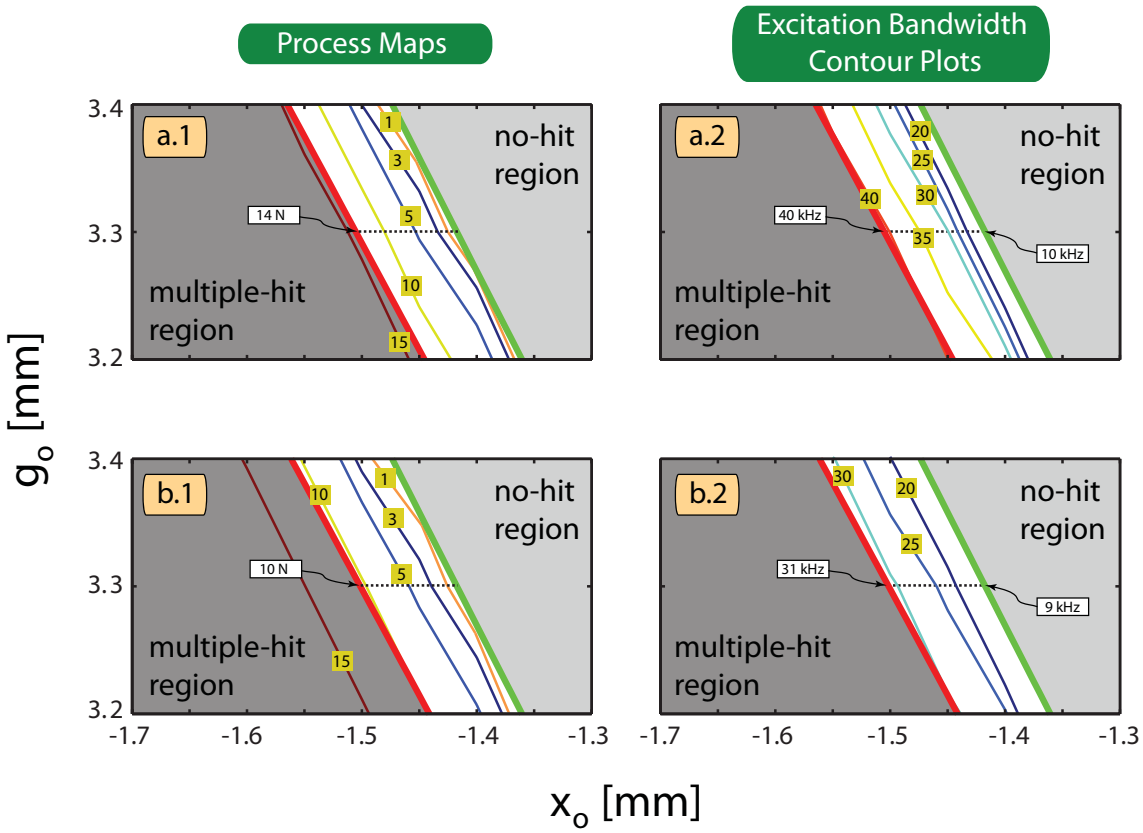

Figure 6.15: Effect of impact tip radius on process maps and excitation bandwidth contour plots: **(a)** r = 0.3 mm, **(b)** r = 1.2 mm.

In contrast, although the utmost care has been taken to retain the impact location, the impact area for manual impacts was calculated as 10.94 mm^2. These results indicate that the IES provides a high level of impact-location repeatability, well-superior to the manual application of a miniature impact hammer.

To evaluate the repeatability in terms of impact force magnitude and bandwidth, a similar testing procedure is followed. Again, 50 consecutive hits are performed using the IES and the miniature impact hammer. It is noted here that only 30 out of 50 hits were single hits when using the miniature impact hammer, while all 50 hits were single hits when using the IES: This observation also indicates the advantage of the IES system over manual application of miniature impact hammers. As such, when comparing the bandwidths, only the single-hit cases are considered. Figure 6.17 shows the measured impact force profiles, excitation bandwidths and their distributions. In this study, excitation bandwidth for a given impact force profile is defined as that frequency at which the normalized magnitude reduces to -10 dB [111]. A statistical analysis indicated that the average impact force magnitude and associated standard deviation were 15.83 N and 0.54 N, respectively, and

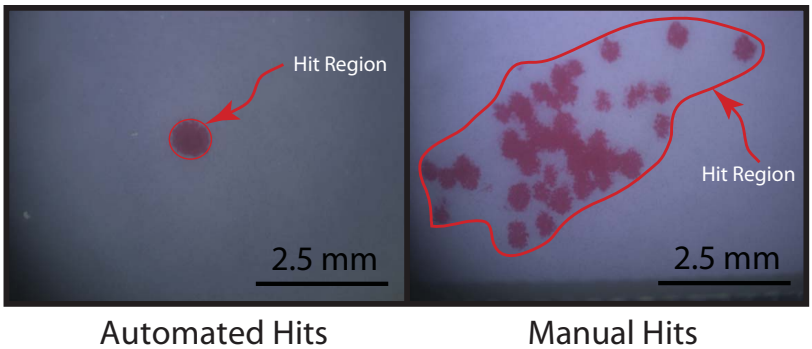

Figure 6.16: Impact location variability obtained **(a)** using the designed IES, **(b)** with manual hits using a miniature impact hammer.

those for the miniature impact hammer were 20.72 N and 8.82 N, respectively. Furthermore, the average bandwidth and associated standard deviation for the IES were 29.83 kHz and 0.43 kHz, respectively, and those for the miniature hammer were 20.59 kHz and 4.18 kHz, respectively.

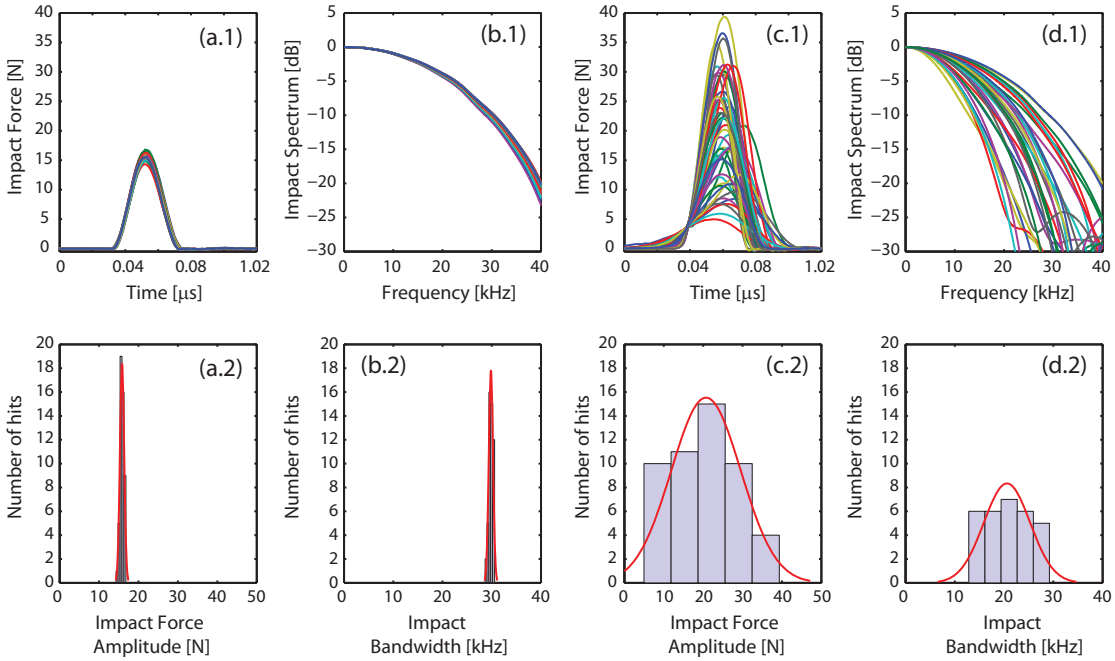

Figure 6.17: Impact force amplitude and excitation bandwidth variability obtained **(a)** using the designed IES, **(b)** with manual hits.

To further evaluate the repeatability of the modal testing when using the designed IES, the coherence of the modal data measured from the cast-iron block using the LDV system was analyzed. Figure 6.18 shows the coherences calculated for each of the IES and manual

impact tests. As above, only the 30 single-hit tests were considered in the case of manual impacts. It is seen that better (higher) coherence values can be obtained when using the IES. Indeed, the coherence values obtained using the IES are above 0.95 for the entire bandwidth, even for the anti-resonance regions. Therefore, it is clear that the IES provides significant advantages over (manually used) miniature impact hammers in terms of repeatability (force, bandwidth, impact location), force control, and impact bandwidth.

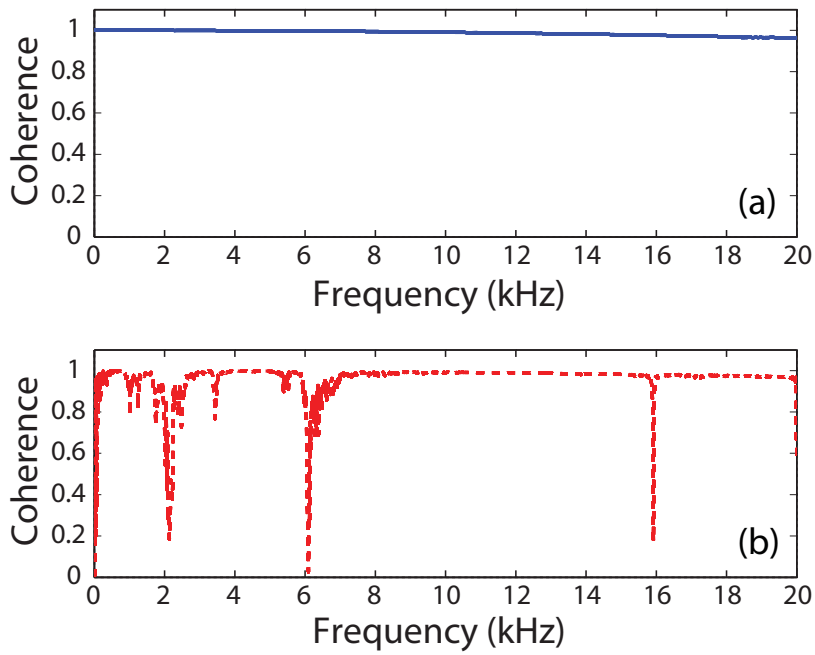

Figure 6.18: Coherence plots calculated using **(a)** the designed IES and **(b)** manual hits (obtained only averaging the test in which single-hits are obtained).

6.7 Application of the IES: Modal Testing of a Miniature Contact Probe

To demonstrate the application of the IES on a miniature structure, a set of modal tests on a miniature contact probe were conducted. The experimental setup constructed for this case is depicted in Fig. 6.19. The miniature contact probe includes a flexure based body, piezoelectric elements (for actuation and sensing of contact) and a contact tip. The system is excited using the IES and the response is measured using the LDV system.

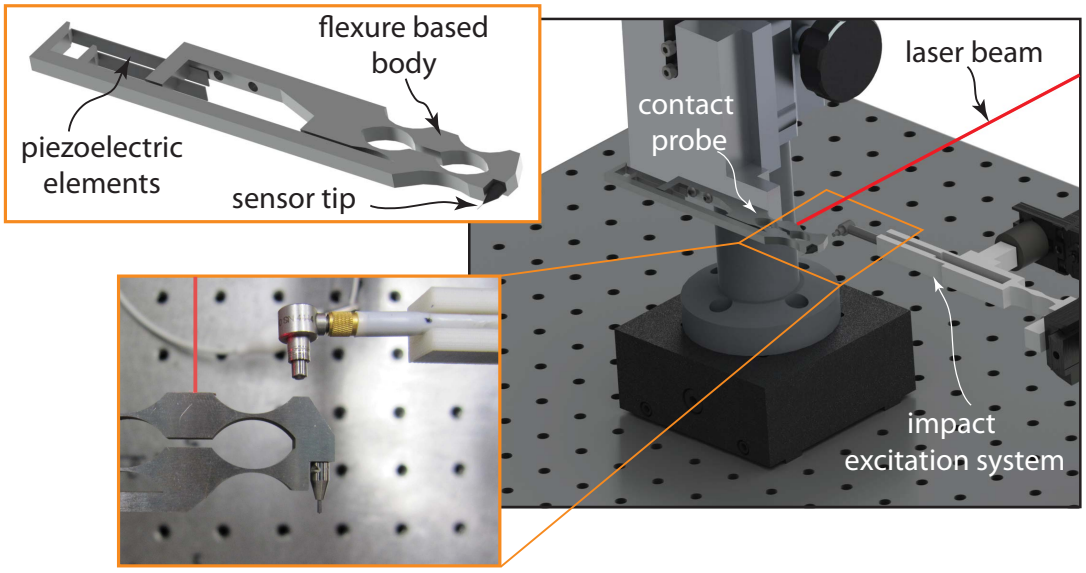

Figure 6.19: Modal testing of a miniature contact probe using the IES.

To prevent damage to the fragile features and piezoelectric elements of the miniature contact probe, the impact force during modal testing must be kept below a specific limit. In this study, the force limit is assumed to be 10 N. To select a set of control parameters (x_o and g_o) satisfying the preliminarily set test requirements, a process map is created for each of the IES flexure geometries using the developed model (see Fig. 6.20). The coefficient of restitution is selected to be 0.95 for a steel-steel impact [116]. The impact mass was 1.8 g.

Figures 6.20(a)-6.20(c) show the no hit (gray), multiple hit (black), and single hit (white) regions for different flexure geometries. From the created process maps, any set of control parameters that fall within the single-hit region with an impact force below 10 N can be selected. One such point for each of the flexure geometry is selected (as indicated by circular markers in Figs. 6.20(a)-6.20(c)) and the associated impact force and frequency spectra are compared to those from the experiments in Figs. 6.20(d)-6.20(f). It is observed that for all the selected parameter sets, the simulation results are in excellent agreement with those obtained from experimentation.

Next, a direct comparison between the FRFs obtained using the IES with those obtained through manual hits using the miniature impact hammer is completed. Both systems are used to obtain ten impacts to remove the unbiased noise from the data. Figure 6.21 shows the obtained FRFs and the corresponding coherence plots. Importantly, when using manual hits, achieving ten single-hit impacts necessitated applying approximately 100 impacts. In contrast, all of the ten impacts were single-hit impacts when using the IES. One of the

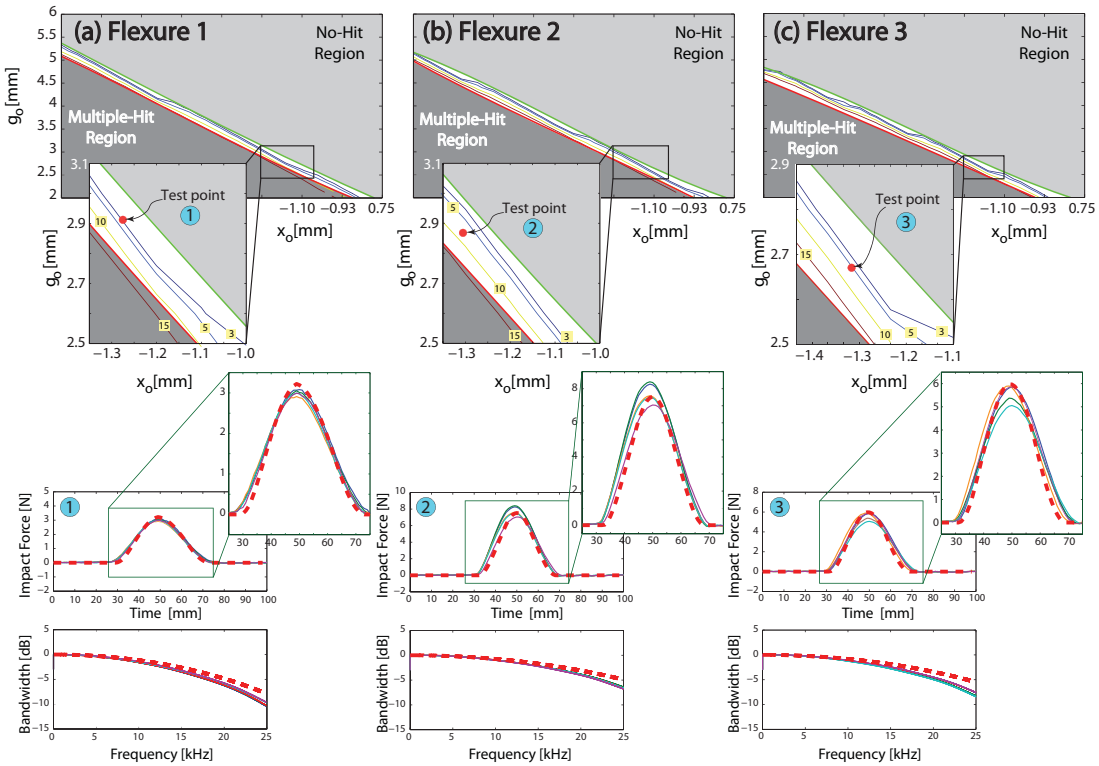

Figure 6.20: **(a-c)** Contour plots generated for control parameter selection for experimentation on the contact probe. **(d-f)** Comparison of simulation and experimental results for the selected control parameter sets (solid lines: experimental results, dashed line: simulation result).

main difficulties in performing the experiments using manual impacts was due to the small thickness of the contact probe (4 mm): This confirms a specific challenge in modal testing of miniature structures and the associated need for the IES system. As such, it can be concluded that the IES provides an effective means to apply impact excitations for modal testing of miniature structures.

6.8 Summary and Conclusions

This chapter has presented the design and evaluation of a novel impact excitation system (IES) for modal testing of miniature structures. The IES enables obtaining high frequency-bandwidth and controlled force excitations to miniature structures in a repeatable fashion. The system includes a flexure-based body that hosts an instrumented (force sensor) impact tip and an electromagnetic mechanism to provide initial deflection to and release of the body. To select system parameters that yield single-hit impacts with specified bandwidth and force

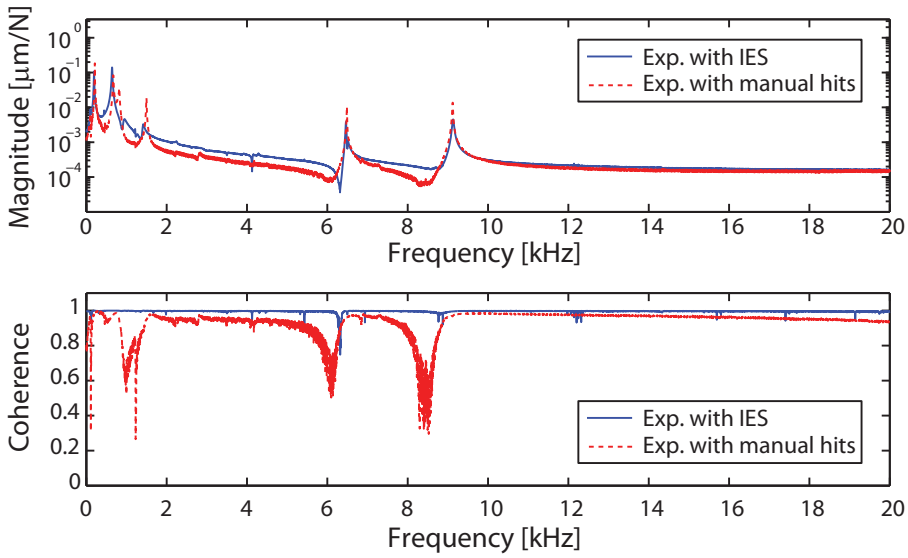

Figure 6.21: FRFs and corresponding coherence plots obtained using the designed IES (solid lines) and manual hits (dashed lines).

magnitude, a dynamic model of the IES is developed and experimentally validated. Using this model, process maps that relate the system parameters to impact bandwidth and force magnitude are constructed. The excitations from the IES and a (manually used) miniature impact hammer are compared. The application of the IES is demonstrated through modal testing of a precision contact probe.

The following specific conclusions are drawn from this work;

- The dynamic model of the IES effectively captures the behavior of the system, including hit type (no, single, or multiple hits), impact force magnitude, and impact bandwidth. As such, the model can be used effectively to identify system parameters that will produce single-hit impacts with specified bandwidth and force magnitude. Using the presented model, process maps that relate the system response metrics to the IES parameters can be generated; the process maps provide an effective means of user guidance for selecting appropriate control parameters for single-hit impacts.

- The impact excitations applied using the IES (on a rigid cast-iron block) produce very repeatable impact locations, impact forces, and impact bandwidths. In comparison to the manual application of a miniature impact hammer, the IES brings significant improvements in terms of repeatability, bandwidth, force-magnitude control, and testing procedure (reduced testing time). As a result, excellent coherence values are obtained when using the IES.

- For a set of parameters, the IES is shown to reach an excitation bandwidth of 25 kHz during the experiments. A parametric study of the IES (with limited range of parameters) indicated that impact bandwidths above 43 kHz can be obtained. Similarly, the impact forces within 1 N to 19 N (and above) can be obtained. Furthermore, through judicious choice of system parameters, the impact bandwidth and force magnitude can be selected independently.

- The application of the IES is demonstrated through modal testing of a miniature contact probe, which indicated that the IES can be used to obtain high quality frequency response functions, even for the anti-resonance regions.

Overall, it is concluded that the presented IES system can be used to provide repeatable, controlled-force, and high-bandwidth excitations for modal testing of miniature systems. Furthermore, the developed model can be used to successfully and rapidly identify parameters that will result in single-hit impacts with specified impact force and bandwidth or to evaluate the performance of different design alternatives for the IES.

Chapter 7

Dynamics of Ultra-High-Speed (UHS) Spindles used for Micromachining

"Six months in the lab can save an afternoon in the library."

-Albert Migliori

Micromachining dynamics commonly dictate the attainable accuracy and throughput that can be obtained from micromachining operations. The dynamic behavior of miniature UHS spindles used in micromachining critically affects micromachining dynamics. As such, there is a strong need for effective techniques to characterize the dynamic behavior of miniature UHS spindles. This chapter presents a systematic experimental approach to obtain the speed-dependent two-dimensional dynamics of miniature UHS spindles through experimental modal analysis.

7.1 Experimental Setup

Figure 7.1 shows the testbed constructed to perform experimental modal analysis of miniature UHS spindles. The miniature UHS spindle under examination is placed on a cast iron platform. An aluminum frame is constructed around the spindle to allow attaching the fiber-optic measurement lasers and associated optics. The entire experimental setup is placed on a vibration isolation table (Newport RS 4000 with tuned damping) to eliminate potential external effects from noise.

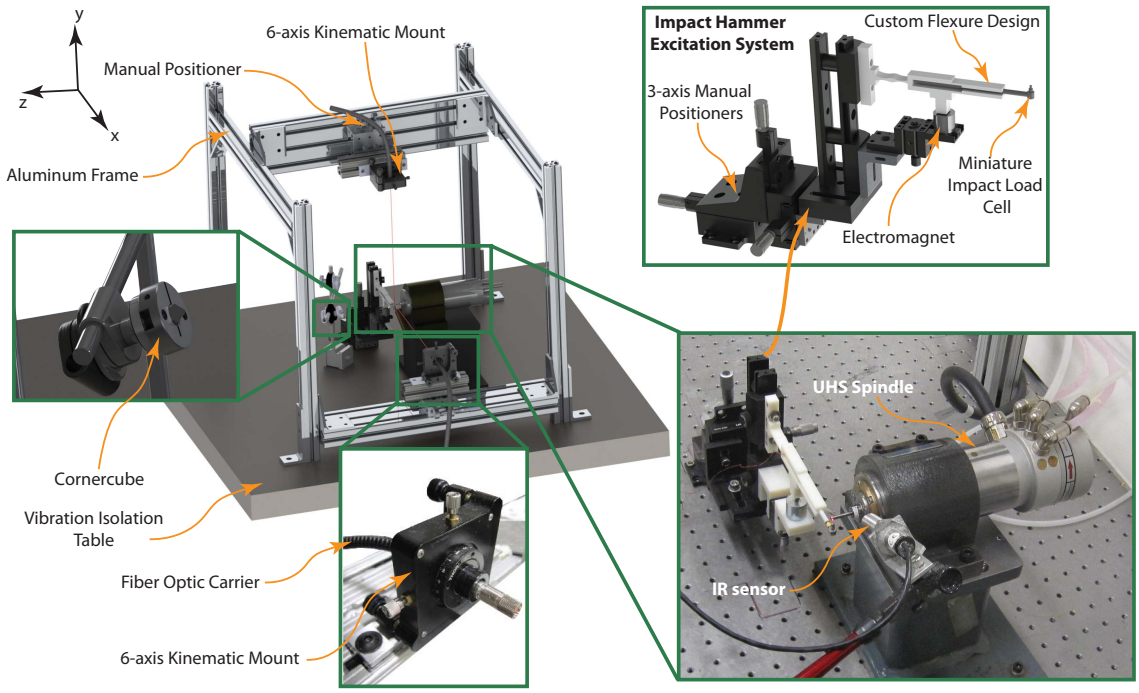

Figure 7.1: The experimental setup for obtaining speed-dependent dynamics of miniature UHS spindles.

7.1.1 Dynamic excitations

To provide dynamic excitations to the spindle in two mutually orthogonal (horizontal and vertical) directions, the IES described in Chapter 6 is used. In designing the IES, the excitation bandwidth, the amplitude of the impact force, and repeatability of the impacts are the main considerations. The bandwidth of the impact excitations is required to capture the dynamic excitations (up to 20 kHz) from forces experienced during micromachining. Also, the impact force magnitudes should be small (preferably ≤ 20 N) so that no physical damage is imparted on the miniature UHS spindle. Lastly, the excitations should be repeatable in terms of bandwidth, force magnitude, and the impact location —especially considering increased sensitivity to uncertainties due to the miniature size of the spindles and the artifacts.

To identify the appropriate system parameters for the IES for exciting the dynamics of the UHS spindle being tested, the methodology described in Chapter 6 is followed. This methodology involves the use of a simulation framework, which includes a dynamic model of the flexure-based body and the impact tip, an empirical model of the electromagnetic force and damping, and a Hertzian model of the impact event.

Figure 7.2 shows a set of ten impact forces and associated frequency spectrum obtained

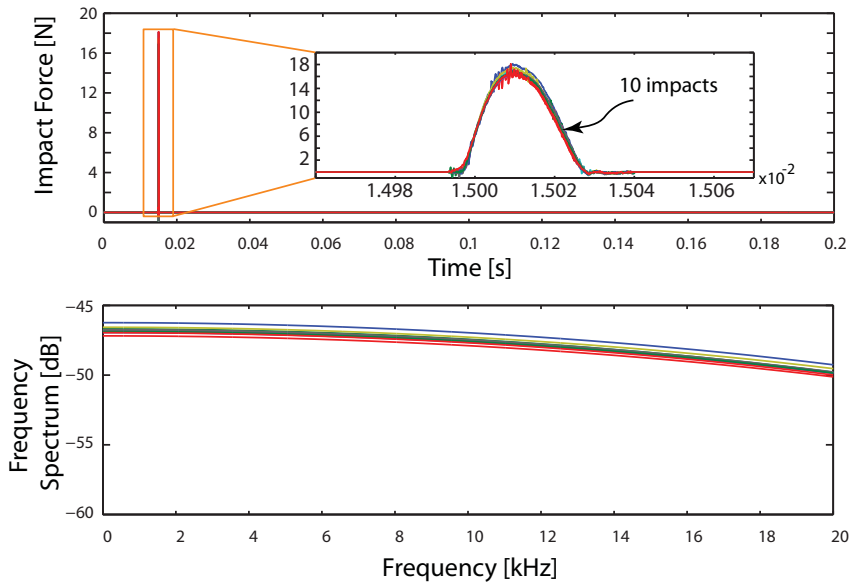

Figure 7.2: Excitation force applied at the tip of the cylindrical artifact in time (top) and frequency (bottom) domain (for a 5 mm overhang length and 50,000 rpm spindle speed).

when providing excitations to the miniature UHS spindle. A statistical analysis performed to assess the repeatability of the impact excitations showed that the average impact force magnitude and associated standard deviation are 17.2 N and 0.5 N, respectively. Furthermore, the bandwidth of all of the impact excitations are above 20 kHz. Therefore, the use of the IES allows providing repeatable dynamic excitations to the miniature UHS spindle with a controlled force magnitude and sufficient bandwidth.

7.1.2 Measurement of dynamic response

The response of the system in the horizontal (x) and vertical (y) directions are measured simultaneously by two independent fiber optic LDVs (Polytec® MSA-400). Each fiber optic LDV system includes differential fiber-optic carriers that enables both absolute and relative measurement of motions. To configure the x and y lasers in a mutually perpendicular arrangement, each laser fiber is attached to a six-axis kinematic mount (see Fig. 7.1), and an alignment procedure is followed (see Section 7.1.4 below). The six-axis kinematic mounts provide independent translational (within ∓ 1 mm range) and angular (within ∓ 5 degrees range) motions. This approach, which involves conducting measurements along the two-mutually orthogonal directions using stationary sensors, is referred as a *fixed-sensitive* measurement [123].

Since the measurements are performed on a rotating artifact, in addition to the dynamic

response arising from the impact excitation, *unwanted spindle motions* arising from the tool-spindle centering errors (tool-attachment erros) and the spindle error motions (radial, axial, and tilt motions at the measurement location) will be present in the measured displacement signal [20, 85]. To characterize the dynamic behavior of the spindle, the dynamic response associated with the provided excitation should be isolated. For this purpose, to remove the unwanted spindle motions from the measured data, an infrared (IR) sensor (Monarch infrared optical sensor), which provides a reference for the angular position of the artifact, is utilized in the experimental setup. The details of the procedure for isolating the dynamic response is given Section 7.1.6.

7.1.3 Data acquisition

A data acquisition system consisting of a National Instruments PXI-1033 chassis with a PXI-6259 data acquisition board is used to identify the dynamics of the miniature UHS spindles. A LabView^{TM} based code is developed to execute various experimental and post-processing tasks that include acquiring the impact excitation force and the two (orthogonal) displacement signals (measured by the fiber optic LDVs), generating the control signal for the electromagnet (for the automated release mechanism of the IES), windowing of the excitation force, and frequency-domain processing of the acquired signals.

7.1.4 Laser beam alignment

To identify the spindle dynamics in two dimensions, the measurements need to be performed in two mutually orthogonal directions. Thus, the accurate alignment of laser beams in mutually orthogonal directions is highly critical. In the alignment procedure, the voltage signals that indicates the intensity of the reflected laser beam is used. The amplitude of the voltage signal varies with the laser beam focus and the angular orientation of the laser beam with respect to the normal of the measurement surface. The voltage signal becomes maximum if the laser beam is focused on, and perpendicular to, the measurement surface.

Figure 7.3 shows the alignment procedure for the laser beams. To align the laser beams accurately, first, a coarse alignment step is completed (see Fig. 7.3(a)). In this step, the laser beams are shined onto the precision (cylindrical) artifact and each laser beam is made perpendicular to the artifact surface using the six-axis kinematic mounts. Subsequently, a focusing objective attached to the end of the fiber-optic carrier is used to maximize the intensity of the reflected laser beam. The course alignment step only makes the laser beams perpendicular to the measurement surface (i.e., they may not be mutually orthogonal).

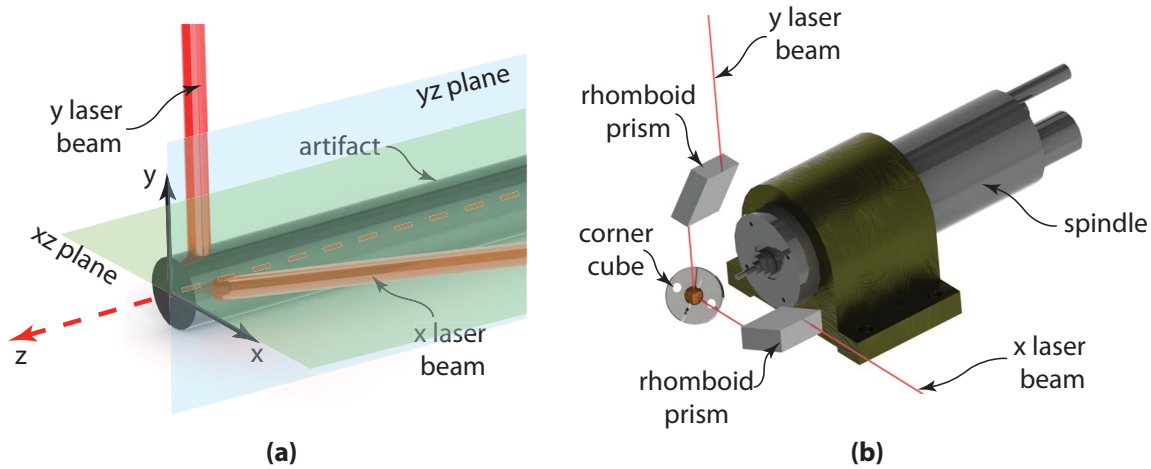

Figure 7.3: Alignment of laser beams: **(a)** coarse alignment, **(b)** fine alignment.

After completing the rough alignment step, a fine alignment procedure (see Fig. 7.3(b)) is followed to attain mutual perpendicularity of the laser beams. For this purpose, two rhomboid prisms and a corner cube are employed. The rhomboid prism is used to shift the axis of the laser beam by a fixed distance, while keeping the laser beam parallel to the original axis (in this case, the beams are shifted by 35 mm). Using the rhomboid prisms, both laser beams are shifted to shine upon the corner cube. The corner cube, which is used as the perpendicularity reference, is made from a custom fabricated retro-reflector by coating the back side with aluminum to get three mirror faces that are perpendicular to each other within 10 arc-secs. Then, the voltage signals showing the intensity of the reflected laser beam is maximized by adjusting the orientation of the corner cube and adjusting the angular orientation using the kinematic mounts. Therefore, the perpendicularity of the two laser beams are achieved. To check the perpendicularity with respect to the artifact, the rhomboid prisms are removed and the laser beams are moved back to the artifact surface. To maximize the intensity of the reflected laser beams, only the translational motions of the kinematic mounts are used, since, in the previous step, the laser beams are made perpendicular to each other. Therefore, completion of the alignment procedures ensures that the laser beams are both perpendicular to the measurement surface and orthogonal with respect to each other.

The unwanted spindle motions depend upon the spindle speed [20, 124]. Therefore, axial-, radial-, and tilt-axis shifts may occur in the measurement location, which reduces the strength of reflected laser signal. In such a case, the translational motions of the six-axis kinematic mounts are used to regain the maximum signal strength for measurement.

7.1.5 Test procedure

To identify the dynamics of miniature UHS spindles, experimental modal analysis is performed to obtain FRFs (both direct and cross terms) in two mutually orthogonal directions. Figure 7.4 shows the experimental procedure, where the red lines are the LDV laser beams that measure the motions. The system is excited at three different locations (points A, B, and C that are separated from each other by a distance S) along the length of the artifact and simultaneous measurements in x and y directions are performed at point A. From these measurements, direct and cross receptances are obtained and used to obtain rotational FRFs at the artifact tip. Although the obtained dynamic response includes both the spindle and the attached artifact, measured dynamic response at the artifact tip is referred as the spindle dynamics in this study. This is justifiable since for each spindle-collet-tool combination, a tool shank will be included in the system. As such, the measured dynamics of the spindle-collet-artifact can be coupled (e.g., using substructuring techniques) with the dynamics of the tool beyond the 5 mm overhang length to obtain the tip point FRFs of the spindle-collet-tool assembly.

The FRF matrix for the measurement points (A, B, and C) can be expressed as

$$[G] = \begin{bmatrix} R_{AA} & R_{AB} & R_{AC} \\ R_{BA} & R_{BB} & R_{BC} \\ R_{CA} & R_{CB} & R_{CC} \end{bmatrix} \tag{7.1}$$

where

$$R_{ij} = \begin{bmatrix} H_{ij}^{xx} & H_{ij}^{xy} & L_{ij}^{x\phi_x} & L_{ij}^{x\phi_y} \\ H_{ij}^{yx} & H_{ij}^{yy} & L_{ij}^{y\phi_x} & L_{ij}^{y\phi_y} \\ N_{ij}^{\phi_x x} & N_{ij}^{\phi_x y} & P_{ij}^{\phi_x\phi_x} & P_{ij}^{\phi_x\phi_y} \\ N_{ij}^{\phi_y x} & N_{ij}^{\phi_y y} & P_{ij}^{\phi_y\phi_x} & P_{ij}^{\phi_y\phi_y} \end{bmatrix} . \tag{7.2}$$

Here, the first superscript represents the measurement degree of freedom (DOF) and the second superscript represents the excitation DOF. Similarly, the first subscript denotes the location where the response is measured from and the second subscript denotes the location at where the force/moment is applied. H is the FRF relating the displacement to the applied force, L is the FRF relating the displacement to the applied moment, N is the FRF relating the angular motion to the applied force, and P is the FRF relating the angular motion to the applied moment.

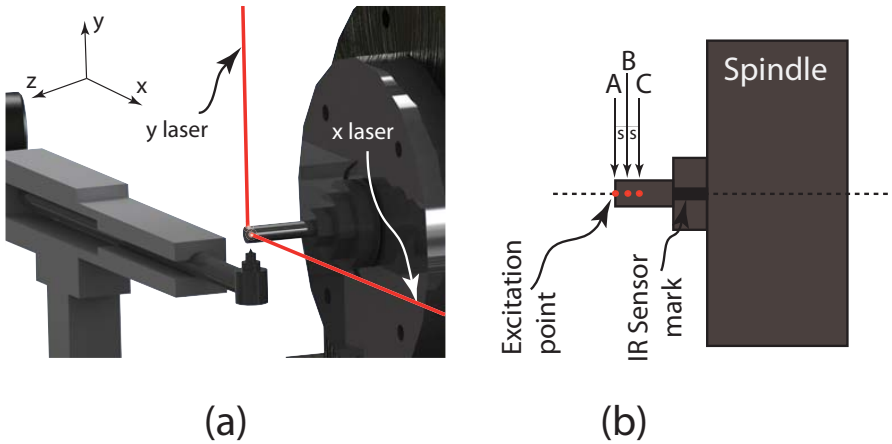

Figure 7.4: Experimental procedure: **(a)** CAD Models showing the spindle, cylindrical artifact, and the IES, **(b)** Schematic diagram indicating the impact and measurement locations.

To populate the matrix given in Eq. (7.2) for point A (which is referred as the FRF matrix for the spindle), modal tests are performed as described above. From these measurements, direct and cross receptances (H_{ij}) are calculated and used to obtain rotational FRFs (L_{AA}, N_{AA}, and P_{AA}) at the artifact tip. To calculate L (the FRF that relates the displacement to the applied moment), a second-order backward finite difference method, similar to that in [125] is followed as

$$L_{AA} = \frac{3H_{AA} - 4H_{AB} + H_{AC}}{2S} \tag{7.3}$$

where S is the distance between the measurement points. Assuming linearity, N should be equal to L from the reciprocity of the FRF matrix. The rotational FRF, P, can be found as

$$\begin{aligned} P_{AA} &= \frac{F_A}{q_A}\frac{q_A}{M_A}\frac{\Phi_A}{F_A} \\ &= \frac{1}{H_{AA}} L_{AA} N_{AA} = \frac{L_{AA}^2}{H_{AA}} \ , \end{aligned} \tag{7.4}$$

where q, Φ, F_A, and M_A are the translational and angular displacements, and the force and moment at point A, respectively.

The spindle dynamics could vary with the spindle speed and/or collet pressure. To capture such potential changes on the miniature UHS spindle dynamics, several experiments (following the described procedure) are carried out considering **(1)** different spindle speeds ranging from 50,000 rpm to 170,000 rpm with 20,000 rpm steps (a total of 7 different spindle

speeds), and **(2)** collet pressures of 621 kPa and 655 kPa. For each test condition and test location, ten repetitions are performed and averaged to remove the unbiased noise from the calculated FRFs.

7.1.6 Removal of unwanted spindle error motions

Although an ideal spindle has only one degree of freedom (DOF), which is the rotation about its rotational axis (i.e., around z axis), due to the eccentricity and tilt arising from attachment errors of the artifact (tool-spindle centering errors), and the axis of rotation errors (spindle error motions), radial motions[12] will exist in the measured signal even for a perfect artifact [20, 124]. As such, the data measured from the motion ensuing the dynamic excitation includes not only the dynamic response, but also the data arising from the unwanted spindle motions. To determine the spindle dynamics accurately, these unwanted spindle motions need to be removed from the measured data. Previously, Filiz *et al.* [46] and Cheng *et al.* [76] used a time-domain filtering approach to remove the unwanted spindle motions. However, time-domain filtering approach may not work well due to the fluctuations in spindle speed and the uncertainties in determining the cycle start and end instants (especially important at high rotational speeds). Therefore, to overcome these issues, a frequency domain filtering algorithm is developed and implemented in this study.

In this filtering approach, the measured data (Fig. 7.5(a)) is divided into two regions: Range 1 includes both the impact (dynamic) response and the unwanted spindle motions, whereas Range 2 region includes only the unwanted spindle motions (i.e., the steady part after the transient vibrations diminish). The basic idea in this frequency domain filtering approach is to remove the frequency content of the unwanted (steady-state) motions from frequency content of the transient part. If successful, this approach will isolate the dynamic response of the spindle arising from the impact excitation.

To divide the measured data into two regions while minimizing the possible signal leakage, the IR sensor data (see Fig. 7.5(b)) is used. The IR sensor data enables accurately identifying the start and end instants of each cycle. Therefore, a fixed number of (full) cycles could be taken to represent the behavior of both regions, thus preventing leakage during the calculation of Fast Fourier transform (FFT). However, the duration of each cycle may differ from each other (i.e., the length of the data for Range 1 and Range 2 may differ) due to the speed fluctuations ($\pm \sim$200 rpm). Therefore, the frequency resolution becomes

[12]The magnitude of these radial motions measured at low speeds from a surface (e.g., spindle collet or artifact) is commonly referred to as '*runout*'.

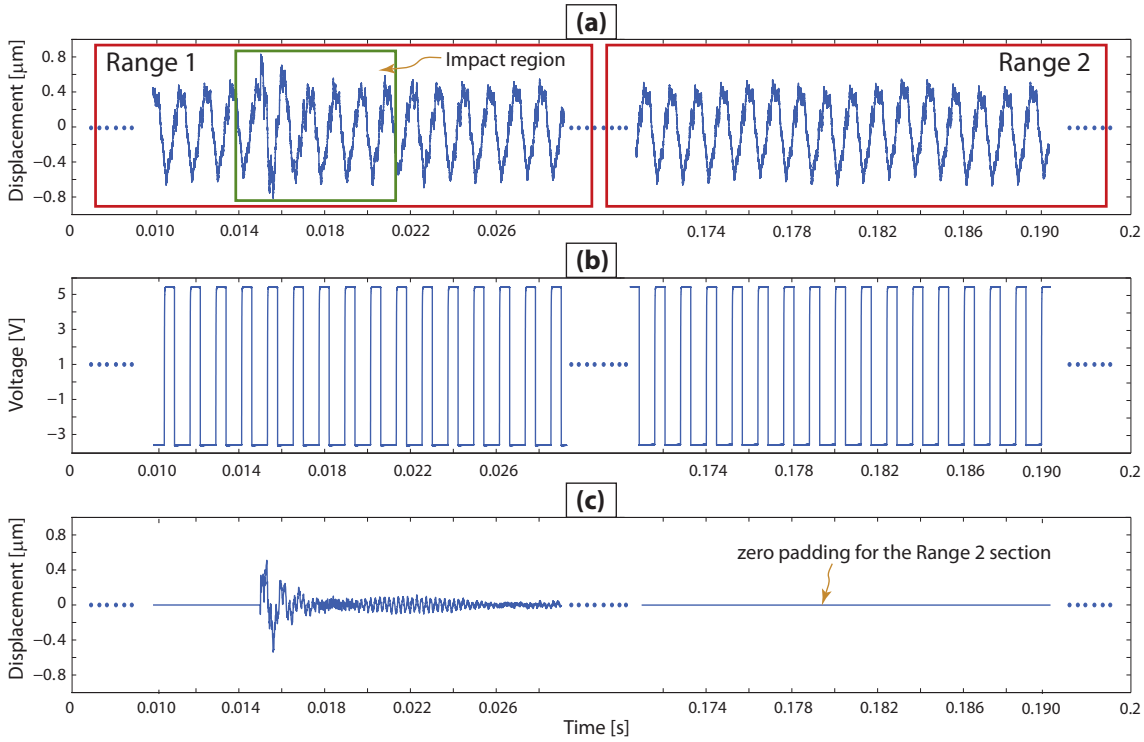

Figure 7.5: Steps of frequency domain filtering approach: **(a)** Raw displacement data, **(b)** IR sensor data, **(c)** Response of the spindle due to the impact (filtered data).

different after calculating the FFT of each region. To address this issue, an interpolation algorithm is used to match the frequency resolution between the two ranges. Figure 7.6 shows the FFT of each region.

As seen in Figs. 7.6(a) and 7.6(b), the FFT of the Range 1 data includes the frequency content of impact response (the damped peaks) and the unwanted spindle motions (the sharp narrow peaks). To determine the exact frequency (location) of the sharp narrow peaks, the FFT of the Range 2 data is used. Once the exact frequencies of the unwanted spindle motions are found, they are filtered out using a linear interpolation of the complex values neighboring the sharp peaks in the FFT of the Range 1 data [126]. Using this procedure, the frequency spectrum of the dynamic response is isolated (see Fig. 7.6(c)). To obtain the time domain dynamic response of the spindle, inverse FFT of the frequency spectrum of the isolated data is calculated. Furthermore, a zero padding procedure is applied to match the length of the isolated data to the length of the raw data. Figure 7.5(c) shows the time domain dynamic response of the spindle after the removal of unwanted spindle motions.

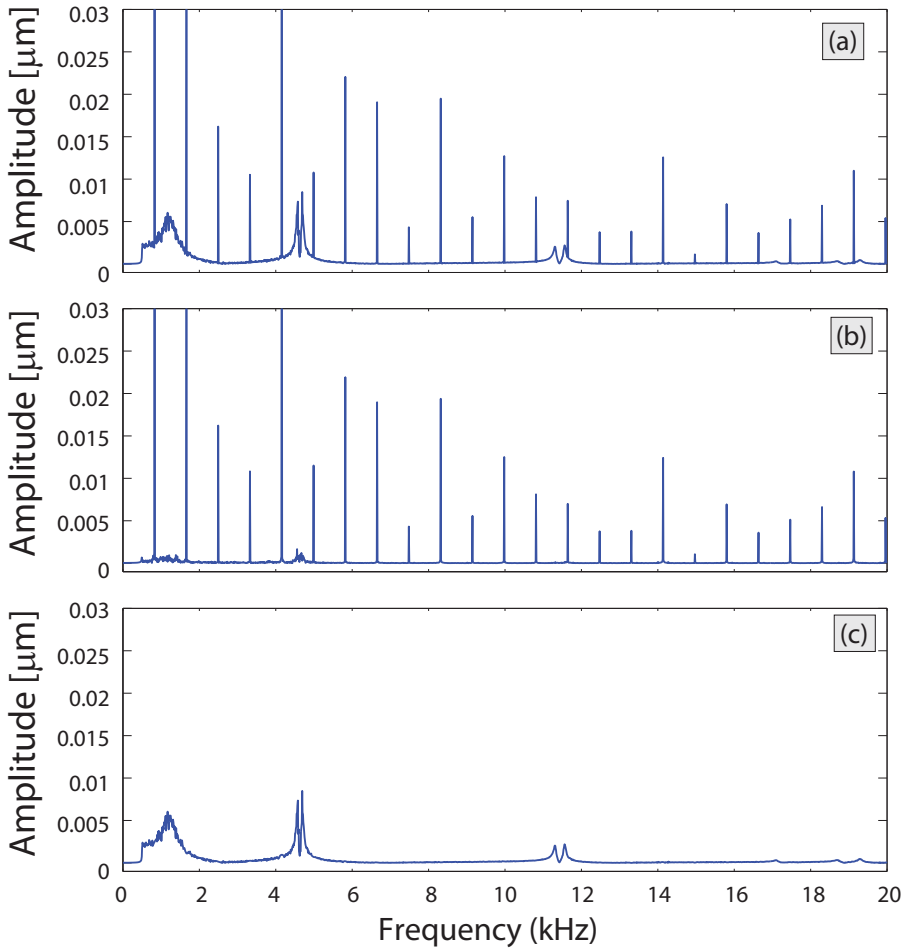

Figure 7.6: Frequency spectrum of: **(a)** Range 1 that includes both the dynamic response and the unwanted spindle motions, **(b)** Range 2 that includes only the unwanted spindle motions, and **(c)** filtered data that include only the dynamic response.

7.1.7 Processing of measurement data to obtain FRFs

To obtain the spindle dynamics in terms of the FRFs, the measured impact force and filtered displacement signals are used. Instead of directly calculating the ratio of the Fourier transforms of the input signal (impact force data) to output signal (displacement measurement), auto and cross power-spectra of each signal are calculated to minimize the effect of noise. In this approach, the FRF is calculated using the arithmetic mean of the lower (H_1) and upper (H_2) bound FRFs as

$$H_{ik}(jw) = \frac{1}{2}\left[H_{1_{ik}}(jw) + H_{2_{ik}}(jw)\right] \tag{7.5}$$

where

$$H_{1_{ik}}(jw) = \frac{\bar{S}_{R_k F_i}(jw)}{\bar{S}_{R_k R_k}(jw)} \quad \text{and} \quad H_{2_{ik}}(jw) = \frac{\bar{S}_{F_i F_i}(jw)}{\bar{S}_{F_i R_k}(jw)}. \tag{7.6}$$

Here, the subscripts (i and k) indicate the measurement and excitation directions, respectively. H_1 is the ratio of the averaged cross spectrum $\bar{S}_{R_k F_i}(jw)$ to the averaged input autospectrum $\bar{S}_{R_k R_k}(jw)$. Similarly, H_2 is the ratio of the averaged output autospectrum $\bar{S}_{F_i F_i}(jw)$ to the averaged backwards cross spectrum $\bar{S}_{F_i R_k}(jw)$.

7.2 Results and Discussion

In this section, the presented experimentation methodology is applied to identify the dynamics of a miniature UHS spindle (ASC 200 Fischer Precise air-bearing spindle). *First*, the step-by-step procedure for obtaining the FRF matrix (see Eq. (7.2)) representing the spindle dynamics is demonstrated when the spindle is rotated at 50,000 rpm spindle speed. *Second*, the speed dependent spindle dynamics is investigated through experiments at seven different spindle speeds between 50,000 rpm and 170,000 rpm with 20,000 rpm steps. And *third*, the effect collet pressure is analyzed, where the experiments are performed for two collet pressure values of 621 kPa and 655 kPa.

7.2.1 Obtaining spindle dynamics

In this section, the procedure used for obtaining the dynamics of the miniature UHS spindle is presented. As described above, in this work, the spindle dynamics refers to the dynamic behavior measured at the tip of the artifact, and include dynamics of the spindle and the attached artifact with 5 mm overhang. The spindle dynamics is represented by a 4×4 FRF matrix (see Eq. (7.2)) calculated at point A (tip point of the artifact). The upper left quarter of this matrix that includes the force-to-displacement FRFs (H_{AA}) is directly obtained by exciting the system at point A. In this example, the overhang length of the artifact was set to 5 mm. To populate the remaining part of the FRF matrix (i.e., the rotational FRFs), the measurement data obtained from the tests performed at points A (5 mm away from the collet —the tip point), B (4 mm away from the collet), and C (3 mm away from the collet) are used together to determine the rotational FRFs (L_{AA}, N_{AA}, and P_{AA}) through a finite difference approach (see Eq. (7.3)).

In the first step, the IES was arranged to excite the spindle-collet-artifact system at

point A (see Fig. 7.4). The impact excitation was first applied along the x direction, and the LDV measurements were made from both x (used to calculate the direct FRF, H_{AA}^{xx}) and y (used to calculate the cross FRF, H_{AA}^{yx}) directions at the same axial plane as that includes point A. Subsequently, the impact excitation was moved to the y direction by rotating the IES by 90 degrees, and similar experiments were performed while impacting along the y direction (used to calculate the direct (H_{AA}^{yy}) and cross (H_{AA}^{xy}) FRFs). To minimize the effect of unbiased noise, ten repetitions were performed and averaged for the calculation of each FRF.

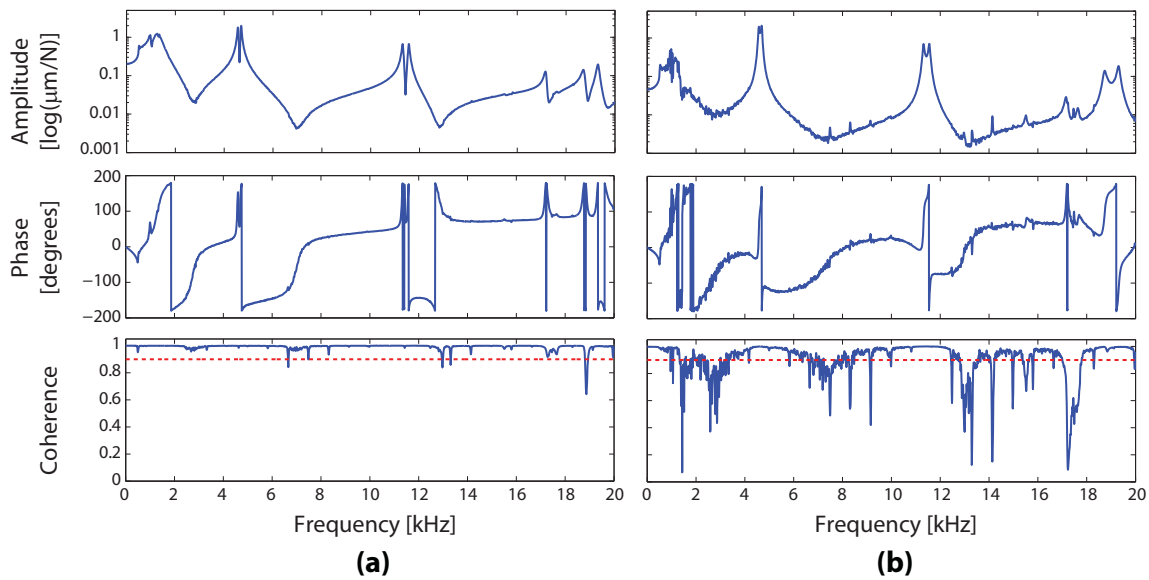

Figure 7.7: **(a)** Direct (H_{AA}^{yy}), and **(b)** cross (H_{AA}^{xy}) FRFs calculated at point A for the spindle speed of 50,000 rpm.

In the second step, the frequency domain filtering algorithm described above is applied to isolate the dynamic response by removing the unwanted spindle motions from the measured data. This isolated response is then used to calculate the FRFs from Eqs. (7.5)-(7.6). The amplitude and phase plots of the obtained direct (H_{AA}^{xx}) and cross (H_{AA}^{yx}) FRFs measured at point A, as well as the corresponding coherence plots, are given in Fig. 7.7 for the spindle speed of 50,000 rpm. The dashed (red) lines in the coherence plots shows the 90% coherence value. Apart from the antiresonance regions and the regions where the actual response is very small, the coherence values are close to unity for the direct FRF within the frequency range of 0 kHz - 20 kHz (see Fig. 7.7(a)). For the cross FRF, other than the resonance regions, the very small response causes lower coherence values (see Fig. 7.7(b)). However, the coherence values for the important regions in the vicinity of resonant peaks

are consistently above 90%, and thus, are deemed satisfactory. It can be concluded that the presented filtering technique successfully isolates the dynamic response of the spindle-holder/collet-tool system from unwanted spindle motions, thereby enabling obtaining high quality direct and cross FRFs within the targeted 20 kHz bandwidth.

Next, similar measurements were performed by exciting the system at points B and C. Although the excitation location is moved to (separately along the x and y directions) points B and C, the LDV measurements remained at point A, thereby providing the required cross measurements between the points. All the obtained FRFs (from excitations on points A, B, and C in both the x and y directions) were then inserted into Eq. (7.3) to calculate the moment-to-displacement FRF (L_{AA}). Due to the reciprocity of the FRF matrix, the force-to-displacement FRF (N_{AA}) is equal to the displacement-to-moment FRF. Lastly, using Eq. (7.4), the moment-to-angular displacement FRF (P_{AA}) can be found. The 4×4 FRF matrix obtained for 50,000 rpm spindle speed is given in Fig. 7.8. Although the rotational terms seem to include a higher level of noise, it is noted that the amplitudes of the rotational terms away from the resonance regions are significantly smaller compared to the displacement-to-force terms due to the short overhang length, and thus, the axes of the corresponding FRFs are different in the given figures from those of displacement-to-force FRFs.

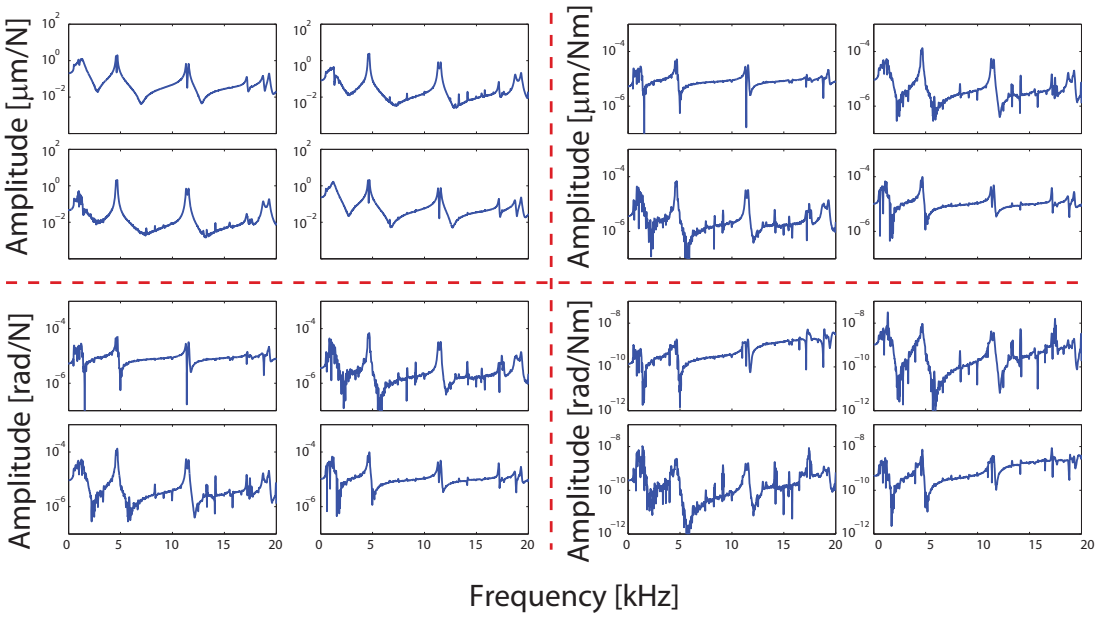

Figure 7.8: Magnitudes (in logarithmic scale) of the FRF matrix at point A for the spindle speed of 50,000 rpm.

To ensure that the obtained FRFs represent the system behavior accurately, the uncertainty of the measured complex-valued FRFs must be quantified. In this work, uncertainty quantification is performed by following the approach presented in [127]. The analysis considers the overall uncertainty consisting of statistical variations and imperfect calibration coefficients for both the impact load cell (with a calibration uncertainty of $\mp 3.7\%$) and LDV system (with a calibration uncertainty of $\mp 1\%$) sensors. To determine the uncertainty arising from the statistical variations, the FRF covariance matrix, which is composed of both the standard variances of the real and imaginary components of the FRFs and the estimated covariance between the real and imaginary components of the FRFs, is calculated. The sum of the eigenvalues of the calculated covariance matrix at each frequency is then taken as a measure of the total variance, and this sum is used to quantify the uncertainty arising from statistical variations as a scalar. To determine the uncertainty arising from imperfect calibration coefficients, the FRFs are expressed in terms of the calibration coefficients and the corresponding voltage values as described in [127]. The standard variances for the calibration coefficients are calculated by assuming a uniform distribution with 100% confidence, and the covariance matrix is computed using a bivariate form of the Gaussian error propagation law for complex numbers [128]. Similarly, the sum of the eigenvalues of this matrix at each frequency is taken as a measure of total variance and used to quantify the uncertainty due to imperfect calibration coefficients as a scalar. Then, the overall uncertainty is found by summing the scalar values calculated for the statistical variations and imperfect calibration coefficients at each frequency. As a result, it is found that the overall uncertainty is less than 3% for each of the FRFs and the uncertainty around the natural frequencies are less than 1%. Figure 7.9 shows the uncertainty analysis plots for the entire range of the calculated FRFs obtained at three different spindle speeds (50 krpm, 110 krpm, and 150 krpm) with the corresponding FRF plots. Therefore, it is concluded that the dynamic characteristics of the miniature UHS spindles can be determined reliably and repeatably within a frequency bandwidth of 20 kHz using the presented approach.

To quantitatively assess the effect of different parameters on spindle dynamics, modal parameters (natural frequencies and associated damping ratios) needs to be identified from the FRF matrix (at point A). To ensure a single characteristic equation for the entire 4×4 FRF matrix, a global curve fitting procedure based on the rational fractional polynomial method is applied [129]. This approach simultaneously captures the behavior of the entire 4×4 FRF matrix. Table 7.1 summarizes the extracted natural frequencies and associated damping ratios of the FRF matrix given in Fig. 7.8 for the first eight modes. Note that the effect of different parameters (spindle speed and collet pressure) could induce changes

Table 7.1: Natural frequencies and associated damping ratios of the FRF matrix given in Fig. 7.8.

Mode Number	Natural frequency (ω) [kHz]	Damping ratio (η) [%]
1	1.25	6.8
2	4.57	0.4
3	4.69	0.4
4	11.31	0.7
5	11.55	0.7
6	17.17	1.2
7	18.73	2.4
8	19.31	2.8

in these modal parameters. Therefore, these modal parameters can be directly used to quantitatively assess the changes in spindle dynamics.

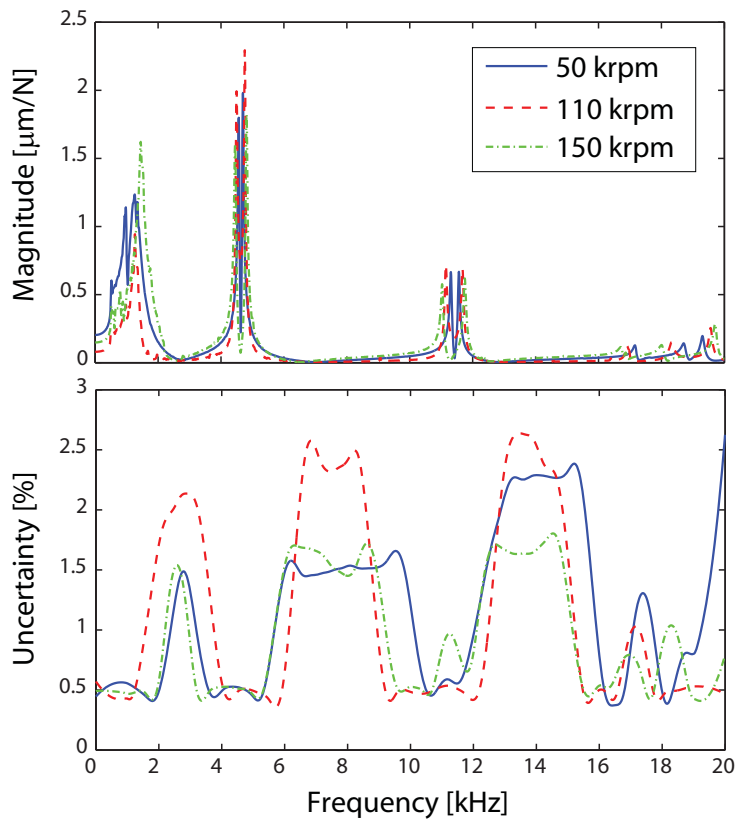

Figure 7.9: Uncertainty analysis for three different spindle speeds.

As seen in Table 7.1, the tested miniature UHS spindle has eight modes within the frequency range of interest (0 kHz - 20 kHz). The first natural frequency of the miniature UHS spindle is at 1250 Hz. The corresponding damping ratio for this mode is found to be

6.8%, which is rather a highly damped mode compared to the higher modes. Furthermore, there are closely spaced modes pairs that arise due to the gyroscopic effects. This well-known phenomenon arises from the changes in effective stiffness of two (orthogonal) bending mode pairs. The splitted mode pairs are also referred as *forward* and *backward* whirl modes [130]. More importantly, these splitted mode pairs are very lightly damped; thus, their effect on machining stability should be investigated in detail.

7.2.2 Effect of spindle speed

To study the effect of spindle speed on the dynamics of the miniature UHS spindle, the presented experimental procedure is followed for seven different spindle speeds ranging from 50,000 rpm to 170,000 rpm with 20,000 rpm steps. As an example, Fig. 7.10 and Fig. 7.11 show the H_{AA}^{xx} element of the FRF matrix at point A at different spindle speeds and the corresponding coherence plots. As observed from the coherence plot, at certain speed ranges (particularly, when the spindle speed is close to the first natural frequency of the spindle dynamics), there is increasing instants of isolated frequency pockets (especially anti-resonance areas), where the coherence drops. However, this is expected, and these isolated drops in coherence would not significantly affect the quality of FRFs. As seen from Fig. 7.11, the coherence values in the vicinity of resonant peaks are consistently above 90% for the entire tested spindle speeds, and thus, are deemed satisfactory. From Fig. 7.10, two main inferences can be made:

1. The splitting-behavior of the whirling mode pairs can easily be seen in the calculated FRFs with increasing spindle speed. The natural frequencies corresponding to 2nd-3rd mode pairs, 4th-5th mode pairs, and 7th-8th mode pairs split due to the gyroscopic effects. While the gyroscopic effects increases the stiffness for the forward modes, this effect is reversed for the backward modes (resulting a decrease in stiffness). Therefore, the bending mode pairs split into two as observed in Fig. 7.10. Furthermore, as expected the effect of rotational speed on higher modes are greater than that on the lower modes since the rotary inertia effects increase for the higher modes.

2. The modes that do not show splitting behavior are either the torsional/axial modes of the system or modes that are related to the non-rotary parts of the miniature UHS spindle. Although the effect of gyroscopic terms is small, the natural frequencies still vary with increasing speed. This is due to the fact that the gyroscopic terms are affecting the stiffness of torsional/axial modes and the torsional/axial displacements

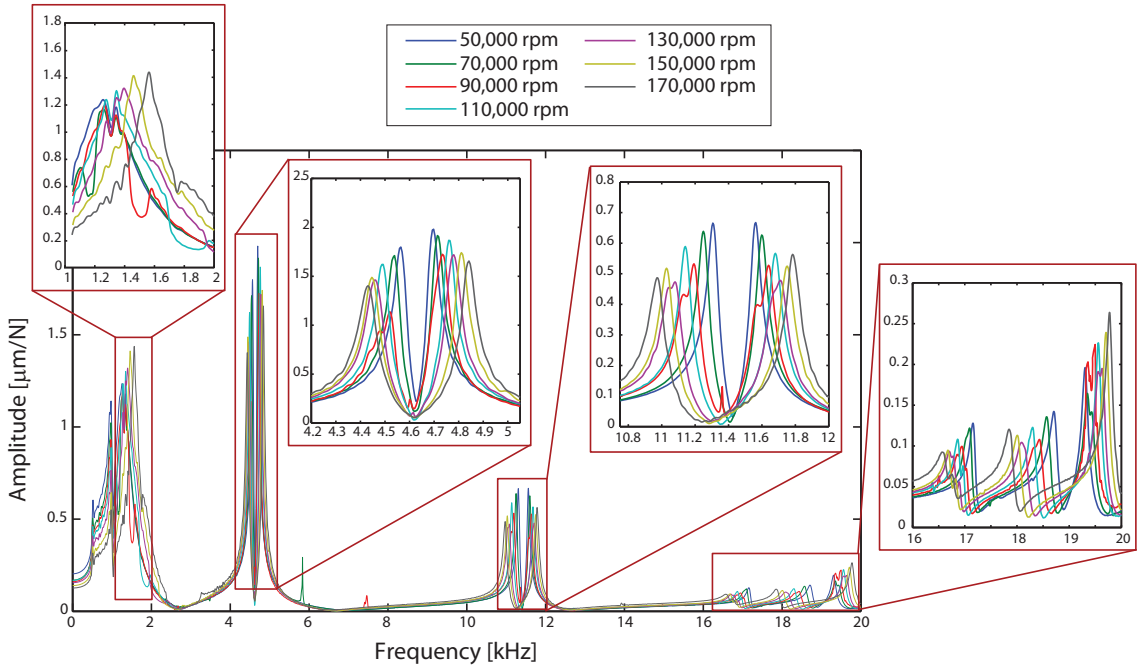

Figure 7.10: Effect of spindle speed on the amplitude of direct receptance (H_{AA}^{xx}) in the horizontal (x) direction at point A.

are coupled with the bending displacements through second order strain-displacement terms [62].

To further explore the effect of spindle speed, modal parameters of the FRFs for each spindle speed were identified (through a global curve fitting procedure described in Sec. 7.2.1). Figures 7.12(a) and 7.12(b) show the variations of natural frequencies and associated damping ratios with respect to the spindle speed, respectively. As discussed, the splitting behavior of the whirling mode pairs (2nd-3rd, 4th-5th, and 7th-8th modes) can be seen clearly (see Fig. 7.12(a)). However, the largest effect of spindle speed is on the damping ratio of the modes. Apart from the seventh mode, the damping ratio of all other modes are increasing with spindle speed. The largest increase is on the second mode (backward whirling mode of the first whirling mode pairs) with an increase of 75%. Another important result is that the damping of the first mode is more than twice of the damping ratios of the other modes. Note that these identified modal parameters are based on measured FRFs that are obtained using a fixed-sensitive direction (i.e., as seen by a stationary observer). If needed, these modal parameters can be converted to the modal parameters for a rotating sensitive direction [30, 131].

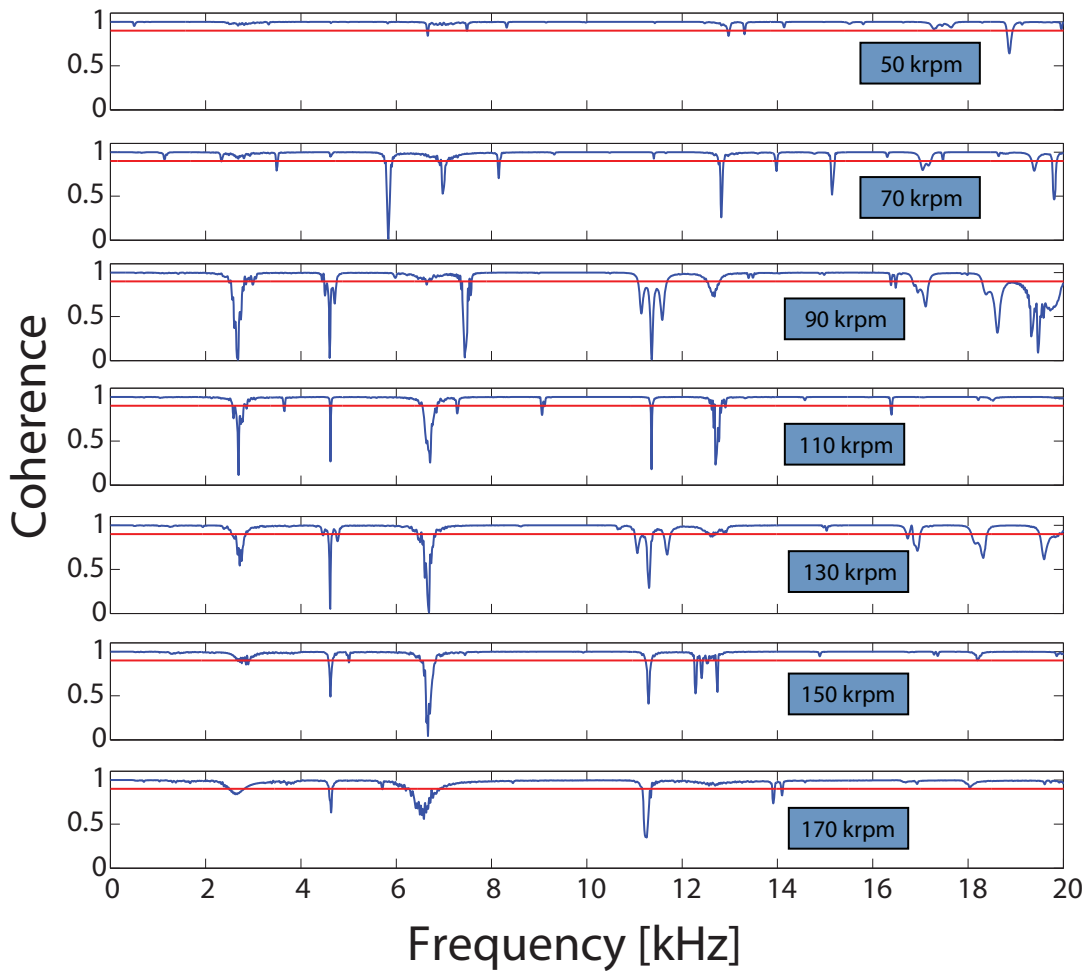

Figure 7.11: Effect of spindle speed on the coherence of direct receptance (H_{AA}^{xx}) in the horizontal (x) direction at point A.

In Fig. 7.12(a), the dashed red line shows the 1X-synchronous line. By definition, the critical speed (at which the vibration amplitudes reach their maximum values) of rotating structures can be determined as the intersections of the 1X-synchronous line with the damped natural frequencies of the structure [130]. Therefore, as observed from Fig. 7.12(a), the critical speed for the tested spindle is found to be 80,000 rpm. To validate this, a simple experimentation where the runout[13] (total indicator reading) values measured from the artifact surface at point A are determined for different spindle speeds (ranging from 50,000 rpm to 170,000 rpm with 10,000 rpm steps). Figure 7.13 shows the change of runout value as a function of spindle speed. As expected, the maximum value of the runout is observed as 4 μm at 80,000 rpm of spindle speed. This increase in measured runout arises from the

[13]The runout is a single value that represents the peak-to-peak amplitude of the measured displacement data [20].

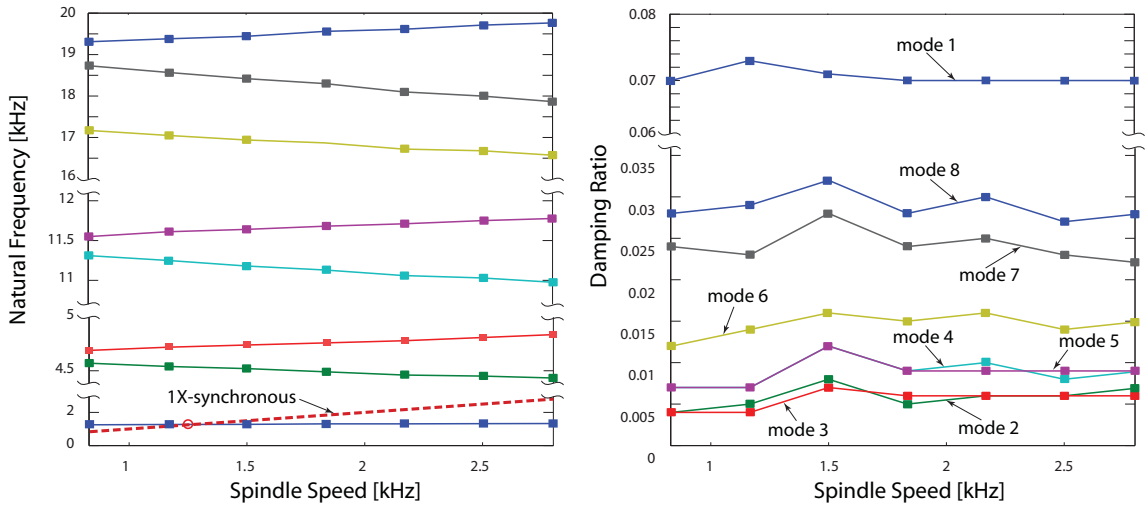

Figure 7.12: Effect of spindle speed on natural frequencies and associated damping ratios of the spindle. The dashed red line shows the 1X-synchronous line.

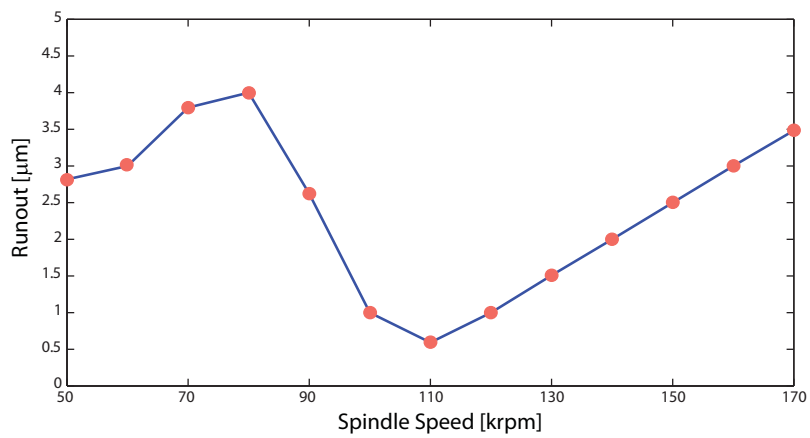

Figure 7.13: Change of runout measured from the cylindrical artifact surface at point A as a function of spindle speed.

dynamic response to the excitation provided by the rotating eccentricity, which is caused by imperfect alignment of the artifact axis to the average axis of rotation [20, 124].

7.2.3 Effect of collet pressure

The collet pressure could cause a change in the contact stiffness between the cutting tool (the portion inside the collet) and the collet. Such a change in contact stiffness has been observed to alter the dynamic response of the spindles at the macro scale [132]. To assess the effect of collet pressure on the dynamics of miniature UHS spindles, an analysis was performed, where collet pressure of 621 kPa and 655 kPa are specified , and the corresponding FRF matrices

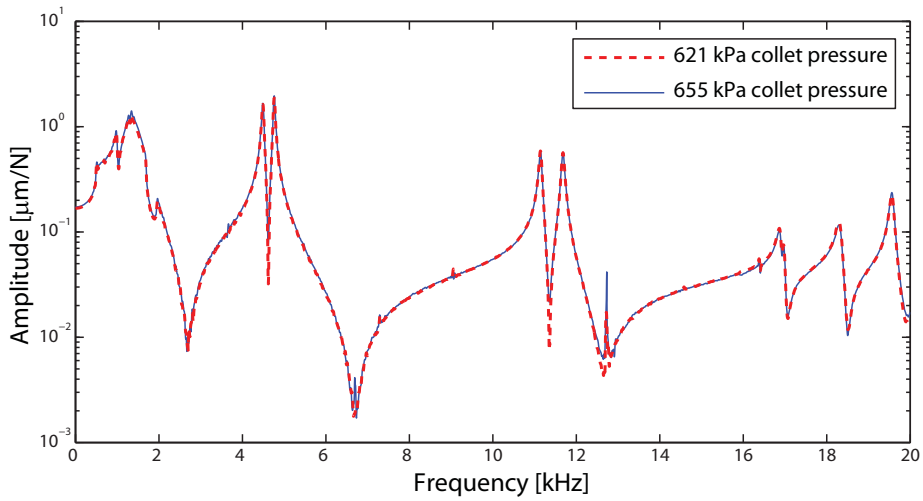

Figure 7.14: Effect of collet pressure on the H_{AA}^{xx} element of the FRF matrix for 110,000 rpm spindle speed.

at point A were calculated[14]. Figure 7.14 shows the comparison of direct receptances (H_{AA}^{xx}) obtained in the horizontal (x) direction for 110,000 rpm spindle speed.

As observed from Fig. 7.14, the collet pressure does not have a significant effect on the dynamics of this spindle. The only differences in the calculated FRFs are the antiresonance regions or the regions where the response is very small; this is expected since, at those regions, the coherence values are also below 90% coherence value.

7.3 Summary and Conclusions

This chapter presented an experimental methodology to determine the speed-dependent dynamics of the miniature UHS spindles. To provide dynamic excitation to the system, a custom-made impact excitation system (IES) is used. The IES enables controlling the impact force magnitudes and bandwidth to simultaneously achieve repeatable single-hit impacts while preventing damage to the spindle (especially to the fragile aerodynamic bearings) by limiting the impact force magnitude. To measure the dynamic motions (displacement) of the spindle, two fiber optic LDVs are utilized. Two determine the dynamics of the miniature UHS spindle in two mutually orthogonal directions, an alignment procedure is performed to ensure the perpendicularity of the two laser beams to the measurement surface and orthogonality with respect to each other. The measured total displacement data are post-processed using a frequency domain filtering approach to isolate the dynamic

[14]Based on the manufacturer's data, the miniature UHS spindle (ASC 200 Fischer Precise) has a range from 621 kPa to 655 kPa.

response by removing the displacements from the unwanted spindle motions. Then, using the isolated response of the spindle and the excitation force signal, the FRFs of the spindle are calculated. Subsequently, the effects of spindle speed and collet pressure on spindle dynamics are investigated using the developed approach.

The following specific conclusions are drawn from this work:

- The presented technique enables accurate determination of the two-dimensional speed-dependent dynamics of the miniature UHS spindles within a 20 kHz bandwidth in the form of FRFs with uncertainties less than 3% for the entire frequency bandwidth (less than 1% for the resonance regions.) The technique was demonstrated by modal testing a UHS air-bearing spindle at different speeds (up to 170,000 rpm) and collet pressures.

- The custom-designed IES provides reproducible and controlled force impact excitations up to a 20 kHz frequency bandwidth, and thus, enables effective modal testing of miniature UHS spindles.

- At high frequencies, the amplitude of the cross FRFs are comparable to those of the direct FRFs, and thus, have a strong effect on the spindle dynamics. Therefore, accurate dynamic characterization of miniature UHS spindles necessitates capturing the two-dimensional dynamic behavior.

- Spindle speed has a strong effect on both the natural frequencies and associated damping ratios of the miniature UHS spindle. As expected, the whirling mode pairs split with increasing spindle speed. This splitting behavior is more dominant for higher modes since the rotary inertia effects are larger for those modes.

- The critical speed of the miniature UHS spindle tested in this work was found to be 80,000 rpm (1333 kHz), which is in agreement with the runout values measured at different spindle speeds. Importantly, the critical speed is within the operating range of the this miniature UHS spindle.

- The experiments performed at two different collet pressures showed that the collet pressure does not have a significant effect on the dynamics of the miniature UHS spindle tested in this work within the range of allowable collet pressures.

Chapter 8

Modeling and Experimentation for Three-Dimensional Dynamics of Macro-scale Endmills

"Coming together is a beginning; keeping together is progress; working together is success."

-Henry Ford

This chapter presents a model for the three-dimensional (3D) dynamic response of endmills while considering the actual fluted cross-sectional geometry and pretwisted shape of the tools. The model is solved using the spectral-Tchebychev (ST) technique. The bending and the coupled torsional-axial behavior of four different fluted endmills is compared to finite element model (FEM) predictions and experimental results obtained using modal testing under free-free boundary conditions. To demonstrate its application, the 3D-ST model for the fluted section of a commercial endmill is coupled to the spindle-holder to predict the tool-point dynamics using receptance coupling substructure analysis (RCSA) with a flexible connection. The coupled model is validated through experiments.

8.1 Modeling and Spectral-Tchebychev Solution of Macro-scale Endmill Dynamics

Figure 8.1 shows the parameterized geometry of a traditional macro-scale endmill. The diameter of the shank section is commonly referred to as the tool diameter, d_s. Other

geometric parameters include the helix angle Ψ, the shank length L_s, the flute length L_f, number of flutes, and the cross-sectional geometry of the fluted region.

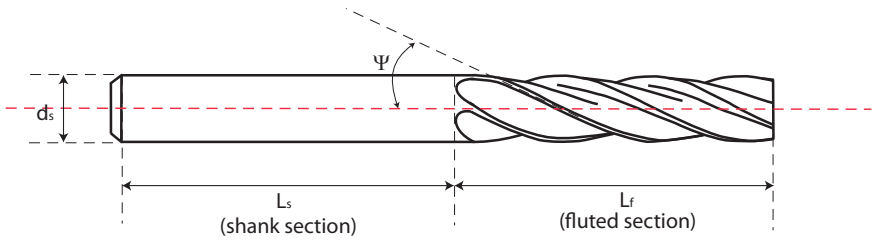

Figure 8.1: Macro-endmill geometry.

Due to its simple circular cross-section, the axial, torsional, and bending deflections of the shank region are uncoupled. Thus, an appropriate 1D beam models (e.g., the Timoshenko beam model) is sufficient to describe the dynamics of the shank. However, the fluted section with its pretwisted geometry and complex cross-section causes the axial and torsional deflections to be coupled. Furthermore, unlike those of the shank portion, bending deflections of the fluted portion are not symmetric. As a result, accurately capturing the dynamic behavior of the fluted section necessitates use of 3D modeling techniques. Therefore, to simultaneously achieve numerical efficiency and modeling accuracy, similar to the micro endmill case, a 1D model for the shank and a 3D model for the fluted section are used. The extended Hamilton's principle is applied to obtain the IBVP for the each of the shank and fluted sections. The complete model is then obtained by combining the shank (1D) and fluted (3D) portions through CMS as described in the previous chapters.

8.2 Receptance Coupling Substructure Analysis

To demonstrate the application of the 3D-ST model for obtaining the tool-point dynamics, the RCSA technique is used. Figure 8.2 shows the schematic of the THSM assembly used for experimental validation. The free-free response of the fluted portion of the tool was obtained analytically by the 3D-ST technique. Using the three-component RCSA technique for tool point dynamics prediction [23], the modeled holder was coupled to the archived spindle-machine dynamics and this result was subsequently coupled (using a flexible connection) to the free-free response of the tool. The component coordinates are identified in Figs. 8.3 and 8.4.

The receptance matrices for the assembly, G_{ij}, and substructures, R_{ij}, can be represented as shown in Eq. (8.1), where ω is the frequency, X_i and x_i are the assembly and substructure

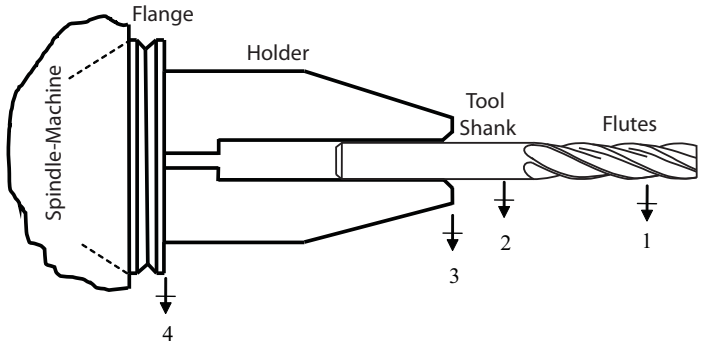

Figure 8.2: THSM assembly and coordinates.

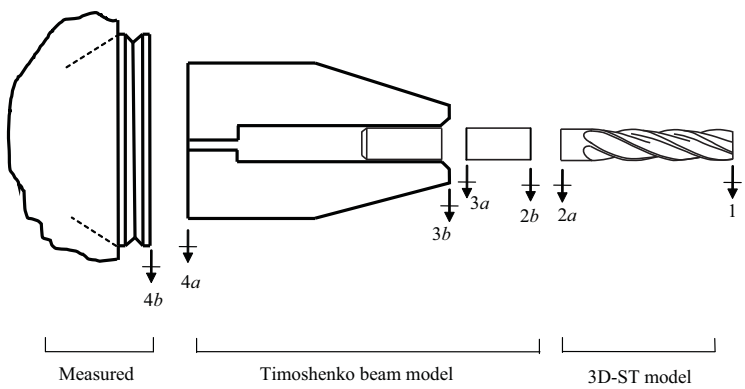

Figure 8.3: RCSA components with coordinates.

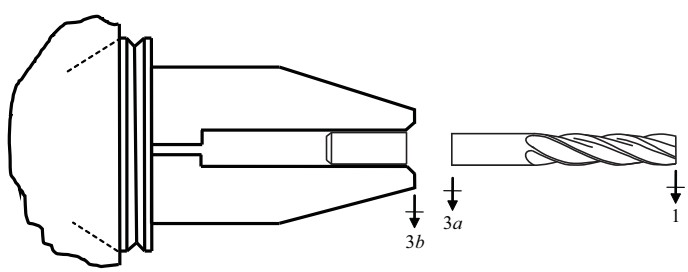

Figure 8.4: Component coordinates for flexible coupling.

displacements at the coordinate location i, Θ_i and θ_i are the assembly and substructure rotations, F_j and f_j are the assembly and substructure forces applied at the coordinate location j, and M_j and m_j are the assembly and substructure and moments.

$$G_{ij}(\omega) = \begin{bmatrix} H_{ij} & L_{ij} \\ N_{ij} & P_{ij} \end{bmatrix} = \begin{bmatrix} \frac{X_i}{F_j} & \frac{X_i}{M_j} \\ \frac{\Theta_i}{F_j} & \frac{\Theta_i}{M_j} \end{bmatrix} \quad and \quad R_{ij}(\omega) = \begin{bmatrix} h_{ij} & l_{ij} \\ n_{ij} & p_{ij} \end{bmatrix} = \begin{bmatrix} \frac{x_i}{f_j} & \frac{x_i}{m_j} \\ \frac{\theta_i}{f_j} & \frac{\theta_i}{m_j} \end{bmatrix}. \tag{8.1}$$

Using RCSA, the assembly dynamics at coordinate 1 is obtained in two steps. First, the

modeled free-free receptances of the holder-shank component are coupled to the free-free receptances of the remainder of the tool (fluted part) using Eqs. (8.2)-(8.5).

$$G_{11}(\omega) = R_{11}(\omega) - R_{12a}(\omega)\left[R_{2b2b}(\omega) + R_{2a2a}(\omega)\right]^{-1} R_{2a1}(\omega) \tag{8.2}$$

$$G_{3a1}(\omega) = R_{3a2b}(\omega)\left[R_{2b2b}(\omega) + R_{2a2a}(\omega)\right]^{-1} R_{2a1}(\omega) \tag{8.3}$$

$$G_{3a3a}(\omega) = R_{3a3a}(\omega) - R_{3a2b}(\omega)\left[R_{2b2b}(\omega) + R_{2a2a}(\omega)\right]^{-1} R_{2b3a}(\omega) \tag{8.4}$$

$$G_{13a}(\omega) = R_{12a}(\omega)\left[R_{2b2b}(\omega) + R_{2a2a}(\omega)\right]^{-1} R_{2b3a}(\omega) \tag{8.5}$$

This coupling result represents the tool model with end coordinates 1 and $3a$ (G_{11}, G_{13a}, G_{3a3a}, and G_{3a1}). Second, the modeled free-free receptances of the holder with portion of the shank inside it is coupled to the spindle machine receptances.

$$G_{3b3b}(\omega) = R_{3b3b}(\omega) - R_{3b4a}(\omega)\left[R_{4b4b}(\omega) + R_{4a4a}(\omega)\right]^{-1} R_{4a3b}(\omega) \tag{8.6}$$

The free-free receptances are then considered as a component, using the receptance matrices R_{11}, R_{13a}, R_{3a3a} and R_{3a1}. G_{3b3b} is considered as R_{3b3b}. Third, the holder-spindle-machine component is then flexibly coupled to the tool using translational and rotational spring constants assembled in the stiffness matrix k. The RCSA equation for the flexible coupling tool point FRF [133] is provided in Eq. (8.7).

$$G_{11}(\omega) = R_{11}(\omega) - R_{13a}(\omega)\left[R_{3b3b}(\omega) + R_{3a3a}(\omega) + \frac{1}{k}\right]^{-1} R_{3a1}(\omega) \tag{8.7}$$

Identification of the stiffness matrix k is discussed in section 8.6.

8.3 Experimental Methods

This section describes the experimental setup and procedures used for validating the presented 3D-ST solution. For this purpose, a set of modal tests were conducted on the four different endmills described in Table 8.1. Each of the four-flute endmills has different geometries (shank diameter, shank length, flute length, and helix angle). Endmills 1-3 were machined from aluminum blanks so that the cross-sectional geometry was explicitly known; the geometry for the commercial endmill (identified as endmill 4) was determined by sectioning through EDM.

Table 8.1: Properties of the endmills used for validation experiments (all parameters except the helix angle were measured using digital calipers with a resolution of 0.01 mm).

	Endmill 1	Endmill 2	Endmill 3	Endmill 4
Shank diameter (mm)	38.20	38.17	38.20	12.66
Shank length (mm)	101.35	102.98	77.66	66.40
Flute length (mm)	201.14	175.23	200.44	84.41
Helix angle (mm)	30	30	30	30
Material	Aluminum	Aluminum	Aluminum	Carbide

8.3.1 Description of endmill geometries

The accuracy, and thus effective application, of the 3D-ST solution for macro-endmills requires accurate knowledge of the geometry and material parameters of the endmills. In particular, cross-sectional geometry, twist rate, and the geometry of the transition region (from the shank to the fluted portion) must be well known. To facilitate evaluation of the 3D-ST model for well-known geometries and for a range of geometric parameters, a set of aluminum endmills (test endmills) were fabricated using five-axis machining. Since the aluminum endmills were described using a 3D solid model (SolidWorks®), their geometry was accurately defined within the accuracy of the manufacturing technique. The cross-sectional geometry of the endmills are given in Fig. 8.5(a).

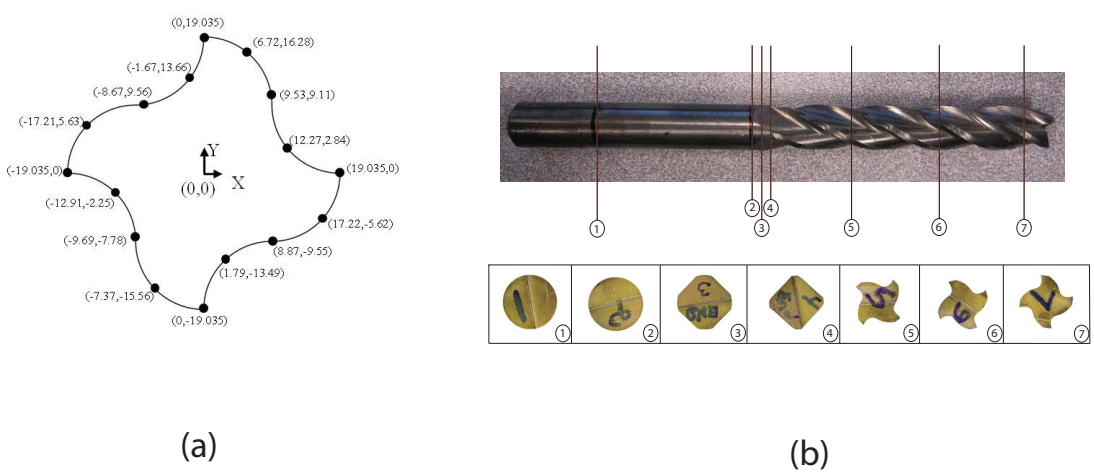

Figure 8.5: Cross-section of **a)** endmills 1-3 (coordinates are provided in mm), **b)** endmill 4.

To enable further assessment of the 3D-ST solution, a commercial (solid) carbide endmill (endmill 4) was selected for testing. However, the detailed information about the cross-sectional geometry was not available. Therefore, the endmill was sectioned by EDM, and

the cross-section was imaged at several locations, as shown in Fig. 8.5(b). To identify the boundaries (periphery), MATLAB® image-processing toolbox was then used to identify the boundaries (periphery), and sample points along the periphery were extracted to define the cross-section.

8.3.2 Experimental setups and conditions

To determine the natural frequencies of the aluminum endmills, the FRFs of the endmills were obtained by impact testing. Fig. 8.6 shows the experimental procedure used to obtain the bending and torsional natural frequencies of the endmill. To approximate the unconstrained boundary conditions, the endmills were placed on a soft foam. The very low stiffness of the foam base relative to the endmills provided a reasonable approximation for unconstrained (free-free) boundary conditions. The FRFs were measured by exciting them using a miniature impact hammer (PCB 0841A17, sensitivity 46.95 N/V) and recording the corresponding vibration using a low mass accelerometer (PCB 352C23, sensitivity 1727 m/Vs^2).

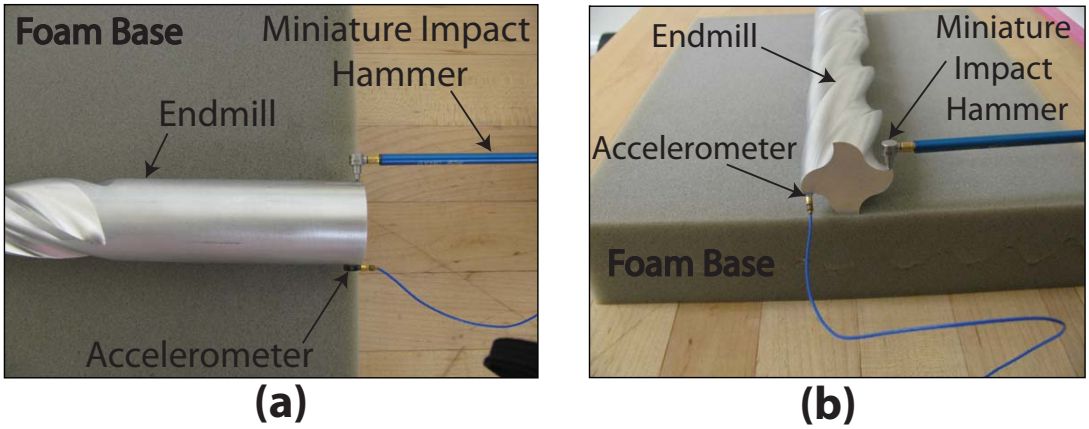

Figure 8.6: Impact hammer experimentation setup: **a)** Direct FRF measurement at the endmill shank end **b)** Torsional measurement.

Depending on the locations of the accelerometer and hammer impact, direct and cross FRFs, H_{ij}, were obtained, where i and j represents the measurement and force locations, respectively. For instance, in the configuration shown in Fig. 8.6(a), the accelerometer was placed at the shank end, and the force was applied at the same location (from the other side of the endmill). Therefore, the direct FRF at the endmill's shank end was obtained.

Figure 8.6(b) shows the experimental procedure used to identify the torsional natural

frequencies. The endmill was excited by applying the force to one flute in the tangential direction and the response was recorded in the same direction using an accelerometer placed on the opposite flute. In these experiments both the bending and the torsional natural frequencies were excited. The results for the first eight natural frequencies were recorded.

The resonant frequencies of the solid carbide endmill span a considerably wider range than those of the aluminum endmills. Therefore, the hammer impact test described above cannot be effectively used to determine the first eight natural frequencies of endmill 4.

Figure 8.7(a) shows the experimental setup used for obtaining the natural frequencies of the solid carbide endmill. The endmill was suspended using flexible elastic bands from two sections along its length to approximate unconstrained boundary conditions. The dynamic excitations within a frequency range of 0-40 kHz were provided using a 3 mm by 4 mm piezoelectric element with a 125 μm thickness. As shown in Fig. 8.7(b), the piezoelectric element was glued onto the macro endmill shank. When a voltage is applied, the piezoelectric element expands and contracts along its polarization axis. A pseudo-random excitation having a range of 0-40 kHz with 140 V amplitude was supplied to the piezoelectric element. For each experiment, 50 measurements of 0.320 seconds each were completed and averaged to eliminate unbiased noise.

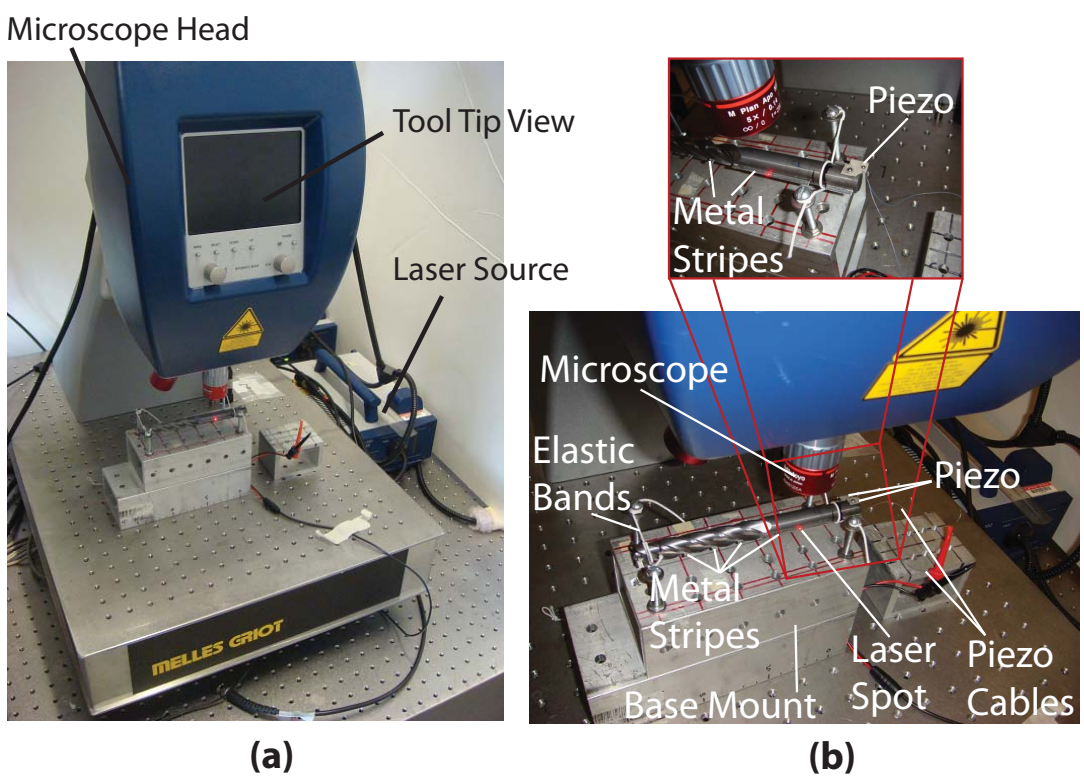

Figure 8.7: Experimental setup for endmill 4 (carbide endmill).

Table 8.2: Endmill material properties.

	E (GPa)	$\rho\,(\frac{kg}{m^3})$	ν
Aluminum	70	2700	0.33
Carbide	580	14500	0.24

The response is measured using an LDV system (Polytec® MSA-400) with two fiber-optic laser sources. Each fiber-optic laser source splits into a pair of channels and, therefore, both relative and absolute measurements can be performed. During the experiments, the fiber-optic laser sources were fed through a microscope to reduce the laser-beam spot sizes. For the measurements presented in this study, a 5X objective is used to obtain a spot size of 2.8 μm was used.

The axis of the endmill is located in the vicinity of the nodal line of the torsional motions. Therefore, measurements along the axis of the endmill does not provide accurate determination of the torsional modes. To facilitate measuring the torsional modes, metal strips (0.22 mm by 3.12 mm) were glued to the sides of the macro endmill. The response measured from the metal strips amplifies the torsional motions, thereby enabling accurate determination of torsional/axial natural frequencies.

8.4 Alternative Modeling Techniques for Comperative Analysis

In this section, two alternative approaches for modeling the dynamics of the Table 8.1 endmills are described. The main purpose of this study is to provide a comparative analysis of the 3D-ST technique with two other popular solution approaches. First, a FE solution of the endmill dynamics using a commercial solver is outlined. Next, simplified 1D solution of the endmill dynamics using four different equivalent cross-section formulations is provided.

8.4.1 Finite element modeling (FEM) of macro-endmills

Using the geometry of the four endmills, FE models were constructed. Analysis were performed on the meshed solid model of each endmill using the commercial software ANSYS® Workbench (SOLID186 elements). Table 8.2 lists the material properties (Young's modulus E, density, ρ, and Poisson's ratio, ν). Modal analysis was used to identify the natural frequencies.

The convergence of the FE model was evaluated for all endmills based on the changes in the second torsional natural frequency to ensure that a sufficient number of elements were included. Table 8.3 summarizes the convergence study for the FE model of endmill 1. The convergence study was performed in a consecutive way, where the percent change in natural frequencies were calculated between the two consecutive FE simulations taking the finer meshed model as reference.

Table 8.3: Convergence study for endmill 1 from Table 8.1.

Second torsional natural frequency (Hz)	Number of nodes	Number of elements	% change in natural frequencies with increasing number of nodes
7776.5	3056	578	—
7756.3	4077	792	-0.26
7746.3	7226	1485	-0.13
7742.4	20689	4488	-0.05
7739.3	22454	4828	-0.04

8.4.2 Equivalent diameter approach

One of the common approaches to describe the dynamics of the fluted section is to approximate it as a uniform circular cross-section beam with an equivalent diameter. Four methods were applied to calculate this diameter: **(1)** the cross-sectional area; **(2)** the area moment of inertia of the cross-section; **(3)** the volume; and **(4)** the mass.

1. The cross-sectional area of the fluted portion, A_f, was obtained from the solid model (endmills 1-3) or analysis of cross-section image (endmill 4) and the corresponding equivalent diameter, d_{eq_A}, was calculated using

$$d_{eq_A} = \sqrt{\frac{4\,A_f}{\pi}}. \tag{8.8}$$

2. The area moment of inertia for the modeled cross-section of the fluted portion, I_f, was determined and the equivalent diameter, d_{eq_I}, was calculated using

$$d_{eq_I} = \left(\frac{64\,I_f}{\pi}\right)^{\frac{1}{4}}. \tag{8.9}$$

3. The volume of the fluted section, V_f, was obtained and the equivalent diameter was

determined by Eq. (8.10).

$$d_{eq_V} = \sqrt{\frac{4\,V_f}{\pi\,L_f}} \tag{8.10}$$

4. The mass of the endmill, m, can be expressed as the sum of the mass of the shank (first expression on the left hand side of Eq. (8.11)) and the mass of the fluted portion (second expression)

$$\rho\,\frac{\pi\,d_s^2\,L_s}{4} + \rho\,\frac{\pi\,d_{eq_M}^2\,L_f}{4} = m, \tag{8.11}$$

where d_{eqM} is the equivalent diameter of the fluted portion. By weighing the endmill and substituting nominal value for the density and geometry of the endmill, the equivalent diameter was calculated according to Eq. (8.12). The benefit of this approach is that no tool model is required, unlike the first three methods.

$$d_{eq_M} = \sqrt{\frac{4}{\pi\,L_f}\left(\frac{m}{\rho} - \frac{\pi\,d_s^2\,L_s}{4}\right)} \tag{8.12}$$

Table 8.4 lists the equivalent diameter (in mm) calculated by the four methods for the four endmills.

Table 8.4: Equivalent diameter of endmills.

	d_{eq_A} (mm)	d_{eq_I} (mm)	d_{eq_V} (mm)	d_{eq_M} (mm)
Aluminum	30.40	31.10	30.96	31.55
Carbide	9.90	10.10	9.95	9.92

8.5 Modal Assessment

8.5.1 Comparison of tool modeling techniques

In this section, the natural frequencies obtained using modal testing, the ST method, and FE simulations are compared to assess the accuracy of the 3D-ST technique for modeling endmill dynamics. Table 8.5 provides the natural frequencies from 3D-ST, FEM, and experimentation, as well as the percent differences between the modes obtained from different methods. The labeled mode shapes (as bending or torsional/axial) are identified according

to the calculated deformations. The bending modes are represented by B_{ij} where i is the mode number and j is the principal direction of deformation. The coupled torsional-axial modes are represented by TA_i where i is the mode number.

Table 8.5: Comparison of the experimental and predicted natural frequencies

Endmill 1	B_{11}	B_{12}	B_{21}	B_{22}	TA_1	B_{31}	B_{32}	TA_2
Experiment (Hz)	1426	1430	4059	4068	4218	7530	7543	7777
FE (Hz)	1400	1403	4000	4002	4115	7484	7492	7739
3D-ST (Hz)	1404	1407	4007	4023	4091	7486	7497	7750
Difference (%) between ST and FEM	0.28	0.32	0.17	0.53	-0.60	0.03	0.06	0.14
Difference (%) between FE and Experiment	-1.81	-1.92	-1.45	-1.62	-2.42	-0.61	-0.68	-0.49
Difference (%) between ST and Experiment	-1.54	-1.60	-1.28	-1.10	-3.00	-0.58	-0.62	-0.34

Endmill 2	B_{11}	B_{12}	TA_1	B_{21}	B_{22}	TA_2	B_{31}	B_{32}
Experiment (Hz)	1710	1717	4716	4802	4811	8558	8698	8719
FE (Hz)	1691	1691	4606	4776	4776	8523	8673	8674
3D-ST (Hz)	1690	1695	4583	4772	4790	8563	8665	8680
Difference (%) between ST and FEM	-0.06	0.22	-0.51	-0.08	0.30	0.47	-0.09	0.07
Difference (%) between FE and Experiment	-1.12	-1.47	-2.32	-0.55	-0.72	-0.40	-0.28	-0.52
Difference (%) between ST and Experiment	-1.18	-1.26	-2.81	-0.63	-0.43	0.06	-0.37	-0.45

Endmill 3	B_{11}	B_{12}	TA_1	B_{21}	B_{22}	TA_2	B_{31}	B_{32}
Experiment (Hz)	1634	1638	4414	4588	4596	8412	8602	8615
FE (Hz)	1611	1611	4349	4523	4524	8286	8556	8558
3D-ST (Hz)	1612	1615	4315	4529	4551	8293	8561	8568
Difference (%) between ST and FEM	0.07	0.21	-0.79	0.13	0.60	0.09	0.06	0.13
Difference (%) between FE and Experiment	-1.40	-1.64	-1.46	-1.42	-1.57	-1.49	-0.54	-0.66
Difference (%) between ST and Experiment	-1.34	-1.43	-2.24	-1.30	-0.98	-1.41	-0.48	-0.54

Endmill 4	B_{11}	B_{12}	B_{21}	B_{22}	TA_1	B_{31}	B_{32}	TA_2
Experiment (Hz)	2487	2487	7343	7343	11273	13515	13515	20071
FE (Hz)	2463	2471	7242	7248	11365	13283	13336	20143
3D-ST (Hz)	2486	2495	7271	7272	11384	13337	13393	20163
Difference (%) between ST and FEM	0.93	0.98	0.40	0.33	0.17	0.41	0.43	0.10
Difference (%) between FE and Experiment	-0.96	-0.64	-1.37	-1.29	0.82	-1.72	-1.33	-0.36
Difference (%) between ST and Experiment	-0.05	0.33	-0.98	-0.96	0.99	-1.32	-0.91	0.46

For each of the endmills, the percent errors between the ST method and experimentation are seen to be less than 3.0%. This small difference between the 3D-ST and experimental natural frequencies could be the result of differences between the modeled and actual geometry and the non-uniform/inaccurate material properties. Furthermore, it is observed that the largest errors occur in the first torsional mode, which suggests that it is the most sensitive mode to geometric uncertainties. A comparison between natural frequencies from

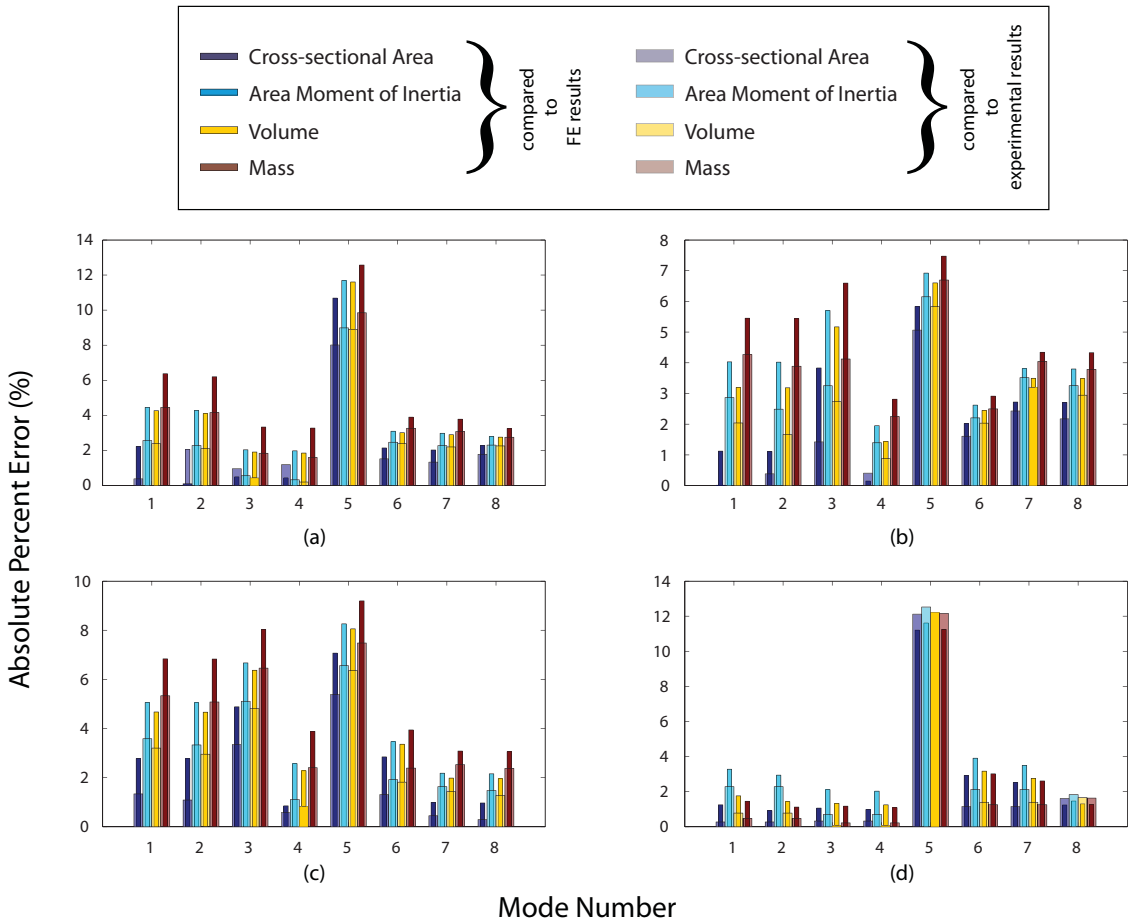

Figure 8.8: Absolute percent errors of the approximate methods for **a)** Endmill 1; **b)** Endmill 2; **c)** Endmill 3; **d)** Endmill 4.

the 3D-ST and FEM results, on the other hand, show a difference less than 0.8% for all four endmills and modes. This good match between the 3D-ST and FEM results, which use identical geometries and material properties, also supports this hypothesis. It should be noted that the dynamic response is very sensitive to the geometry of the transition region. Therefore, it is critical to accurately capture this geometry.

For a more in-depth assessment of the 3D-ST model, the MAC was used [99, 100] to compare the mode shapes with the ones obtained from FE simulations. Accordingly, a minimum MAC value of 0.855, 0.993, 0.966, and 0.931 and the average MAC values of 0.975, 0.995, 0.992, and 0.989 are obtained for endmills 1, 2, 3, and 4, respectively.

The equivalent diameter simplification for the twisted fluted section of the tool was also evaluated. Figure 8.8 provide the percent errors for each of the approximate methods with respect to the results of the FEM results for each mode.

Table 8.6: Carbide endmill/blank and holder material properties.

	$E\,(GPa)$	$\rho\,(\frac{kg}{m^3})$	ν
Tool	580	14500	0.24
Holder	200	7800	0.29

The general trend of the percent errors was similar for each tool model. Comparing the different approximation methods, the most accurate equivalent diameter was obtained using the cross-sectional area and the least accurate approach was the method based on the endmill mass. Also, considering all four approximation methods for each mode, the largest errors ($> 10\%$) was observed for the first torsional mode. Furthermore, the approximation errors depend strongly on the particular geometric parameters of the endmills. Therefore, these approximations should be used carefully. The 3D-ST modeling approach presented in this study avoids such errors while retaining numerical efficiency.

8.6 Tool Point Measurements and Predictions

Tool point measurements were performed and predictions were completed on a Mikron UCP-600 Vario five-axis machining center. Predictions and measurements of the tool point FRFs are presented here for three different overhang lengths (118.7 mm, 124.78 mm, and 127.59 mm) of endmill 4 (150.8 mm total length) inserted in a steel tapered thermal shrink fit holder. The tool point FRFs were measured by exciting the tool tip with a miniature impact hammer (PCB 0841A17, sensitivity 46.95 N/V) and recording the corresponding vibration with a low mass accelerometer (PCB 352C23, sensitivity 1727 m/Vs^2). Also, measurements were performed with the same shrink fit holder using a carbide blank of approximately the same length as the endmill (152.8 mm). The overhang lengths of the blank were adjusted to match the three overhang lengths of the tool. Figure 8.9 shows the dimensions of the holder and blank for an overhang length of 127.68 mm. Table 8.6 lists the tool and holder material properties used for modeling both the endmill and blank. The component model for one blank-holder combination is shown in Fig. 8.10, and the corresponding dimensions are listed in Table 8.7. Figure 8.11 shows the comparison of the measured and the predicted carbide blank tool-point FRF for three different overhang lengths.

It is observed in Fig. 8.11 that the predicted natural frequencies are higher than those from the experiments. This is attributed to the assumption of a rigid connection between the tool and the holder at coordinate 2 in Fig. 8.12. Since no connection is rigid in reality,

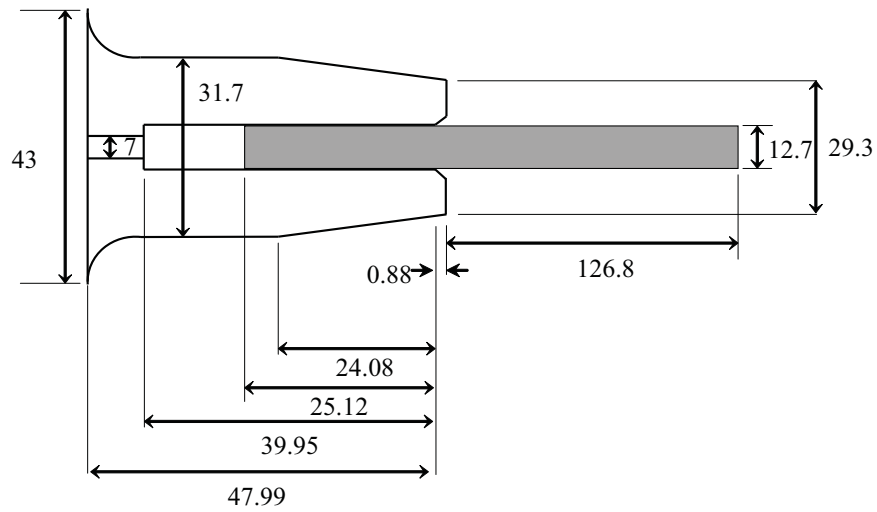

Figure 8.9: Holder and blank dimensions for 127.68 mm overhang length (All dimensions are in mm).

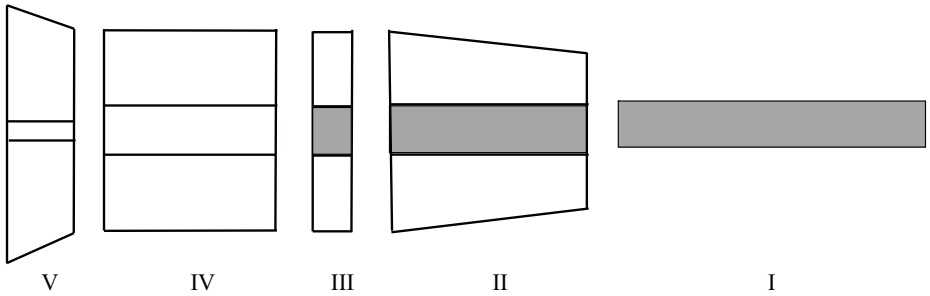

Figure 8.10: Blank-holder model components.

Table 8.7: Component dimensions for 127.68 mm overhang length.

Dimensions (mm)	Component				
	V	IV	III	II	I
Outer diameter (d_0), left	43	31.7	31.7	31.7	12.7
Outer diameter (d_0), right	31.7	31.7	31.7	29.3	12.7
Inner diameter (d_i), left	7	12.7	12.7	12.7	0
Inner diameter (d_i), right	7	12.7	12.7	12.7	0
Length, L	8.04	14.83	1.04	24.08	127.68

a flexible connection between the tool and the holder was implemented.

The flexible coupling of the components is carried out in two steps: **(1)** the spindle-machine is first rigidly coupled to the holder and the portion of the shank inside the holder; **(2)** the holder-spindle-machine component is then flexibly coupled to the blank outside the

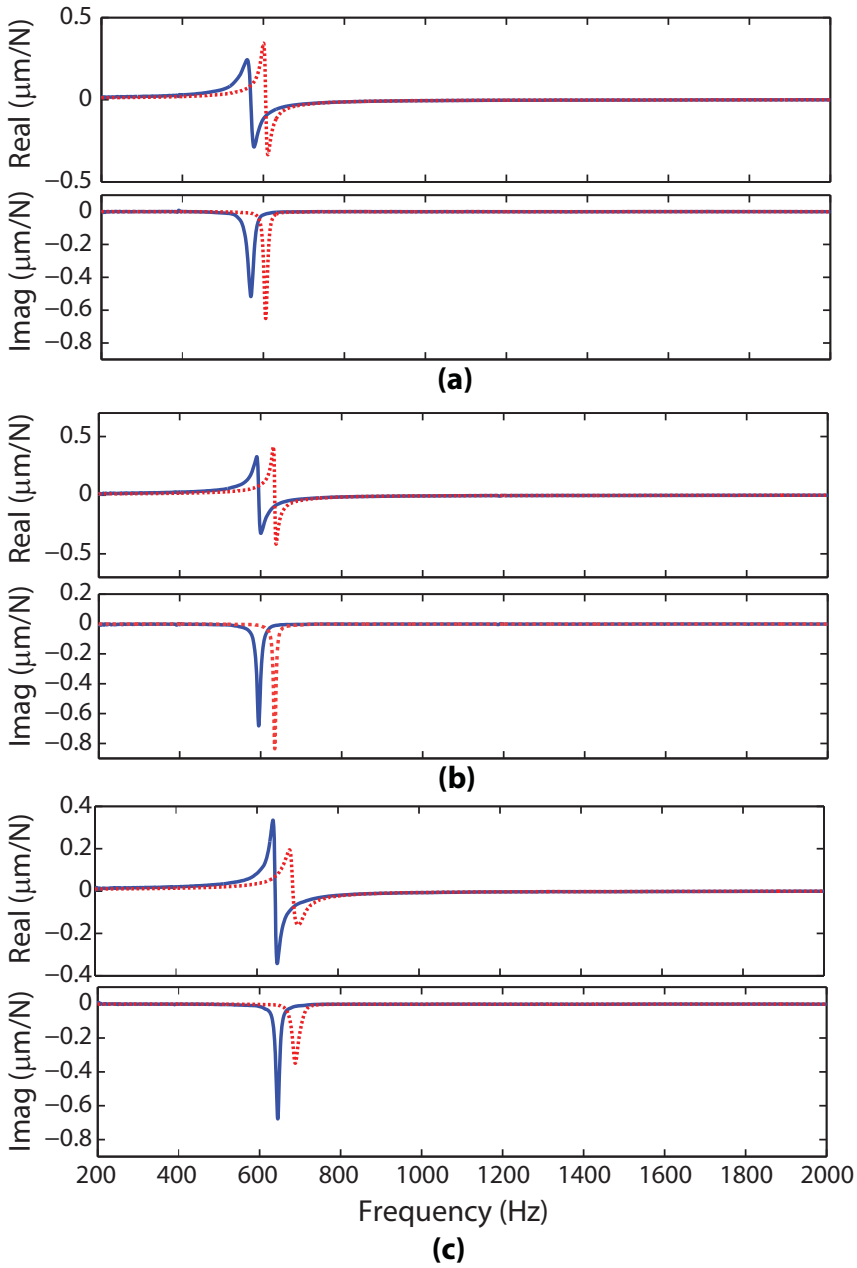

Figure 8.11: Measured (solid line) and predicted (dotted line) tool point FRFs for the carbide tool blank with overhang lengths of: **a)** 127.68 mm; **b)** 124.35 mm; and **c)** 118.62 mm (rigid connection).

holder using translational and rotational spring constants assembled in the stiffness matrix k. The RCSA equation for the flexible coupling tool point FRF in case of the blank is provided in Eq. (8.13). The stiffness matrix [133] is given by Eq. (8.14), where k_{xf}, $k_{\theta f}$, k_{xm}, and $k_{\theta m}$ are the displacement-to-force, rotation-to-force, displacement-to-moment, and rotation-to-moment stiffness values, respectively ($k_{\theta f}$ and k_{xm} were assumed equal due to

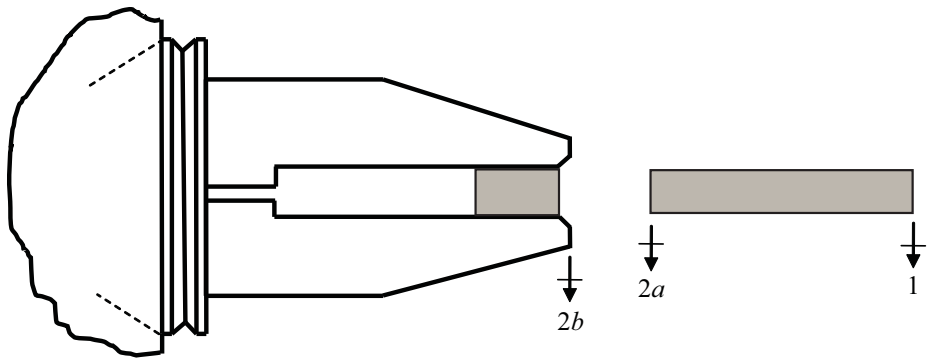

Figure 8.12: Component coordinates for flexible coupling in case of blank.

reciprocity).

$$G_{11}(\omega) = R_{11}(\omega) - R_{12a}(\omega)\left[R_{2b2b}(\omega) + R_{2a2a}(\omega) + \frac{1}{k}\right]^{-1} R_{2a1}(\omega) \tag{8.13}$$

$$k = \begin{bmatrix} k_{xf} & k_{xm} \\ k_{\theta f} & k_{\theta m} \end{bmatrix} \tag{8.14}$$

To identify the stiffness matrix, one overhang length of the blank (124.35 mm) was considered and an optimization procedure based on a genetic algorithm was implemented. The variables were the three stiffness values, and the objective function to be minimized is given by Eq. (8.15), where the difference between the imaginary parts of the measured (m) and predicted (p) tool point FRFs was squared and summed over all frequencies within the range of interest.

$$min\left[\sqrt{\sum\left(Im(H_m) - Im(H_p)\right)^2}\right] \tag{8.15}$$

The k matrix values obtained by this approach (see Table 8.8) were used to predict the tool point FRFs for other overhang lengths of the blank as well as the endmill. The comparison of the measurements and predictions for the three overhang lengths of the carbide blank is shown in Fig. 8.13. Table 8.9 lists the percent errors between the measured and predicted natural frequencies.

Table 8.10: Percent error between measurement and prediction for the carbide endmill.

	Percent error (%) in natural frequency	
Overhang length (mm)	Rigid Coupling	Flexible coupling
127.59	10.1	2.5
124.78	10.2	4.0
118.70	10.4	3.6

Table 8.8: Stiffness matrix values.

k_{xf} (N/m)	$k_{\theta f}$ (N/rad)	$k_{\theta m}$ (Nm/rad)
3.05x10^6	3.07x10^6	0

Table 8.9: Percent error between measurement and prediction.

	Percent error (%) in natural frequency	
Overhang length (mm)	Rigid Coupling	Flexible coupling
127.68	6.3	0.18
124.35	6.6	0
118.62	6.7	0.26

The stiffness values given in Table 8.8 were used to predict the THSM assembly tool point FRFs for the carbide endmill with different overhang lengths. Figure 8.14 shows the measured and predicted results. The percent errors of the predicted natural frequency with respect to the measured values for three overhang lengths are listed in Table 8.10.

8.7 Summary and Conclusion

This chapter presented new modeling results for the 3D dynamic behavior of macro-scale milling tools using the ST technique. The actual complex cross-sectional geometry and the pretwisted shape of endmills were taken into account during modeling. The bending and torsional behavior of three endmills with known cross-section was modeled and verified against both FE models and experiments (impact testing with free-free boundary conditions). Model validation was also performed for a commercial carbide endmill. The difference between the experiments and the ST method predictions was seen to be less than

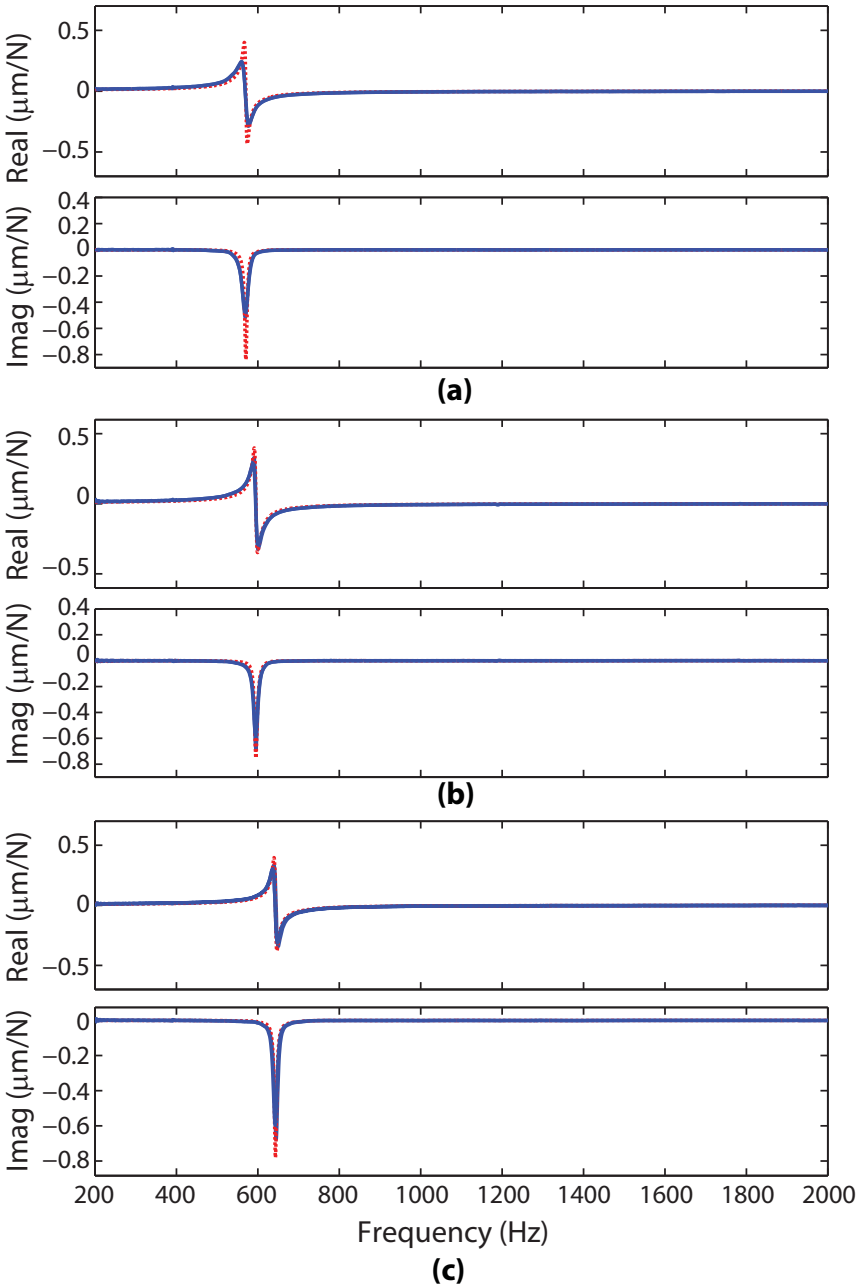

Figure 8.13: Measured (solid line) and predicted (dotted line) tool point FRFs for the carbide tool blank with overhang lengths of: **a)** 127.68 mm; **b)** 124.35 mm; and **c)** 118.62 mm (flexible connection).

3% for all the four tools for the first six bending modes and first two torsional/axial modes. The natural frequencies from the FE model and the 3D-ST method were seen to match with less than 1% difference.

To demonstrate the application of the modeling approach, the 3D-ST model of a com-

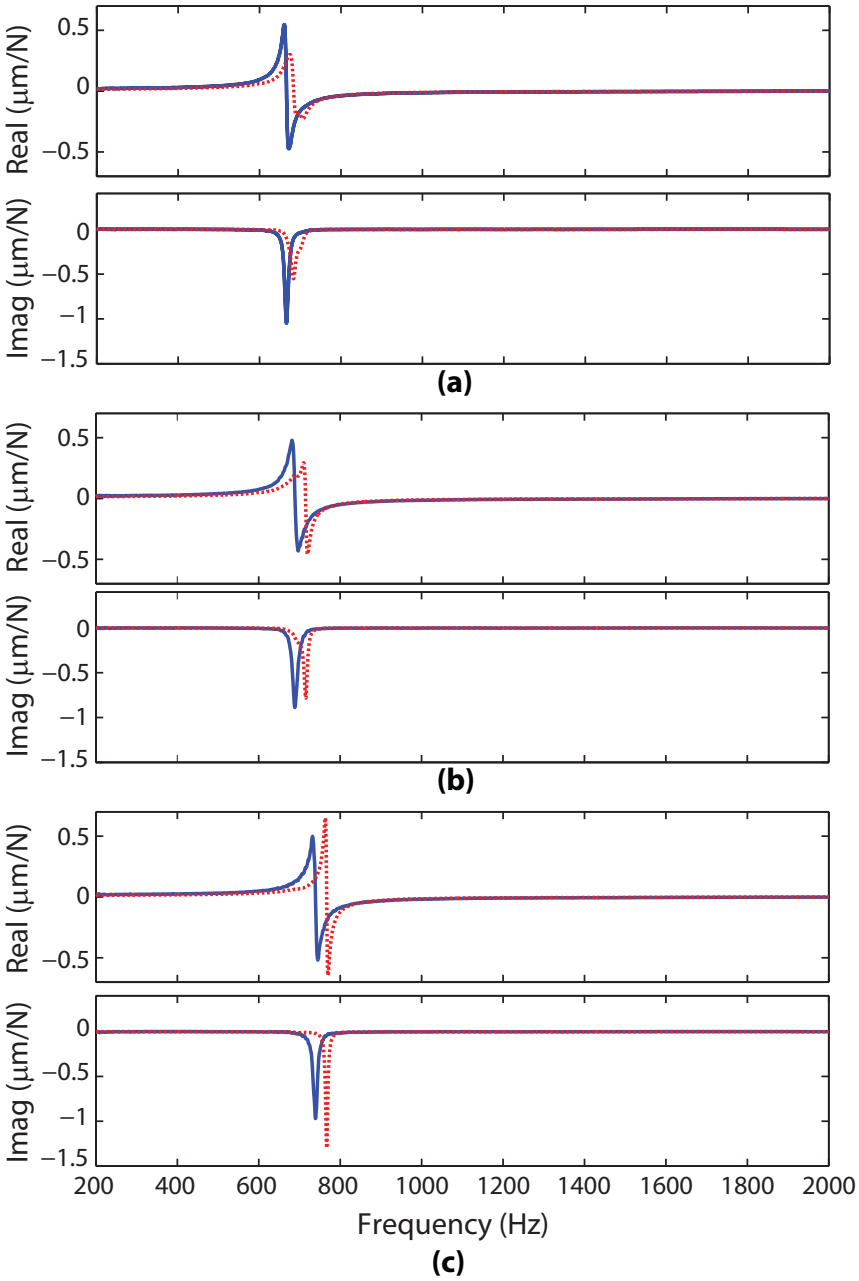

Figure 8.14: Measured (solid line) and predicted (dotted line) tool point FRFs for the carbide endmill with overhang lengths of: **a)** 127.59 mm; **b)** 124.78 mm; and **c)** 118.7 mm (flexible connection).

mercial carbide endmill was coupled to the Timoshenko beam model of a shrink fit holder and the measured spindle receptances using RCSA. The tool point measurements and predictions were compared for three different overhang lengths. A flexible connection between the tool and the holder was implemented, where the holder-tool interface stiffness values were determined using a carbide blank and a genetic algorithm-based optimization tech-

nique. The stiffness values were used to predict the tool point FRFs of other blanks with different overhang lengths, as well as the endmill with various overhang lengths. The maximum error between the natural frequency of the tool point measurement and prediction was less than 1% for the carbide blank and less than 4% for the aluminum endmills.

Chapter 9

Summary and Conclusions

"Every end is a new beginning."

-Proverb

Micromachining dynamics commonly dictate the attainable accuracy and throughput that can be obtained from micromachining operations. To understand the micromachining dynamics, in this thesis, it is aimed to construct new modeling techniques and develop an experimental methodology to predict, understand, and analyze the vibrational behavior of micro-scale cutting tools and miniature UHS spindles. Although the presented solution technique and experimental methodology could be applied to determine the dynamics of other complex structures (such as rotor blades, wind turbines, etc.), the presented work was specifically focused on understanding the dynamics of micromachining processes, which is central to understanding the process stability.

In the modeling part of the work, first, a series based solution approach, the three-dimensional (3D) spectral Tchebychev (3D-ST) based technique (that uses 3D elasticity equations), is derived to predict the (coupled) 3D dynamics of pretwisted structures. Then, the developed solution technique is advanced further to predict the rotational dynamics of rotating/spinning (complex) structures. And finally, the dynamics of (rotating) cutting tools is investigated, and the natural frequencies and mode shapes are compared to those found from finite element (FE) simulations. Based on the modeling work, the following specific conclusions are obtained:

- The developed 3D-ST technique enables accurate and computationally efficient solutions for the coupled 3D linear/nonlinear dynamics of stationary and rotating complex structures (including pretwisted structures having curved cross-sections).

- The natural frequencies and mode shapes found from the 3D-ST solution are in excellent agreement with those found from 3D-FEM solutions. The differences between the natural frequencies are found to be less than 1% for each investigated structure, the MAC values are always greater than 0.9 for all the modes investigated. However, due to the exponential convergence characteristics of Tchebychev polynomials, the computational cost of the 3D-ST approach is at least three-to-four times lower than that of the 3D-FEM approach.

- Although the 1D/2D solution approaches give accurate results for simple geometries such as beams and thin plates, large errors in predicting natural frequencies are observed when predicting the dynamics of (rotating/stationary) pretwisted structures. Instead, the 3D-ST solution can be used to attain accurate solutions without appreciable increase in computational cost.

- Since the 3D-ST approach uses 3D elasticity equations and the actual geometry of the structure, the cross-sectional stress, strain, and deformation distributions for a given operational deflection shape can be obtained; and thus, provides important insights into vibrational characteristics of pretwisted beam.

- To demonstrate the application of the developed ST approach in obtaining high-fidelity dynamic models of cutting tools, *first*, the (rotational dynamics) dynamics of micro-scale cutting tools are predicted. In the modeling approach, the shank and taper sections (that have simple circular cross-sections) of the micro endmills are modeled with 1D-ST approach derived by Yagci *et al.* [29], and the fluted region is modeled with the developed 3D-ST technique. The change of natural frequencies with rotation speed is investigated and compared with FE results. The maximum difference in natural frequencies and minimum MAC number obtained from the two solution approaches are calculated to be less than 1% and greater than 0.9995, respectively. Furthermore, the system matrices obtained using the presented approach are used to model the dynamic behavior in response to arbitrary force inputs, and thus, orbital motions of the micro endmill tip is investigated for different tool attachment configurations and at different spindle speeds and tooth-passing frequencies.

  Second, to show one of the broader impacts of the developed ST technique in this thesis, a collaborative research was performed with T. Schmitz (Professor of Mechanical Engineering and Engineering Science Department in University of North Carolina Charlotte). In this work, the dynamics of macro-scale cutting tools are modeled with the developed ST solution approach. The derived model of cutting macro-scale tools

were validated through the comparison of the 3D-ST results to those found by FE simulations and modal experiments. In this study, also a demonstration of the modeling approach to obtain the tool tip dynamics was presented by coupling the tool dynamics with the experimentally obtained spindle dynamics using receptance coupling substructure analysis (RCSA). It was observed that the maximum error between the natural frequency of the tool point measurement and prediction was less than 1% for the carbide blank and less than 4% for the aluminum endmills.

In the second part of the thesis, a new experimental methodology is devised to enable modal testing of miniature UHS spindles while rotating. It is shown that the experimental work has been successful in characterizing the speed-dependent two-dimensional dynamics of miniature UHS spindles. To overcome the limitations of the conventional modal testing techniques considering providing the excitation force, a novel impact excitation system (IES) is designed and constructed. The corresponding dynamic response is measured via two-fiber optic LDVs. Furthermore, since the modal tests are performed while the spindle is rotating, a frequency domain filtering approach is developed and implemented to isolate the dynamic response of the spindle to the excitation force. Based on the experimental work, the following specific conclusions are obtained:

- The constructed impact excitation system (IES) enables obtaining repeatable, high frequency bandwidth, and controlled force excitation to (miniature) structures. The application of the IES is demonstrated several structures, including characterizing miniature contact probes, miniature dynamometers [134], and miniature UHS spindles. For all cases, accurate and repeatable FRFs (even for anti-resonance regions while modal testing of stationary structures) are obtained up to 25 kHz bandwidth.

- The presented experimental methodology is demonstrated on a miniature air-bearing UHS spindle rotating up to 170,000 rpm, and enabled accurate identification of the two-dimensional speed-dependent dynamics within a 20 kHz bandwidth in the form of FRFs with uncertainties less than 3% for the entire frequency bandwidth (note that for the resonance regions, the uncertainty is less than 1%).

- It is observed that the natural frequencies and associated damping ratios are highly affected by the spindle speed.

To sum up, the research presented in this thesis has two main outcomes: **(1)** the fundamental part (developed 3D-ST modeling approach) enables accurately and efficiently predicting the 3D dynamic behavior of 3D structures (including the gyroscopic effects) seen

in many engineering applications, **(2)** the application of the developed modeling technique and the experimental methodology (to investigate the rotating spindle dynamics) sheds light on the effect of rotational speed on micromachining dynamics, and thus, enables effective methods to control and minimize the vibrations during micromachining processes to increase the dimensional and surface quality.

Chapter 10

Future Work

"Always in motion is the future."

-Yoda (The Empire Strikes Back)

The research conducted as a part of this thesis enabled analytical and experimental techniques/tools to better understand the dynamics of rotating (micro-scale) cutting tools and miniature UHS spindles. The future work of this research can be divided into two categories. The first category constitutes the future plans regarding the dynamics of micromachining processes including obtaining the tool-tip dynamics to investigate the micromachining dynamics and to correlate the process parameters with the performance metrics (such as geometrical quality) and process throughput. The second category constitutes the future goals to improve the versatility and robustness of the developed ST technique such that a spectral-based modeling software can be developed (similar to commercially available FE software). The specific work for each of the categories is described in the following sections.

10.1 Future Work Regarding the Micromachining Dynamics

10.1.1 Creating and evaluating a 3D dynamic characterization approach for UHS spindles

As described in Chapter 7, the spindle dynamics is obtained using a two-axis measurement. However, the experimental methodology can be extended to identify the 3D dynamic response of UHS spindles at different spindle speeds and collet torques to include the axial vibrations of the spindle. To address this, a short custom made (carbide) artifact, that has

a short (approximately a few millimeters) section with a larger radius at the end face of the artifact, can be attached to the spindle. In addition to the impact tests performed along the x and y directions at multiple z positions, additional impact tests will be performed exciting the structure at the end face of the artifact enabling investigating the axial vibrations of the spindles.

10.1.2 Characterizing and modeling dynamics of different miniature UHS spindles at varying spindle speeds

The developed experimental methodology (Chapter 7) can be used to characterize the dynamics of different UHS spindles at various spindle speeds, collet torques, and artifact lengths inside the collet. The FRFs obtained through the experiments will provide information to understand how spindle speed, collet torque, and artifact length inside the collet affect the dynamics of different UHS spindles. Also, to construct a dynamic model for the UHS spindle, a global multi-DOF complex curve fitting approach based on the orthogonal Forsythe polynomial [129] can be used.

10.1.3 Combining the dynamics of the micro-scale cutting tools and miniature UHS spindles

The 3D dynamic behavior of rotating micro-tools with their complex geometry, and their coupling with the spindle dynamics, are critical for determining the dynamic response at the tool tip. To combine experimentally obtained UHS spindle dynamics with the 3D rotating micro-tool dynamics models, 3D substructure synthesis techniques (either in frequency or in spatial domain) should be applied. In Chapter 8, it is shown that for the macro-scale scale case, the tool tip dynamics can be obtained by coupling the analytically obtained tool dynamics with the experimentally obtained spindle dynamics through receptance coupling substructure analysis (RCSA). However, experimental application and evaluation of this approach must be completed for predicting 3D dynamics at the micro-tool tip.

10.1.4 Constructing a simulation framework incorporating spindle error motions and machining dynamics

The inherent error motions of UHS spindles and the centering (tool-attachment) errors result in non-ideal radial, axial, and tilt motion of the tool tip. These motions are functions of the rotation angle, and include components at fundamental (spindle) frequency, its integer

multiples (synchronous), and non-integer multiples (asynchronous). The commonly considered tool-tip runout does not fully capture either the frequencies or the angular variations of these motions, and only refers to a constant amplitude (the total indicator reading-TIR). Anandan *et al.* [20, 124] showed that the non-ideal motions are strong functions of the spindle type (air or contact bearing), and can be sufficiently large to impose significant limitations to attainable dimensional and surface quality due to the deviation of the axis of rotation.

Besides the rotating-unbalance type excitation due to the spindle error motions, during machining cutting forces also act on the micro-tools; thereby coupling the non-ideal motions and dynamic behavior, resulting in complex dynamic motions of the tool tip. This coupling may be very significant for micromachining processes considering the high rotational speeds experienced and high flexibility of the micro-scale cutting tools. Furthermore, if a simulation framework is constructed, vibrations, forces, and surface quality during micro-machining processes can be predicted to fully understand the dynamic behavior at the micro-tool tip.

10.1.5 Investigating the stability of the micromachining processes

To analyze the micromachining dynamics and perform stability analysis, the combined 3D dynamic model of the micro-tool/UHS spindle system should be integrated with the non-ideal motions of UHS spindles and a mechanistic cutting force model. The combined model can be validated through direct measurements from the rotating micro-tool tip. Furthermore, stability analyses can be performed for various micro-tool/spindle combinations and corresponding stability lobe diagrams can be obtained. The stability lobe diagrams basically give stable cutting parameters; depth of cut and spindle speed. To validate the obtained stable cutting parameters, machining experiments can be performed.

10.2 Future Work Regarding the Developed ST Technique

It is highly challenging to predict the dynamics of (assembled) structures that are too large or complex to be analyzed as a whole. In this thesis, it has been shown that the developed spectral-Tchebychev technique provides accurate and highly efficient dynamic models of structures. However, to address the challenge of predicting the dynamics of assembled structures, the already developed spectral-Tchebychev technique should be improved to be more versatile and robust. To achieve this goal, first, a substructuring algorithm needs to be implemented to divide a complex structure into minimum/optimal number of simpler

geometries. Furthermore, the ST technique should be improved to predict the dynamics of

- two-dimensional structures (such as plates and shells) to increase the numerical efficiency,
- hollow 3D structures,
- spiral structures, where the structure's axis is not straight,
- structures having anisotropic material properties.
- structures having geometric and material nonlinearities.

Besides increasing the capabilities of the ST approach, its robustness should also be advanced such that

- cross-section mapping to different geometries should be developed (e.g., triangular or circular mapping algorithms),
- an automated mapping algorithm should be implemented,
- solutions should also be able to be performed on polar coordinates.

Bibliography

[1] B. Bediz, E. Korkmaz, R. Khilwani, C. Donahue, G. Erdos, L. Falo Jr., O. B. Ozdoganlar, Dissolvable microneedle arrays for intradermal delivery of biologics: Fabrication and application, Pharmaceutical Research 31 (1) (2014) 117–135.

[2] S. Filiz, L. Xie, L. E. Weiss, O. B. Ozdoganlar, Micromilling of microbarbs for medical implants, International Journal Machine Tools and Manufacture 48 (3-4) (2008) 459–472.

[3] T. D. Y. Kozai, Z. Gugel, X. Li, P. J. Gilgunn, R. Khilwani, O. B. Ozdoganlar, G. K. Fedder, D. J. Weber, X. T. Cui, Chronic tissue response to carboxymethyl cellulose based dissolvable insertion needle for ultra-small neural probes, Biomaterials 35 (2014) 9255–9268.

[4] S. Supekar, B. A. Gozen, B. Bediz, O. B. Ozdoganlar, S. J. Skerlos, Feasibility of supercritical carbon dioxide based metalworking fluids in micromilling, Journal of Manufacturing Science and Engineering 135 (2013) 024501.

[5] H. H. Yoo, C. Pierre, Modal characteristic of a rotating rectangular cantilever plate, Journal of Sound and Vibration 259 (1) (2003) 81–96.

[6] F. K. Ehmann, D. Bourell, M. L. Culpepper, T. J. Hodgson, T. R. Kurfess, M. Madou, K. Rajuskar, R. E. Devor, International assessment of research and development in micromanufacturing, Technical Report (2005).

[7] P. Salomon, Nexus market analysis report for MEMS and micro-systems, Technical Report (2005).

[8] X. Liu, R. E. DeVor, S. G. Kapoor, K. F. Ehmann, The mechanics of machining at the microscale: Assessment of the current state of the science, Journal of Manufacturing Science and Engineering 126 (4) (2004) 666–678.

[9] J. Tlusty, Manufacturing Processes and Equipment, Prentice Hall, Upper Saddle River, NJ, 2000.

[10] T. L. Schmitz, K. S. Smith, Machining Dynamics: Frequency Response to Improved Productivity, Springer, New York, NY, 2009.

[11] M. B. G. Jun, X. Liu, R. E. DeVor, S. G. Kapoor, Investigation of the dynamics of microend milling — Part I: Model development, Journal of Manufacturing Science and Engineering 128 (4) (2006) 893–900.

[12] M. P. Vogler, R. E. DeVor, S. G. Kapoor, Microstructure-level force prediction model for micro-milling of multi-phase materials, Journal of Manufacturing Science and Engineering 125 (2) (2003) 202–209.

[13] N. Fang, P. Dewhurst, Slip-line modeling of built-up edge formation in machining, International Journal of Mechanical Sciences 47 (7) (2005) 1079–1098.

[14] X. Liu, R. E. DeVor, S. G. Kapoor, An analytical model for the prediction of minimum chip thickness in micromachining, Journal of Manufacturing Science and Engineering 128 (2) (2006) 474–481.

[15] M. B. G. Jun, C. Goo, M. Malekian, S. Park, A new mechanistic approach for micro end milling force modeling, Journal of Manufacturing Science and Engineering 134 (1) (2012) 011006.

[16] K. W. Kim, W. Y. Lee, H.-C. Sin, A finite element analysis for the characteristics of temperature and stress in micro-machining considering the size effect, International Journal of Machine Tools and Manufacture 39 (9) (1999) 1507–1524.

[17] Y. Cao, Y. Altintas, A general method for the modeling of spindle-bearing systems, Journal of Mechanical Design 126 (6) (2004) 1089–1104.

[18] Y. Altintas, G. Stepan, D. Merdol, Z. Dombovari, Chatter stability of milling in frequency and discrete time domain, CIRP Journal of Manufacturing Science and Technology 1 (2008) 35–44.

[19] T. L. Schmitz, J. C. Ziegert, C. Stanislaus, A method for predicting chatter stability for systems with speed-dependent spindle dynamics, in: Aerospace Engineering Transactions of the North American Manufacturing Research Institute of SME, Vol. 32, 2004, pp. 17–24.

[20] K. P. Anandan, O. B. Ozdoganlar, An LDV-based methodology for measuring axial and radial error motions when using miniature ultra-high-speed (UHS) micromachining spindles, Precision Engineering 37 (2013) 172–186.

[21] T. L. Schmitz, M. A. Davies, M. D. Kennedy, Tool point frequency response prediction for high-speed machining by RCSA, Journal of Manufacturing Science and Engineering 123 (4) (2001) 700.

[22] O. Tekinalp, A. Ulsoy, Modeling and finite element analysis of drill bit vibrations, Journal of Vibration, Acoustics, Stress, and Reliability in Design 111 (2) (1989) 148–155.

[23] T. L. Schmitz, G. S. Duncan, Three-component receptance coupling substructure analysis for tool point dynamics prediction, Journal of Manufacturing Science and Engineering 127 (4) (2005) 781–790.

[24] K. Subrahmanyam, J. Rao, Coupled bending-bending vibrations of pretwisted tapered cantilever beams treated by the Reissner method, Journal of Sound and Vibration 82 (4) (1982) 577–592.

[25] D. Hodges, Torsion of pretwisted beams due to axial loading, Technical Report, National Aeronuatics and Space Administration (1980).

[26] J. K. Knowles, E. Reissner, Torsion and extension of helicoidal shells, Applied Mathematics 27 (4) (1960) 409–422.

[27] S. Filiz, O. B. Ozdoganlar, A three-dimensional model for the dynamics of micro-endmills including bending, torsional and axial vibrations, Precision Engineering 35 (1) (2011) 24–37.

[28] B. Bediz, U. Kumar, T. Schmitz, O. B. Ozdoganlar, Modeling and experimentation for three-dimensional dynamics of endmills, International Journal of Machine Tools and Manufacture 53 (2012) 39–50.

[29] B. Yagci, S. Filiz, L. A. Romero, O. B. Ozdoganlar, A spectral-Tchebychev technique for solving linear and nonlinear beam equations, Journal of Sound and Vibration 321 (1-2) (2009) 375–404.

[30] S. Filiz, L. A. Romero, O. B. Ozdoganlar, An analytical model for micro-endmill dynamics, Journal of Vibration and Control 14 (8) (2008) 1125–1150.

[31] B. Dawson, Coupled bending-bending vibrations of pre-twisted cantilever blading treated by the Rayleigh-Ritz energy method, Journal of Mechanical Engineering Science 10 (5) (1968) 381–388.

[32] A. Rosen, Structural and dynamic behavior of pretwisted rods and beams, Applied Mechanics Reviews 44 (1991) 483–515.

[33] J. Rao, The fundamental flexural vibration of a cantilever beam of rectangular cross section with uniform taper, Aeronautical Quarterly 16 (1965) 139–144.

[34] W. Carnegie, J. Thomas, The coupled bending-bending vibration of pre-twisted tapered blading, Journal of Engineering Industry 94 (1) (1972) 255–266.

[35] E. Mayrab, D. Gilsinn, Buckling loads and natural frequencies of drill bits and fluted cutters, Journal of Engineering Industry 106 (3) (1984) 196–204.

[36] A. Rosen, R. Loewy, M. Mathew, Use of twisted principal coordinates and non-physical coordinates in blade analysis, Vertica 11 (3) (1987) 541–572.

[37] M. L. Chen, Y. S. Liao, Vibrations of pretwisted spinning beams under axial compressive loads with elastic constraints, Journal of Sound and Vibration 147 (3) (1991) 497–513.

[38] J. Banerjee, Free vibration analysis of a twisted beam using the dynamic stiffness method, International Journal of Solids and Structures 38 (2001) 6703–6722.

[39] Y. Gong, K. Ehmann, C. Lin, Analysis of dynamic characteristics of micro-drills, Journal of Materials Processing Technology 141 (1) (2003) 16–28.

[40] T. H. Young, C. Y. Gau, Dynamic stability of spinning pretwisted beams subjected to axial random forces, Journal of Sound and Vibration 268 (1) (2003) 149–165.

[41] B.-W. Huang, The drilling vibration behavior of a twisted microdrill, Journal of Manufacturing Science and Engineering 126 (4) (2004) 719–726.

[42] R. Gupta, S. Rao, Finite element eigenvalue analysis of tapered and twisted Timoshenko beams, Journal of Sound and Vibration 56 (2) (1978) 187–200.

[43] B. Yardimoglu, T. Yildirim, Finite element model for vibration analysis of pre-twisted Timoshenko beam, Journal of Sound and Vibration 273 (2004) 741–754.

[44] S. Ho, C. Chen, Free transverse vibration of an axially loaded non-uniform spinning twisted Timoshenko beam using differential transform, International Journal of Mechanical Sciences 48 (11) (2006) 1323–1331.

[45] S. Filiz, O. B. Ozdoganlar, Microendmill dynamics including the actual fluted geometry and setup errors — Part I: Model development and numerical solution, Journal of Manufacturing Science and Engineering 130 (3) (2008) 031120.

[46] S. Filiz, A. Tulsian, N. Kota, O. B. Ozdoganlar, Obtaining the speed-dependent dynamics of an ultra-high-speed miniature spindle through experimental modal analysis, in: International Conference on Micromanufacturing, 2008.

[47] A. Rosen, Theoretical and experimental investigation of the nonlinear torsion and extension of initially twisted bars, ASME Transactions Journal of Applied Mechanics 50 (1983) 321–326.

[48] D. H. Hodges, Nonlinear equations for dynamics of pretwisted beams undergoing small strains and large rotations, Technical Report, National Aeronuatics and Space Administration Moffett Field CA AMES Research Center (1985).

[49] S. Balhaddad, D. Onipede. Jr, Three-dimensional free vibration of pretwisted beams, AIAA Journal 36 (8) (1998) 8–12.

[50] A. Rosen, The effect of initial twist on the torsional rigidity of beams — Another point of view, ASME Transactions Journal of Applied Mechanics 47 (1980) 389–392.

[51] S. Krenk, A linear theory for pretwisted elastic beams, Journal of Applied Mechanics 50 (1983) 137–142.

[52] S. Filiz, O. B. Ozdoganlar, Coupled torsional-axial vibrations of micro- and macro-drills, in: Transactions of NAMRI/SME, 2009, pp. 57–65.

[53] K.-C. Liu, J. Friend, L. Yeo, The axialtorsional vibration of pretwisted beams, Journal of Sound and Vibration 321 (2009) 115–136.

[54] P. V. Bayly, S. A. Metzler, A. J. Schaut, K. A. Young, Theory of torsional chatter in twist drills: Model, stability analysis and composition to test, Journal of Manufacturing Science and Engineering 123 (4) (2001) 552.

[55] J. Roukema, Y. Altintas, Time domain simulation of torsionalaxial vibrations in drilling, International Journal of Machine Tools and Manufacture 46 (15) (2006) 2073–2085.

[56] S. K. Sinha, Combined torsional-bending-axial dynamics of a twisted rotating cantilever Timoshenko beam with contact-impact loads at the free end, Journal of Applied Mechanics 74 (3) (2007) 505–522.

[57] S. Filiz, O. B. Ozdoganlar, A model for bending, torsional, and axial vibrations of micro- and macro-drills including actual drill geometry — Part I: Model development and numerical solution, Journal of Manufacturing Science and Engineering 132 (4) (2010) 041017.

[58] S. Filiz, O. B. Ozdoganlar, A model for bending, torsional, and axial vibrations of micro- and macro-drills including actual drill geometry — Part II: Model validation and application, Journal of Manufacturing Science and Engineering 132 (4) (2010) 041018.

[59] S. Filiz, B. Bediz, L. A. Romero, O. B. Ozdoganlar, A spectral-Tchebychev solution for three-dimensional vibrations of parallellepipeds under mixed boundary conditions, Journal of Applied Mechanics 79 (5) (2012) 051012.

[60] M. Sari, E. A. Butcher, Natural frequencies and critical loads of beams and columns with damaged boundaries using Chebyshev polynomials, International Journal of Engineering Science 48 (2010) 862–873.

[61] G. Genta, Dynamics of Rotating Systems, Springer Science+Business Media, New York, NY, 2005.

[62] S. H. Hashemi, S. Farhadi, S. Carra, Free vibration analysis of rotating thick plates, Journal of Sound and Vibration 323 (2009) 366–384.

[63] G. Genta, M. Silvagni, On centrifugal softening in FEM rotordynamics, Journal of Applied Mechanics 81 (2013) 1–10.

[64] L. Li, D. Zhang, W. Zhu, Free vibration analysis of a rotating hubfunctionally graded material beam system with the dynamic stiffening effect, Journal of Sound and Vibration 333 (5) (2014) 1526–1541.

[65] C.-L. Liao, Y.-H. Dang, Structural characteristics of spinning pretwisted orthotropic beams, Computers and Structures 44 (4) (1992) 715–731.

[66] H. Lee, Dynamic stability of spinning pre-twisted beams, International Journal of Solids and Structures 31 (18) (1994) 2509–2517.

[67] N. Popplewell, D. Chang, Free vibrations of a stepped, spinning Timoshenko beam, Journal of Sound and Vibration 203 (4) (1997) 717–722.

[68] S. D. Yu, W. L. Cleghorn, Free vibration of a spinning stepped Timoshenko beam, Journal of Applied Mechanics 67 (2000) 839–841.

[69] S. C. Lin, K. M. Hsiao, Vibration analysis of a rotating Timoshenko beam, Journal of Sound and Vibration 240 (2) (2001) 303–322.

[70] J. Banerjee, H. Su, D. Jackson, Free vibration of rotating tapered beams using the dynamic stiffness method, Journal of Sound and Vibration 298 (2006) 1034–1054.

[71] S. Filiz, B. Bediz, L. A. Romero, O. B. Ozdoganlar, Three dimensional dynamics of pretwisted beams with curved cross-sections: A spectral-Tchebychev solution, Journal of Sound and Vibration 333 (2014) 2823–2839.

[72] H. H. Yoo, S. K. Kim, Flapwise bending vibration of rotating plates, International Journal for Numerical Methods in Engineering 55 (7) (2002) 785–802.

[73] S. M. Hashemi, M. J. Richard, A new dynamic finite element (DFE) formulation for lateral free vibrations of Euler-Bernoulli spinning beams using trigonometric shape functions, Journal of Sound and Vibration 220 (4) (1999) 601–624.

[74] M. Rantatalo, J. Aidanpää, B. Göransson, P. Norman, Milling machine spindle analysis using FEM and non-contact spindle excitation and response measurement, International Journal of Machine Tools and Manufacture 47 (7-8) (2007) 1034–1045.

[75] M. S. Kumar, Rotor dynamic analysis using ANSYS, in: K. Gupta (Ed.), IUTAM Symposium on Emerging Trends in Rotor Dynamics, Vol. 1011 of IUTAM Bookseries, Springer Netherlands, Dordrecht, 2011.

[76] C. C.-H. Cheng, T. L. Schmitz, G. S. Duncan, Rotating tool point frequency response prediction using RCSA, Machining Science and Technology 11 (2004) (2007) 433–446.

[77] B. Bediz, E. Korkmaz, B. A. Gozen, O. B. Ozdoganlar, Dynamic characterization of a miniature ultra-high-speed (UHS) spindle through experimental modal analysis, in: Proceedings of the 12th euspen International Conference, 2012.

[78] A. Erturk, H. N. Ozguven, E. Budak, Analytical modeling of spindle-tool dynamics on machine tools using Timoshenko beam model and receptance coupling for the prediction of tool point FRF, International Journal of Machine Tools and Manufacture 46 (15) (2006) 1901–1912.

[79] K. Gupta, O. B. Ozdoganlar, S. G. Kapoor, R. E. DeVor, Modeling and prediction of hole profile in drilling, Part 2: Modeling hole profile, Journal of Manufacturing Science and Engineering 125 (1) (2003) 14.

[80] E. B. Kivanc, E. Budak, Structural modeling of end mills for form error and stability analysis, International Journal of Machine Tools and Manufacture 44 (11) (2004) 1151–1161.

[81] P. Albertelli, M. Goletti, M. Monno, A new receptance coupling substructure analysis methodology to improve chatter free cutting conditions prediction, International Journal of Machine Tools and Manufacture 72 (2013) 16–24.

[82] J. Tian, S. G. Hutton, Chatter instability in milling systems with flexible rotating spindles — A new theoretical approach, Journal of Manufacturing Science and Engineering 123 (1) (2001) 1–9.

[83] C. H. Chen, K. W. Wang, Y. C. Shin, An integrated approach toward the dynamic analysis of high-speed spindles, Part I: System model, Journal of Vibration and Acoustics 116 (1994) 506–513.

[84] G. L. Xiong, J. M. Yi, C. Zeng, H. K. Guo, L. X. Li, Study of the gyroscopic effect of the spindle on the stability characteristics of the milling system, Journal of Materials Processing Technology 138 (2003) 379–384.

[85] E. R. Marsh, Precision Spindle Metrology, Destech Publications, Inc., 2nd edition, 2009.

[86] C. J. Wilson, D. B. Bogy, An experimental modal analysis technique for miniature structures, Journal of Vibration and Acoustics 118 (1) (1996) 1–9.

[87] O. B. Ozdoganlar, B. D. Hansche, T. G. Carne, Experimental modal analysis for microelectromechanical systems, Experimental Mechanics 45 (6) (2005) 498–506.

[88] S. Filiz, C. M. Conley, M. B. Wasserman, O. B. Ozdoganlar, An experimental investigation of micro-machinability of copper 101 using tungsten carbide micro-endmills, International Journal of Machine Tools and Manufacture 47 (2007) 1088–1100.

[89] S. S. Park, R. Rahnama, Robust chatter stability in micro-milling operations, CIRP Annals - Manufacturing Technology 59 (1) (2010) 391–394.

[90] V. Aran, E. Budak, An experimental study on dynamics and stability of miniature end mills, Advanced Materials Research 223 (2011) 869–878.

[91] X. Jin, Y. Altintas, Chatter stability model of micro-milling with process damping, Journal of Manufacturing Science and Engineering 135 (3) (2013) 031011.

[92] O. B. Ozdoganlar, B. D. Hansche, T. G. Carne, Modal testing techniques for microelectromechanical systems (MEMS), in: Proc. 4th International Symposium on MEMS and Nanotechnology, 2003, pp. 124–129.

[93] Y. F. Chou, L. C. Wang, On the modal testing of microstructures: Its theoretical approach and experimental setup, Transactions of the ASME 123 (1) (2001) 104–109.

[94] S. W. Lee, R. Mayor, J. Ni, Dynamic analysis of a mesoscale machine tool, Journal of Manufacturing Science and Engineering 128 (1) (2006) 194–203.

[95] L. Meirovitch, Fundamentals of Vibrations, McGraw Hill, 2001.

[96] J. P. Boyd, Chebyshev and Fourier Spectram Methods, second edi Edition, Dover, New York, NY, 2001.

[97] D. Gottlieb, S. A. Orszag, Numerical Analysis of Spectral Methods, Theory and Applications, SIAM-CBMS, Philedelphia, PA, 1977.

[98] E. B. Becker, Finite Elements Volume 1 - An Introduction, Prentice-Hall, New Jersey, 1986.

[99] R. J. Allemang, The modal assurance criterion – Twenty years of use and abuse, International Journal of Engineering Science 37 (2003) 14–23.

[100] D. J. Ewins, Modal Testing: Theory, Practice and Application, Research Studies Press, 2000.

[101] H. H. E. Leipholz, Theory of Elasticity, Noordhoff International Publishing, Leyden, 1974.

[102] P. Marugabandhu, J. H. Griffin, A reduced-order model for evaluating the effect of rotational speed on the natural frequencies and mode shapes of blades, Journal of Engineering for Gas Turbines and Power 125 (2003) 772–776.

[103] P. Nair, S. Durvasula, On quasi-degeneracies in plate vibration problems, International Journal of Mechanical Sciences 15 (12) (1973) 975–986.

[104] D. Greenwood, Principles of Dynamics, Englewood Cliffs, NJ:Prentice Hall, 1965.

[105] S. Liu, G. Trenkler, Hadamard, khatri-rao, kronecker and other matrix products, International Journal of Information and Systems Sciences 4 (1) (2008) 160–177.

[106] E. Carrera, S. Brischetto, P. Nali, Classical Plate/Shell Theories, in Plates and Shells for Smart Structures: Classical and Advanced Theories for Modeling and Analysis, John Wiley & Sons, Chichester, UK, 2011.

[107] B. Bediz, K. Uttara, O. B. Ozdoganlar, T. L. Schmitz, Three-dimensional endmill dynamics: Modal development and experimental validation, in: MSEC, 2011, pp. 1–8.

[108] R. M. Lin, W. J. Wang, Structural dynamics of microsystems – Current state of research and future directions, Mechanical Systems and Signal Processing 20 (5) (2006) 1015–1043.

[109] L. Hermans, H. Van Der Auweraer, Modal testing and analysis of structures under operational conditions: Industrial applications, Mechanical Systems and Signal Processing 13 (2) (1999) 193–216.

[110] K. A. Ramsey, Experimental modal analysis, structural modifications and FEM analysis on a desktop computer, Sound and Vibration 17 (2) (1983) 19–27.

[111] Agilent, The fundamentals of modal testing, Technical Report (2000).

[112] J. S. Burdess, A. J. Harris, D. Wood, R. J. Pitcher, D. Glennie, A system for the dynamic characterization of microstructures, Journal of Microelectromechanical Systems 6 (4) (1997) 322–328.

[113] T. W. Wu, C.-K. K. Lee, R. H. Wang, Micro-impact technique and its applications., in: Materials Research Society Symposium, Vol. 308, 1993, pp. 133–139.

[114] A. Akay, T. Hodgson, Acoustic radiation from the elastic impact of a sphere with a slab, Applied Acoustics 11 (4) (1978) 285–304.

[115] D. Gugan, Inelastic collision and the Hertz theory of impact, American Journal of Physics 68 (10) (2000) 920–924.

[116] W. Goldsmith, Impact — The Theory and Physical Behaviour of Colliding Solids, Edward Arnold (Publishers) Ltd; First Edition edition, 1960.

[117] G. Gilardi, Literature survey of contact dynamics modeling, Mechanism and Machine Theory 37 (10) (2002) 1213–1239.

[118] PCB, PCB Piezotronics, Model 086E80 - Miniature impact hammer specification sheet, Technical Report (2012).

[119] N. F. Smith, D. M. Tanner, S. E. Swanson, S. L. Miller, Non-destructive resonant frequency measurement on MEMS actuators, 39th Annual International Reliability Physics Symposium (2001) 99–105.

[120] P. J. Gary, Flexure Devices, British Scientific Instruments Research Association, 1954.

[121] J. D. Kraus, D. A. Fleisch, Electromagnetics: with Applications, McGraw Hill, 1999.

[122] H. Lankarani, Continuous contact force models for impact analysis in multibody systems, Nonlinear Dynamics 5 (1994) 193–207.

[123] ASME B89.3.4 2010, Axes of rotation: Methods for specifying and testing, Technical Report (2010).

[124] K. P. Anandan, A. S. Tulsian, A. Donmez, O. B. Ozdoganlar, A technique for measuring radial error motions of ultra-high-speed miniature spindles used for micromachining, Precision Engineering 36 (1) (2011) 104–120.

[125] S. S. Sattinger, A method for experimentally determining rotational mobilities of structures, in: Proceedings of International Modal Analysis Conference, 1980, pp. 167–181.

[126] C. L. Groover, M. W. Trethewey, K. P. Maynard, M. S. Lebold, Removal of order domain content in rotating equipment signals by double resampling, Mechanical Systems and Signal Processing 19 (3) (2005) 483–500.

[127] H. S. Kim, T. L. Schmitz, Bivariate uncertainty analysis for impact testing, Measurement Science and Technology 18 (11) (2007) 3565–3571.

[128] B. D. Hall, On the propagation of uncertainty in complex-valued quantities, Metrologia 41 (3) (2004) 173–177.

[129] M. H. Richardson, D. L. Formenti, Parameter estimation from frequency response measurements using rational fraction polynomial, in: Proceedings of International Modal Analysis Conference, 1982, pp. 167–181.

[130] E. Swanson, C. D. Powell, S. Weissman, A practical review of rotating machinery critical speeds and modes, Sound and Vibration (2005) 10–17.

[131] H. Irretier, F. Reuter, Experimental modal analysis of rotating disk systems, in: Design Engineering Technical Conferences, 1995, pp. 1201–1206.

[132] K. M. Medicus, T. L. Schmitz, Evaluating the tool point dynamic repeatability for high-speed machining applications, in: Proceedings of the 16th Annual ASPE Meeting, Vol. 19, 2001, pp. 357–360.

[133] T. L. Schmitz, K. Powell, D. Won, G. S. Duncan, W. G. Sawyer, J. Ziegert, Shrink fit tool holder connection stiffness/damping modeling for frequency response prediction in milling, International Journal of Machine Tools and Manufacture 47 (9) (2007) 1368–1380.

[134] E. Korkmaz, B. Bediz, B. A. Gozen, O. B. Ozdoganlar, Dynamic characterization of multi-axis dynamometers, Precision Engineering 38 (1) (2013) 148–161.